

Thermodynamics and Kinetics of Hydrogen Sulfide Corrosion of Mild Steel at Elevated  
Temperatures

A dissertation presented to  
the faculty of  
the Russ College of Engineering and Technology of Ohio University

In partial fulfillment  
of the requirements for the degree  
Doctor of Philosophy

Shujun Gao

August 2018

© 2018 Shujun Gao. All Rights Reserved.

This dissertation titled  
Thermodynamics and Kinetics of Hydrogen Sulfide Corrosion of Mild Steel at Elevated  
Temperatures

by  
Shujun Gao

has been approved for  
the Department of Chemical and Biomolecular Engineering  
and the Russ College of Engineering and Technology by

Marc Singer  
Assistant Professor of Chemical and Biomolecular Engineering

Dennis Irwin  
Dean, Russ College of Engineering and Technology

## Abstract

Shujun Gao, Ph.D., August 2018, Chemical Engineering

### Thermodynamics and Kinetics of Hydrogen Sulfide Corrosion of Mild Steel at Elevated Temperatures

Director of Dissertation: Marc Singer

As geologic environments associated with oil and gas production have become increasingly aggressive, aqueous corrosion at high temperatures in the presence of hydrogen sulfide ( $H_2S$ ) is more frequently encountered. The understanding of sour corrosion mechanisms is an important but still largely elusive target, especially at high temperatures. The purpose of this project is to explore the thermodynamics and kinetics of  $H_2S$  corrosion at high temperature, and to develop a thermodynamic model to predict the corrosion product layer formation, as well as a mechanistic kinetic model to predict the corrosion rate of mild steel at high temperature in the presence of  $H_2S$ .

The first part of the project focused on the development of experimental and safety procedures to investigate layer formation and corrosion mechanisms in high temperature environments. This included the development and validation of a water chemistry model for a closed system especially designed to properly control the experimental parameters.

In the second part of this project, the effects of temperature (80~200°C), exposure time (1~21 days), and partial pressure of  $H_2S$  (0.1~2.0 bar) were thoroughly investigated. Significant and somehow unexpected findings were obtained:

- A  $\text{Fe}_3\text{O}_4$  layer was always identified on the steel surface although this type of corrosion products was thermodynamically less stable than FeS.  $\text{Fe}_3\text{O}_4$  formed very fast at the initial stage of corrosion and was responsible for the quick decrease of the corrosion rate.
- The  $\text{Fe}_3\text{O}_4$  layer experienced a continuous process of formation (due to corrosion at the steel/ $\text{Fe}_3\text{O}_4$  interface) and conversion to iron sulfide (at the  $\text{Fe}_3\text{O}_4$ /FeS interface). The transformation of the outer iron sulfide layer was also observed at high temperature and thoroughly documented for the first time. The general transformation sequence was identified as mackinawite  $\rightarrow$  troilite  $\rightarrow$  pyrrhotite  $\rightarrow$  pyrite. With the increase of temperature, time, and partial pressure of  $\text{H}_2\text{S}$ , iron sulfide transformed to thermodynamic more stable state. The roles of these different layers in corrosion were also examined and discussed.
- The outer FeS layers also formed via a precipitation mechanism from the bulk solution.

An overall mechanism for the corrosion of carbon steel in high temperature  $\text{H}_2\text{S}$  environments was proposed based on the experimental observations. Existing thermodynamic and kinetic models were adapted following a mechanistic approach and validation was performed with experimental data. By keeping the formation region of  $\text{Fe}_3\text{O}_4$  in an  $\text{H}_2\text{S}$  environment, the main modification to the formation region of  $\text{Fe}_3\text{O}_4$  in an  $\text{H}_2\text{S}$  environment. The kinetics of  $\text{Fe}_3\text{O}_4$  formation and conversion were determined experimentally and were successfully incorporated into the mechanistic kinetic model. Corrosion

trends and rates, as well as layers thickness could be predicted with relative accuracy (less than 20% error).

## Dedication

*To*

*My parents, Yiyin Gao, Ronglian Zhang*

*My sisters, Meijuan Gao, Lijuan Zhang*

*And all other family members*

## Acknowledgments

I would like to express my deep appreciation to my Ph.D. advisor, Dr. Marc Singer, for his dedication, direction, and guidance for this project. He devoted himself to every stage of this project, from proposal to experimental design, from results interpretation to paper writing. I have learned a lot from him and grown toward mature in academics and personality. I appreciate his help and supervision from the bottom of my heart.

I would like to take this chance to thank Dr. Bruce Brown, my project leader for his help and advice for the research. He is always so patient and never gets mad at the mistakes I made. I appreciate the help and guidance from Dr. Srdjan Nesic. His profound knowledge leads me always in the right direction. Special thanks go to Dr. Yoon-Seok Choi for his help in the modeling part. My research was also benefited a lot from the involvement and discussion of Dr. David Young and Dr. Peng Jin. Thank you all!

I give my thanks to Alexis Barxias, Cody Shafer, Becky Gill, Martin Colahan, Izzy Anyanwu, Juan Dominguez Olivo, Saba Esmaeely, etc., for your help and support. Thanks to all the staff and students at ICMT. I could not have 'survived' from H<sub>2</sub>S without you!

The members of my graduate committee including Dr. Jason Trembly, Dr. Dina Lopez, and Dr. Rebecca Barlag are highly appreciated for their hard working for reviewing this dissertation.

I express my thanks to the sponsor companies for their financial support and research academic advisory.

Last but not least, my deep love and appreciation to my parents, Yiyin Gao and Ronglian Zhang, and my beautiful twin sisters, Meijuan Gao and Lijuan Zhang. They always stand behind me and support me throughout my Ph.D. study.

## Table of Contents

	Page
Abstract .....	3
Acknowledgments.....	7
List of Tables .....	14
List of Figures .....	16
Nomenclature .....	25
Chapter 1. Introduction .....	28
Chapter 2: Literature Review.....	30
2.1 CO <sub>2</sub> Corrosion of Steel at Elevated Temperatures .....	30
2.2 H <sub>2</sub> S Corrosion of Steel at Low Temperatures (< 80°C) .....	31
2.3 H <sub>2</sub> S Corrosion of Steel at High Temperatures (> 80°C).....	33
2.4 Polymorphous Iron Sulfides and Related Phases.....	36
Chapter 3: Objectives.....	41
3.1 Research Gaps and Objectives.....	41
3.2 Hypotheses .....	42
Chapter 4: Water Chemistry Model for H <sub>2</sub> S-H <sub>2</sub> O System at High Temperatures.....	44
4.1 Introduction.....	44
4.2 Model Development.....	44
4.3 Parametric Study.....	47
Chapter 5: Effect of High Temperature on the Kinetics of Corrosion and Layer Formation on Mild Steel in Sour Environments.....	50
5.1 Introduction.....	50

	10
5.2 Experimental .....	50
5.3 Results and Discussion .....	55
5.3.1 Corrosion rates .....	55
5.3.2 Corrosion products .....	57
5.3.3 Surface profilometry .....	61
5.3.4 Formation of iron oxide .....	63
5.3.5 Formation of iron sulfide .....	65
5.4 Summary .....	69
Chapter 6: Effect of Exposure Time on the Formation and Transformation among Iron Sulfide and Iron Oxide Layers at High Temperature.....	
	70
6.1 Introduction.....	70
6.2 Experimental.....	70
6.3 Results and Discussion .....	71
6.3.1 Corrosion rates .....	71
6.3.2 Outer iron sulfide layer content .....	73
6.3.3 Inner iron oxide layer.....	80
6.3.4 Surface profilometry .....	87
6.4 Summary .....	88
Chapter 7: Formation Mechanisms of Iron Oxide and Iron Sulfide at High Temperature in Aqueous H <sub>2</sub> S Corrosion Environments .....	
	89
7.1 Introduction.....	89
7.2 Hypotheses .....	89

	11
7.3 Experimental .....	90
7.4 Results and Discussion .....	93
7.4.1 Sequence of Fe <sub>3</sub> O <sub>4</sub> /FeS formation .....	93
7.4.2 Iron sulfide formation mechanism .....	106
7.4.3 Descriptive model for the Fe <sub>3</sub> O <sub>4</sub> /FeS formation mechanisms at high temperature .....	109
7.5 Summary .....	111
Chapter 8: Effect of H <sub>2</sub> S Partial Pressure on the Corrosion Rate and Layer Formation on Mild Steel at High Temperature .....	113
8.1 Introduction .....	113
8.2 Experimental .....	114
8.3 Results and Discussion .....	114
8.3.1 Corrosion rates .....	114
8.3.2 Outer iron sulfide layer .....	116
8.3.3 Inner Fe <sub>3</sub> O <sub>4</sub> layer .....	121
8.3.4 Surface profilometry .....	123
8.4 Summary .....	125
Chapter 9: A Modified Thermodynamic Model for the Prediction of Mild Steel Corrosion Products at High Temperature in H <sub>2</sub> S Environments .....	126
9.1 Introduction .....	126
9.2 Experimental .....	127
9.3 Results and Discussion .....	128

	12
9.3.1 Does Fe <sub>3</sub> O <sub>4</sub> eventually disappear with longer exposure time? .....	128
9.3.2 Model modification.....	129
9.3.3 Model comparison .....	132
9.4 Summary .....	133
Chapter 10: A Kinetic Model for the High Temperature Corrosion of Mild Steel in Aqueous H <sub>2</sub> S Environments .....	134
10.1 Introduction.....	134
10.2 Electrochemical Kinetics of Fe <sub>3</sub> O <sub>4</sub> Formation.....	134
10.2.1 Introduction.....	134
10.2.2 Experimental .....	135
10.2.3 Results and discussion .....	137
10.3 Electrochemical Kinetics of Fe <sub>3</sub> O <sub>4</sub> Conversion.....	141
10.3.1 Introduction.....	141
10.3.2 Experimental .....	141
10.3.3 Results and discussion .....	143
10.4 Model Construction .....	153
10.4.1 Review of Zheng's model.....	154
10.4.2 Current model construction.....	156
10.5 Model Implementation.....	159
10.6 Model Verification.....	163
10.7 A Parametric Study.....	169
10.8 Summary.....	172

	13
Chapter 11: Conclusions and Future Work.....	173
11.1 Conclusions.....	173
11.2 Future Work.....	174
References.....	176
Appendix I: Thermodynamic (Pourbaix Diagrams) Calculation.....	189
Appendix II: Calculation Parameters for the Electrochemical Reactions .....	194
Appendix III: Mass Transfer Characterization in the Autoclave.....	197
Appendix IV: The Mathematical Derivations for the Mass Conservation Equations ....	202

## List of Tables

	Page
Table 1. Iron sulfides typically encountered in H <sub>2</sub> S corrosion environments [40,41,42].	36
Table 2. Chemical composition of the API 5L X65 carbon steel (wt. %).	51
Table 3. Experimental details.	52
Table 4. Test matrix for the effect of temperature.	52
Table 5. Summary of initial conditions and theoretical calculated final conditions.	66
Table 6. Test matrix for the effect of time.	71
Table 7. Summary of the theoretical calculated final conditions at 120°C.	79
Table 8. Estimated Fe <sub>3</sub> O <sub>4</sub> and FeS layer thickness with different exposure time.	84
Table 9. Test matrix.	93
Table 10. Schematic diagrams for Fe <sub>3</sub> O <sub>4</sub> /FeS formation mechanisms at higher temperatures in a sour environment.	109
Table 11. Test matrix for the effect of pH <sub>2</sub> S.	114
Table 12. Summary of the theoretical calculated final conditions at 120°C.	120
Table 13. Experimental details for Fe <sub>3</sub> O <sub>4</sub> conversion.	127
Table 14. Experimental details for the kinetics of Fe <sub>3</sub> O <sub>4</sub> formation.	136
Table 15. Modeling parameters for Fe <sub>3</sub> O <sub>4</sub> formation Reaction (13).	141
Table 16. Experimental details for Fe <sub>3</sub> O <sub>4</sub> RDE.	143
Table 17. Equations used for modeling Fe <sub>3</sub> O <sub>4</sub> conversion current.	151
Table 18. Fitting parameters for modeling Fe <sub>3</sub> O <sub>4</sub> conversion current.	152
Table 19. Thermodynamic data of species considered in current study.	190

Table 20. Equilibrium reactions considered in current study. .... 191

Table 21. Calculation parameters for the electrochemical reactions ..... 194

## List of Figures

	Page
Figure 1. Corrosion products at different temperatures; left: 80°C, FeCO <sub>3</sub> (oblong prisms) and Fe <sub>2</sub> (OH) <sub>2</sub> CO <sub>3</sub> (thin plates); right: 200°C, Fe <sub>3</sub> O <sub>4</sub> , 4 days, pCO <sub>2</sub> =1 bar at 25°C. Reprinted from [27].	31
Figure 2. Corrosion products at different temperatures, left: 25°C, mackinawite; right: 80°C, mackinawite with some pyrrhotite, pH 6.0, 10% H <sub>2</sub> S, 4 days. Reprinted from [32], as permitted by NACE International.	32
Figure 3. Corrosion rate and corrosion products at 220°C with 10% H <sub>2</sub> S, p <sub>total</sub> = 2000 psi. Reprinted from [37], permitted by NACE International.	34
Figure 4. Effect of temperature on Pourbaix diagrams for H <sub>2</sub> S-H <sub>2</sub> O-Fe system, [H <sub>2</sub> S] <sub>aq</sub> = 9.4×10 <sup>-3</sup> M, [Fe <sup>2+</sup> ] = 10 ppm, [Fe <sup>3+</sup> ] =10 <sup>-6</sup> M): (a) mackinawite, (b) mackinawite/greigite, (c) mackinawite/greigite/pyrrhotite, (d) mackinawite/greigite/pyrrhotite/pyrite. Reprinted from [32], permitted by NACE International.	35
Figure 5. Corrosion product sequence of carbon steel in aqueous H <sub>2</sub> S solution [37].	40
Figure 6. Process of modeling the water chemistry in a closed system at high temperatures.	45
Figure 7. K <sub>H2S</sub> and K <sub>a,1</sub> values in molality and molarity at different temperatures.	47
Figure 8. (a) Effect of V <sub>liq</sub> /V <sub>gas</sub> ratio on the concentrations of sulfur species, and (b) the total amount of H <sub>2</sub> S in a 7 L autoclave, T=25°C, pH <sub>2</sub> S=0.10 bar.	48

Figure 9. Effect of temperature on concentrations of sulfur species at (a) constant $p_{H_2S}=0.1$ bar and (b) constant $[H_2S]_{aq}=0.00385$ mol/L ( $p_{H_2S}=0.1$ bar@80°C), pH=4.00. .....	49
Figure 10. Experimental 7 L Hastelloy autoclave setup. ....	51
Figure 11. Corrosion rate at different temperatures from LPR measurement, $[H_2S]_{aq}=0.00385$ mol/L, pH=4.00, 4 days, $B=23$ mV/decade. ....	56
Figure 12. Comparison of corrosion rates between LPR and weight loss, $[H_2S]_{aq}=0.00385$ mol/L, pH=4.00, 4 days, $B=23$ mV/decade. ....	56
Figure 13. XRD patterns of corrosion products on the steel surface at different temperatures, $[H_2S]_{aq}=0.00385$ mol/L, pH=4.00, 4 days.....	58
Figure 14. SEM of morphologies and cross-sections at 80°C (left) and 120°C (right), $[H_2S]_{aq}=0.00385$ mol/L, pH=4.00, 4 days. ....	60
Figure 15. SEM of morphologies and cross-sections at 160°C (left) and 200°C (right), $[H_2S]_{aq}=0.00385$ mol/L, pH=4.00, 4 days. ....	61
Figure 16. Surface profilometry after removing corrosion products at 80°C (left) and 120°C (right), $[H_2S]_{aq}=0.00385$ mol/L, pH=4.00, 4 days. ....	62
Figure 17. Surface profilometry after removing corrosion products at 160°C (left) and 200°C (right), $[H_2S]_{aq}=0.00385$ mol/L, pH=4.00, 4 days. ....	63
Figure 18. Pourbaix diagram for Fe-CO <sub>2</sub> -H <sub>2</sub> O system (a) at 80°C and (b) 200°C, 1 bar CO <sub>2</sub> at 25°C. ....	64

Figure 19. Pourbaix diagram for Fe-H <sub>2</sub> S-H <sub>2</sub> O system [32], (a) 80°C, mackinawite, (b) 120°C, pyrrhotite (troilite), (c) 160°C, pyrrhotite, and (d) 200°C, pyrite/pyrrhotite, other input parameters are in Table 5.....	68
Figure 20. Corrosion rate for different test durations from LPR measurements, T=120°C, pH <sub>2</sub> S=0.10 bar, initial pH=4.0, B=23 mV/decade. ....	72
Figure 21. Comparison of average corrosion rates between the integrated average of LPR measurements and weight loss, T=120°C, pH <sub>2</sub> S=0.10 bar, initial pH=4.0, B=23 mV/decade. ....	73
Figure 22. XRD patterns of corrosion products on the steel surface for different test durations, T=120°C, pH <sub>2</sub> S=0.10 bar, initial pH=4.0.....	75
Figure 23. SEM morphologies and cross sections for 1 day (left) and 4 days (right), T=120°C, pH <sub>2</sub> S=0.10 bar, initial pH=4.0.....	77
Figure 24. SEM morphologies and cross sections for 7 days (left) and 21 days (right), T=120°C, pH <sub>2</sub> S=0.10 bar, initial pH=4.0.....	78
Figure 25. Pourbaix diagrams for Fe-H <sub>2</sub> S-H <sub>2</sub> O system by considering (a) mackinawite, (b) pyrrhotite (troilite), (c) pyrrhotite, and (d) pyrite/pyrrhotite, T=120°C, other input parameters are in Table 7.....	80
Figure 26. (a) FIB sample preparation; (b) thin area for TEM analysis; (c) EDS line scan result; (d) selected area diffraction (SAD) pattern. T=120°C, pH <sub>2</sub> S=0.20 bar, initial pH=4.0, 4 days. ....	82
Figure 27. EDS mapping results for Fe, O and S distribution for different experiment durations, T=120°C, pH <sub>2</sub> S=0.10 bar, initial pH=4.0.....	84

Figure 28. Layer thickness of Fe <sub>3</sub> O <sub>4</sub> and iron sulfides after different exposure time, and compared with the LPR corrosion rates from experimental data and Zheng's model [9], M: mackinawite, T: troilite, Py: pyrrhotite, P: pyrite, T=120°C, pH <sub>2</sub> S=0.10 bar, initial pH=4.0. Light blue dots: experimental Fe <sub>3</sub> O <sub>4</sub> layer thickness, light blue line: fitting Fe <sub>3</sub> O <sub>4</sub> layer thickness, red dots: experimental iron sulfide layer thickness, red curve: fitting iron sulfide layer thickness, dark blue dots: experimental corrosion rate, green curve: Zheng's model corrosion rate. ....	86
Figure 29. Surface profilometry after removing corrosion products (a) 1 day, mackinawite; (b) 4 days, troilite; (c) 7 days, pyrrhotite/pyrite; (d) 21 days, pyrrhotite/pyrite. T=120°C, pH <sub>2</sub> S=0.10 bar, initial pH=4.0. ....	87
Figure 30. Experiment design to test hypothesis #1. ....	91
Figure 31. Experiment design to test hypothesis #2. ....	93
Figure 32. Experimental Set #1 - LPR corrosion rate in experiments without H <sub>2</sub> S (green), with 0.1 bar H <sub>2</sub> S (blue), and with preformed Fe <sub>3</sub> O <sub>4</sub> layer for one-day, X65, 1 wt.% NaCl solution, T=120°C, initial pH=4.0, B=23 mV/decade.....	96
Figure 33. XRD patterns of X65 specimen in experiment without H <sub>2</sub> S after different test durations, 1 wt.% NaCl solution, N <sub>2</sub> purged, T=120°C, initial pH=4.0. ....	97
Figure 34. Cross-section and EDS mapping results for X65 specimen in experiment without H <sub>2</sub> S after 1 day, 1 wt.% NaCl solution, T=120°C, initial pH=4.0. ....	98
Figure 35. The growth of Fe <sub>3</sub> O <sub>4</sub> layer with time, shown by cross-sections of X65 specimens in the experiment without H <sub>2</sub> S after different test durations (obtained in separate experiments), 1 wt.% NaCl solution, T=120°C, initial pH=4.0.....	99

Figure 36. The thickness of Fe <sub>3</sub> O <sub>4</sub> layer with time in the experiment without H <sub>2</sub> S, X65, 1 wt.% NaCl solution, T=120°C, initial pH=4.0.....	99
Figure 37. EDS mapping results for X65 specimen from the experiment without H <sub>2</sub> S with, with 0.1 bar H <sub>2</sub> S, and with preformed Fe <sub>3</sub> O <sub>4</sub> layer, 1 wt.% NaCl solution, T=120°C, initial pH=4.0. ....	101
Figure 38. Solubility limit for Fe <sub>3</sub> O <sub>4</sub> and mackinawite with the increase of temperature, pH=4.0, p <sub>H<sub>2</sub>S</sub> =0.1 bar.....	102
Figure 39. Saturation value for Fe <sub>3</sub> O <sub>4</sub> and mackinawite at initial pH 4.0 and 5.0, [Fe <sup>3+</sup> ]=1×10 <sup>-10</sup> M, T=120°C, p <sub>H<sub>2</sub>S</sub> =0.1 bar.....	104
Figure 40. Saturation value for Fe <sub>3</sub> O <sub>4</sub> and mackinawite at 25°C and 120°C, [Fe <sup>3+</sup> ]=1×10 <sup>-10</sup> M, p <sub>H<sub>2</sub>S</sub> =0.1 bar, initial pH=4.0 (pH lines for 25°C and 120°C overlap in the graph). ....	105
Figure 41. XRD patterns of preformed Fe <sub>3</sub> O <sub>4</sub> layer on Ni specimen before and after H <sub>2</sub> S was introduced, 1 wt.% NaCl solution, T=120°C, initial pH=4.0. ....	108
Figure 42. EDS mapping results for the cross section of preformed Fe <sub>3</sub> O <sub>4</sub> layer on Ni specimen before and after H <sub>2</sub> S was introduced, 1 wt.% NaCl solution, T=120°C, p <sub>H<sub>2</sub>S</sub> =0.1 bar, initial pH=4.0. ....	108
Figure 43. LPR corrosion rate at different p <sub>H<sub>2</sub>S</sub> , T=120°C, initial pH=4.0, B=23 mV/decade. ....	115
Figure 44. Comparison of corrosion rates measured by LPR average and weight loss at different p <sub>H<sub>2</sub>S</sub> , T=120°C, initial pH=4.0, 4 days.....	116

Figure 45. XRD patterns of corrosion products on the steel surface at different $\text{pH}_2\text{S}$ , $T=120^\circ\text{C}$ , initial $\text{pH}=4.0$ , 4 days. ....	117
Figure 46. SEM morphologies: (a) and (b) troilite, $\text{pH}_2\text{S}=0.10$ bar, (c) and (d) pyrrhotite, $\text{pH}_2\text{S}=0.10$ bar, $T=120^\circ\text{C}$ , initial $\text{pH}=4.0$ , 4 days. ....	118
Figure 47. SEM morphologies: (a) and (b) pyrrhotite/pyrite, $\text{pH}_2\text{S}=1.0$ bar, (c) and (d) pyrite, $\text{pH}_2\text{S}=2.0$ bar, $T=120^\circ\text{C}$ , initial $\text{pH}=4.0$ , 4 days. ....	119
Figure 48. Pourbaix diagrams for Fe- $\text{H}_2\text{S}$ - $\text{H}_2\text{O}$ system by considering mackinawite/greigite/pyrrhotite/pyrite (a) $\text{pH}_2\text{S}=0.10$ bar, (b) $\text{pH}_2\text{S}=0.50$ bar, (c) $\text{pH}_2\text{S}=1.0$ bar, (d) $\text{pH}_2\text{S}=2.0$ bar, $T=120^\circ\text{C}$ , other input parameters are in Table 12. ....	121
Figure 49. EDS mapping results for Fe, O and S distribution at different $\text{pH}_2\text{S}$ , $T=120^\circ\text{C}$ , initial $\text{pH}=4.0$ , 4 days. ....	122
Figure 50. Layer thickness of $\text{Fe}_3\text{O}_4$ at different $\text{pH}_2\text{S}$ , $T=120^\circ\text{C}$ , initial $\text{pH}=4.0$ , 4 days. ....	123
Figure 51. Surface profilometry after removing the corrosion products (a) 0.10 bar $\text{H}_2\text{S}$ , troilite, (b) 0.50 bar $\text{H}_2\text{S}$ , pyrrhotite, (c) 1.0 bar $\text{H}_2\text{S}$ pyrrhotite/pyrite, (d) 2.0 bar $\text{H}_2\text{S}$ , pyrite. $T=120^\circ\text{C}$ , initial $\text{pH}=4.0$ , 4 days. ....	124
Figure 52. Cross-section and EDS mapping results for Fe, O and S distribution, $T=160^\circ\text{C}$ , $\text{pH}_2\text{S}=2.0$ bar, initial $\text{pH}=4.0$ , 21 days. ....	129
Figure 53 Pourbaix diagrams for (a) Fe- $\text{H}_2\text{O}$ system at $120^\circ\text{C}$ ; (b) Fe- $\text{H}_2\text{S}$ - $\text{H}_2\text{O}$ system at $120^\circ\text{C}$ ; modified Pourbaix diagrams for (c) Fe- $\text{H}_2\text{S}$ - $\text{H}_2\text{O}$ system at $120^\circ\text{C}$ ; (d) Fe- $\text{H}_2\text{S}$ - $\text{H}_2\text{O}$ system at $25^\circ\text{C}$ , (b), (c), (d) consider 0.1 bar $\text{H}_2\text{S}$ , $[\text{Fe}^{2+}]=5$ ppm, and mackinawite only. ....	131

Figure 54. Modified Pourbaix diagrams for Fe-H <sub>2</sub> S-H <sub>2</sub> O system (a) 120°C; (b) 25°C, 0.1 bar H <sub>2</sub> S, [Fe <sup>2+</sup> ]=5 ppm, consider mackinawite/troilite/greigite/pyrrhotite/pyrite.....	132
Figure 55. Pourbaix diagrams for Fe-H <sub>2</sub> S-H <sub>2</sub> O system at 120°C generated by (a) the Geochemist's Workbench (GWB) based on thermos.com.V8.R6+.dat; (b) OLI Corrosion Analyzer (OLI), 0.1 bar H <sub>2</sub> S, [Fe <sup>2+</sup> ]=5 ppm, consider mackinawite/troilite/greigite/pyrrhotite/pyrite.....	133
Figure 56. Potentiodynamic sweeps on Ni in 4 L autoclave with and without adding Fe <sup>2+</sup> , 120°C, N <sub>2</sub> , pH 4.0, 500 rpm.....	138
Figure 57. Potentiodynamic sweeps on Ni in 4 L autoclave with different rotating speed and different concentration of Fe <sup>2+</sup> , (a) 120°C, (b) 160°C, N <sub>2</sub> , pH 4.0, black lines: modelling data.....	139
Figure 58. 2 L glass cell Fe <sub>3</sub> O <sub>4</sub> RDE setup.....	142
Figure 59. Potentiodynamic sweeps on X65 RDE, 40°C, N <sub>2</sub> purged, pH 4.0, and solid black lines: experiment, dash lines: modeling data. ....	144
Figure 60. XRD pattern for the purchased Fe <sub>3</sub> O <sub>4</sub> material. ....	145
Figure 61. Potentiodynamic sweeps on Fe <sub>3</sub> O <sub>4</sub> RDE, 40°C, N <sub>2</sub> purged, pH 4.0, and solid lines: experiment, dash lines: modeling data (based on carbon steel electrode). ....	147
Figure 62. Potentiodynamic sweeps on Fe <sub>3</sub> O <sub>4</sub> RDE, 40°C, 1200 rpm, (a) pH 4.0, red: 0% H <sub>2</sub> S, purple: 1% H <sub>2</sub> S, (b) red: 1% H <sub>2</sub> S, pH 4.0, blue: 5% H <sub>2</sub> S, pH 4.0, black: 1% H <sub>2</sub> S, pH 5.0.....	149
Figure 63. SEM images and EDS results for Fe <sub>3</sub> O <sub>4</sub> RDE after potentiodynamic sweep in 1% H <sub>2</sub> S, 40°C, pH 4.0, 1200 rpm. ....	150

Figure 64. Modeling results for $\text{Fe}_3\text{O}_4$ conversion, (a) different pH: pH 5.0 and 4.0, 40°C, 1% $\text{H}_2\text{S}$ , 1200 rpm; (b) different $\text{H}_2\text{S}$ : 1% and 5%, 40°C, pH 4.0, 1200 rpm; (c) different rotation speed: 600 and 1200 rpm, 40°C, pH 4.0, 1% $\text{H}_2\text{S}$ ; (d) different temperature: 40°C and 80°C, pH 4.0, 1% $\text{H}_2\text{S}$ , 1200 rpm. Black solid lines: experimental data, the rest are modeling data.....	153
Figure 65. Zheng’s model construction without a corrosion product layer.....	155
Figure 66. Zheng’s model construction with a corrosion product layer.....	156
Figure 67. Current “4-nodes” model construction with two corrosion product layers... ..	157
Figure 68. Current model prediction compared with experiment results and Zheng’s model, 120°C, 0.1 bar $\text{H}_2\text{S}$ , pH 4.0, 21 days.....	164
Figure 69. Layer thickness from experimental results and current model predictions, 120°C, 0.1 bar $\text{H}_2\text{S}$ , pH 4.0.....	165
Figure 70. Experiment results (left) compared with current model predictions (right) at different temperatures, 0.1 bar $\text{H}_2\text{S}$ , pH 4.0, 4 days, (a) 80°C, (b) 120°C, (c) 160°C, (d) 200°C.....	166
Figure 71. Experiment results compared with current model predictions with different $\text{pH}_2\text{S}$ , 120°C, pH 4.0, 4 days, (a) 0.1 bar, (b) 0.5 bar, (c) 1.0 bar, (d) 2.0 bar.....	167
Figure 72. Layer thickness from experiment results and current model predictions at different $\text{pH}_2\text{S}$ , 120°C, pH 4.0, 4 days.....	168
Figure 73. Effect of high temperature on the corrosion rate from current model predictions, 0.1 bar $\text{H}_2\text{S}$ , pH 4.0, 4 days.....	170

Figure 74. Effect of pH <sub>2</sub> S on the corrosion rate from current model predictions, 120°C, pH 4.0, 4 days. ....	171
Figure 75. Effect of pH on the corrosion rate from current model predictions, 120°C, 0.1 bar H <sub>2</sub> S, 4 days.....	172
Figure 76. Potentiodynamic sweeps on Ni electrode in 0.5 M KOH + 0.01 M K <sub>3</sub> Fe(CN) <sub>6</sub> + 0.01 M K <sub>4</sub> Fe(CN) <sub>6</sub> ·3H <sub>2</sub> O solution, (a) 40°C, (b) 80°C, 4 L SS autoclave.....	198
Figure 77. Experimental Sherwood, Reynolds, and Schmidt numbers (points), and Equation (79) fitting (black line), 4 L SS autoclave. ....	199
Figure 78. Potentiodynamic sweeps on Ni electrode in 0.5 M KOH + 0.01 M K <sub>3</sub> Fe(CN) <sub>6</sub> + 0.01 M K <sub>4</sub> Fe(CN) <sub>6</sub> ·3H <sub>2</sub> O solution, (a) 40°C, (b) 60°C, 7 L Hastelloy autoclave.....	200
Figure 79. Experimental Sherwood, Reynolds, and Schmidt numbers (points), and equation (80) fitting (black line), 7 L Hastelloy autoclave. ....	200
Figure 80. Potentiodynamic sweeps on X65 in 4 L Autoclave, 40°C, N <sub>2</sub> , pH 4.0, 1000 rpm, black line: experiment data, dash lines: modeling data. ....	201

### Nomenclature

$\alpha_c$	Transfer coefficient of electrochemical reaction
$A$	Area of the electrode (specimen), cm <sup>2</sup>
$b$	Tafel slope, V/decade
$c_j$	Concentration of species $j$ , mol/L
$c_{j\_b}$	Concentration of species $j$ in bulk solution, mol/L
$c_{j\_m}$	Concentration of species $j$ at Fe <sub>3</sub> O <sub>4</sub> /FeS interface (middle layer), mol/L
$c_{j\_s}$	Concentration of species $j$ at steel surface, mol/L
$CR$	Corrosion rate, mm/yr
$d$	Diameter of the impeller, m
$D$	Diffusion coefficient, m <sup>2</sup> /s
$\rho$	Density, kg/m <sup>3</sup>
$\Delta H$	Enthalpy of activation, kJ/mol
$\Delta t$	Successive time step, s
$c_j$	Concentration of species $j$ , mol/L
$E$	Applied potential, V
$E_{rev}$	Reversible potential, V
$\varepsilon$	Porosity
$F$	Faraday constant, A·s/mol
$i$	Current density, A/m <sup>2</sup>
$i_{Fe}$	Fe dissolution current, A/m <sup>2</sup>

$i_{H^+}$	$H^+$ reduction current, $A/m^2$
$i_{H_2S}$	$H_2S$ reduction current, $A/m^2$
$i_{H_2O}$	$H_2O$ reduction current, $A/m^2$
$i_{Fe_3O_4}$	$Fe_3O_4$ formation current, $A/m^2$
$i_{FeS}$	$Fe_3O_4$ conversion to $FeS$ current, $A/m^2$
$i_\alpha$	Charge transfer current density, $A/m^2$
$i_{lim}$	Limiting current density, $A/m^2$
$i_{ref}$	Reference current density, $A/m^2$
$K_{H_2S}$	$H_2S$ gas dissolution constant, $mol/L/bar$
$K_{a,1}$	$H_2S$ first dissociation constant, $mol/L$
$K_{a,2}$	$H_2S$ second dissociation constant, $mol/L$
$K_w$	$H_2O$ dissociation constant, $mol^2/L^2$
$k_m$	Total mass transfer coefficient through boundary and $FeS$ layer, $m^2/s$
$k'_m$	Mass transfer coefficient through $Fe_3O_4$ layer, $m^2/s$
$M$	Molecular weight, $g/mol$
$p_{H_2S}$	Partial pressure of $H_2S$ , $bar$
$R$	Gas constant, $J/mol/K$
$R_{Fe_3O_4}$	Formation rate of $Fe_3O_4$ layer, $mol/m^2/s$
$Re$	Reynolds number
$Sc$	Schmidt number

$Sh$	Sherwood number
$T_c$	Temperature in Celsius, °C
$T_K$	Temperature in Kelvin, K
$T_{ref}$	Reference temperature in Kelvin, K
$\tau$	Tortuosity
$\nu$	Kinematic viscosity, cm <sup>2</sup> /s
$\omega$	Angular rotation speed, rad/s
$n$	Reaction order
$z$	Number of electrons transferred

## Chapter 1. Introduction

A survey conducted by NACE (National Association of Corrosion Engineers) International in 2016 reports that corrosion costs are equivalent to 3.4% of the global Gross Domestic Product (US \$2.5 trillion) [1]. The oil and gas industry, which includes exploration, production, and transportation sectors, carries a big part of this cost [1]-[5]. Therefore, understanding corrosion mechanisms and implementing proper corrosion control strategies have been of great interest to scientists and engineers worldwide.

Corrosion of carbon steel in the presence of hydrogen sulfide ( $H_2S$ ) has been a key challenge in the oil and gas industry since the 1940s [6]. It has been intensely investigated over the past decades and a relatively good level of understanding has been achieved for low temperature environments ( $< 80^\circ C$ ) [7]-[11]. However,  $H_2S$  corrosion at elevated temperatures ( $> 80^\circ C$ ) has been minimally investigated and the associated mechanisms for the encountered corrosion phenomena are consequently poorly understood. The exploration and drilling conditions for petroleum involve ever high pressure and high temperature (HPHT) environments in combination with high  $H_2S$  content [12]-[14]. By 2008, at least 11% of new well drilling operations were expected to occur at temperatures exceeding  $177^\circ C$  [15]. HPHT wells are now very common worldwide, from the North Sea and the Gulf of Mexico to Southeast Asia, Africa, and South America [16]. Unfortunately, the likelihood of encountering  $H_2S$  corrosion also correlates with the increase of temperature in these wells [17]. High temperatures and high pressures in combination with  $H_2S$  lead to many engineering challenges, and potential for pipeline and equipment failures, especially in downhole environments [18]-

[20]. Materials selection and adoption of appropriate corrosion inhibition strategies are of critical importance to maintain production, minimize risk, and protect the environment.

High temperature has a significant effect on [21]-[23].

- Corrosion rate.
- Kinetics of formation of iron sulfide polymorphs and related phases.
- Kinetics of phase transformations.

The physical properties of the corrosion products and their potential interaction may also lead to surface heterogeneity, onset of galvanic corrosion, and localized attack [24]-[26]. Therefore, a comprehensive understanding of the electrochemical and physicochemical processes involved is necessary to be able to predict and mitigate H<sub>2</sub>S corrosion at elevated temperatures.

In this research project, the mechanisms of layer formation and their effects on corrosion kinetics at high temperature in H<sub>2</sub>S environments are thoroughly investigated, and new thermodynamic and kinetic models are developed accordingly.

## Chapter 2: Literature Review

### 2.1 CO<sub>2</sub> Corrosion of Steel at Elevated Temperatures

CO<sub>2</sub> is present in almost every single oil and gas field, while some also contain H<sub>2</sub>S. Both of these acid gases contribute to the severity of the corrosion attack, albeit in different ways. Compared to its H<sub>2</sub>S counterpart, CO<sub>2</sub> corrosion at low and elevated temperatures is well defined [27]-[31]. The section below describes basic concepts and changes that occur when temperature increases in CO<sub>2</sub> environments, covering the water chemistry, corrosion kinetics, and the formation of corrosion products.

The hydration and dissociation constants for CO<sub>2</sub> and carbonic species have been validated up to 250°C using broadly the same mathematical expressions routinely applied at low temperatures. In CO<sub>2</sub>-H<sub>2</sub>O systems, the pH of the CO<sub>2</sub> saturated solution typically increases with temperature at fixed CO<sub>2</sub> partial pressure due to the decrease in gas solubility [27].

Over the temperature range from 80~200°C, general corrosion rates were shown to decrease with increasing temperature and were strongly dependent on the formation of corrosion product, and especially Fe<sub>3</sub>O<sub>4</sub> (magnetite) formation [27]. Autoclave experiments conducted in a temperature range of 80°C to 250°C revealed a maximum corrosion rate at 120°C for 0.1 bar pCO<sub>2</sub>. Since the experiments were performed in a closed system, the results were also naturally highly dependent on the water chemistry and hydrodynamic conditions [28].

The thermodynamics, as well as the mechanisms of CO<sub>2</sub> corrosion at high temperatures, have also been modeled and verified. In the range of 80~150°C, as shown

in Figure 1, the corrosion products were identified by X-ray diffraction as  $\text{FeCO}_3$  and  $\text{Fe}_2(\text{OH})_2\text{CO}_3$ , while in the temperature range of  $200\sim 250^\circ\text{C}$ , the corrosion product was identified to be exclusively  $\text{Fe}_3\text{O}_4$  [27], [29]. At high temperatures, the kinetics of  $\text{Fe}_3\text{O}_4$  formation are very fast and thus tend to slow down the corrosion rate.

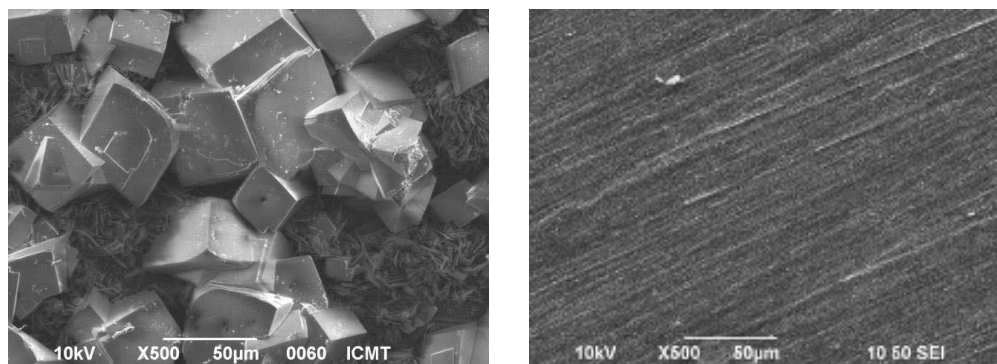


Figure 1. Corrosion products at different temperatures; left:  $80^\circ\text{C}$ ,  $\text{FeCO}_3$  (oblong prisms) and  $\text{Fe}_2(\text{OH})_2\text{CO}_3$  (thin plates); right:  $200^\circ\text{C}$ ,  $\text{Fe}_3\text{O}_4$ , 4 days,  $p\text{CO}_2 = 1$  bar at  $25^\circ\text{C}$ . Reprinted from [27].

## 2.2 $\text{H}_2\text{S}$ Corrosion of Steel at Low Temperatures ( $< 80^\circ\text{C}$ )

Over the past several decades,  $\text{H}_2\text{S}$  corrosion at low temperatures has been extensively studied [8], [9], [32]-[36] and significant progress has been made related to understanding its mechanisms. As a result, kinetic and thermodynamic models have been built and verified.

Although many aspects of  $\text{H}_2\text{S}$  corrosion remain elusive, several commonly accepted conclusions can be made. The initial “layer free” corrosion rate increases with temperature, but the increase of total cathodic current ( $\text{H}^+$ ,  $\text{H}_2\text{S}$ , and  $\text{H}_2\text{O}$  reductions,

summarized in Chapter 10) is more significant than that of the anodic current (Fe oxidative dissolution) in the polarization curves [9]. At 25°C, when conditions are reported to favor the formation of a corrosion product layer, a porous and non-protective mackinawite layer grows on the steel surface (Figure 2). At 80°C, a dense and adherent corrosion product layer, composed of mackinawite and pyrrhotite, forms that confers good protectiveness [32]. Temperature can accelerate both the rates of corrosion as well as the rate of corrosion product layer formation. Consequently, a peak corrosion rate is often present when increasing the temperature at a fixed pH<sub>2</sub>S [33].

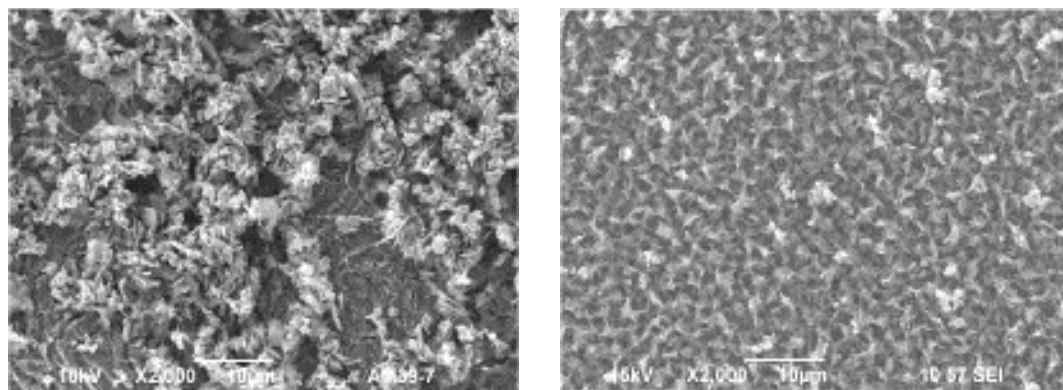


Figure 2. Corrosion products at different temperatures, left: 25°C, mackinawite; right: 80°C, mackinawite with some pyrrhotite, pH 6.0, 10% H<sub>2</sub>S, 4 days. Reprinted from [32], as permitted by NACE International.

Two layer formation mechanisms were proposed in previous studies [34], [37]: direct reaction (solid-state reaction) and precipitation. Direct reaction suggests that H<sub>2</sub>S adsorbs on the steel surface and directly reacts to form an iron sulfide layer [37]. The

precipitation mechanism requires aqueous  $\text{Fe}^{2+}$  and  $\text{S}^{2-}$  concentrations to reach the solubility limit so that the iron sulfide layer can precipitate on the steel surface [34].

In terms of modeling, Zheng developed a kinetic model for corrosion rate prediction and mackinawite layer growth [9]. It was assumed that the corrosion rate was controlled by a combination of mass transfer processes and electrochemical reactions [8]. This is important since mass transfer is not as dependent on temperature as reaction rates [34]. Ning also constructed a thermodynamic model utilizing Pourbaix diagrams for the prediction of stable iron sulfide phase formation [32]. However, both the above mentioned models are only verified up to  $80^\circ\text{C}$ . These models are also described in detail in Section 10.4.1 as they constitute the starting point of modeling efforts related to  $\text{H}_2\text{S}$  corrosion in high temperature environments.

### **2.3 $\text{H}_2\text{S}$ Corrosion of Steel at High Temperatures ( $> 80^\circ\text{C}$ )**

$\text{H}_2\text{S}$  corrosion at high temperatures has been poorly investigated, in large part due to the inherent difficulty of conducting meaningful experiments. Until now, only two studies on the subject can be found in the open literature and the first, which is discussed below, was published more than 20 years ago. According to the authors, the corrosion rate at  $220^\circ\text{C}$  decreased with time due to iron sulfide growth controlled by direct reaction of  $\text{H}_2\text{S}$  with surface iron, as shown in Figure 3. The corrosion rate eventually reached a stable value due to the balance between layer growth and metal dissolution. Under these conditions, the main corrosion product was identified as pyrrhotite, while traces of pyrite were present. Magnetite was also identified close to the steel surface but the authors stated that only traces could be detected [37].

Another recent study suggested the presence of pyrrhotite at 130°C by characterization using scanning electron microscopy (SEM) and transmission electron microscopy (TEM) [39].

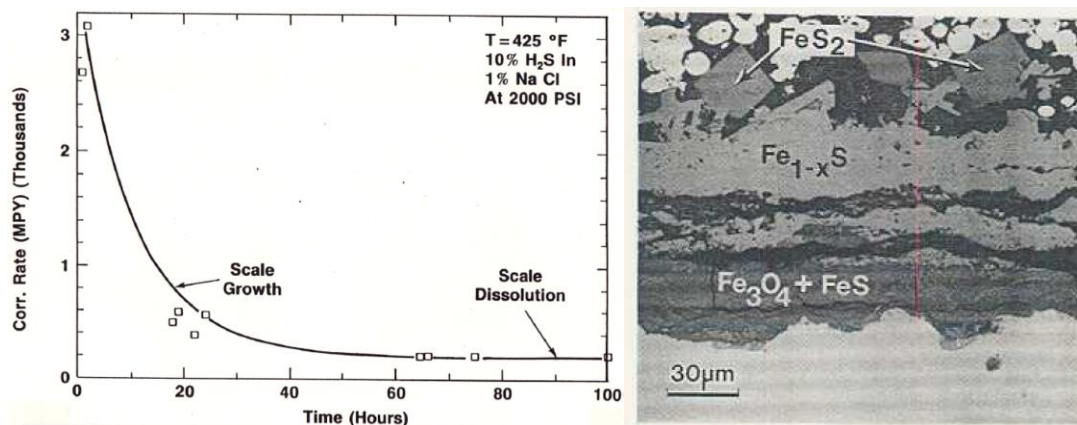


Figure 3. Corrosion rate and corrosion products at 220°C with 10% H<sub>2</sub>S,  $p_{\text{total}} = 2000$  psi. Reprinted from [37], permitted by NACE International.

More recently, Ning [32] used thermodynamic data extended to higher temperatures and generated corresponding Pourbaix diagrams, as shown in Figure 4. The author found that, when temperature increases, the iron sulfide stability regions tend to move towards more negative potentials and, more importantly, lower pH values. Considering the typical operating conditions encountered in simulated oil and gas production systems ( $2 < \text{pH} < 8$  and  $-0.7 \text{ V} < E \text{ vs. SHE} < -0.4 \text{ V}$ ), this means that, at higher temperatures, iron sulfide corrosion products are thermodynamically stable over an effectively wider range of pH values. However, while pyrite is the most thermodynamically stable iron sulfide, it is still difficult to predict which corrosion

products (mackinawite, greigite, pyrrhotite, and pyrite) will be kinetically favored and will actually be present on the steel surface depending on the temperature, exposure time, and partial pressure of  $\text{H}_2\text{S}$ . Consequently, it is necessary to perform a series experiments to identify which of the kinetically or thermodynamically favored corrosion product layers will be present at the steel surface. This is one of the main objectives of this project.

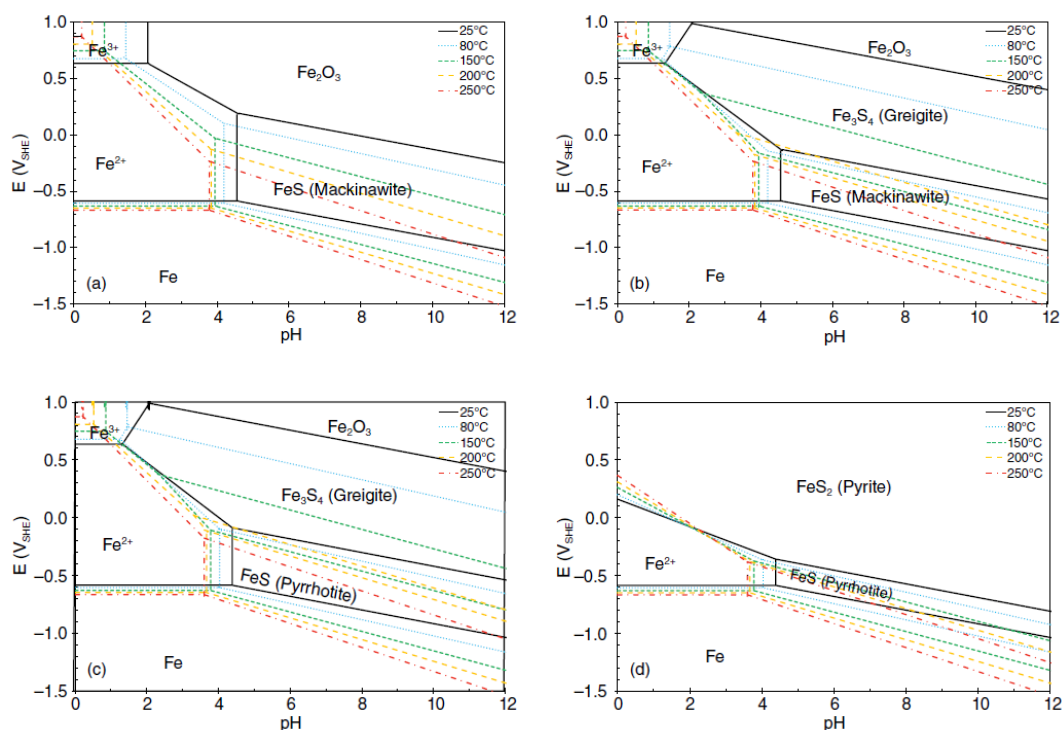


Figure 4. Effect of temperature on Pourbaix diagrams for  $\text{H}_2\text{S}$ - $\text{H}_2\text{O}$ - $\text{Fe}$  system,  $[\text{H}_2\text{S}]_{\text{aq}} = 9.4 \times 10^{-3} \text{ M}$ ,  $[\text{Fe}^{2+}] = 10 \text{ ppm}$ ,  $[\text{Fe}^{3+}] = 10^{-6} \text{ M}$ : (a) mackinawite, (b) mackinawite/greigite, (c) mackinawite/greigite/pyrrhotite, (d) mackinawite/greigite/pyrrhotite/pyrite. Reprinted from [32], permitted by NACE International.

## 2.4 Polymorphous Iron Sulfides and Related Phases

Many types of iron sulfide exist such as mackinawite, cubic iron sulfide, troilite, pyrrhotite, greigite, and pyrite. In this section, their physicochemical properties as well as occurrence in corrosion are summarized. Their mechanisms of formation and transformation are also reviewed. Table 1 summarizes iron sulfides, with an emphasis on those typically encountered in H<sub>2</sub>S corrosion environments.

Table 1. Iron sulfides typically encountered in H<sub>2</sub>S corrosion environments [40]-[42].

<i>Name</i>	<i>Formula</i>	<i>Crystal Structure</i>	<i>Properties</i>
Amorphous iron sulfide	FeS	Non-crystalline	Unstable, rapidly converts into mackinawite.
Mackinawite	FeS	Tetragonal; stacked layers of “2D” FeS sheets	Metastable, iron sulfide phase that primarily precipitates from aqueous solutions. Initial corrosion product.
Cubic FeS	FeS	Cubic	Unstable, transforms into mackinawite, troilite or pyrrhotite. Does not form in the presence of oxygen or chlorides.
Troilite	FeS	Hexagonal	Stoichiometric member of the Fe <sub>1-x</sub> S group (x=0). Morphologies needle-like, flower-like, and beam-shaped.

Table 1 continued.

<i>Name</i>	<i>Formula</i>	<i>Crystal Structure</i>	<i>Properties</i>
Pyrrhotite	$\text{Fe}_{1-x}\text{S}$ ( $x=0\sim 0.17$ )	Hexagonal $\text{Fe}_{10}\text{S}_{11}$ , Monoclinic $\text{Fe}_7\text{S}_8$ , or Orthorhombic	With vacancies, p-type semiconductor. Can co-exist with troilite, both are thermodynamically stable.
Smythite	$\text{Fe}_{3+x}\text{S}_4$ ( $x=0\sim 0.3$ )	Trigonal- Hexagonal	Metastable, related to the $\text{Fe}_{1-x}\text{S}$ group. Has not been reported as a corrosion product.
Greigite	$\text{Fe}_3\text{S}_4$	Cubic	Metastable $\text{Fe}^{\text{II}}\text{Fe}^{\text{III}}$ sulfide, Associated with fresh water systems.
Pyrite	$\text{FeS}_2$	Cubic	Stable iron(II) disulfide, can exist as n-type semiconductor. Common cubic and framboidal (raspberry-like) morphologies. Pyrite and pyrrhotite are the most stable iron sulfides.
Marcasite	$\text{FeS}_2$	Orthorhombic	Metastable iron(II) disulfide. Common mineral in hydrothermal systems and sedimentary rocks. Has not been reported as a corrosion product.

As shown in Table 1, iron sulfides can display significant variations in phase composition, crystal structure, crystal size, morphology, and crystallographic orientation at a corroding steel surface. One phase or a mixture of different phases of these iron sulfides can form the corrosion product layer, which can display different layer thickness, porosity, tortuosity associated with diffusion processes, and resistivity. This will affect the mass and electron transport kinetics and, therefore, change the rates and/or the types of corrosion that occur.

The formation, transformation, and protectiveness of such iron sulfide layers are governed by pH, temperature,  $p_{\text{H}_2\text{S}}$ , exposure time, and brine chemistry. Smith [43] proposed that mackinawite formation is very fast and that it can dissolve back into the solution if it is not supersaturated. In these conditions, the corrosion process is controlled by the dissolution rate of mackinawite. Sardisco, *et al.*, [44] studied the effect of the pH of aqueous  $\text{H}_2\text{S}$  solutions on the protectiveness conferred by such corrosion products. The results showed that the protectiveness of the iron sulfide layer changed with pH. Between pH 6.5 to 8.8, mackinawite was the least protective layer, compared to pyrite. Ren, *et al.*, [45] observed that when the partial pressure of  $\text{H}_2\text{S}$  increased, fine grains of pyrrhotite formed that made the layer more compact and continuous, leading to a decrease of the general corrosion rate and lowered pitting tendency. Ning, *et al.*, [10] have found that the appearance of pyrite can initiate and sustain localized corrosion on steel.

The growth and phase transitions of such polymorphous iron sulfides, with different stoichiometric ratios and structures, are complex to understand. Direct observations are difficult to perform as some of these phases are unstable in certain environments and act as transition states. Even the first step of mackinawite formation is not well defined as it has been described both as a solid-state reaction and chemisorption [9]. Transformations among iron sulfides at  $21^\circ\text{C}$  were summarized by Shoesmith, *et al.* [37], as shown in Figure 5. At low temperature, the reported sequence of the reaction products with time is mackinawite  $\rightarrow$  cubic  $\text{FeS}$   $\rightarrow$  troilite  $\rightarrow$  pyrrhotite  $\rightarrow$  greigite (transition state)  $\rightarrow$  pyrite [46]. Bai, *et al.*, [46] stated that at atmospheric pressure, mackinawite is the only iron sulfide that forms up to  $90^\circ\text{C}$ , while at higher pressure the

main iron sulfide phases encountered are mackinawite, cubic FeS, and troilite. Troilite was also reported to be the final corrosion product at 50°C and 10 bar H<sub>2</sub>S for up to a 96 hour exposure time. However, the authors found greigite and pyrite only after 21 hours at the same conditions [48], which is somewhat contradictory to Shoesmith's findings. They also used transmission electron microscopy (TEM) to directly observe the transition of cubic FeS into greigite and mackinawite into greigite. Benning *et al.* [49] concluded that mackinawite can transform to pyrite only in 'slightly oxidizing' environments such as in the presence of mixed Fe<sup>2+</sup>/Fe<sup>3+</sup> valences or sulfur species with oxidation states intermediate between sulfate and sulfide. They also directly observed greigite as a true intermediate on the pathway from mackinawite to pyrite by using energy dispersive X-ray diffraction (ED-XRD) [50]. The iron sulfides transformation reactions, starting from mackinawite (FeS) and all the way to pyrite (FeS<sub>2</sub>), involve iron sulfide phases that are gradually richer in sulfur. This implies that the elemental sulfur could also play an important role in the different reaction steps involved in the transformation processes. Indeed, Peiffer, *et al.*, [51] detected element sulfur (S<sup>0</sup>) when they synthesized pyrite from ferric hydroxides and hydrogen sulfide.

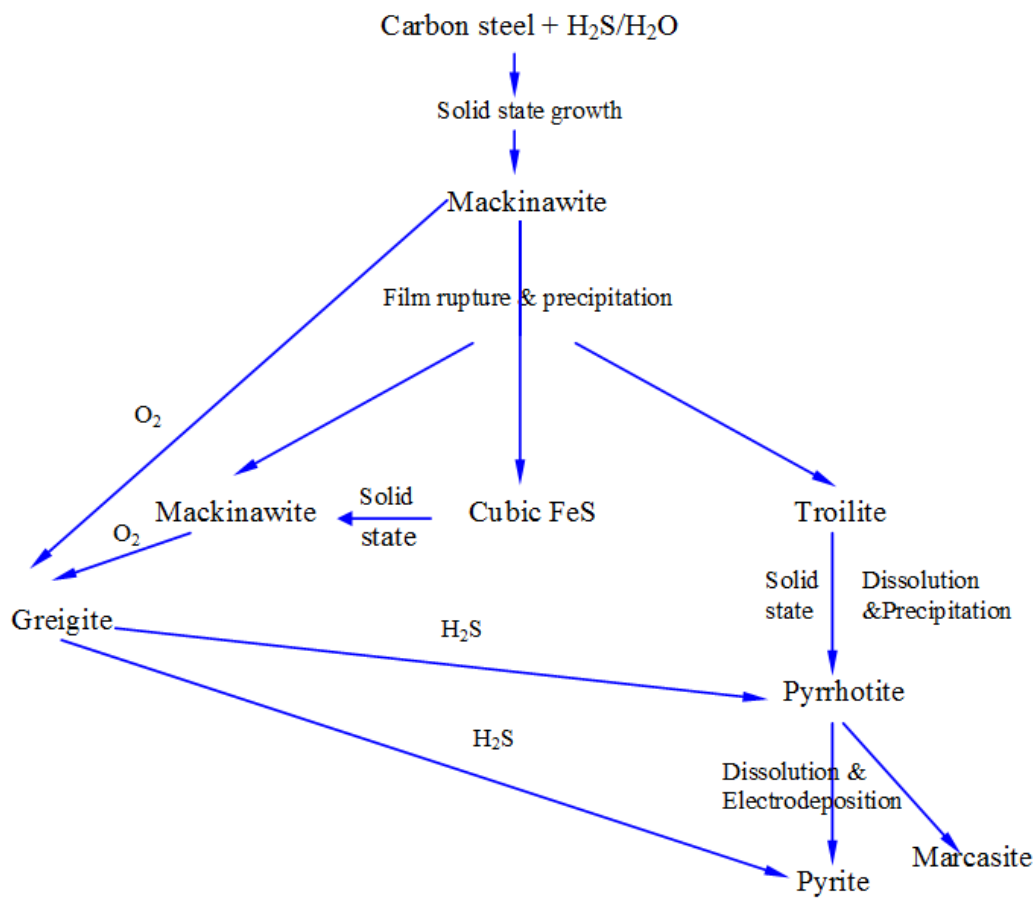


Figure 5. Corrosion product sequence of carbon steel in aqueous  $\text{H}_2\text{S}$  solution [37].

## Chapter 3: Objectives

### 3.1 Research Gaps and Objectives

Reviewing the above literature, several gaps can be clearly identified:

- Although some experimental work has been reported at low temperature, experimental conditions such as pH and  $p_{H_2S}$  are often not well controlled or even characterized during the test, which makes the conducted experiments and generated results unrepeatable and contradictory. Considering that the formation/transformation and properties of iron sulfides are highly dependent on the water chemistry, controlling the operating parameters is of prime importance.
- Although some efforts have been made by most researchers to examine and characterize the corrosion products obtained at the end of their tests, no explanation or attempts to predict and model the encountered phenomena based on thermodynamics and kinetics have been proposed.
- Investigation of sour corrosion at elevated temperatures is almost nonexistent. High temperature is expected to significantly affect the formation and transformation of iron sulfides. In  $CO_2$  environment,  $Fe_3O_4$  was identified as the main corrosion product rather than  $FeCO_3$  at  $250^\circ C$ . The very scarce information available seems to indicate that  $Fe_3O_4$  could also be present in sour environments. No comprehensive attempt to investigate the effect of high temperature on the formation and transformation of iron sulfide polymorphs, and consequently, their roles in corrosion, has been performed.

- No prediction model for sour corrosion of mild steel and corrosion product formation at high temperatures has been proposed to date.

The global objectives of the project are to study the kinetics and mechanism of H<sub>2</sub>S corrosion at high temperatures, and to expand the range of validity of existing mechanistic corrosion models to high temperatures. To achieve this objective, it is necessary to complete specific goals as follows:

1. Build a water chemistry model for H<sub>2</sub>S-H<sub>2</sub>O system at high temperatures.
2. Identify the effect of high temperature on the kinetics of corrosion and layer formation on mild steel in sour environments.
3. Investigate the effect of exposure time on the formation and transformation mechanisms among iron sulfide and iron oxide layers at high temperature.
4. Explore the effect of H<sub>2</sub>S partial pressure on the corrosion rate and layer formation on mild steel at high temperature.
5. Verify or rebuild the previously constructed thermodynamic model (Pourbaix diagrams) for the Fe-H<sub>2</sub>S-H<sub>2</sub>O system at high temperatures.
6. Develop a kinetic model for the effect of high temperature towards corrosion rate of mild steel in H<sub>2</sub>S environments based on Zheng's model [9].

### **3.2 Hypotheses**

- At high temperature, iron sulfides that are more thermodynamically stable such as pyrrhotite and pyrite, rather than mackinawite, will form due to fast kinetics, and consequently affect the corrosion rate and even promote localized corrosion.

- $\text{Fe}_3\text{O}_4$  can also form at high temperature by analogy with  $\text{CO}_2$  corrosion, and greatly decrease the corrosion rate.
- $\text{Fe}_3\text{O}_4$  will initially form at the steel surface and iron sulfide (mackinawite) will eventually precipitate on top of it once FeS saturation conditions are met. Then,  $\text{Fe}_3\text{O}_4$  will go through a simultaneous and continuous process of formation, at the steel/ $\text{Fe}_3\text{O}_4$  interface, and transformation to FeS, at the  $\text{Fe}_3\text{O}_4$ /FeS interface.

## Chapter 4: Water Chemistry Model for H<sub>2</sub>S-H<sub>2</sub>O System at High Temperatures

### 4.1 Introduction

As discussed above, the corrosion kinetics, the formation/transformation and properties of iron sulfides are highly dependent on water chemistry. Consequently, controlling the operating parameters is of prime importance. In this dissertation, all high temperature experiments were conducted in an autoclave. In order to control the experimental parameters, such as partial pressure of H<sub>2</sub>S and pH in the autoclave, a water chemistry model at high temperatures in a closed system was needed. A closed system (such as an autoclave) is a system that will be isolated after initially purging with gas to a designated pressure. Unlike an open system (typically a glass cell), the gas partial pressures in a closed system are not constant; the H<sub>2</sub>S in the gas phase dissolves into water and will not be replenished. It is actually extremely difficult to adjust parameters such as solution pH once the system has been pressurized. Instead of trying to control the operating parameters during the test, a different approach is taken which involves the prediction of test conditions based on the accurate determination for the corresponding conditions (pH, p<sub>H<sub>2</sub>S</sub>) at room temperatures and atmospheric conditions.

### 4.2 Model Development

The chemistry model development methodology is as shown in Figure 6:

- Step #1: Input the desired parameters of T, p<sub>H<sub>2</sub>S</sub>, and pH at equilibrium in operating conditions (high temperature);
- Step #2: Set the volume ratio between liquid phase and gas phase;

- Step #3: Apply molar balance for sulfur species and calculate all the dissolution and dissociation constants in a closed system;
- Step #4: Considering a closed system (molar balance) and the solution electroneutrality, calculate the corresponding parameters at 25°C and use these parameters as the initial set up conditions.

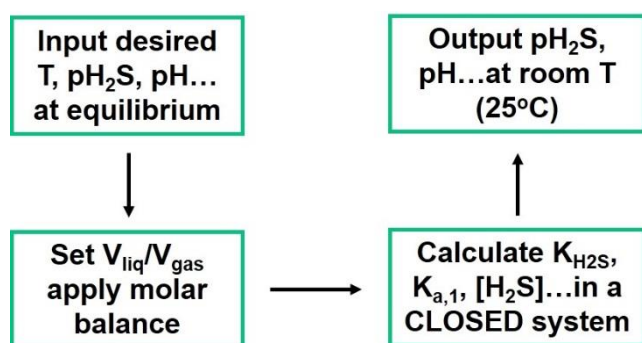


Figure 6. Process of modeling the water chemistry in a closed system at high temperatures.

Care must be taken to select expressions of several physical quantities and equilibrium constants valid at high temperature.

The first important factor is the water density since it experiences considerable changes at high temperatures and will significantly affect the water chemistry. The most widely accepted expression was reported by Jones [52]:

$$\rho = \frac{999.83952 + T_c(16.945176 + T_c(-7.9870401 \times 10^{-3} + T_c(-46.170461 \times 10^{-6} + T_c(105.56302 \times 10^{-9} - 280.54253 \times 10^{-12} T_c))))}{1.0 + 16.87985 \times 10^{-3} T_c} \quad (1)$$

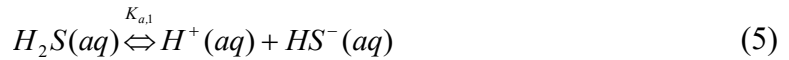
where  $\rho$  is water density in  $\text{kg/m}^3$ , and  $T_c$  is temperature in  $^\circ\text{C}$ . This expression was selected to be used in this model because it is adopted by the International Committee of Weights and Measures.

Secondly, equilibrium constants  $K_{H_2S}$ ,  $K_{a,1}$  and  $K_{a,2}$  were chosen based on work described by Suleimenov [53], [54] and Ning [55] (Equations (2)-(10)), but modified from molality to molarity. Originally, these values were expressed in molality ( $\text{mol/kg}\cdot\text{bar}$ ), but were used in molarity ( $\text{mol/L}\cdot\text{bar}$ ) since the numerical values are very close at temperatures under  $100^\circ\text{C}$  [55], [56]. However, as shown in Figure 7, when used at higher temperature (typically above  $100^\circ\text{C}$ ), large differences can appear (for example, more than 25% error appears at  $250^\circ\text{C}$ ).



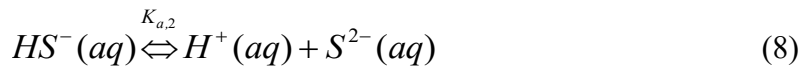
$$K_{H_2S} = \frac{[H_2S]}{p_{H_2S}} \quad (3)$$

$$K_{H_2S} = 10^{-(634.27+0.2709T_K-0.00011132T_K^2-16719/T_K-261.9\log T_K)} \quad (4)$$



$$K_{a,1} = \frac{[H^+][HS^-]}{[H_2S]} \quad (6)$$

$$K_{a,1} = 10^{782.43945+0.361261T_K-1.6722\times 10^{-4}T_K^2-20565.7315/T_K-142.7417222\ln T_K} \quad (7)$$



$$K_{a,2} = \frac{[H^+][S^{2-}]}{[HS^-]} \quad (9)$$

$$K_{a,2} = 10^{-(23.93-0.030446T_K+2.4831\times 10^{-5}T_K^2)} \quad (10)$$

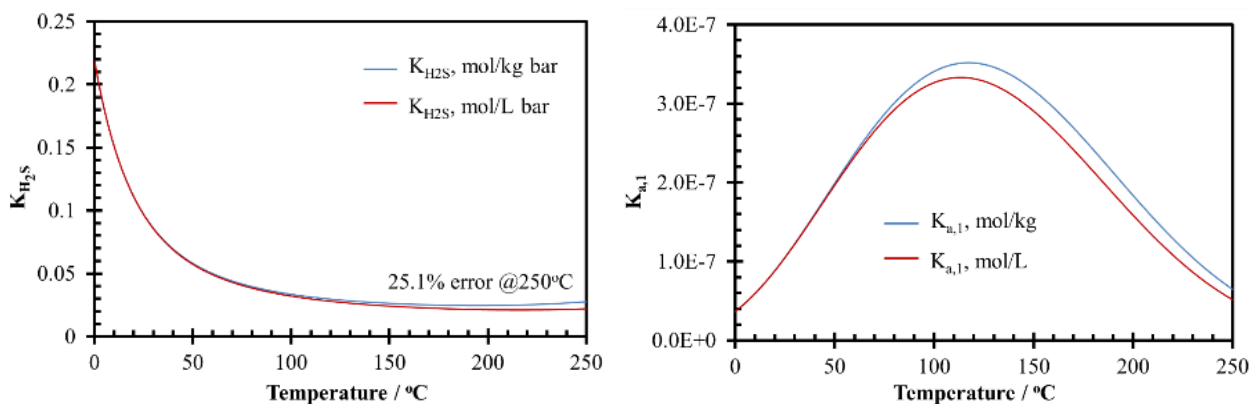


Figure 7.  $K_{H_2S}$  and  $K_{a,1}$  values in molality and molarity at different temperatures.

### 4.3 Parametric Study

A parametric study is completed to assess the validity of the predictions of species concentrations at different temperatures. The effect of  $V_{liq}/V_{gas}$  ratio on the water chemistry is shown in Figure 8. Being able to anticipate and understand the effect of this ratio is important since, ideally, the test conditions should simulate an open system where the partial pressure of  $H_2S$  is constant. This is not possible in an autoclave setup but the characteristics of an open system can be approached quite closely if the right conditions are selected. Figure 8 shows clearly that the behaviors of  $[H_2S]_{aq}$ ,  $[HS^-]$  and  $[S^{2-}]$  concentrations are different in an open and closed system at higher pH values. The discrepancy is more apparent at a lower liquid / gas volume ratio (*i.e.*, a large volume of gas). The total amount of  $H_2S$  that needs to be injected into the 7 L autoclave increases with decreasing gas volume for a fixed  $H_2S$  partial pressure. On the other hand, choosing a low liquid volume would lead to rapid change in chemistry due to the release of corrosion product. At a  $V_{liq}/V_{gas}$  ratio of 6, the discrepancy between open and close system is minimized. This ratio is therefore chosen in this work for every experimental

temperature. Since the  $V_{\text{liq}}/V_{\text{gas}}$  ratio is kept at 6 for all the experiments and since the water density changes with temperature, care had to be taken to ensure that the correct mass of water was introduced in the autoclave during the experimental setup phase. For example, 5.68 kg and 5.46 kg of water are added in the autoclave at 25°C for 120°C and 160°C experiments, respectively. Once the operating conditions are reached, the liquid/vapor equilibrium dictates that some of the water molecules will be in the vapor phase: around 1 g water in the gas phase ( $p_{\text{H}_2\text{O}}=1.99$  bar) at 120 °C and 3 g of that ( $p_{\text{H}_2\text{O}}=6.19$  bar) at 160°C, for example. The evaporation of liquid water will consequently have a negligible effect on the targeted  $V_{\text{liq}}/V_{\text{gas}}$  ratio.

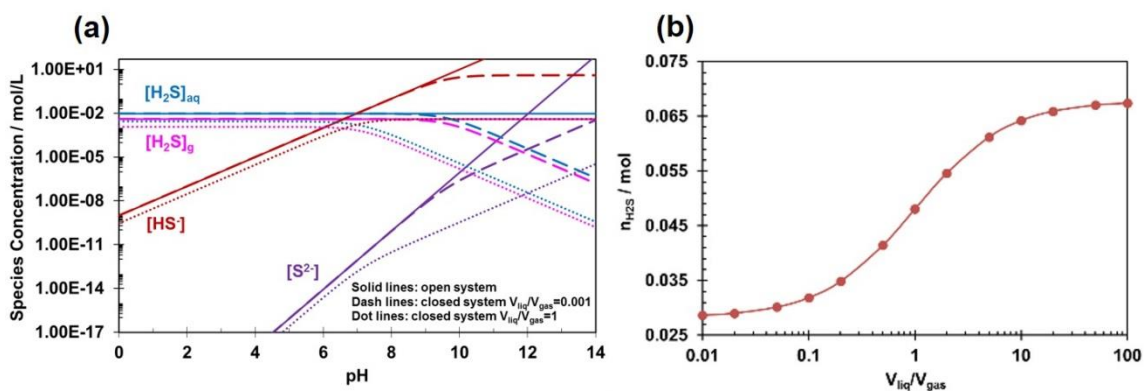


Figure 8. (a) Effect of  $V_{\text{liq}}/V_{\text{gas}}$  ratio on the concentrations of sulfur species, and (b) the total amount of  $\text{H}_2\text{S}$  in a 7 L autoclave,  $T=25^\circ\text{C}$ ,  $p_{\text{H}_2\text{S}}=0.10$  bar.

The effect of temperature on the concentrations of sulfide species at a fixed 0.1 bar pressure of  $\text{H}_2\text{S}$  is shown in Figure 9(a). All the species concentrations significantly vary with increasing temperature. However, what really matters is not  $p_{\text{H}_2\text{S}}$  but the dissolved  $\text{H}_2\text{S}$  in the solution  $[\text{H}_2\text{S}]_{\text{aq}}$ . In this work,  $[\text{H}_2\text{S}]_{\text{aq}}$  was kept at 0.00385 mol/L for every temperature tested. This corresponds to 0.1 bar  $\text{H}_2\text{S}$  at 80°C and to progressively

higher  $\text{pH}_2\text{S}$  values as temperature is increased (Figure 9(b)).  $\text{H}_2\text{S}$  corrosion at  $80^\circ\text{C}$ ,  $120^\circ\text{C}$ ,  $160^\circ\text{C}$ , and  $200^\circ\text{C}$  is investigated in the next chapter.

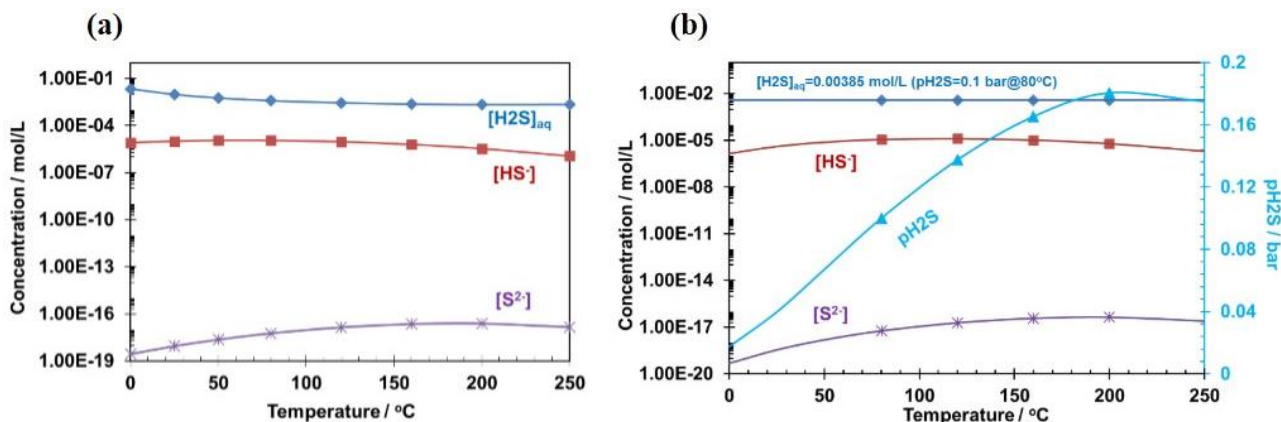


Figure 9. Effect of temperature on concentrations of sulfur species at (a) constant  $\text{pH}_2\text{S}=0.1$  bar and (b) constant  $[\text{H}_2\text{S}]_{\text{aq}}=0.00385$  mol/L ( $\text{pH}_2\text{S}=0.1$  bar@ $80^\circ\text{C}$ ),  $\text{pH}=4.00$ .

Experimentally speaking, the water chemistry at high temperature should be monitored and compared with theoretical values. Currently, due to the lack of a reliable reference electrode in high temperature and high pressure  $\text{H}_2\text{S}$  environments,  $\text{pH}$  could not be measured *in situ*. However, the chemistry is calculated considering literature data ( $\rho$ ,  $K_{\text{H}_2\text{S}}$ ,  $K_{\text{a},1}$ , and  $K_{\text{a},2}$ ) that have been verified up to  $250^\circ\text{C}$  [52]-[54]. Therefore, the water chemistry was back-calculated by characterization of liquid samples taken at the end of each experiment, which is also presented in the next chapter.

## Chapter 5: Effect of High Temperature on the Kinetics of Corrosion and Layer Formation on Mild Steel in Sour Environments

### 5.1 Introduction

As reviewed above, there is no systematic study on the effect of high temperature ( $> 80^{\circ}\text{C}$ ) on the  $\text{H}_2\text{S}$  corrosion of mild steel. Therefore, the first series of experiments is to determine the corrosion rate of mild steel and characterize the corrosion products in sour environments at temperatures ranging from  $80^{\circ}\text{C}$  to  $200^{\circ}\text{C}$ . Moreover, it is also necessary to clarify if  $\text{Fe}_3\text{O}_4$  can also form at high temperature by analogy with  $\text{CO}_2$  corrosion.

### 5.2 Experimental

Experiments were performed in a 7 L Hastelloy autoclave, shown in Figure 10. A three-electrode setup was used to conduct linear polarization resistance (LPR) measurements using a potentiostat. The working electrode was a cylindrical sample made from UNS K03014 (API 5L X65) carbon steel. The chemical composition of this tempered martensitic steel is shown in Table 2. A Pt-coated Nb counter electrode and a commercial Zr/ZrO<sub>2</sub> high temperature, high pressure pH probe was used as a pseudo reference electrode. The pH probe's reference serves as a reference electrode (exact potential still unknown) as long as its potential is stable at the desired test conditions [57]. Four flat 10×10×2 mm specimens were also attached to a stabilized shaft using a PTFE-coated 304 stainless steel wire. A centrally located impeller was used to keep the solution fully mixed during each test.

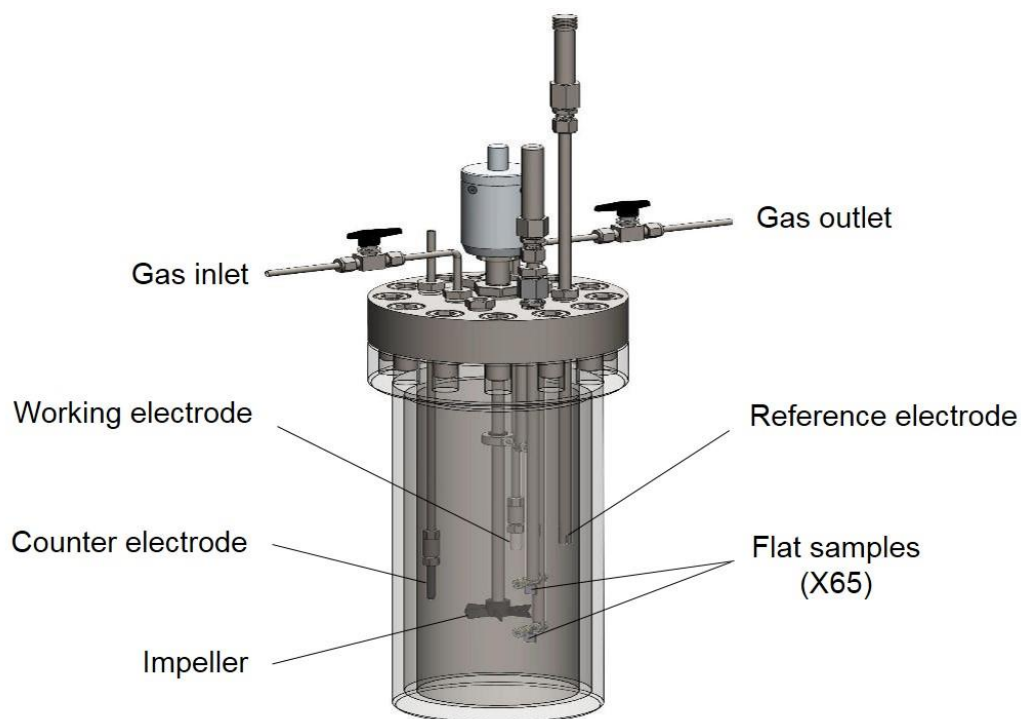


Figure 10. Experimental 7 L Hastelloy autoclave setup.

Table 2. Chemical composition of the API 5L X65 carbon steel (wt. %).

Cr	Mo	S	V	Si	C	P	Ni	Mn	Fe
0.14	0.16	0.009	0.047	0.26	0.13	0.009	0.36	1.16	Balance

The experimental details and test matrix are summarized in Table 3 and Table 4. The experimental conditions related to the different tested temperatures were calculated according to the water chemistry model described in Chapter 4.

Table 3. Experimental details.

Parameter	Description
System	7 L Hastelloy autoclave
Solution	1 wt.% NaCl
Specimen	API 5L X65
Stirring Speed	1000 rpm
Duration	4 days
Measurement Methods	Weight loss, LPR, (Zr/ZrO <sub>2</sub> as a pseudo-reference electrode), H <sub>2</sub> S concentration (GC)
Surface Characterization	XRD, SEM/EDS, Profilometry

Table 4. Test matrix for the effect of temperature.

Parameter	Values			
Temperature, °C	80	120	160	200
pH <sub>2</sub> S, bar	0.10	0.14	0.17	0.18
Total pressure, bar	8.92	11.89	17.55	28.40
pH	4.00			
[H <sub>2</sub> S] <sub>aq</sub> , mol/L	0.00385			
Duration, days	4			

A key experimental goal is to start each experiment with a bulk pH of 4.00, once the targeted temperature has been reached. This is achieved by following the experimental procedure outlined below.

- The 1 wt.% NaCl solution was purged with N<sub>2</sub> overnight at room temperature;
- pH was adjusted to the room temperature condition by using a deaerated HCl solution (1 M) based on the water chemistry calculation;

- The API 5L X65 specimens were mounted onto the autoclave lid and put into place;
- The electrolyte was further deoxygenated by purging with N<sub>2</sub> for another 1 hour (to avoid oxygen contamination during pH adjustment);
- The gas-out valve was closed and N<sub>2</sub> was used to pressurize the system to ensure there were no leaks;
- The system was then depressurized and H<sub>2</sub>S was rapidly introduced to the desired pressure (Table 4) from a 10%(v) H<sub>2</sub>S(N<sub>2</sub>) gas mixture;
- The autoclave was then heated up to the desired temperature (initial condition) in a stepwise manner to avoid overheating. It took about 30 min to heat the autoclave from room temperature to 120°C;
- After reaching the targeted experimental temperature, LPR was conducted between ±5 mV vs. OCP at a scan rate of 0.125 mV/s. However, this OCP was measured with respect to the pseudo Zr/ZrO<sub>2</sub> electrode and thus not recorded;
- After 4 days, which was enough to get a relatively stable corrosion rate [58], the autoclave was cooled to *ca.* 50°C;
- The H<sub>2</sub>S concentration in the gas phase was then measured by gas chromatography (GC);
- N<sub>2</sub> was used to purge the system, and remove remaining H<sub>2</sub>S, for ~3 hours;
- The autoclave lid was opened (using an H<sub>2</sub>S sensor to ensure there was no H<sub>2</sub>S remaining) and pH was measured at atmospheric conditions, then the Fe<sup>2+</sup> concentration of the solution determined using a spectrophotometer;

- The corroded samples were retrieved and characterized by X-ray diffraction (XRD), scanning electron microscopy/energy dispersive X-ray spectroscopy (SEM/EDS), and surface profilometry.

### Safety Notes

Hydrogen sulfide is a notorious and extremely toxic gas that is frequently associated with oil and gas production. According to Occupational Safety and Health Administration (OSHA) safety guides, 10 ppm is the permissible exposure limit (PEL) for 8 hours a day. Exposure to a concentration of even lower than 10 ppm can cause personal health issues such as dizziness and nausea. A concentration of 100 ppm can lead to immediate danger to life or health (IDLH).

All the experiments followed the Institute for Corrosion and Multiphase Technology (ICMT) protocol for working with H<sub>2</sub>S. Annual H<sub>2</sub>S safety training was required before working with H<sub>2</sub>S. A self contained breathing apparatus (SCBA) was required for working in the H<sub>2</sub>S room with an equally equipped “buddy” outside the room watching the activities. A pressure test was always performed for the autoclave using N<sub>2</sub> before H<sub>2</sub>S injection.

### 5.3 Results and Discussion

**5.3.1 Corrosion rates.** Figure 11 shows the corrosion rates over time at 80°C, 120°C, 160°C, and 200°C as measured by LPR. The slope of the LPR line corresponds to the polarization resistance  $R_p$ . The solution resistance  $R_s$  can be obtained from EIS measurement. The corrosion current  $i_{corr}$  (A/cm<sup>2</sup>) can then be calculated by:

$$i_{corr} = \frac{B}{R_p - R_s} \quad (11)$$

The corrosion current was converted to corrosion rate by using the following equation [27]:

$$CR = \frac{M_w i_{corr}}{nF\rho A} \quad (12)$$

where  $M_w$  is the molar mass of iron (55.8 g/mol),  $n$  is the number of electrons transferred,  $F$  is Faraday's constant,  $\rho$  the density of iron (7.87 g/cm<sup>3</sup>),  $A$  the electrode area in cm<sup>2</sup>.

Then, the average LPR corrosion rate was compared with the weight loss (WL) corrosion rate and the  $B$  value was optimized, if needed.

It can be seen that the initial corrosion rates increased with increasing temperature, and then quickly decreased to stable corrosion rates of 4.1, 3.8, 1.8 and 2.5 mm/y, respectively, from lowest to highest temperature. Overall, the steady-state corrosion rate decreased with temperature except at 200°C.

The time-averaged corrosion rates obtained from weight loss (WL) are shown in Figure 7. They are in good agreement with the time-integrated corrosion rate from LPR using a  $B$  value of 23 mV/decade.

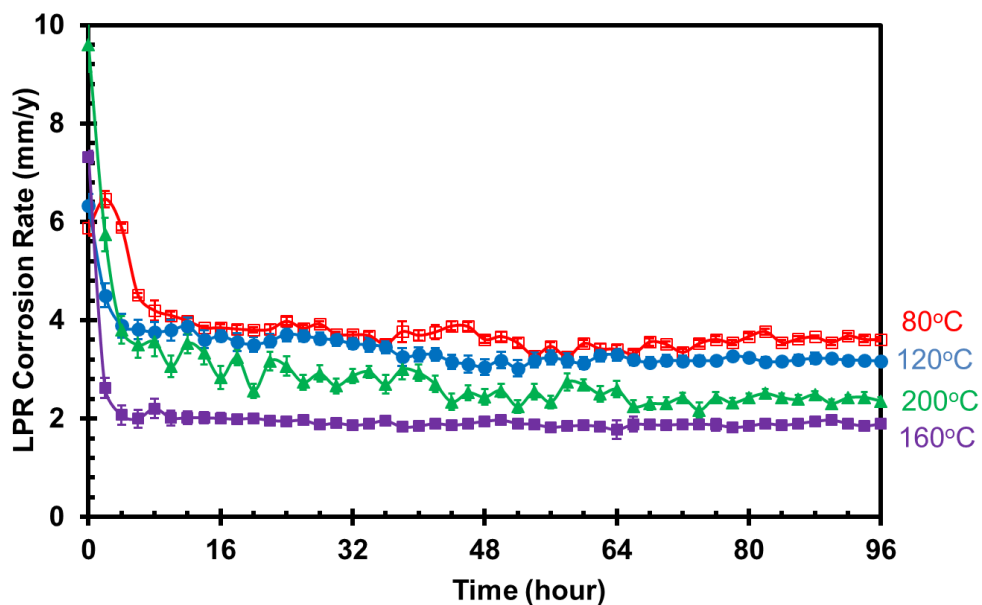


Figure 11. Corrosion rate at different temperatures from LPR measurement,  $[\text{H}_2\text{S}]_{\text{aq}}=0.00385$  mol/L, pH=4.00, 4 days,  $B=23$  mV/decade.

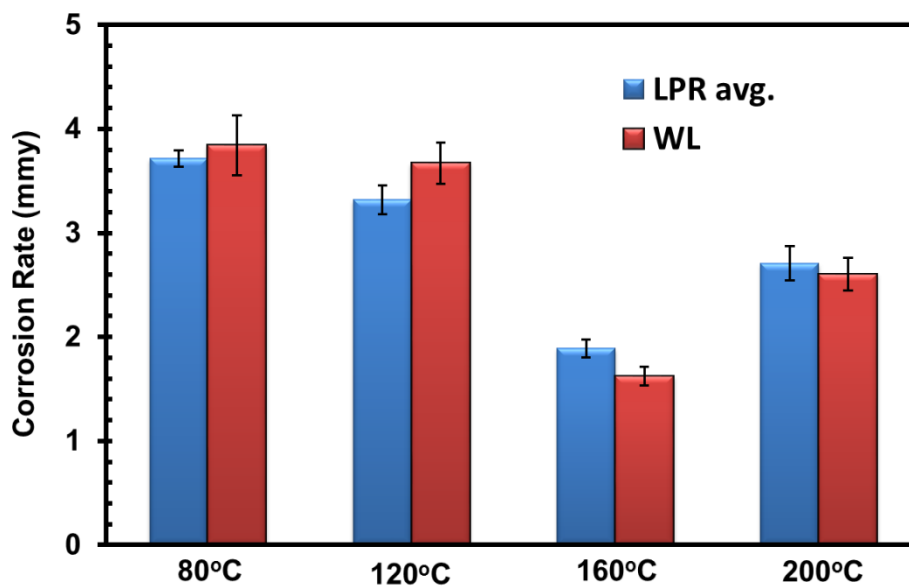


Figure 12. Comparison of corrosion rates between LPR and weight loss,  $[\text{H}_2\text{S}]_{\text{aq}}=0.00385$  mol/L, pH=4.00, 4 days,  $B=23$  mV/decade.

**5.3.2 Corrosion products.** The corrosion products on the steel surface were characterized by XRD, as shown in Figure 13. It is important to mention that X-rays are only able to penetrate through the first few microns of the corrosion product layer. While mackinawite (FeS) was the main corrosion product detected at 80°C, troilite (FeS), pyrrhotite ( $\text{Fe}_{1-x}\text{S}$ ,  $x=0\sim 0.17$ ), and pyrrhotite/pyrite ( $\text{FeS}_2$ ) became the dominant species as temperature was increased. With increasing temperature, the corrosion product became richer in sulfur; this is an indication of enhanced reaction kinetics for phase transformations. It is also important to notice that the  $\alpha$ -Fe peaks are absent in the XRD patterns at 120°C, 160°C, and 200°C, inferring that the corrosion product is relatively thick since the X-rays cannot penetrate through the metal substrate.

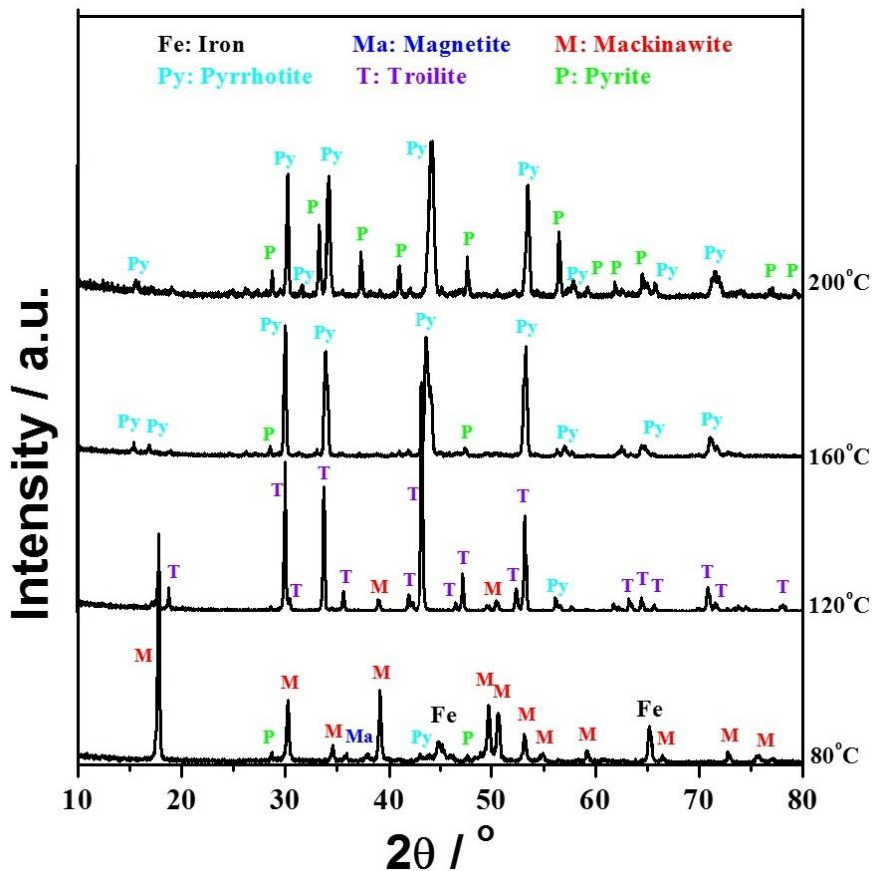
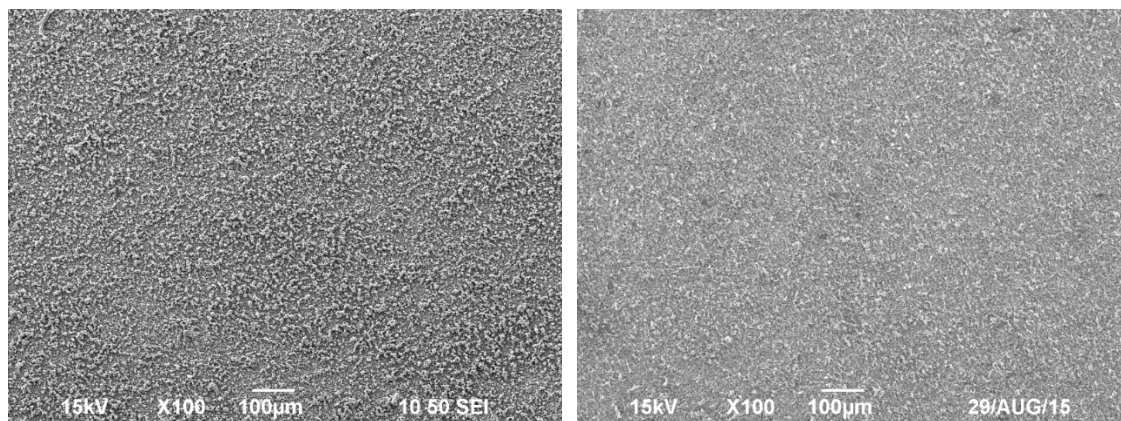


Figure 13. XRD patterns of corrosion products on the steel surface at different temperatures,  $[H_2S]_{aq}=0.00385$  mol/L, pH=4.00, 4 days.

The morphologies of the formed corrosion products were also characterized by SEM analysis of the frontal and cross-sectional views, as shown in Figure 14 and Figure 15. The SEM for the 80°C specimen shows a mackinawite layer of 15  $\mu\text{m}$  thickness, which is much thinner than the corresponding metal loss thickness calculated to be 42  $\mu\text{m}$ . From the EDS line scan, the outer layer was identified to be likely an iron sulfide (as confirmed by XRD analysis) but an inner layer, which consisted mostly of iron and oxygen was postulated to be an iron oxide. At 120°C, the SEM shows troilite-like

crystals on the surface and a much thicker layer (61~73  $\mu\text{m}$ ). As a reminder, the  $\alpha\text{-Fe}$  peaks are absent in the XRD pattern in this condition as the corrosion product is so thick, preventing the X-rays from reaching the metal substrate. At 160°C, pyrrhotite crystals were clearly observed. The thickness of the layer was only about 10  $\mu\text{m}$ , but still no  $\alpha\text{-Fe}$  peaks were detected by XRD; indicating the corrosion product layer was very dense and compact. This is also probably why the corrosion rate at 160°C was the lowest. The corrosion products changed to planar flaky crystals at 200°C. All the cross-sections show a two-layer structure at every temperature tested: an inner layer comprised of an iron oxide and an outer layer comprised of an iron sulfide. However, the iron oxide was undetected by XRD due to the top layer being too thick and compact for XRD penetration.



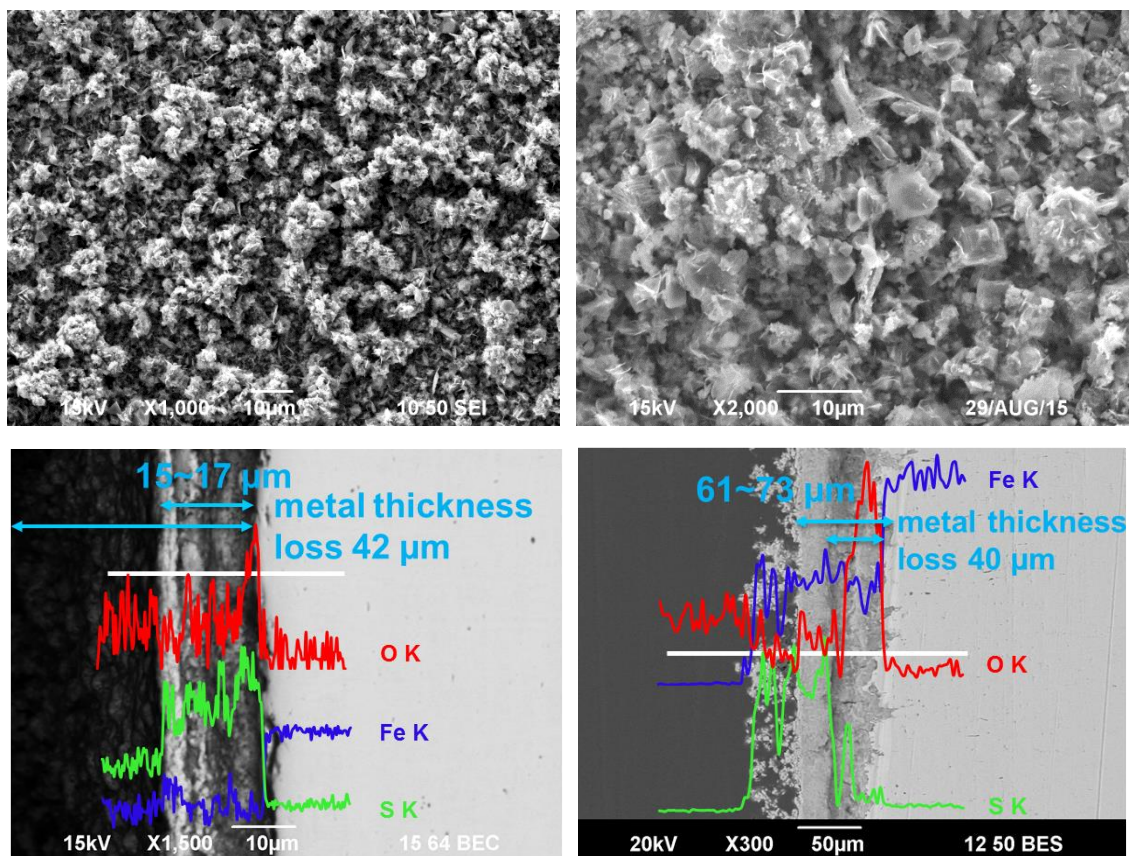
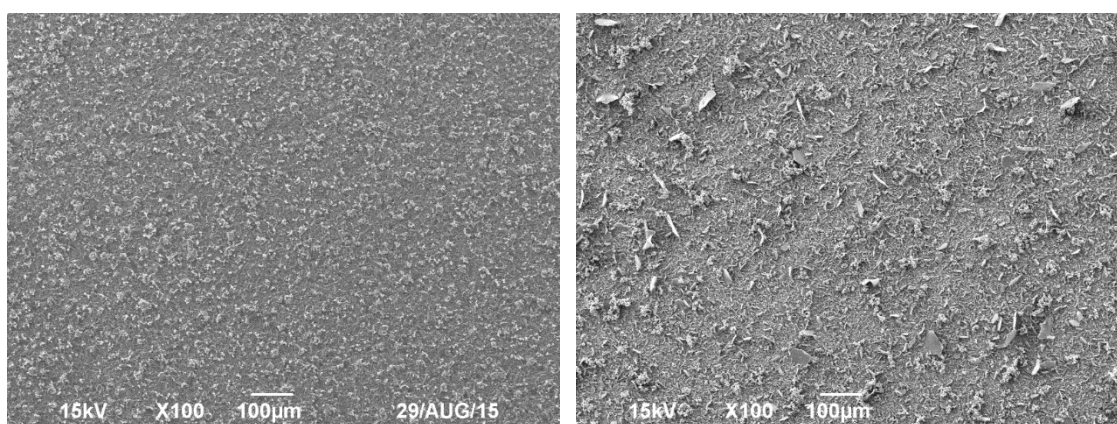


Figure 14. SEM of morphologies and cross-sections at 80°C (left) and 120°C (right),  $[\text{H}_2\text{S}]_{\text{aq}}=0.00385$  mol/L, pH=4.00, 4 days.



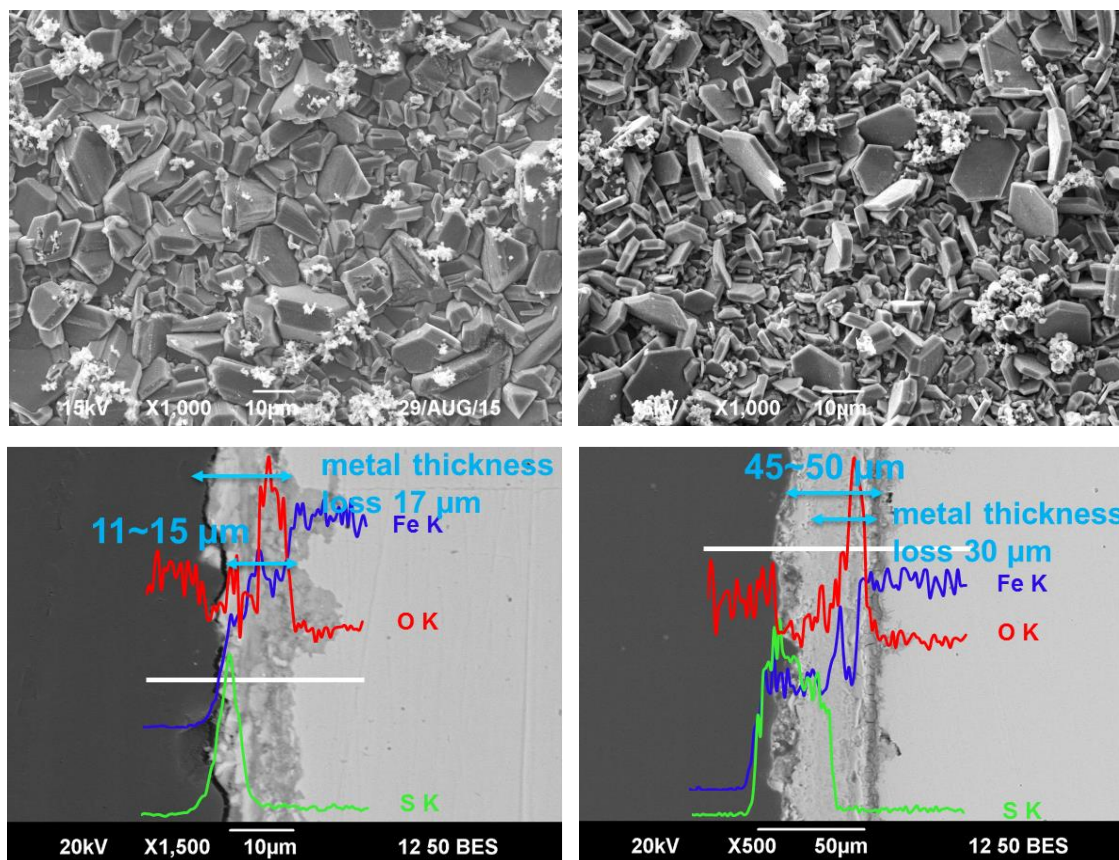


Figure 15. SEM of morphologies and cross-sections at 160°C (left) and 200°C (right),  $[H_2S]_{aq}=0.00385$  mol/L, pH=4.00, 4 days.

**5.3.3 Surface profilometry.** After removal of the corrosion products using Clarke solution [59], the metal surface was characterized by profilometry as shown in Figure 16 and Figure 17. No obvious localized corrosion was observed at 80°C and 120°C. The surface was relatively smooth and the corrosion could be considered as uniform. However, at 160°C some small pits could be observed with around a 1.2 pitting ratio (ratio of maximum pit rate to general corrosion rate) and 1.5 mm/y pit penetration rate. This can be treated only as localized corrosion initiation. At 200°C, many large pits

appeared with a 3.2 pitting ratio and 8.2 mm/y pit penetration rate. The pitting ratio is not accurate since the pitting corrosion overwhelmed the whole general corrosion. Due to severe localized corrosion at this temperature, the stable LPR corrosion rate was slightly higher than at 160°C (Figure 11). These results agree with Ning's previous work [10] where it was found that once there is pyrite formation, localized attack would occur.

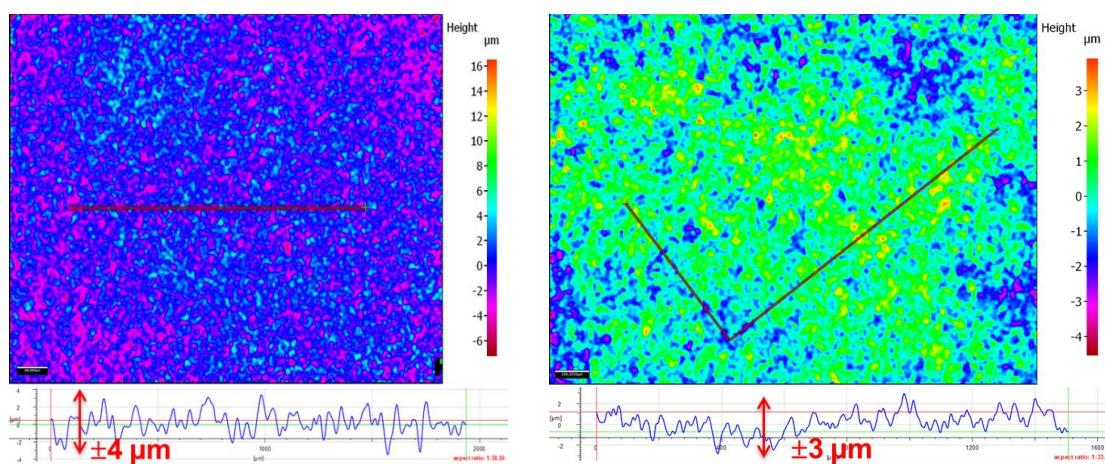
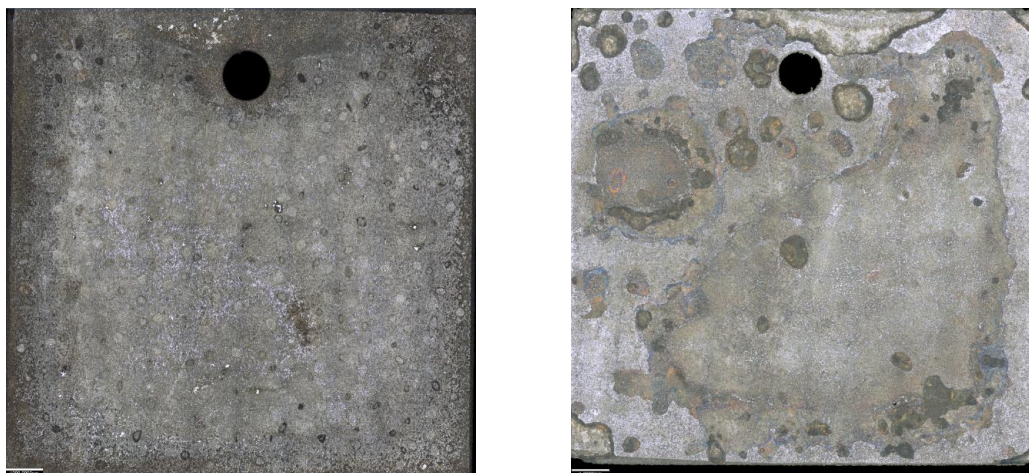


Figure 16. Surface profilometry after removing corrosion products at 80°C (left) and 120°C (right),  $[H_2S]_{aq}=0.00385$  mol/L, pH=4.00, 4 days.



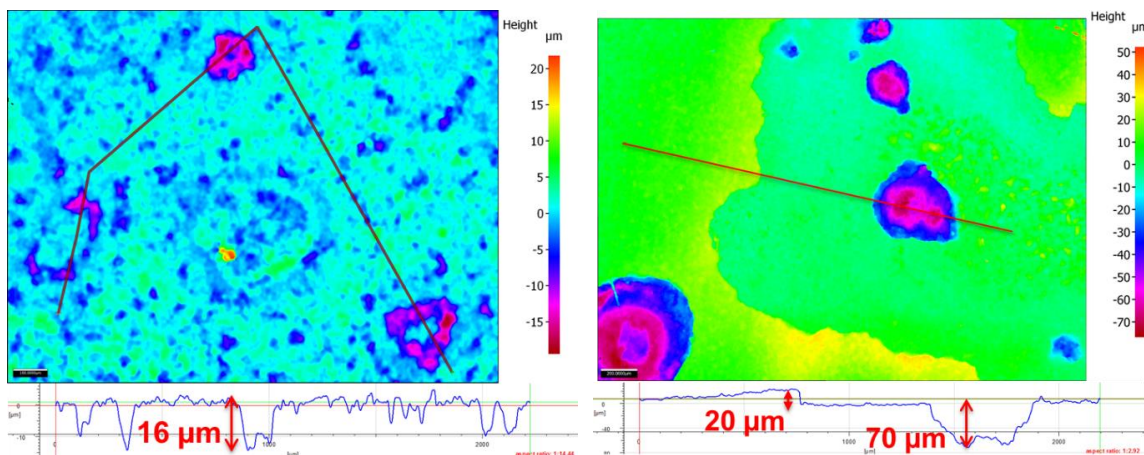


Figure 17. Surface profilometry after removing corrosion products at 160°C (left) and 200°C (right),  $[H_2S]_{aq}=0.00385$  mol/L, pH=4.00, 4 days.

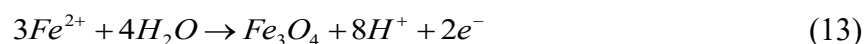
**5.3.4 Formation of iron oxide.** The current results are insufficient to make conclusive mechanistic statements, however, there are some new findings that are worthy of discussion, especially in the context of the existing literature.

Iron oxide was found, at every temperature tested, as the main component of the inner corrosion product layer (Figure 14 and Figure 15). Until now, iron oxide has not been given much attention as a corrosion product in  $H_2S$  corrosion environments. It is hypothesized that this iron oxide is magnetite ( $Fe_3O_4$ ) due to the following observations:

- Two  $Fe_3O_4$  peaks were observed from XRD analysis at 80°C (Figure 13), though they were undetected at other temperatures due to the top layer being either too thick or too compact for X-ray penetration;
- $Fe_3O_4$  was also confirmed as an inner layer from a previous study in sour environments at 220°C [37];

- $\text{Fe}_3\text{O}_4$  is also the main corrosion product at high temperatures in  $\text{CO}_2$  environments [27].

The kinetics of  $\text{Fe}_3\text{O}_4$  formation is very fast, making the scaling tendency (ST is the ratio of precipitation rate to corrosion rate) very high at high temperature. The presence of this iron oxide was confirmed by transmission electron microscopy (TEM) see the next Chapter.  $\text{Fe}_3\text{O}_4$  can form on the metal surface according to Reaction (13):



From the Pourbaix diagram shown in Figure 18, considering a sweet ( $\text{CO}_2$  dominated) system,  $\text{Fe}_3\text{O}_4$  is dominant in a very limited narrow area at potentials more positive than those for  $\text{FeCO}_3$  at  $80^\circ\text{C}$ . When the temperature increases to  $200^\circ\text{C}$ , the possibility of  $\text{Fe}_3\text{O}_4$  being the dominant species is greatly increased. Similarly, in sour corrosion at high temperature, the iron oxides should be taken into account, along with the iron sulfides.

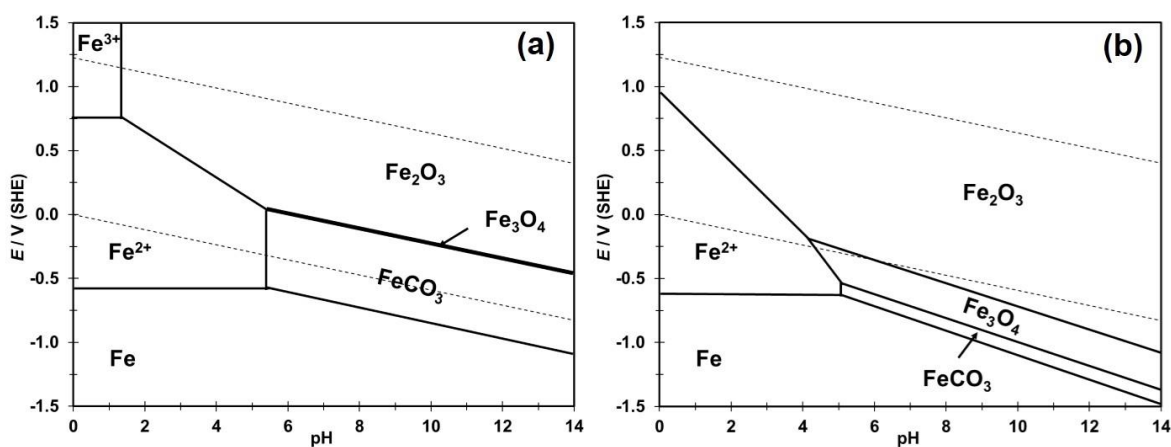
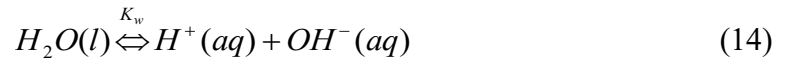


Figure 18. Pourbaix diagram for Fe- $\text{CO}_2$ - $\text{H}_2\text{O}$  system (a) at  $80^\circ\text{C}$  and (b)  $200^\circ\text{C}$ , 1 bar  $\text{CO}_2$  at  $25^\circ\text{C}$ .

**5.3.5 Formation of iron sulfide.** This section compares the thermodynamic predictions for the formation of corrosion products with the experimental results. The thermodynamic prediction model selected for comparison is based on Ning's work (the calculation methodology is described in Appendix I) [32], which has not been verified above 80°C. This exercise is used to highlight gaps in the understanding and modeling work and propose a way forward to extend the domain of validity of the predictions. In order to do so, a good understanding of the water chemistry at operating conditions needs to be developed. However, this constitutes a challenge since no direct measurement of pH and Fe<sup>2+</sup> concentration could be performed *in situ*; some assumptions are needed as described below.

During each test, the gaseous H<sub>2</sub>S and aqueous Fe<sup>2+</sup> concentrations were measured using GC and spectrophotometry, respectively, after cooling down the autoclave (usually to around 50°C). The aqueous Fe<sup>2+</sup> concentration increased over time due to the corrosion process. The water chemistry was calculated at this measured temperature according to Equations (3), (6), (9), (15), and (17):



$$K_w = [H^+][OH^-] \quad (15)$$

$$K_w = 10^{-(29.3868 - 0.0737549T_K + 7.47881 \times 10^{-5}T_K^2)} \quad (16)$$

$$[Na^+] + 2[Fe^{2+}] + [H^+] = [Cl^-] + [HS^-] + 2[S^{2-}] + [OH^-] \quad (17)$$

For the electroneutrality equation (Equation (17)), the [Cl<sup>-</sup>] was known experimentally by recording how much NaCl and HCl were added (for pH adjustment).

There are 5 equations and 5 unknowns ( $[H_2S]_{aq}$ ,  $[HS^-]_{aq}$ ,  $[S^{2-}]_{aq}$ ,  $[H^+]_{aq}$ , and  $[OH^-]_{aq}$ ). At operating conditions the  $[H_2S]_g$  is also unknown and a sixth equation is required: the total amount of sulfide species was calculated by applying a molar balance:

$$\sum S = [H_2S]_g + [H_2S]_{aq} + [HS^-]_{aq} + [S^{2-}]_{aq} = constant \quad (18)$$

It is assumed that no significant gain or loss of  $Fe^{2+}$  occurred during the test “cooling down” procedure, either by FeS precipitation or dissolution. The  $[Fe^{2+}]$  concentration measured at the sampling temperature was assumed to be the same as under the final conditions. At the experimental temperature,  $pH_2S$  is also unknown, in addition to the 5 unknowns mentioned above, but the extra Equation (18) can be used. The calculation results are summarized in Table 5.

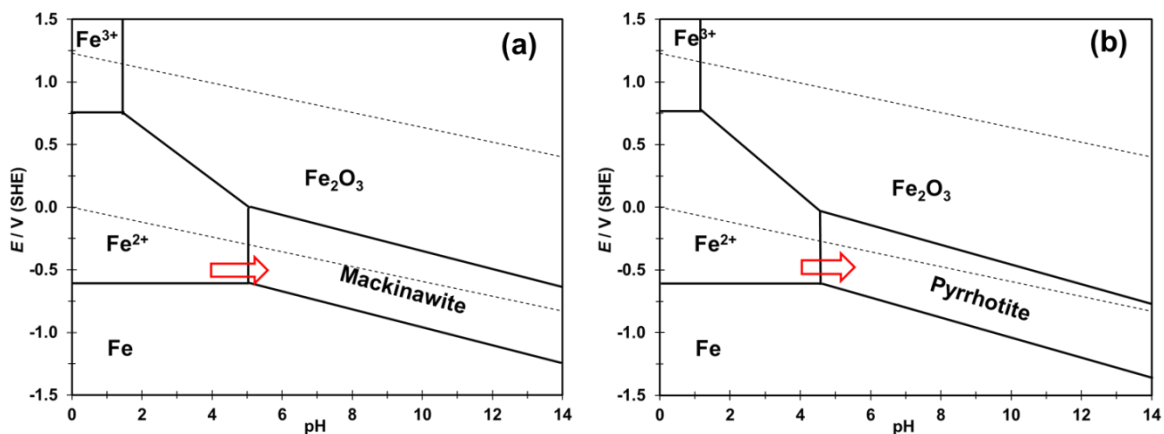
Table 5. Summary of initial conditions and theoretical calculated final conditions.

	Targeted Initial Conditions (pH 4.0)	Final Conditions			H <sub>2</sub> S consumed (calculated based on stoichiometric FeS)	
		pH <sub>2</sub> S, bar (± 0.01 bar)	pH (± 0.1)	Fe <sup>2+</sup> , ppm (± 0.5 ppm)	pH <sub>2</sub> S, bar (± 0.01 bar)	Percentage
80	0.10	0.07	5.47	1.79	0.0023	2.3%
120	0.14	0.11	5.42	5.82	0.0034	2.4%
160	0.14	0.14	5.48	4.26	0.0018	1.3%
200	0.18	0.16	5.78	2.31	0.0045	2.5%

Compared with the targeted initial conditions (calculated based on the total amount of H<sub>2</sub>S introduced in the autoclave), the final pH<sub>2</sub>S decreased slightly due to the

consumption of  $\text{H}_2\text{S}$  during the corrosion process and especially the formation of  $\text{FeS}$ . However, this observation may not be accurate since the concentration of  $\text{H}_2\text{S}$  was only measured at the end of the test. The depletion of  $\text{H}_2\text{S}$  can also be estimated based on the thickness of a stoichiometric  $\text{FeS}$  layer ( $4.84 \text{ g/cm}^3$ ) precipitated on the steel specimen, as shown in Table 5. Assuming a porosity of 0.9 [60], the depletion of  $\text{H}_2\text{S}$  from the gas phase could be up to 2.5%, which is acceptable.

The final pH values all drifted from 4.00 to above 5.40, which represent conditions increasingly favorable for iron sulfide formation. These parameters are used to generate Pourbaix diagrams as shown in Figure 19. The red arrow represents the pH shifting and the likely potential range (around  $-500 \text{ mV vs. SHE}$ ).



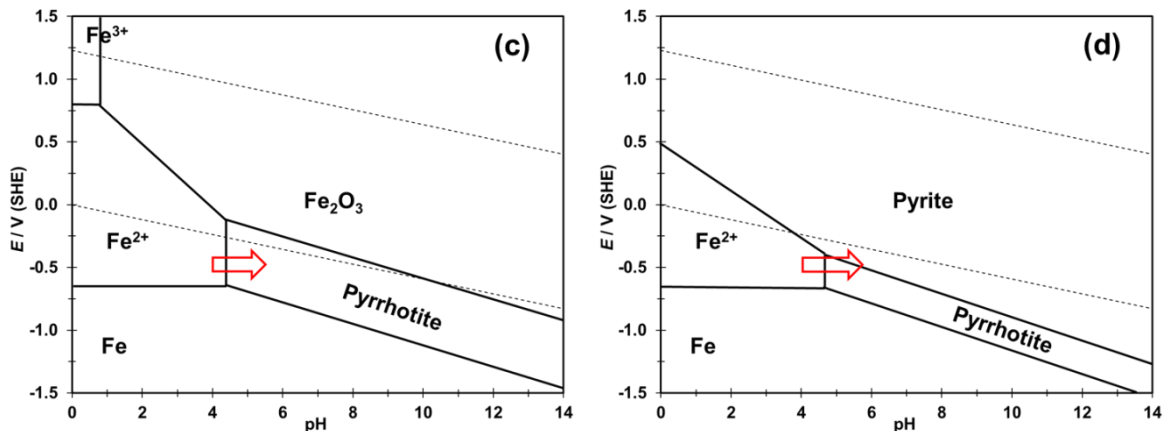


Figure 19. Pourbaix diagram for Fe-H<sub>2</sub>S-H<sub>2</sub>O system [32], (a) 80°C, mackinawite, (b) 120°C, pyrrhotite (troilite), (c) 160°C, pyrrhotite, and (d) 200°C, pyrite/pyrrhotite, other input parameters are in Table 5.

Thermodynamically, pyrrhotite and pyrite are the most stable phases and should be present in the Pourbaix diagrams. Different polymorphs and related phases of iron sulfides were identified experimentally at the different tested temperatures. For comparison purposes, only specific phases or polymorphs of Fe<sub>x</sub>S<sub>y</sub> were considered depending on the experimental conditions: mackinawite at 80°C, mackinawite/ pyrrhotite at 120°C and 160°C, mackinawite/ pyrrhotite/pyrite at 200°C. It can be seen that, at every tested temperature, the final operating conditions seems to match the formation zone of the selected iron sulfide. Particularly at 200°C, the “pH shift” arrow crosses the equilibrium line between pyrrhotite and pyrite, indicating a possible iron sulfide transformation between pyrrhotite and pyrite, which is in good agreement with the XRD data (Figure 13).

## 5.4 Summary

Sour corrosion experiments were successfully conducted at 80°C, 120°C, 160°C and 200°C. Initial corrosion rates increased with increasing temperature. Final corrosion rates, after 4 days of exposure, remained high at between 2 and 4 mm/y.

Iron sulfide transformation was observed for the first time in high temperature H<sub>2</sub>S corrosion. The inner corrosion product was iron oxide (postulated to be Fe<sub>3</sub>O<sub>4</sub>), the outer layer was mainly mackinawite, troilite, pyrrhotite and pyrite at 80°C, 120°C, 160°C, and 200°C, respectively. While thermodynamic modeling predicts pyrrhotite and pyrite as the most stable iron sulfide, other phases (mackinawite and troilite) could also be kinetically favored under different conditions.

## **Chapter 6: Effect of Exposure Time on the Formation and Transformation among Iron Sulfide and Iron Oxide Layers at High Temperature**

### **6.1 Introduction**

In the previous chapter, iron oxide was clearly observed as an inner corrosion product layer at every tested temperature (80°C, 120°C, 160°C, and 200°C). However, according to thermodynamic predictions (Pourbaix diagrams), as shown in Figure 19, iron oxide should not be present in an aqueous H<sub>2</sub>S environment since it is less stable than any of the various iron sulfides that can form. Therefore, further research was warranted to investigate whether the unexpected iron oxide layer would keep growing or, as thermodynamics predicts, would eventually be converted into iron sulfide as the exposure time increases.

As reviewed in Section 2.4, at low temperature, the reported sequence of iron sulfide transformation with time is mackinawite → cubic FeS → troilite → pyrrhotite → greigite (transition state) → pyrite [46]. It is expected that higher temperatures could affect this transformation sequence and proper investigation is fully warranted.

In order to address the research gaps stated above, H<sub>2</sub>S corrosion tests were performed on carbon steel at 120°C with exposure times of 1, 4, 7, and 21 days.

### **6.2 Experimental**

The experimental setup, material, and procedures used in this section are the same as presented in Chapter 5. Certain text matrix parameters, specifically pH and pH<sub>2</sub>S, were calculated based on the water chemistry model described in Chapter 4, as summarized in Table 6. The temperature was selected to be 120°C to avoid the rapid formation of pyrite.

According to the results in Chapter 5, pyrite was expected to form at higher temperatures and causes severe localized attack, which would greatly affect the experimental results. In addition to XRD and SEM/EDS analyses, focused ion beam (FIB) specimen prep and selected area diffraction (SAD) were performed in conjunction with transmission electron microscopy (TEM) to identify the phase identity of the inner iron oxide layer.

Table 6. Test matrix for the effect of time.

Parameter	Value
Temperature	120 °C
pH <sub>2</sub> S	0.10 bar
Total pressure	8.92 bar
Initial pH at 120 °C	4.0
[H <sub>2</sub> S] <sub>aq</sub>	0.00385 mol/L
Rotating speed of impeller	1000 rpm
Duration	1, 4, 7, and 21 day(s)

## 6.3 Results and Discussion

**6.3.1 Corrosion rates.** Figure 20 shows the corrosion rates measured using LPR for nominally identical conditions and different test durations: 1, 4, 7, and 21 days. For all experiments, the initial corrosion rate was around 6 mm/yr, which then decreased rapidly in the first day and stabilized between 2 and 4 mm/yr. Although initial conditions were well controlled, once the autoclave had been closed, there was no control of the operating parameters other than temperature and total pressure. Therefore, it is difficult to know how the water chemistry in the autoclave exactly evolved (pH, H<sub>2</sub>S concentration,

etc.). It has most likely diverged in different experiments leading to some scatter in the experimental results. All four repeats show very similar behavior in the first few days. The longer exposure 7-day experiment showed an unexpected increase in the corrosion rate. However, this was only observed on the working electrode but not on the independent weight loss specimens.

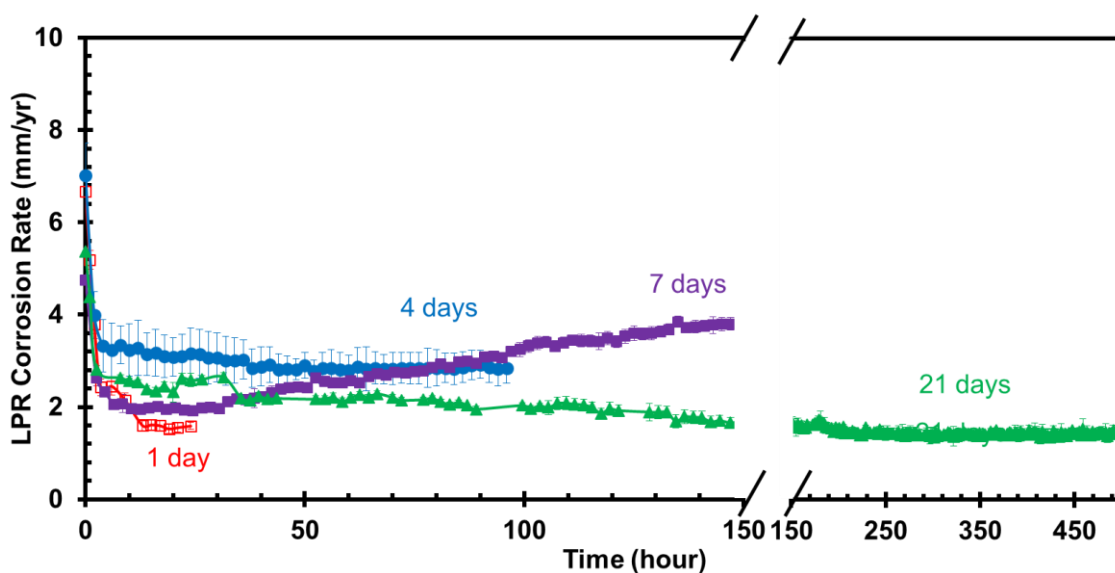


Figure 20. Corrosion rate for different test durations from LPR measurements,  $T=120^{\circ}\text{C}$ ,  $\text{pH}_2\text{S}=0.10$  bar, initial  $\text{pH}=4.0$ ,  $B=23$  mV/decade.

The area under the LPR corrosion rate curves in Figure 20 is compared to the measured WL values in Figure 21. The LPR calculations used a  $B$  value of 23 mV/decade to obtain the mean corrosion rate value, while the error bars reflect the variation in estimating the polarization resistance from the nonlinear current-voltage curves. For the WL specimens, the error bars represent the maximum and minimum values obtained

from the three specimens exposed at the same time to the corrosion environment. It is important to point out that the high temperature electrochemical measurements are inherently difficult to perform, especially in sour environments. Unsatisfactory agreement between LPR and WL measurements is apparent in some conditions, especially in the 7 days exposure experiment. The WL corrosion rate is more reliable and preferred. In these conditions, the LPR corrosion rate only gives, at best, a trend and caution should be taken in interpreting the data.

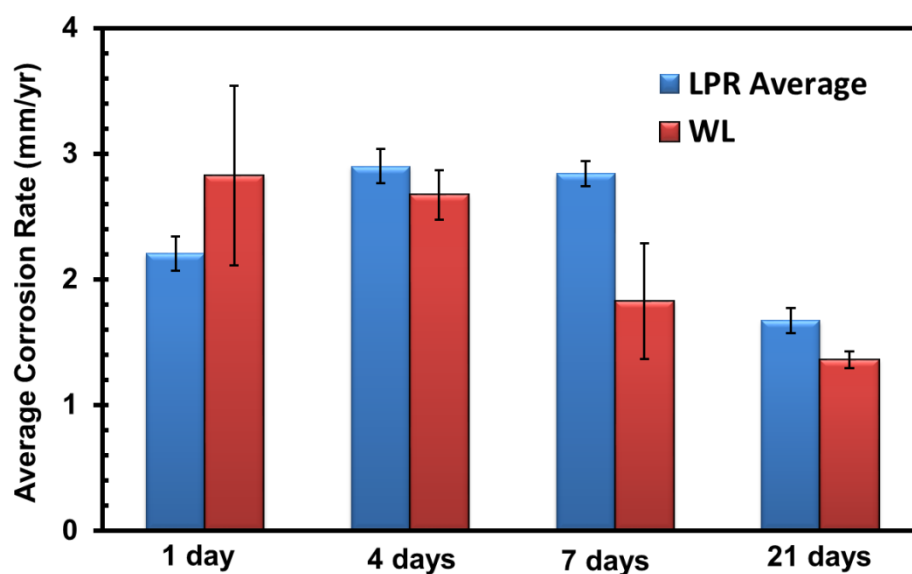


Figure 21. Comparison of average corrosion rates between the integrated average of LPR measurements and weight loss,  $T=120^{\circ}\text{C}$ ,  $p\text{H}_2\text{S}=0.10$  bar, initial  $\text{pH}=4.0$ ,  $B=23$  mV/decade.

**6.3.2 Outer iron sulfide layer.** The outer corrosion product layers on the steel surface were characterized by XRD. From Figure 22, the corrosion product was identified

as pure mackinawite (tetragonal FeS) after 1 day of exposure. Most of the mackinawite transformed to troilite (hexagonal FeS) after 4 days of exposure. Troilite transformed to pyrrhotite ( $\text{Fe}_{1-x}\text{S}$ ,  $0 \leq x \leq 0.17$ ) with a trace amount of pyrite ( $\text{FeS}_2$ ) after 7 days of exposure. After 21 days, more pyrite was observed in addition to pyrrhotite. With increasing time, the corrosion products displayed an increase in sulfur content. Quantitative analysis of acquired XRD data indicates the proportion of pyrite was around 12% after 21 days.

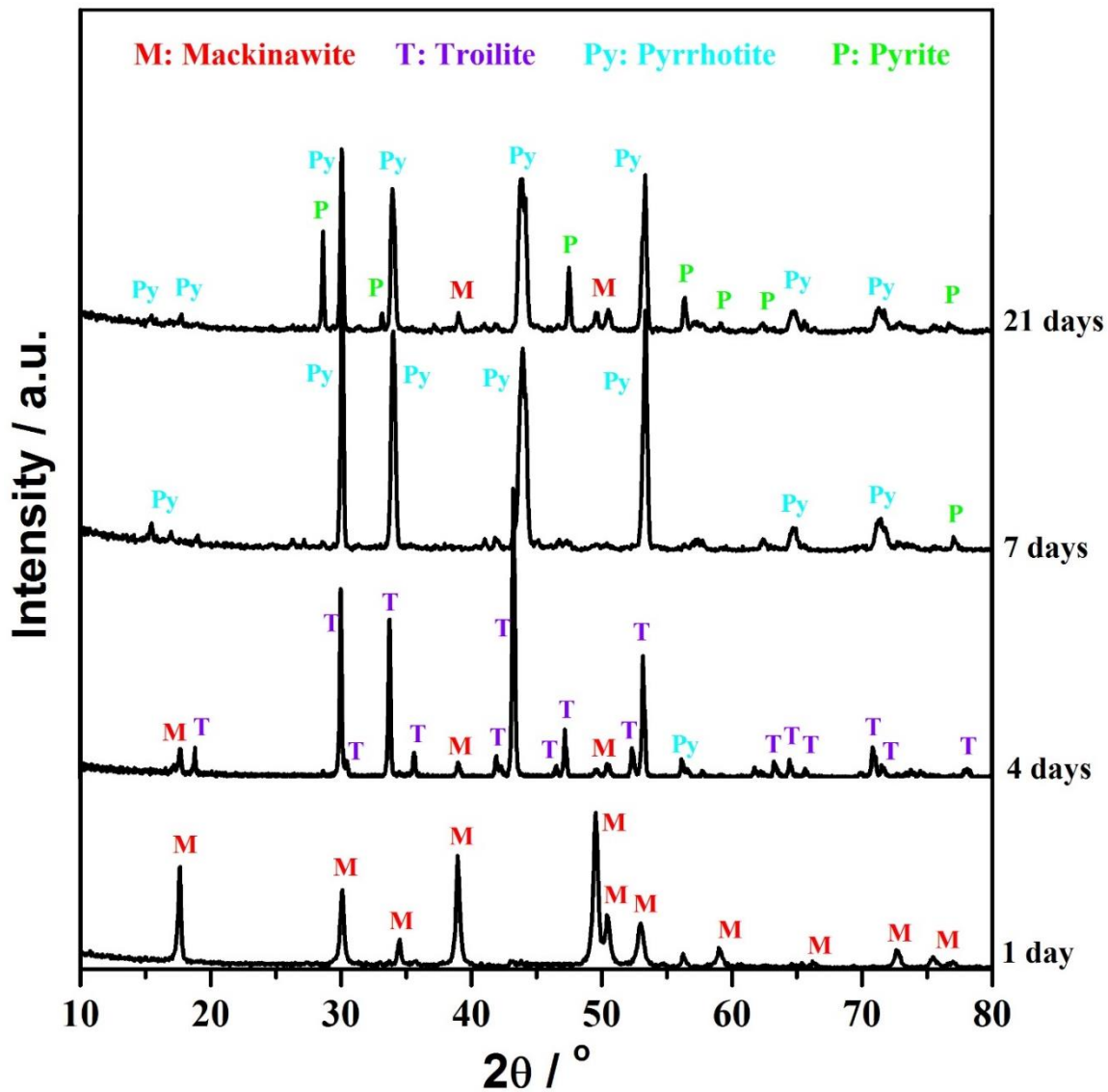


Figure 22. XRD patterns of corrosion products on the steel surface for different test durations,  $T=120^{\circ}\text{C}$ ,  $\text{pH}_2\text{S}=0.10$  bar, initial  $\text{pH}=4.0$ .

The corrosion products and cross-sections were also characterized by SEM as shown in Figure 23 and Figure 24. An inner and an outer corrosion product layer are

apparent in the cross-section analysis. The composition of the inner layer is discussed in the next section while the following paragraphs focus on the outer iron sulfide layer.

After 1 day of exposure, the SEM shows a typical flaky mackinawite [32] product layer approximately 22  $\mu\text{m}$  in thickness. For the 4 day experiment, the SEM shows troilite particles on the surface and a much thicker layer (61~73  $\mu\text{m}$ ). Well-defined hexagonal pyrrhotite prisms appeared on the surface after 7 days. After 21 days of exposure, it can be seen that the crystal size increased with time as the corrosion product layer thickness grew above 100  $\mu\text{m}$ . In summary, the transformation sequence of iron sulfide observed at high temperature was mackinawite (1 day)  $\rightarrow$  troilite (4 days)  $\rightarrow$  pyrrhotite (7 days)  $\rightarrow$  pyrite (12%) and pyrrhotite (88%) (21 days), which is basically the same sequence as seen at low temperature, except that no cubic FeS or greigite was observed. Another difference that can be noted is that the corrosion products observed at low temperature are typically a mixture of more than three iron sulfides without a dominant phase [39], [47], [48], while a major phase was obvious at high temperature in this study. This infers that the observed transformation sequence appears to be more complete at high temperature.

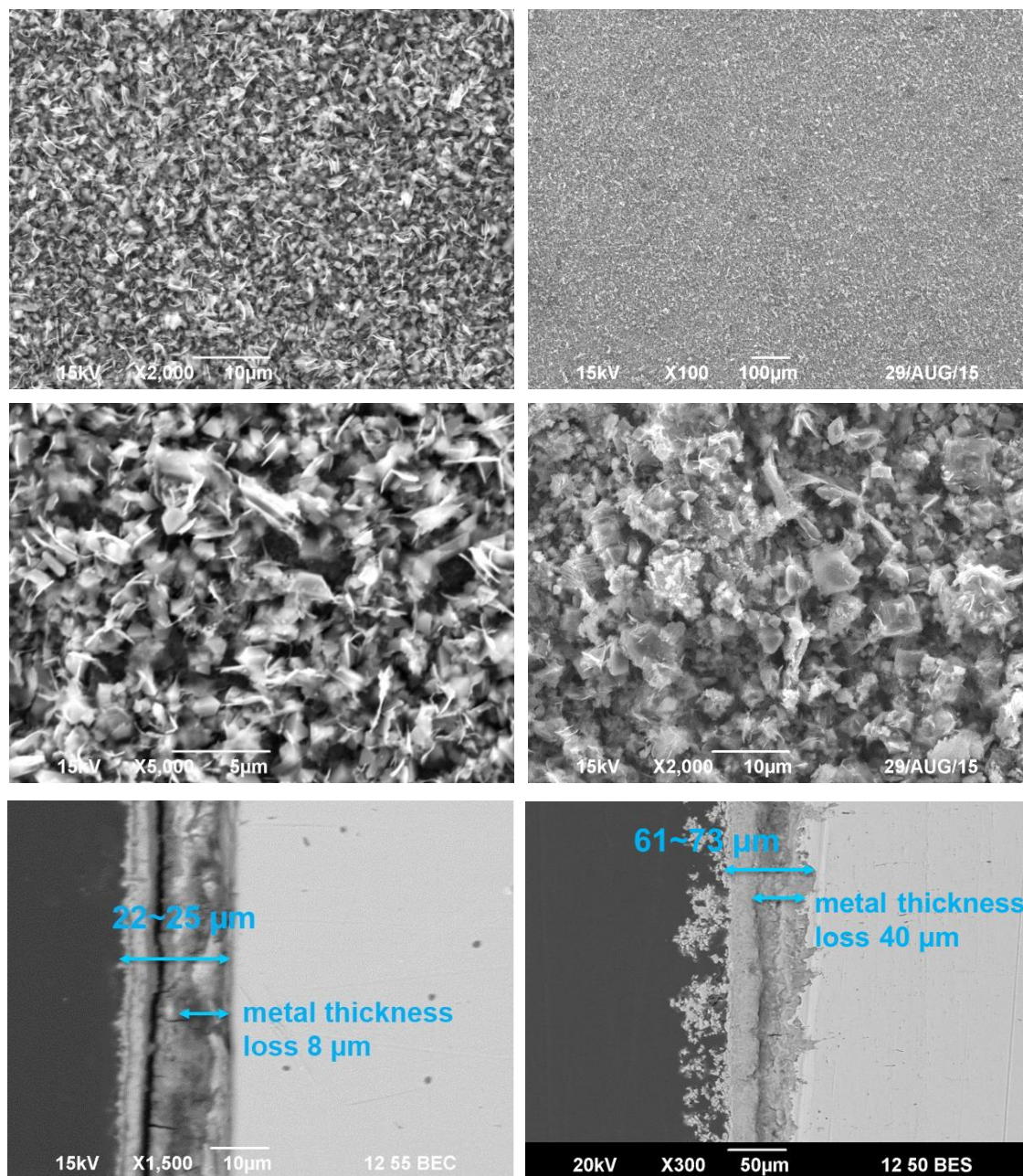


Figure 23. SEM morphologies and cross sections for 1 day (left) and 4 days (right),

T=120°C, p<sub>H<sub>2</sub>S</sub>=0.10 bar, initial pH=4.0.

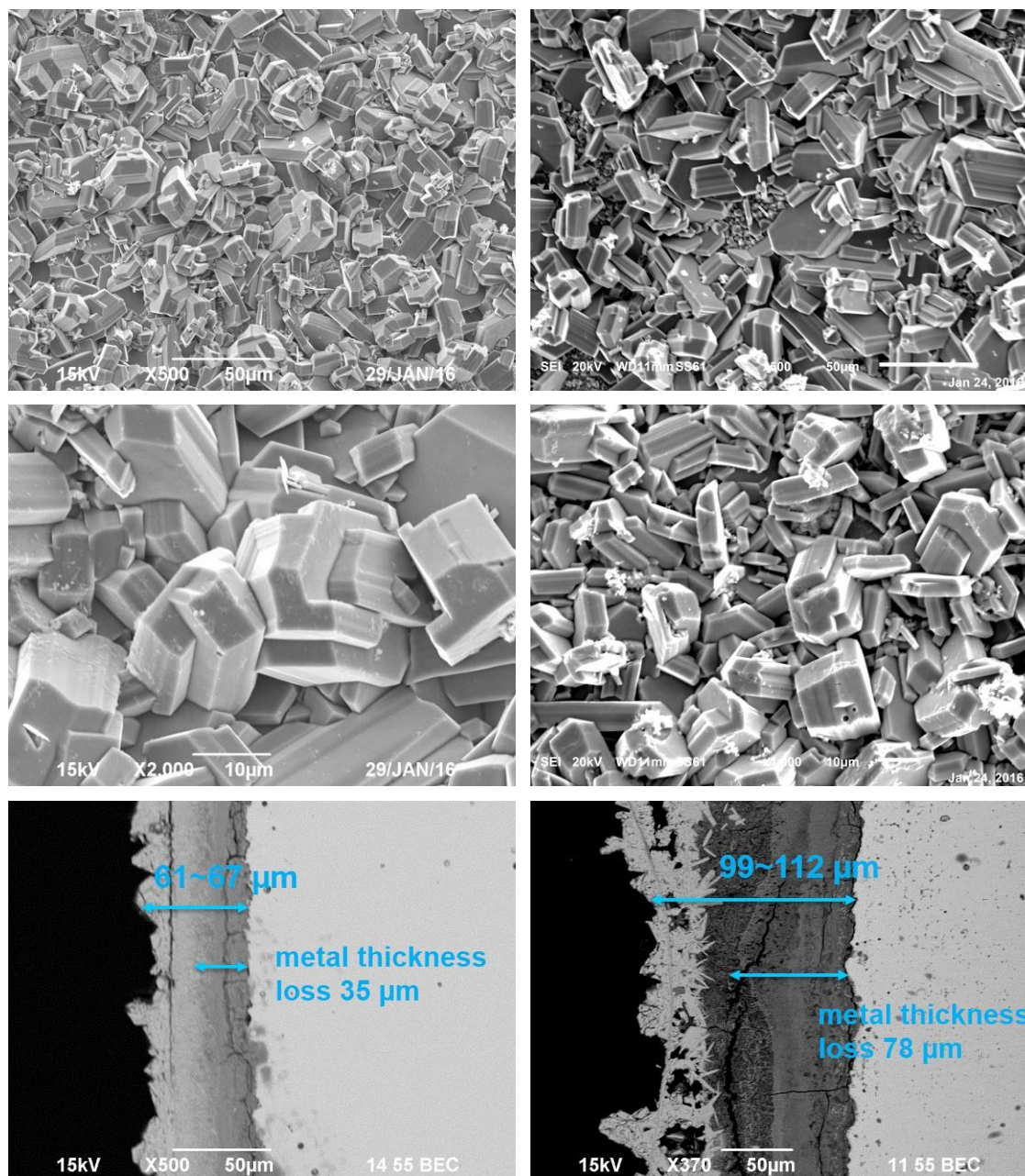


Figure 24. SEM morphologies and cross sections for 7 days (left) and 21 days (right),  $T=120^{\circ}\text{C}$ ,  $\text{pH}_2\text{S}=0.10$  bar, initial  $\text{pH}=4.0$ .

After each experiment, the  $\text{H}_2\text{S}$  and  $\text{Fe}^{2+}$  concentrations were measured using micro gas chromatography (GC) and spectrophotometry, respectively. The experimental

pH and  $\text{pH}_2\text{S}$  can be calculated for the end of the experiment, as shown in Table 7. The details of the calculation are described in Chapter 5.

Table 7. Summary of the theoretical calculated final conditions at 120°C.

Duration, day(s)	Final Conditions		
	$\text{pH}_2\text{S}$ , bar	pH	$\text{Fe}^{2+}$ , ppm
1	0.09	5.7	7.4
4	0.11	5.5	5.8
7	0.09	5.6	5.1
21	0.09	5.5	4.2

The calculated parameters are used as the inputs to generate Pourbaix diagrams, as shown in Figure 25. The vertical position and the width of the arrow in each diagram represent the potential in the final stages of the experiments (which varied between approximately -500 mV vs. SHE). The length of the arrow represents the pH drift experienced during the test from initial pH 4.0 to the final pH 5.5 ~ 5.7, as shown in Table 7. For the 1-day experiment, only mackinawite was considered for the Pourbaix diagram since it always forms as the initial iron sulfide layer [32]. For the 4-day and 7-day experiment, both mackinawite and pyrrhotite were considered in the construction of the diagram (troilite is the end member of the pyrrhotite ( $\text{Fe}_{1-x}\text{S}$ ) series when  $x$  is zero). Mackinawite, pyrrhotite, and pyrite were all included in the analysis for long-term exposure (21 days). It can be seen that all the arrows cross over into the stability regions for different iron sulfides, as identified by XRD. It is noteworthy that the tip of the arrow, which represents the final experimental conditions, is very close to the equilibrium line

between pyrrhotite and pyrite for the 21-day experiment. This suggests a possible transformation reaction between pyrrhotite and pyrite. The experimental XRD results are in good qualitative agreement with the thermodynamic calculations.

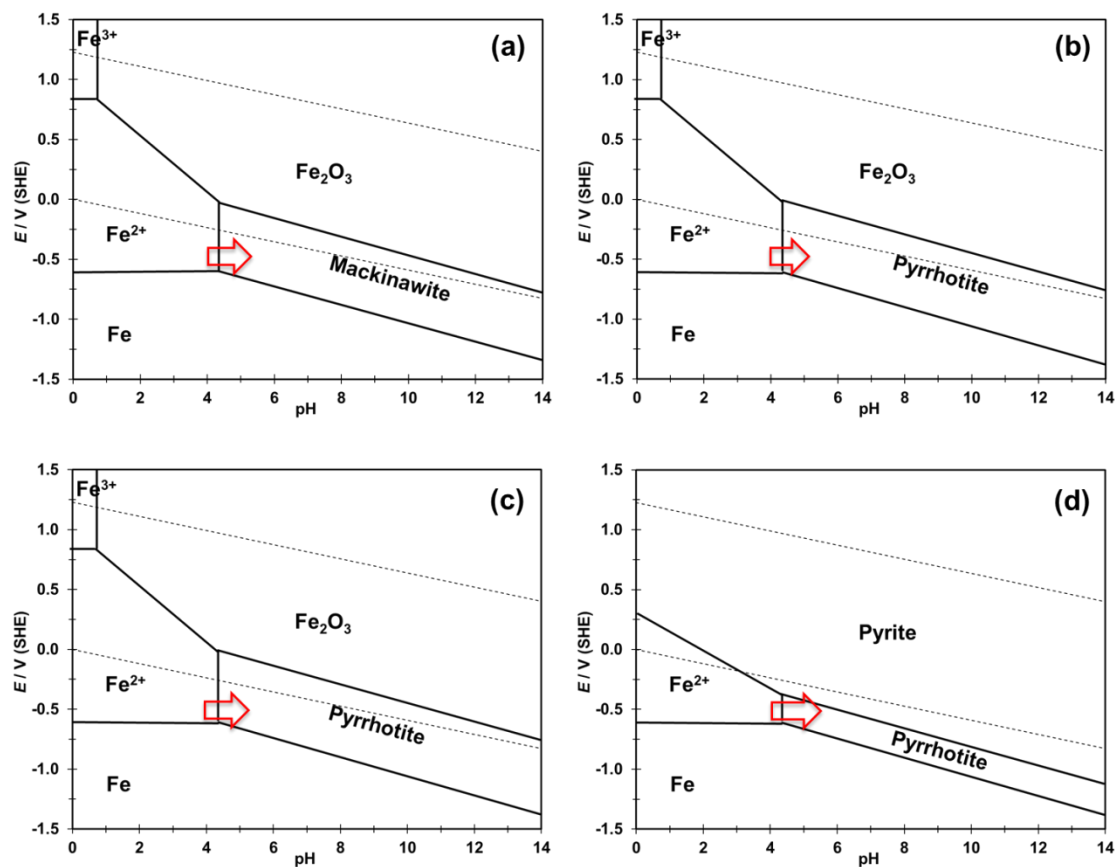


Figure 25. Pourbaix diagrams for Fe-H<sub>2</sub>S-H<sub>2</sub>O system by considering (a) mackinawite, (b) pyrrhotite (troilite), (c) pyrrhotite, and (d) pyrite/pyrrhotite, T=120°C, other input parameters are in Table 7.

**6.3.3 Inner iron oxide layer.** SEM/EDS analysis of specimen cross-sections suggests the presence of a different inner layer, expected to be comprised of iron oxide,

which could not be detected by XRD (Figure 22). This warranted further analysis, because the outer corrosion product layer was too thick and/or too compact so that the X-rays could not penetrate and detect the layers underneath. Therefore, FIB/TEM analysis was conducted to address this issue and to identify this inner layer. The methodology involves the sectioning of a very thin slice of material around the steel/corrosion product layer using a FIB, with subsequent microscopic and elemental analysis using TEM/EDS. Figure 26(a) shows the sample prepared by FIB. The surfaces of the slice were coated with platinum to prevent it from collapsing since it is extremely thin. The area marked by a yellow rectangle was further thinned and analyzed by TEM. As shown in Figure 26(b), it is apparent that there are two interfaces, indicating the existence of multiple layers. The EDS line scan from left to right in Figure 26(c) corresponds to the vertical arrow shown in Figure 26(b). EDS line scan analysis initially only detects Fe, which corresponds to the steel matrix. Above the steel matrix, both Fe and O were detected, demonstrating the inner layer was comprised of an iron oxide layer. Increasing amounts of S was detected in the outermost layer, meaning that the outer layer was made of a mixture of iron oxide and iron sulfide. A selected area diffraction (SAD) pattern collected from the iron oxide layer (Figure 26(b)) identified the  $\text{Fe}_3\text{O}_4$  (125) plane (Figure 26(d)). This is an important discovery since  $\text{Fe}_3\text{O}_4$  can be very protective and greatly slow down the corrosion rate at high temperature, as was confirmed in previous studies of aqueous corrosion at elevated temperatures in  $\text{CO}_2$  environments [27].

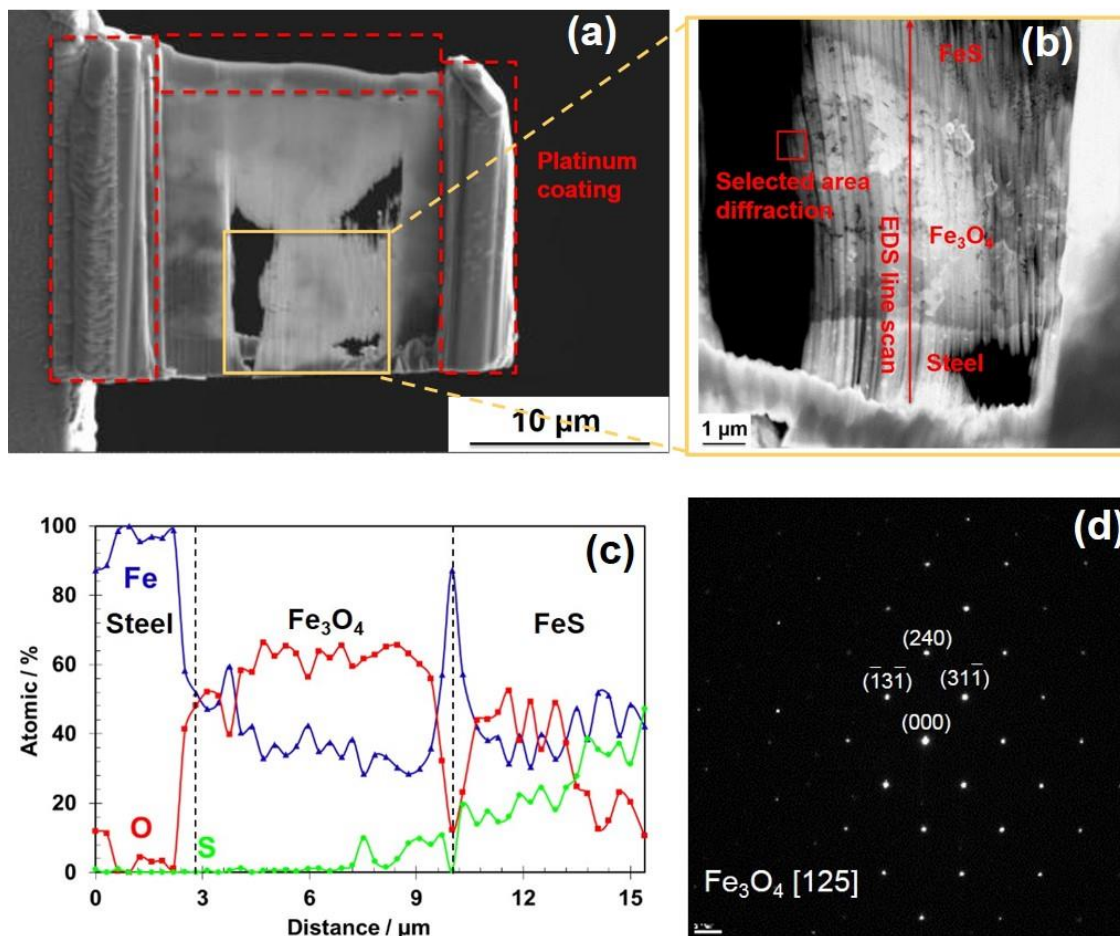


Figure 26. (a) FIB sample preparation; (b) thin area for TEM analysis; (c) EDS line scan result; (d) selected area diffraction (SAD) pattern.  $T=120^{\circ}\text{C}$ ,  $p\text{H}_2\text{S}=0.20$  bar, initial  $\text{pH}=4.0$ , 4 days.

In addition to identifying the composition of the corrosion product layer, one of the objectives of this chapter was to investigate if the thermodynamically less stable  $\text{Fe}_3\text{O}_4$  layer would vanish over time by it converting into more stable species. Figure 27 shows the EDS mapping results of the specimen cross-sections for different experiment durations. The color in each image qualitatively indicates the elemental composition of

each layer (with dark blue and pink representing low and high elemental content, respectively). After the 1 day experiment, the inner  $\text{Fe}_3\text{O}_4$  layer was about 20  $\mu\text{m}$  thick while the outer mackinawite layer was only several microns. The specimen removed from other experiments (1 day, 7 days & 21 days) indicate the iron sulfide layer grew thicker over time. As the scales are different in Figure 27, the magnetite and iron sulfide layer thickness was estimated from the EDS maps, as summarized in Table 8 and shown in Figure 28.

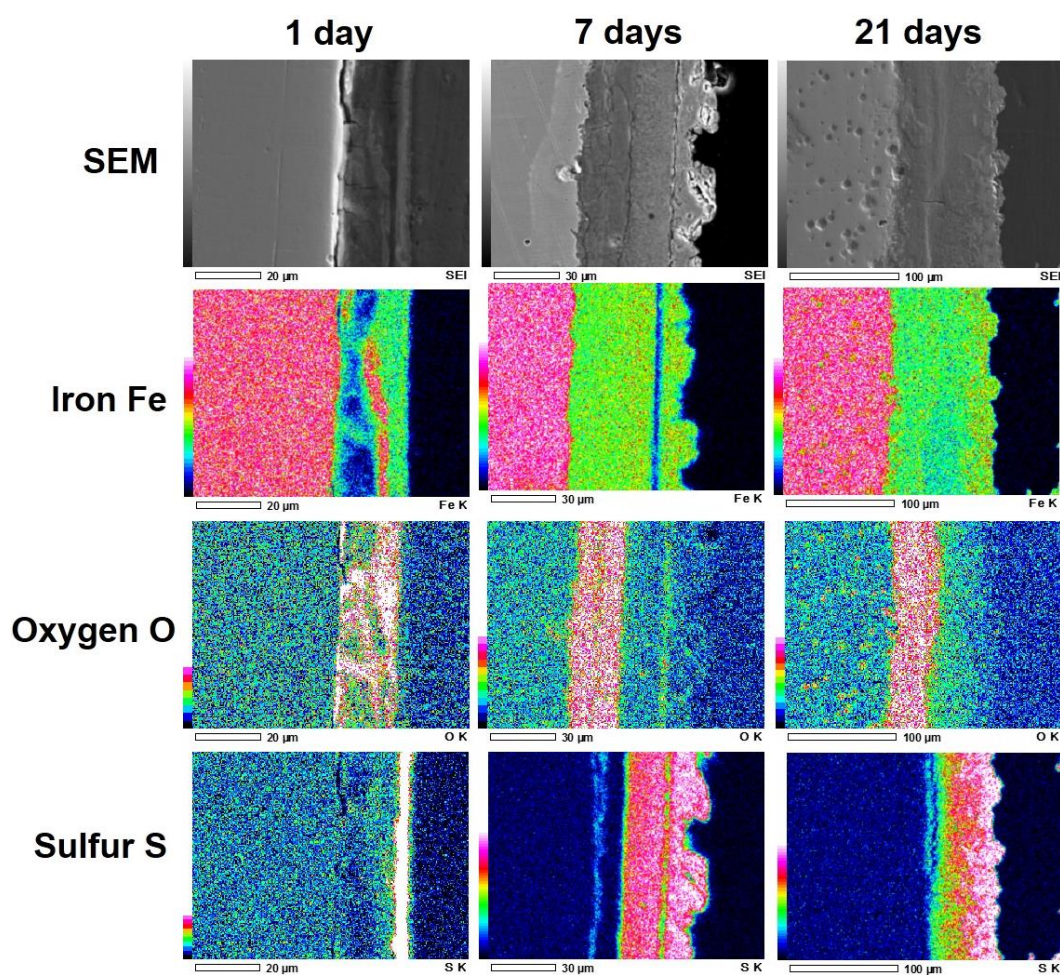


Figure 27. EDS mapping results for Fe, O and S distribution for different experiment durations,  $T=120^{\circ}\text{C}$ ,  $p\text{H}_2\text{S}=0.10$  bar, initial  $\text{pH}=4.0$ .

Table 8. Estimated  $\text{Fe}_3\text{O}_4$  and  $\text{FeS}$  layer thickness with different exposure time.

Duration, day(s)	Layer Thickness, $\mu\text{m}$	
	$\text{Fe}_3\text{O}_4$	Iron sulfide
1	$20.15 \pm 2.10$	$4.90 \pm 0.56$
4	$23.40 \pm 3.20$	$26.60 \pm 4.30$
7	$22.80 \pm 1.80$	$40.20 \pm 3.70$
21	$28.92 \pm 2.50$	$69.88 \pm 4.55$

Interestingly, the thickness of  $\text{Fe}_3\text{O}_4$  remained almost constant at around  $25 \mu\text{m}$ . The oxide layer did not vanish over time although it is thermodynamically less stable than iron sulfide. The thickness of the iron sulfide layer gradually grew from a few micrometers up to  $70 \mu\text{m}$ . This suggests a mechanism involving continuous  $\text{Fe}_3\text{O}_4$  formation due to corrosion at the steel/ $\text{Fe}_3\text{O}_4$  interface, and conversion to iron sulfide, at the  $\text{Fe}_3\text{O}_4/\text{FeS}$  interface. However, this postulated mechanism needs to be confirmed and its relationship to the corrosion rate elucidated. The experimentally measured corrosion rate decreased quickly in the first days when only magnetite and mackinawite formed. However, whether this decrease was due to magnetite or mackinawite formation remains uncertain. This became the subject of the next chapter.

The results reported herein were compared with results of calculations done with the recent  $\text{H}_2\text{S}$  corrosion model developed by Zheng, *et al.* [9], developed using low temperature data ( $< 80^{\circ}\text{C}$ ). It should be stated that Zheng's model is a uniform corrosion

model and only considers mackinawite as the iron sulfide layer. Consequently, it is unsurprising that the initial corrosion rate is overestimated since the model does not take into account the presence of a magnetite layer. The final stable corrosion rate for LPR measurements, Zheng's model are in much better agreement, which is encouraging. Severe localized corrosion experienced with the formation of pyrite in long-term exposures must have influenced the LPR measurements and this phenomenon cannot be captured by Zheng's model. The present study highlights several gaps in the modeling approach, which should, nevertheless, be used as a good starting point building a model for prediction of H<sub>2</sub>S corrosion at high temperature.

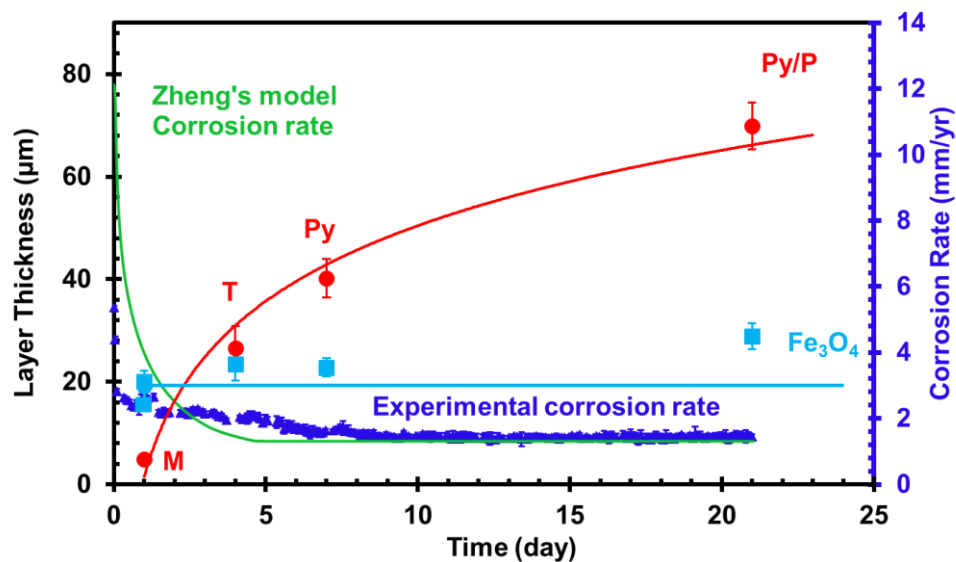


Figure 28. Layer thickness of  $\text{Fe}_3\text{O}_4$  and iron sulfides after different exposure time, and compared with the LPR corrosion rates from experimental data and Zheng's model [9], M: mackinawite, T: troilite, Py: pyrrhotite, P: pyrite,  $T=120^\circ\text{C}$ ,  $p\text{H}_2\text{S}=0.10$  bar, initial  $\text{pH}=4.0$ . Light blue dots: experimental  $\text{Fe}_3\text{O}_4$  layer thickness, light blue line: fitting  $\text{Fe}_3\text{O}_4$  layer thickness, red dots: experimental iron sulfide layer thickness, red curve: fitting iron sulfide layer thickness, dark blue dots: experimental corrosion rate, green curve: Zheng's model corrosion rate.

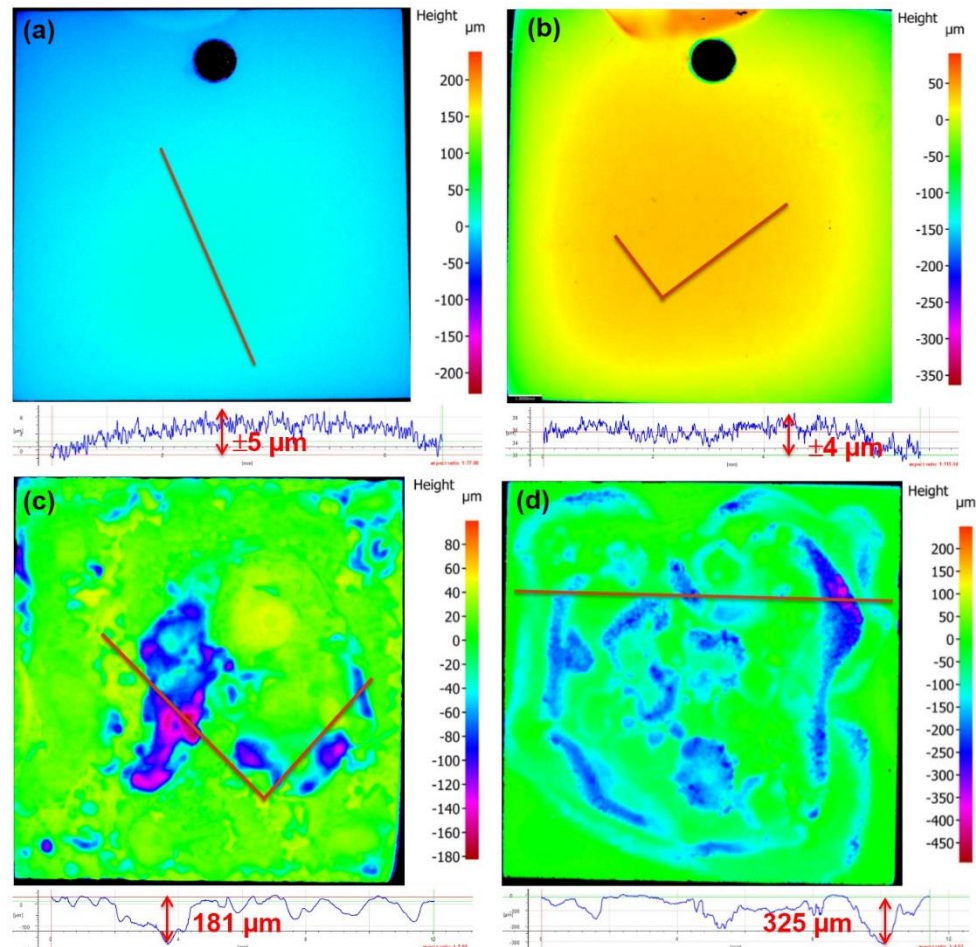


Figure 29. Surface profilometry after removing corrosion products (a) 1 day, mackinawite; (b) 4 days, troilite; (c) 7 days, pyrrhotite/pyrite; (d) 21 days, pyrrhotite/pyrite.  $T=120^{\circ}\text{C}$ ,  $\text{pH}_2\text{S}=0.10$  bar, initial  $\text{pH}=4.0$ .

**6.3.4 Surface profilometry.** After removal of both the inner and outer corrosion products using Clarke solution [59], the metal surface was characterized by profilometry, as shown in Figure 29. No obvious localized corrosion was observed after 1 day and 4 days. The surface was relatively smooth. In the presence of mackinawite and troilite, which were the phases identified in these conditions, the corrosion attack could be

considered to be uniform. However, after 7 days of exposure, when pyrrhotite and a small amount of pyrite formed, localized corrosion was observed with a pit depth of 181  $\mu\text{m}$ , which amounts to a time averaged pit penetration rate of 9.4 mm/yr and a 5.2 pitting ratio (pit penetration rate over uniform corrosion rate). After 21 days exposure time, with more pyrite formation, the localized corrosion progressed further. Some pits were as deep as 325  $\mu\text{m}$ , corresponding to a time averaged pit penetration rate of 5.6 mm/yr and a 4.3 pitting ratio. The results are consistent with previous postulations [61] that link the presence of pyrite to localized corrosion.

#### 6.4 Summary

Although  $\text{Fe}_3\text{O}_4$  is thermodynamically less stable than iron sulfide, it was still detected even after long exposures (up to 21 days). In addition, the  $\text{Fe}_3\text{O}_4$  layer thickness almost did not change with time. The mechanisms behind these observations will be further investigated in the next chapter.

The observed transformation sequence for iron sulfides under these conditions was mackinawite (1 day)  $\rightarrow$  troilite (4 days)  $\rightarrow$  pyrrhotite (7 days)  $\rightarrow$  pyrite (12%)/pyrrhotite (21 days). The thickness of the iron sulfide layer increased with time.

The general corrosion rate rapidly decreased (from approximately 6 mm/yr to 2 mm/yr) on the first day with the formation of  $\text{Fe}_3\text{O}_4$  and mackinawite. Both of these corrosion products are known to decrease the bare general corrosion rate. The general corrosion rate ( $\sim 2$  mm/yr) remained steady as mackinawite transformed to troilite and pyrrhotite. When pyrite formed, severe localized corrosion was observed.

## Chapter 7: Formation Mechanisms of Iron Oxide and Iron Sulfide at High Temperature in Aqueous H<sub>2</sub>S Corrosion Environments

### 7.1 Introduction

Before moving to the next objective of this study (the effect of pH<sub>2</sub>S), the mechanisms behind the formation of Fe<sub>3</sub>O<sub>4</sub> and iron sulfide at high temperature reported in the previous chapters (Chapter 5 and Chapter 6) were further investigated.

Reviewing the results shown in Figure 28, two major gaps in understanding could be identified:

1. The corrosion rate quickly decreased in the first day from 5.5 to 2 mm/yr. Yet, it is not entirely clear which layer, Fe<sub>3</sub>O<sub>4</sub> or mackinawite, was responsible for the decrease of the corrosion rate. Was there a sequence in the layer formation? How fast are these layers forming?
2. The thickness of the inner Fe<sub>3</sub>O<sub>4</sub> layer did not change significantly with time (20 to 30 μm from day 1 to day 21), while the outer iron sulfide layer kept growing with time from 5 μm to reach 90 μm after 21 days. What was the layer growth mechanism of iron sulfide in the presence of a Fe<sub>3</sub>O<sub>4</sub> layer?

### 7.2 Hypotheses

The following hypotheses were proposed to address the above two questions:

1<sup>st</sup> Hypothesis: At high temperature, due to it possessing a higher saturation value than mackinawite, Fe<sub>3</sub>O<sub>4</sub> rapidly forms during the initial stage (first day) of corrosion. The growth rate of the Fe<sub>3</sub>O<sub>4</sub> layer gradually decreases as the corrosion rate, and consequently the rate of Fe<sup>2+</sup> ion release, decreases. At the same time, the conversion of

$\text{Fe}_3\text{O}_4$  to  $\text{FeS}$  proceeds. The process eventually reaches a steady state when the rate of  $\text{Fe}_3\text{O}_4$  formation and conversion become equal, leading to a constant  $\text{Fe}_3\text{O}_4$  layer thickness.

2<sup>nd</sup> Hypothesis: At high temperature, the iron sulfide growth mechanism is mainly through a conversion from  $\text{Fe}_3\text{O}_4$ . The  $\text{Fe}_3\text{O}_4$  simultaneously forms at the steel/ $\text{Fe}_3\text{O}_4$  interface and converts to  $\text{FeS}$  at the  $\text{Fe}_3\text{O}_4$ / $\text{FeS}$  interface.

### 7.3 Experimental

To test the 1<sup>st</sup> hypothesis, Experimental Set #1 was devised and conducted, as shown in Figure 30. It involved the formation and characterization of a  $\text{Fe}_3\text{O}_4$  layer on the surface of a steel specimen in the absence of  $\text{H}_2\text{S}$ . In a subsequent step, the preformed  $\text{Fe}_3\text{O}_4$  was then exposed to  $\text{H}_2\text{S}$  and the changes in the layer composition and morphology were again characterized. The procedure is summarized below:

- Step 1: A X65 carbon steel specimen was immersed into 1 wt.% NaCl solution (purged by  $\text{N}_2$ ) without  $\text{H}_2\text{S}$ . The experimental condition was 120°C at initial pH 4.0. After 1 day, the specimen with preformed  $\text{Fe}_3\text{O}_4$  layer was retrieved, immediately rinsed with deionized water and isopropanol, dried by  $\text{N}_2$  flow, and stored in a nitrogen atmosphere. This step took less than 10 minutes.
- Step 2: The preformed  $\text{Fe}_3\text{O}_4$  carbon steel specimen was exposed under the same condition (1 wt.% NaCl solution, 120°C, initial pH 4.0) containing 0.1 bar  $\text{H}_2\text{S}$ , for 1 day. The transfer step took around 15 minutes.

According to the 1<sup>st</sup> hypothesis, the iron sulfide layer growth should be dominant in Step 2, since the initial  $\text{Fe}_3\text{O}_4$  layer formation step would have already been completed.

Therefore, a much thicker iron sulfide (mackinawite) layer would form compared with the same experiment conducted with no preformed  $\text{Fe}_3\text{O}_4$  layer (see Figure 30 and the first point in Figure 28).

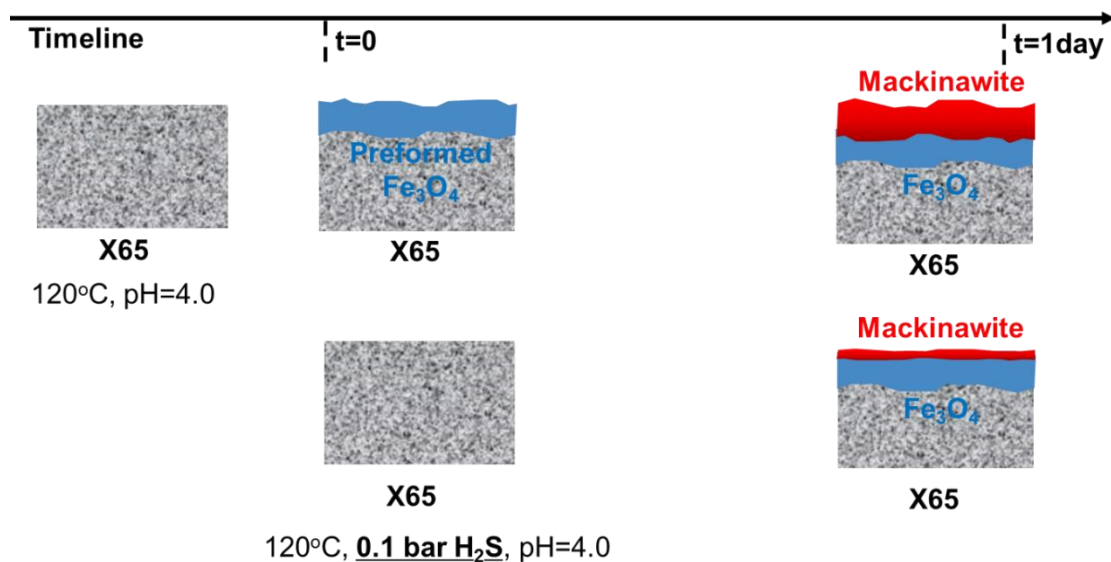


Figure 30. Experiment design to test hypothesis #1.

To verify the 2<sup>nd</sup> hypothesis, Experimental Set #2 was devised and performed, as shown in Figure 31. This set involved the formation of  $\text{Fe}_3\text{O}_4$  on the surface of a nickel specimen in the absence of  $\text{H}_2\text{S}$ . In a subsequent step, the preformed  $\text{Fe}_3\text{O}_4$  was exposed to  $\text{H}_2\text{S}$  and the changes in surface layer morphology and composition were characterized. The procedure is summarized below:

- Step 1: Nickel (Ni) specimens, which should not corrode in the current experimental conditions whether or not  $\text{H}_2\text{S}$  is present, were immersed into a 1 wt.% NaCl solution (purged by  $\text{N}_2$ ) without  $\text{H}_2\text{S}$ . Some X65 steel specimens were

also immersed in the cell at the same time solely to act as a source of  $Fe^{2+}$ . The test condition was still 120°C at an initial pH 4.0. The conditions were selected in order to precipitate  $Fe_3O_4$  on the Ni surface via Reaction 13:



The cathodic reaction(s) associated with Reaction 13 is not identified with certainty as of yet but it is postulated that  $H^+$  reduction and  $H_2S$  reduction are most likely involved.

- Step 2: The Ni specimens with preformed  $Fe_3O_4$  were exposed to a 0.1 bar  $H_2S$  environment under the same conditions (120°C, initial pH 4.0) for 1 day. The estimated time for the whole procedure was the same as the above Experimental Set #1.

Based on the 2<sup>nd</sup> hypothesis, the preformed  $Fe_3O_4$  layer should convert to iron sulfide in Step 2, via Reaction 19. Since there was no  $Fe^{2+}$  replenishment from the steel substrate to form new  $Fe_3O_4$  (Reaction 13), the  $Fe_3O_4$  found at the end of Step 2 should be either very thin or even non-existent if it completely converted to iron sulfide.



The anodic reaction(s) associated with Reaction 19 is also not clearly identified but it could be a combination of Ni,  $H_2S$ ,  $H_2O$  or  $H_2$  oxidations – Ni and  $H_2S$  oxidations being more likely.

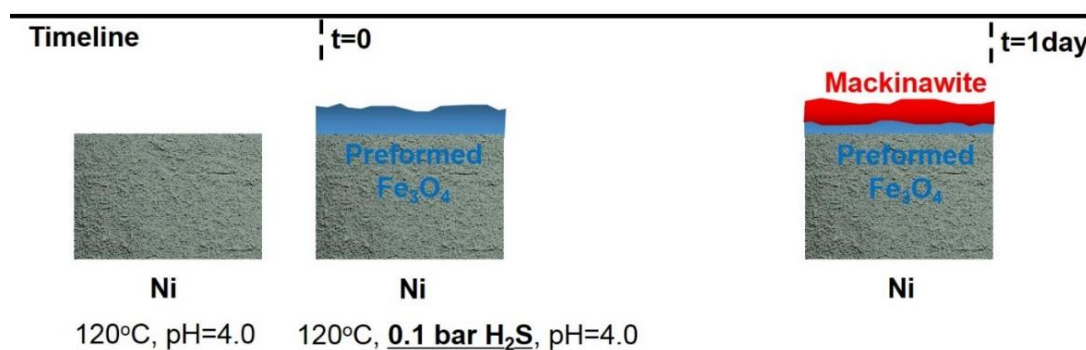


Figure 31. Experiment design to test hypothesis #2.

For the experiments with H<sub>2</sub>S, the setup and procedure are the same as in Chapter 5. For the experiments without H<sub>2</sub>S, a 7 L stainless steel autoclave was used instead of a Hastelloy one. The same procedure was followed except that no H<sub>2</sub>S was involved. The test matrix is summarized in Table 9.

Table 9. Test matrix.

Parameter	Value
Temperature	120 °C
pH <sub>2</sub> S	0 or 0.10 bar
Initial pH	4.0
Rotation speed	1000 rpm

## 7.4 Results and Discussion

**7.4.1 Sequence of Fe<sub>3</sub>O<sub>4</sub>/FeS formation.** The corrosion rates obtained in Experimental Set #1 are shown in Figure 32. Three lines are displayed representing the experimental data obtained “with H<sub>2</sub>S” (0.1 bar), “without H<sub>2</sub>S”, and “with preformed

Fe<sub>3</sub>O<sub>4</sub>” (preformed Fe<sub>3</sub>O<sub>4</sub> later exposed to H<sub>2</sub>S environment). The “time zero” on the x-axis represents the time when the experimental temperature reached 120°C.

Looking first at the results from the experiment “with H<sub>2</sub>S” and the experiment “without H<sub>2</sub>S”, it is clear that the LPR corrosion rates for both conditions decrease relatively quickly with time. The LPR corrosion rate from the experiment “without H<sub>2</sub>S” gradually decreased during the first 50 hours of exposure and reached a stable corrosion rate of 0.5 mm/yr. The LPR corrosion rate from the experiment “with H<sub>2</sub>S” dropped in the first 2 hours from over 5 mm/yr to about 2.8 mm/yr and then slowly decreased before eventually stabilizing around 2 mm/yr.

The results from the experiment “with preformed Fe<sub>3</sub>O<sub>4</sub>” are plotted in red in Figure 32. The plot includes the first day of the experiment used to preform the Fe<sub>3</sub>O<sub>4</sub> layer in the absence of H<sub>2</sub>S. The corrosion rate experienced by the specimen during the Fe<sub>3</sub>O<sub>4</sub> layer formation (red dots in Figure 32) was logically similar to the one obtained during the first day of the experiment “without H<sub>2</sub>S” (green dots in Figure 32). The specimen with the preformed Fe<sub>3</sub>O<sub>4</sub> was then transferred to the H<sub>2</sub>S environment at the 1-day mark. The LPR corrosion rate in the experiment “with preformed Fe<sub>3</sub>O<sub>4</sub>” restarted at 3.5 mm/yr, which is lower than the initial LPR rate obtained the experiment “with H<sub>2</sub>S” (5.5 mm/yr). This result demonstrates that the Fe<sub>3</sub>O<sub>4</sub> layer alone offers additional protection in an H<sub>2</sub>S environment. The relatively high initial corrosion rate (3.5 mm/yr) value could be due to some cracking and/or spalling, created when the specimen was transferred, as the Fe<sub>3</sub>O<sub>4</sub> layer was expected to provide higher initial corrosion protection in the H<sub>2</sub>S environment. The corrosion rate did decrease sharply in the next few hours of

exposure but stabilized at 1.8 mm/yr, similarly to the final rate in the experiment “with H<sub>2</sub>S”. In comparison, the Fe<sub>3</sub>O<sub>4</sub> layer alone clearly provided a higher protectiveness as demonstrated in the experiment without H<sub>2</sub>S at the same high temperature [62].

It has been demonstrated that a thin mackinawite layer can form very rapidly and slow down the corrosion rate when the steel is exposed to aqueous H<sub>2</sub>S [56]. The same phenomenon appears in our study: with H<sub>2</sub>S, the corrosion rate quickly dropped in the first 5 hours. Without H<sub>2</sub>S, the drop of the corrosion rate is not as abrupt as with H<sub>2</sub>S, as it gradually decreased during the first 40 hours, but ended up with a much lower corrosion rate. This suggests that the overall protectiveness of Fe<sub>3</sub>O<sub>4</sub> is better than mackinawite, assuming that both environments have similar corrosivity. Obviously, both Fe<sub>3</sub>O<sub>4</sub> and mackinawite are responsible for the decrease of corrosion rate. However, the decrease in corrosion rate always occurs in the first few hours of testing, when the Fe<sub>3</sub>O<sub>4</sub> layer is forming. In addition, the corrosion product layer in contact with the steel surface is always Fe<sub>3</sub>O<sub>4</sub> and the change in corrosion rate does not seem to depend on the FeS layer thickness. This seems to indicate that most of the corrosion protection can be attributed to the Fe<sub>3</sub>O<sub>4</sub> layer.

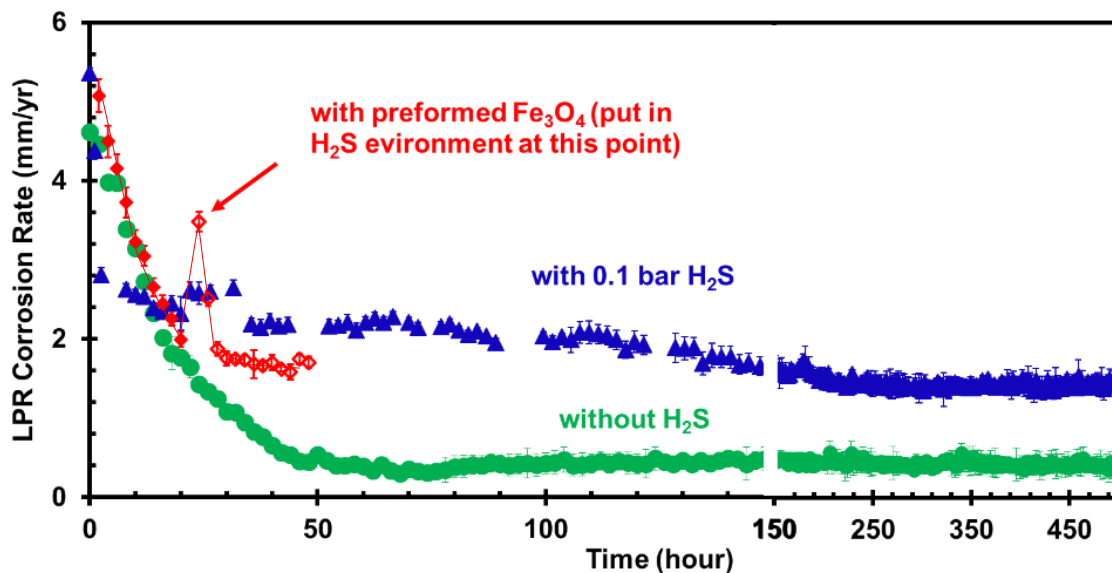


Figure 32. Experimental Set #1 - LPR corrosion rate in experiments without H<sub>2</sub>S (green), with 0.1 bar H<sub>2</sub>S (blue), and with preformed Fe<sub>3</sub>O<sub>4</sub> layer for one-day, X65, 1 wt.% NaCl solution, T=120°C, initial pH=4.0, B=23 mV/decade.

The corrosion products from the experiment “without H<sub>2</sub>S” at high temperature were characterized by X-ray diffraction (XRD) after different test durations, as shown in Figure 33. All the corrosion products were identified as magnetite (Fe<sub>3</sub>O<sub>4</sub>) regardless of the exposure time. The EDS mapping scan, Figure 34, also confirms that the layer was comprised of iron (Fe) and oxygen (O). The intensity of the peaks also did not increase with time and the  $\alpha$ -Fe matrix was already undetectable after the 1 day experiment. This means that the Fe<sub>3</sub>O<sub>4</sub> rapidly became very thick and compact, implying good corrosion protection properties. The thickness after 1 day of exposure was approximately 25  $\mu$ m, which is approximately the same value as the thickness of the oxide layer obtained from the experiment “with H<sub>2</sub>S” for 1 day, as shown in Figure 33 and Figure 34. The fact that

the two  $\text{Fe}_3\text{O}_4$  layer thicknesses are the same seems to indicate that the  $\text{Fe}_3\text{O}_4$  growth during the first day of testing occurs with little interference from  $\text{H}_2\text{S}$ . Consequently, it is proposed that the  $\text{Fe}_3\text{O}_4$  formation was dominant in the first few hours of testing at high temperature even with  $\text{H}_2\text{S}$ . This is discussed in more detail below.

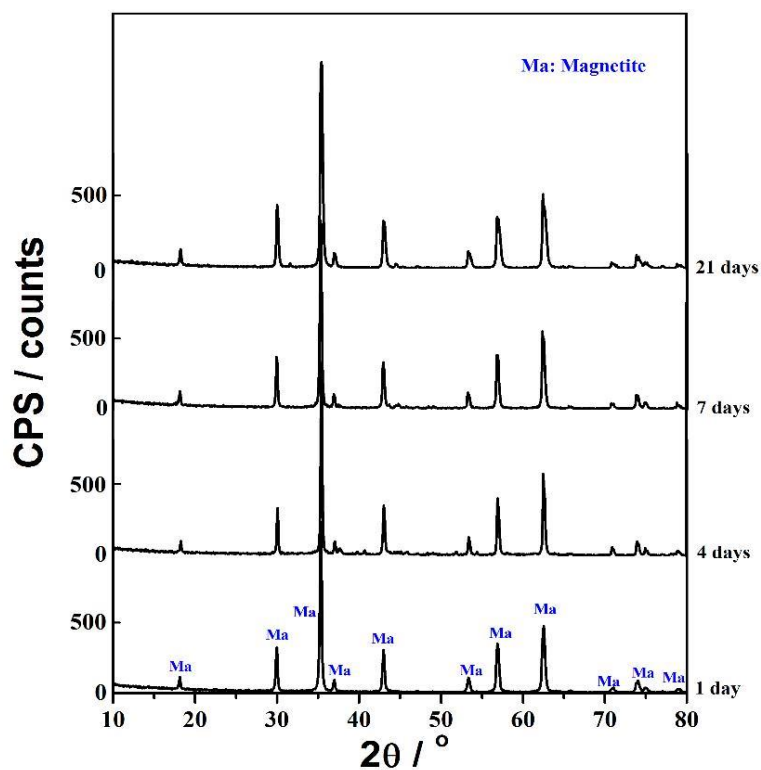


Figure 33. XRD patterns of X65 specimen in experiment without  $\text{H}_2\text{S}$  after different test durations, 1 wt.% NaCl solution,  $\text{N}_2$  purged,  $T=120^\circ\text{C}$ , initial  $\text{pH}=4.0$ .

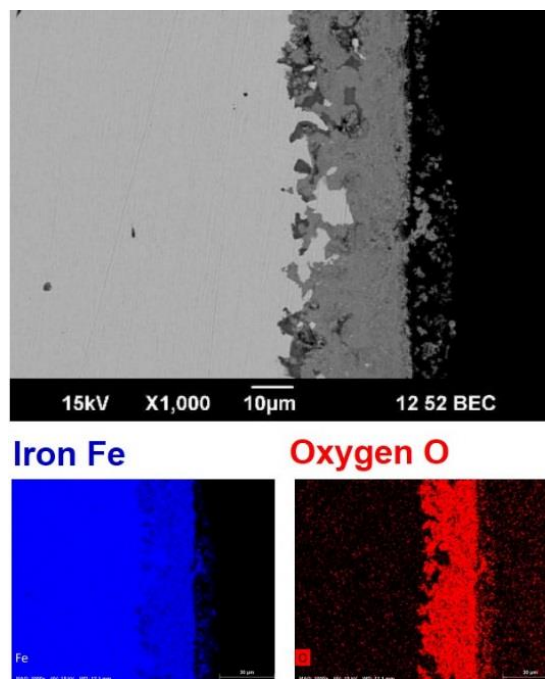


Figure 34. Cross-section and EDS mapping results for X65 specimen in experiment without H<sub>2</sub>S after 1 day, 1 wt.% NaCl solution, T=120°C, initial pH=4.0.

The cross-sections of specimens from the experiment “without H<sub>2</sub>S” are shown in Figure 35. It can be seen that the overall layer thickness increased from 25 µm after 1 day to 80 µm after 21 days. Comparing the growth behavior of Fe<sub>3</sub>O<sub>4</sub> (without H<sub>2</sub>S, Figure 36) and iron sulfide (with H<sub>2</sub>S, Figure 28), the same trend is observed. This could be a coincidence, especially since the thickness of the Fe<sub>3</sub>O<sub>4</sub> layer alone stayed at ~25 µm in the experiment “with H<sub>2</sub>S” and did not increase further with exposure time. However, this could also indicate that the FeS and the Fe<sub>3</sub>O<sub>4</sub> formation rates are inherently linked. This, again, highlights the complexity of the growth mechanism of iron sulfide in the presence of a Fe<sub>3</sub>O<sub>4</sub> layer, which will be discussed later.

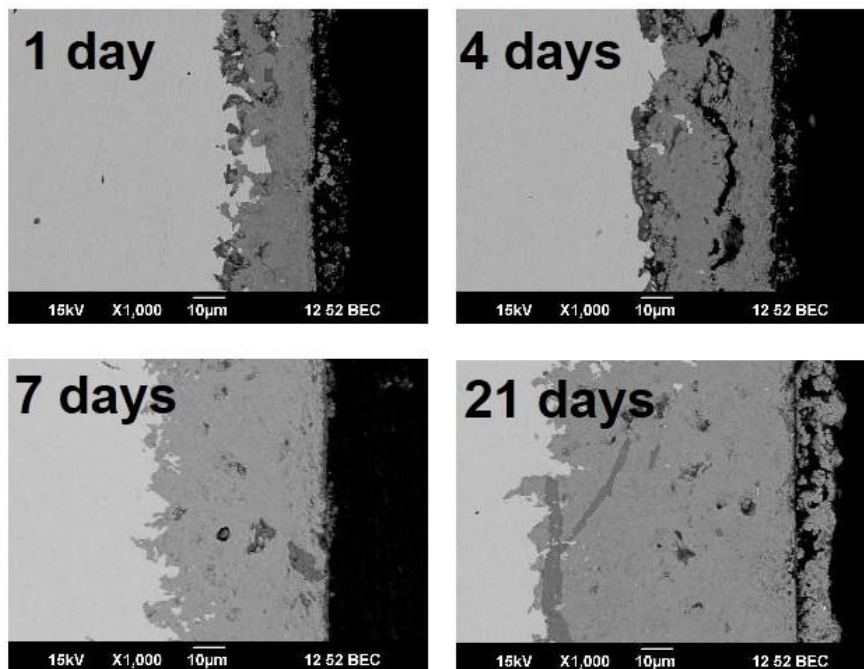


Figure 35. The growth of Fe<sub>3</sub>O<sub>4</sub> layer with time, shown by cross-sections of X65 specimens in the experiment without H<sub>2</sub>S after different test durations (obtained in separate experiments), 1 wt.% NaCl solution, T=120°C, initial pH=4.0.

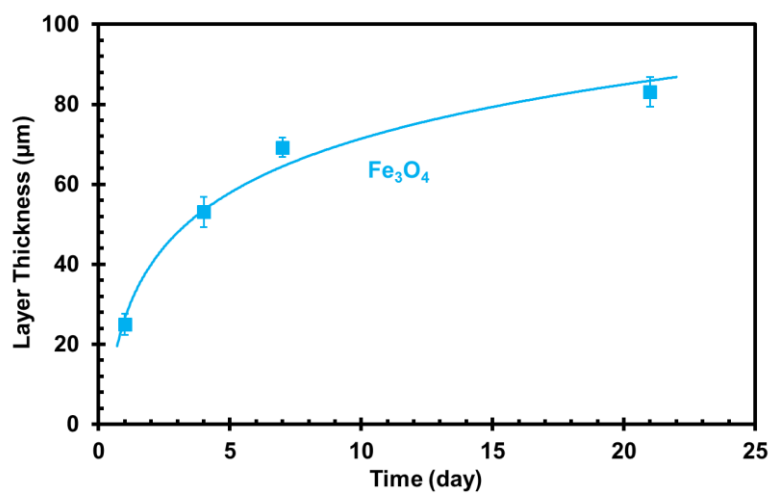


Figure 36. The thickness of Fe<sub>3</sub>O<sub>4</sub> layer with time in the experiment without H<sub>2</sub>S, X65, 1 wt.% NaCl solution, T=120°C, initial pH=4.0.

As mentioned earlier, the X65 steel specimen with preformed  $\text{Fe}_3\text{O}_4$  was exposed to a 0.1 bar  $\text{H}_2\text{S}$  environment under the same conditions. As a reminder, the  $\text{Fe}_3\text{O}_4$  layer was first formed on the steel surface in the absence of  $\text{H}_2\text{S}$  over a 1 day period. The layer was then exposed to  $\text{H}_2\text{S}$  for another day. The EDS mapping results for the cross-sections are shown in Figure 37; all images are at the same magnification for ease of comparison. However, the data related to the experiment “with  $\text{H}_2\text{S}$ ” were obtained using a different EDS detector than for the other two conditions and the display of the results can be more difficult to interpret. In the first row of Figure 37, the highest magnitude concentration of elements is indicated by white pixels and lowest magnitude by blue pixels; in the other two rows, the brightness intensity of the same-color pixels is related to the concentration. The level of color brightness can only be used in a qualitative way and cannot be compared from image to image. In terms of  $\text{Fe}_3\text{O}_4$  layer thickness for the specimen with, without  $\text{H}_2\text{S}$ , and with preformed  $\text{Fe}_3\text{O}_4$  layer, no significant difference can be found. However, the thickness of the outer iron sulfide layer, represented by sulfur (S) content, was much lower without the preformed  $\text{Fe}_3\text{O}_4$  layer (less than 5  $\mu\text{m}$ ) than with the preformed  $\text{Fe}_3\text{O}_4$  layer (around 30  $\mu\text{m}$ ).

These experimental results infer that the formation rate of  $\text{Fe}_3\text{O}_4$  is faster than that of iron sulfide at the tested temperature. This explains why  $\text{Fe}_3\text{O}_4$  is persistently detected while not being thermodynamically favored. In comparison, the presence of  $\text{Fe}_3\text{O}_4$  was not reported at a lower temperature in similar environments. A deeper look into the solubility limit of each corrosion product can help explain this behavior.

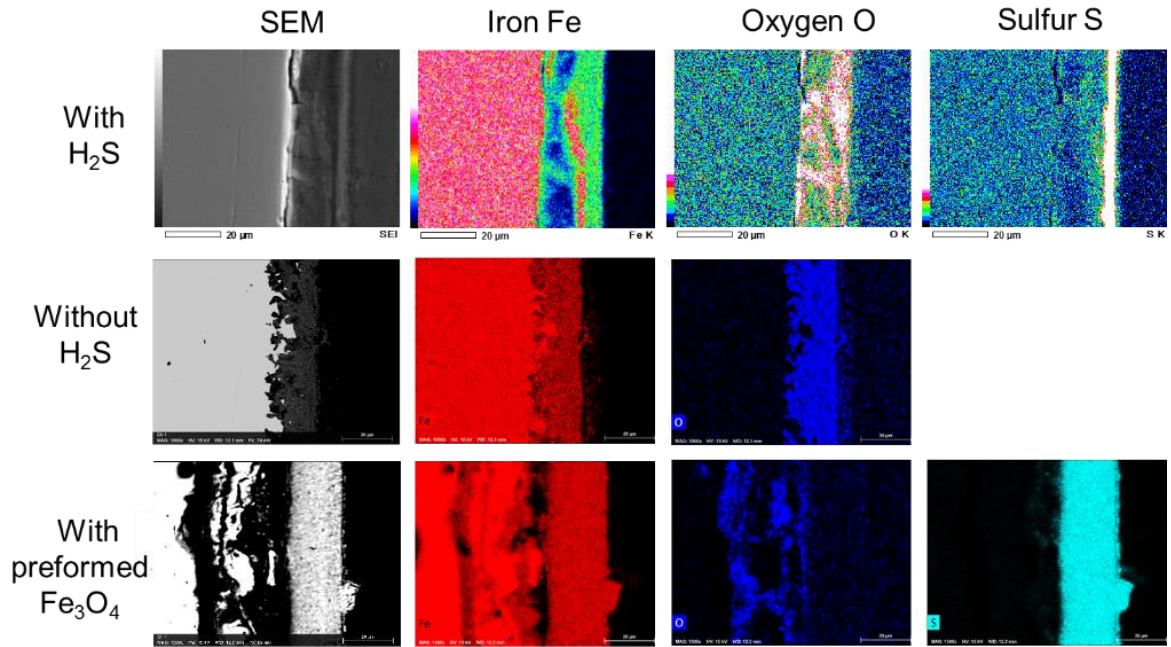
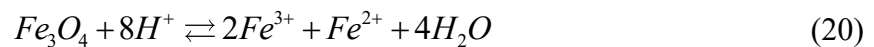


Figure 37. EDS mapping results for X65 specimen from the experiment without H<sub>2</sub>S with, with 0.1 bar H<sub>2</sub>S, and with preformed Fe<sub>3</sub>O<sub>4</sub> layer, 1 wt.% NaCl solution, T=120°C, initial pH=4.0.

The solubility equilibria for Fe<sub>3</sub>O<sub>4</sub> and mackinawite are given by Reactions 20 and 23 with the corresponding solubility limit expressions given by Equations 21 and 24. The Gibbs energy change  $\Delta G$  for Reaction 20 is given in Equation 22. The effect of temperature on the solubility limit is shown in Figure 38. The solubility limit for Fe<sub>3</sub>O<sub>4</sub> experiences a significant drop with the increase of temperature, while in comparison, for mackinawite, the decrease in solubility limit is only moderate.



$$K_{sp, Fe_3O_4} = e^{-\frac{\Delta G}{RT}} \quad (21) [27]$$

$$\Delta G = 2\Delta G(Fe^{3+}) + \Delta G(Fe^{2+}) + 4\Delta G(H_2O) - \Delta G(Fe_3O_4) - 8\Delta G(H^+) \quad (22)$$



$$K_{sp,2} = 10^{\frac{2848779}{T_K} - 6.347 + \log(K_{a,1})} \quad (24) [49]$$

$$K_{a,1} = 10^{782.43945 + 0.361261T_K - 1.6722 \times 10^{-4}T_K^2 - 20565.7315/T_K - 142.7417222 \ln T_K} \quad (7) [49]$$

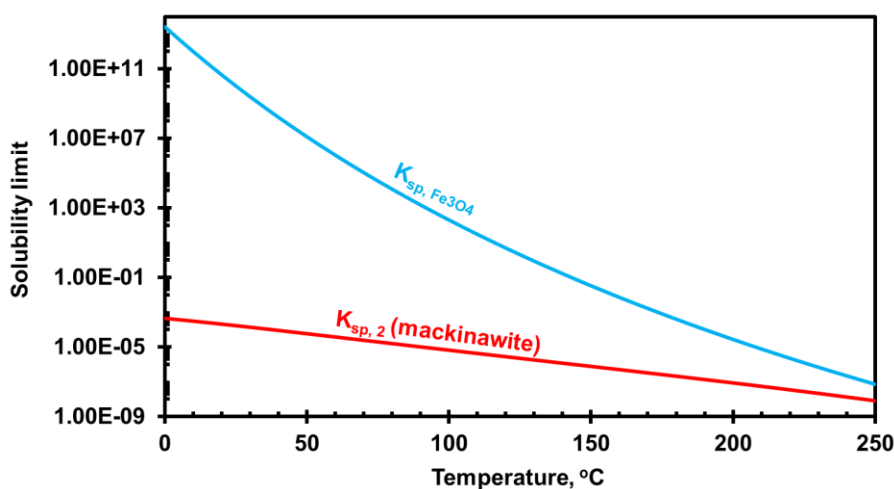


Figure 38. Solubility limit for Fe<sub>3</sub>O<sub>4</sub> and mackinawite with the increase of temperature, pH=4.0, p<sub>H<sub>2</sub>S</sub>=0.1 bar.

The level of saturation value governs the precipitation rate and consequently the layer formation/dissolution rate. The expressions for saturation value of Fe<sub>3</sub>O<sub>4</sub> ( $S_{Fe_3O_4}$ ) and mackinawite ( $S_{mackinawite}$ ) are given in Equations 25 and 26. Assuming reaction (20) and (23) are both in equilibrium at 120°C and pH 4.0, i. e.,  $S_{Fe_3O_4} = S_{mackinawite} = 1$ , this gives a ferric ion concentration [Fe<sup>3+</sup>] close to 1.0×10<sup>-10</sup> M, which means the calculated  $S_{Fe_3O_4}$  may be underestimated compared to earlier similar studies (1.0×10<sup>-6</sup> M) [32].

$$S_{Fe_3O_4} = \frac{[Fe^{3+}]^2[Fe^{2+}]}{[H^+]^8 K_{sp,Fe_3O_4}} \quad (25)$$

$$S_{mackinawite} = \frac{[Fe^{2+}][HS^-]}{[H^+] K_{sp,2}} \quad (26)$$

As soon as the steel specimen is inserted into an aqueous H<sub>2</sub>S environment, iron starts to dissolve and release Fe<sup>2+</sup>, resulting in an increase in pH (considering a closed system such as an autoclave). Figure 39 shows the changes in  $S_{Fe_3O_4}$ , bulk solution pH, and  $S_{mackinawite}$  with an increase in [Fe<sup>2+</sup>] from 0 to 10 ppm in a closed system. The saturation values are based on calculations which only show a trend without consideration of precipitation. By the time the test is started, FeS precipitation could have already been occurring acting as a sink of Fe<sup>2+</sup> ions and slowing down the rate of increase in saturation. In H<sub>2</sub>S environments, the Fe<sup>2+</sup> concentration typically cannot increase past 5 ppm since the  $S_{mackinawite}$  never reaches very high values due to the fast kinetics of FeS precipitation. At 120°C with an initial pH 4.0, Fe<sub>3</sub>O<sub>4</sub> is strongly supersaturated ( $S_{Fe_3O_4} = 10^6$ ) almost immediately after Fe<sup>2+</sup> ions are generated in the solution. In contrast,  $S_{mackinawite}$  requires at least 0.8 ppm of Fe<sup>2+</sup> to reach a saturation of 1. Looking only at saturation levels, Fe<sub>3</sub>O<sub>4</sub> is expected to precipitate and to dominate the layer growth during the initial stage, because  $S_{Fe_3O_4}$  is at least six orders of magnitude greater than  $S_{mackinawite}$  and highly supersaturated. However, the solution pH will increase with time and this could change the ratio of saturation levels. Figure 39 also presents the saturation values at

initial pH 5.0. However, the difference between initial  $S_{Fe_3O_4}$  and  $S_{mackinawite}$  is even higher at pH 5.0, so mildly acidic environments (pH 4 and pH 5) are not expected to largely affect the sequence and rate of layer growth at the tested temperature.

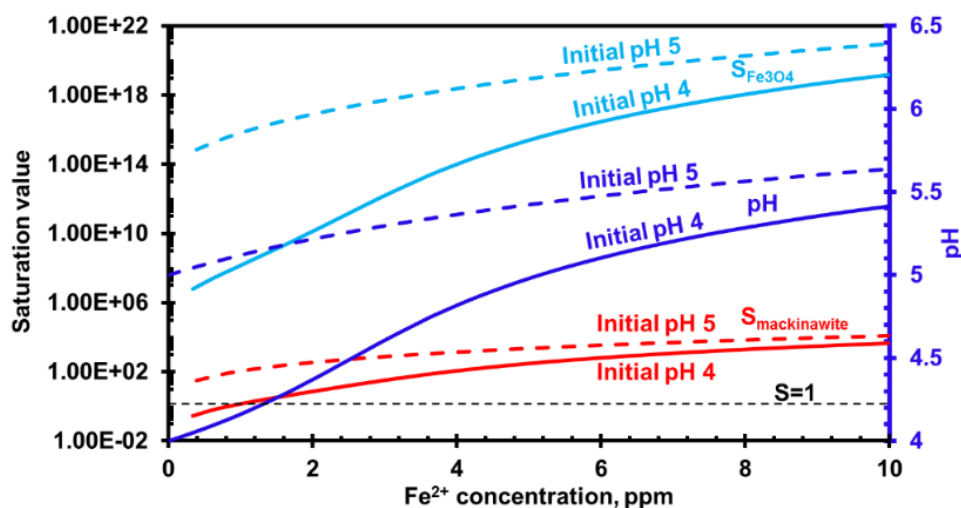


Figure 39. Saturation value for  $Fe_3O_4$  and mackinawite at initial pH 4.0 and 5.0,  $[Fe^{3+}] = 1 \times 10^{-10}$  M,  $T = 120^\circ C$ ,  $pH_2S = 0.1$  bar.

Figure 40 presents the trend of  $S_{Fe_3O_4}$  and  $S_{mackinawite}$  at  $25^\circ C$  and  $120^\circ C$ . It is important to note that at  $25^\circ C$  and for very low ferrous ion concentrations,  $S_{Fe_3O_4}$  is of the same magnitude as  $S_{mackinawite}$ . The saturation level is indeed related to the kinetics of layer formation but other parameters also affect the reaction rates (activation energy, kinetic rate constant). At low temperature, FeS formation is kinetically favored. Considering that  $Fe_3O_4$  is more soluble at lower temperatures (see Figure 38), this explains why  $Fe_3O_4$  is not found at temperatures below  $80^\circ C$  while it forms very quickly

and actually dominates during the initial stages of corrosion at temperatures above 80°C in an H<sub>2</sub>S corrosion environment. Temperature is the key influential factor.

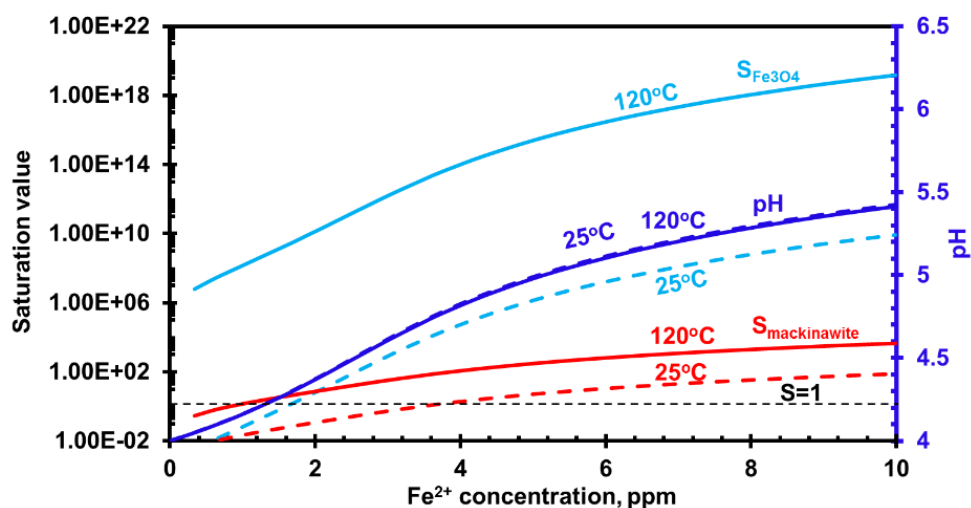


Figure 40. Saturation value for Fe<sub>3</sub>O<sub>4</sub> and mackinawite at 25°C and 120°C, [Fe<sup>3+</sup>]=1×10<sup>-10</sup> M, p<sub>H<sub>2</sub>S</sub>=0.1 bar, initial pH=4.0 (pH lines for 25°C and 120°C overlap in the graph).

In summary, due to a much higher saturation value, Fe<sub>3</sub>O<sub>4</sub> is likely to form. It is hypothesized that it will also form very quickly, faster than mackinawite, during the initial stages of corrosion at temperatures above 80°C in aqueous H<sub>2</sub>S corrosion environments. A thin mackinawite layer is expected to immediately form as well when the steel is exposed to [H<sub>2</sub>S]<sub>aq</sub>, but the thickness of this layer is of the order of nanometers which is several orders of magnitude lower than for Fe<sub>3</sub>O<sub>4</sub> (~ 25 μm) [63]. Therefore, to be more precise, simultaneous growth of Fe<sub>3</sub>O<sub>4</sub> and mackinawite is then expected to occur, but initially the kinetics for Fe<sub>3</sub>O<sub>4</sub> precipitation should dominate at high temperatures.

**7.4.2 Iron sulfide formation mechanism.** After the initial stages of formation, the iron sulfide growth mechanism was investigated in Experimental Set #2 in order to test the 2<sup>nd</sup> hypothesis. The experimental design is shown in Figure 31. The Fe<sub>3</sub>O<sub>4</sub> precipitation was performed on Ni specimens using Fe<sup>2+</sup> ions generated by independently corroding X65 steel specimens immersed in the same solution at 120°C, with an initial pH 4.0 and for 21 days. The Fe<sub>3</sub>O<sub>4</sub> did indeed precipitate on the Ni surface, as identified by XRD in Figure 41. A precipitated Fe<sub>3</sub>O<sub>4</sub> layer (~10 μm) can also be observed from the cross-section analysis in Figure 42 and is confirmed by the EDS mapping analysis. This Ni specimen with the preformed Fe<sub>3</sub>O<sub>4</sub> layer was retrieved, dried, stored, and then exposed for one day in a 0.1 bar H<sub>2</sub>S environment under otherwise same conditions (120°C, initial pH 4.0) to test, and perhaps verify, the 2<sup>nd</sup> hypothesis.

After 1 day of exposure, the Ni specimen was retrieved and again characterized by XRD and SEM/EDS, as shown in Figure 41 and Figure 42. The Fe<sub>3</sub>O<sub>4</sub> layer disappeared and was totally replaced by a mackinawite layer as confirmed by both XRD and EDS. The EDS mapping results show an iron sulfide layer on the Ni surface with no obvious oxygen (O) detected.

The above results seem to validate the 2<sup>nd</sup> hypothesis, stating that the FeS layer grows through Fe<sub>3</sub>O<sub>4</sub> conversion. Without H<sub>2</sub>S present, the Fe<sub>3</sub>O<sub>4</sub> layer increased in thickness over time (Figure 36). With H<sub>2</sub>S present, the Fe<sub>3</sub>O<sub>4</sub> layer stabilized at a specific thickness while the iron sulfide layer increased in thickness with time due to the conversion reaction (Figure 28). Possibly coincidentally, the FeS growth rate is similar to the rate of formation of the Fe<sub>3</sub>O<sub>4</sub> layer observed in Figure 36; which is a further

evidence that  $\text{Fe}_3\text{O}_4$  kept growing and converting to iron sulfide in the aqueous  $\text{H}_2\text{S}$  environment. However, FeS precipitation via Reaction 23 cannot be entirely excluded since  $S_{mackinawite}$  in the bulk did exceed 1. However, previous results show that the  $\text{Fe}^{2+}$  concentration was around 5 ppm [64], which gives a  $S_{mackinawite}$  value around 10 (Figure 39). This value of saturation is not extremely high and would not constitute a high driving force to produce a significant amount of precipitated iron sulfide. A recent corrosion prediction model developed by Zheng, *et al.*, [65] which includes iron sulfide precipitation, predicts the iron sulfide layer thickness to be below 14  $\mu\text{m}$  after 7 days. Compared with the result in Figure 28, the thickness of iron sulfide was above 45  $\mu\text{m}$  after 7 days. This further demonstrates that the main contribution to iron sulfide growth at higher temperatures was through the  $\text{Fe}_3\text{O}_4$  conversion mechanism rather than the precipitation mechanism.

The conclusion from hypothesis #1 was that the  $\text{Fe}_3\text{O}_4$  formation was dominant at the initial stage of corrosion due to high saturation value. Actually, it is hypothesized that it was dominant over the whole test duration, not only at the start of the test. However, the  $\text{Fe}_3\text{O}_4$  layer was thermodynamically less stable and kept converting to iron sulfide. The rate of conversion from  $\text{Fe}_3\text{O}_4$  to FeS eventually matched the rate of  $\text{Fe}_3\text{O}_4$  formation.

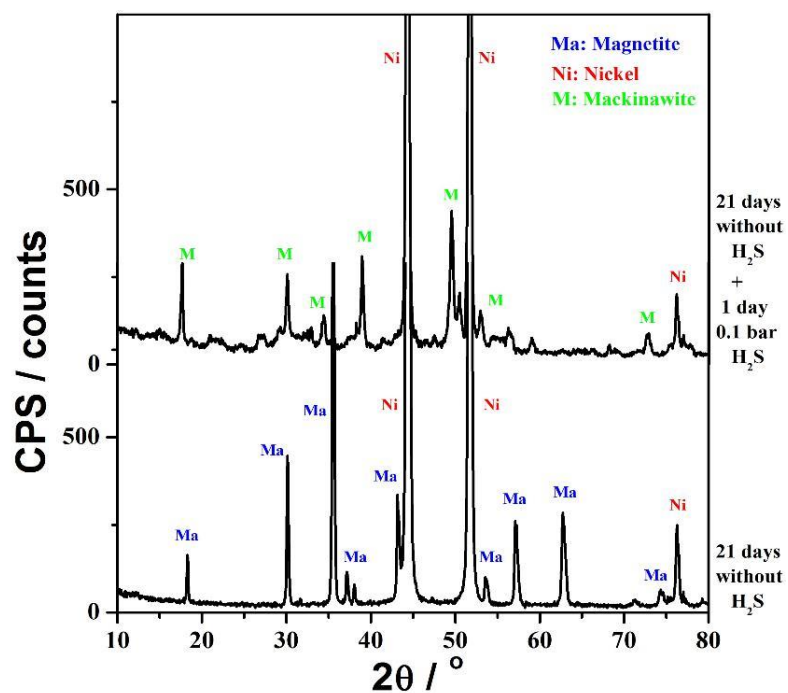


Figure 41. XRD patterns of preformed  $\text{Fe}_3\text{O}_4$  layer on Ni specimen before and after  $\text{H}_2\text{S}$  was introduced, 1 wt.% NaCl solution,  $T=120^\circ\text{C}$ , initial  $\text{pH}=4.0$ .

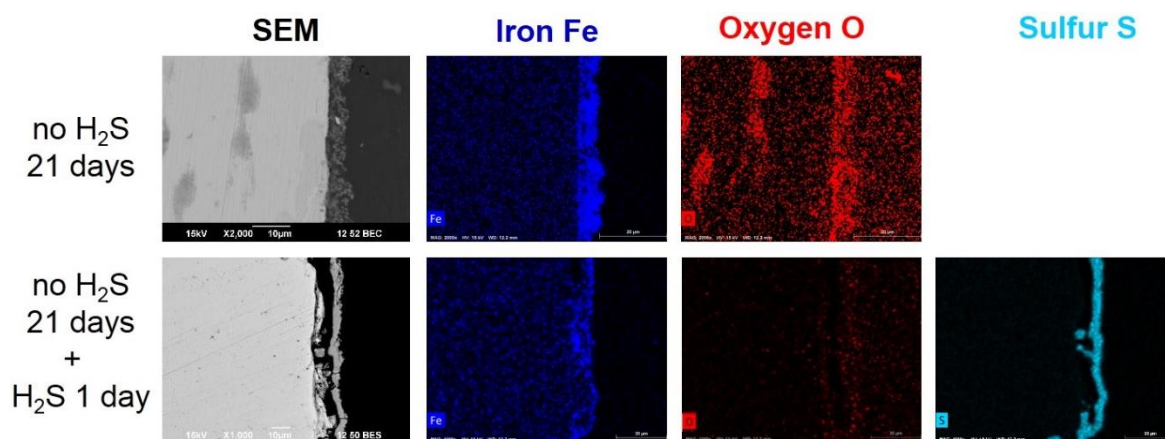


Figure 42. EDS mapping results for the cross section of preformed  $\text{Fe}_3\text{O}_4$  layer on Ni specimen before and after  $\text{H}_2\text{S}$  was introduced, 1 wt.% NaCl solution,  $T=120^\circ\text{C}$ ,  $\text{pH}_2\text{S}=0.1$  bar, initial  $\text{pH}=4.0$ .

**7.4.3 Descriptive model for the Fe<sub>3</sub>O<sub>4</sub>/FeS formation mechanisms at high temperature.** Based on the experimental results, a descriptive model for Fe<sub>3</sub>O<sub>4</sub> and FeS formation mechanisms at high temperature is presented in Table 10.

Table 10. Schematic diagrams for Fe<sub>3</sub>O<sub>4</sub>/FeS formation mechanisms at higher temperatures in a sour environment.

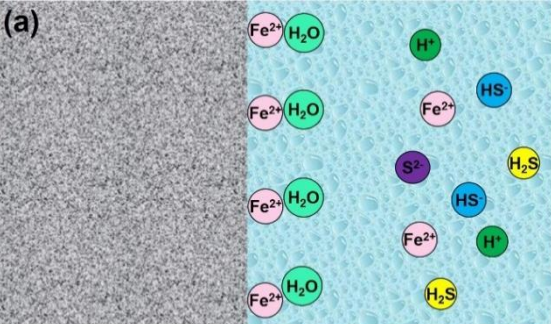
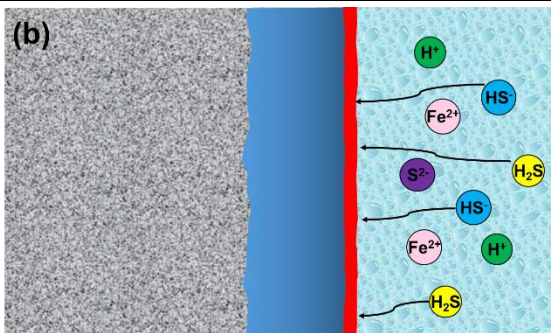
Step	Description	Schematic Diagram
(a)	X65 carbon steel is exposed to H <sub>2</sub> S corrosion environment at high temperature. Fe starts to dissolve and releases Fe <sup>2+</sup> ions in solution.	 <p>(a)</p>
(b)	Fe <sup>2+</sup> reacts with its surrounding H <sub>2</sub> O molecules and Fe <sub>3</sub> O <sub>4</sub> forms quickly via Reaction (13). Fe <sub>3</sub> O <sub>4</sub> layer is protective and the corrosion rate (i.e. the rate of Fe <sup>2+</sup> ion release) decreases. Consequently, the	 <p>(b)</p>

Table 10 continued.

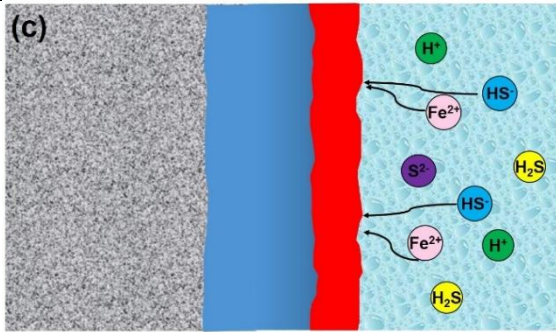
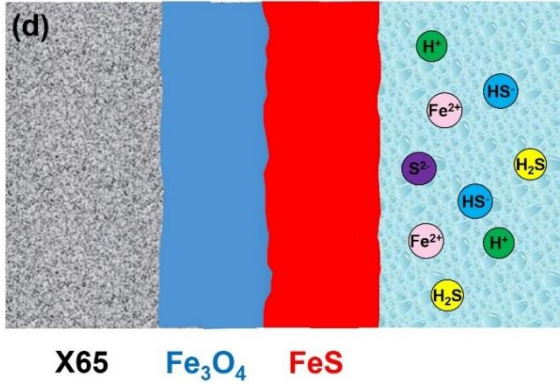
Step	Description	Schematic Diagram
(b)	<p>formation rate of <math>\text{Fe}_3\text{O}_4</math> also decreases which slows down the layer growth rate. Simultaneously, the aqueous <math>\text{H}_2\text{S}</math> reacts with the <math>\text{Fe}_3\text{O}_4</math> layer, on the solution side, which transforms it to iron sulfide via Reaction (19) but initially at a much lower rate than <math>\text{Fe}_3\text{O}_4</math> formation.</p>	
(c)	<p>Iron sulfide formation through <math>\text{Fe}_3\text{O}_4</math> conversion catches up as the formation of <math>\text{Fe}_3\text{O}_4</math> slows down. <math>\text{Fe}_3\text{O}_4</math> continuously forms at the metal surface and converts to iron sulfide at the <math>\text{Fe}_3\text{O}_4/\text{FeS}</math> interface. Eventually, these two reactions occur at a similar rate which stabilizes the thickness of the <math>\text{Fe}_3\text{O}_4</math> layer.</p>	 <p>(c)</p>

Table 10 continued.

Step	Description	Schematic Diagram
(d)	If the bulk FeS saturation value exceeds the solubility limit of iron sulfide, iron sulfide will precipitate at the FeS/solution interface and the FeS layer will grow even further.	 <p>The schematic diagram (d) illustrates the corrosion products on X65 steel in an acidic H<sub>2</sub>S environment. It shows a cross-section of the steel surface with three distinct layers: X65 steel (grey), Fe<sub>3</sub>O<sub>4</sub> (blue), and FeS (red). To the right of the FeS layer is an acidic solution containing Fe<sup>2+</sup>, HS<sup>-</sup>, H<sub>2</sub>S, and H<sup>+</sup> ions.</p>

Other research studies [37], [66], [67] suggested alternative pathways for the layer growth mechanism, either stating that both Fe<sub>3</sub>O<sub>4</sub> and FeS layers grow solely through precipitation (the present work suggests that precipitation is only a minor contributor) or postulating that the layer growth is linked to Fe solid-state outward diffusion through the Fe<sub>3</sub>O<sub>4</sub> lattice. However, the experimental results presented here do not seem to validate either of these mechanisms.

### 7.5 Summary

Due to the higher saturation value at high temperature, the Fe<sub>3</sub>O<sub>4</sub> layer is the dominant corrosion product forming at the steel surface in the initial stages of experiments when steel is exposed to an acidic aqueous H<sub>2</sub>S environment.

Both Fe<sub>3</sub>O<sub>4</sub> and mackinawite are responsible for the initial rapid decrease of the corrosion rate observed in sour environments at high temperature. However, most of the corrosion protection can be attributed to the Fe<sub>3</sub>O<sub>4</sub> layer.

$\text{Fe}_3\text{O}_4$  converts to mackinawite since it is thermodynamically less stable than iron sulfide.  $\text{Fe}_3\text{O}_4$  experiences a simultaneous and continuous process of formation, at the steel/ $\text{Fe}_3\text{O}_4$  interface, and transformation to  $\text{FeS}$ , at the  $\text{Fe}_3\text{O}_4/\text{FeS}$  interface.

## Chapter 8: Effect of H<sub>2</sub>S Partial Pressure on the Corrosion Rate and Layer Formation on Mild Steel at High Temperature

### 8.1 Introduction

The effects of high temperature and exposure time on the H<sub>2</sub>S corrosion kinetics and transformation sequence of iron sulfide have been studied in Chapter 5 and Chapter 6, respectively. In this chapter, the effect of H<sub>2</sub>S partial pressure (pH<sub>2</sub>S) on the corrosion rate of carbon steel and iron sulfide transformation at high temperature is investigated.

Generally, H<sub>2</sub>S plays a dual role. Firstly, it accelerates the corrosion rate by providing an additional cathodic reaction:



Secondly, it favors the formation of an iron sulfide layer by providing more HS<sup>-</sup> ions:



Sun, *et al.*, [68] stated that the kinetics of corrosion drive the rate of corrosion in the low pH<sub>2</sub>S range, while FeS layer formation plays a dominant role in the higher pH<sub>2</sub>S range. Therefore, a maximum in corrosion rate can be observed when increasing pH<sub>2</sub>S, all other conditions being constant. However, the exact pH<sub>2</sub>S values were not reported in the paper. Other literature works also show that the increase of pH<sub>2</sub>S could either cause an acceleration or a retardation of the corrosion rate, depending on pH<sub>2</sub>S, pH, temperature, and exposure time [33], [69]-[72]. However, the water chemistry in these tests was not specified or controlled and the types of corrosion products were not characterized. Moreover, all the above experiments were performed only at low temperatures, and the effect of high temperature is still unknown.

## 8.2 Experimental

The experimental setup, material, and procedures were the same as presented in Chapter 5. The operating parameters such as pH and  $[H_2S]_{aq}$  presented in the test matrix were calculated based on the water chemistry model described in Chapter 4, as summarized in Table 11.

Table 11. Test matrix for the effect of  $pH_2S$ .

Parameter	Value			
Temperature, °C	120			
$pH_2S$ , bar	0.10	0.50	1.0	2.0
$[H_2S]_{aq}$ , mol/L	0.00385	0.01400	0.02800	0.05600
Initial pH	4.0			
Rotating speed, rpm	1000			
Duration, days	4			

## 8.3 Results and Discussion

**8.3.1 Corrosion rates.** The measured corrosion rates obtained with different  $pH_2S$  at 120°C are shown in Figure 43. There was no obvious trend for the initial corrosion rate (3~8 mm/y) probably due to the formation of relatively protective corrosion products before the autoclave reached the high testing temperature, especially at higher  $pH_2S$ . This is, however, inevitable for high temperature and high pressure tests since no adjustment can be made to control the conditions once the autoclave has been closed. After a few hours, the corrosion rates decreased quickly to a stable corrosion rate between 0.4 to 2 mm/yr. The stabilized corrosion rate tended to decrease with increasing

pH<sub>2</sub>S except at 1.0 and 2.0 bar H<sub>2</sub>S. This was attributed to severe localized corrosion with pyrite formation, which will be discussed later.

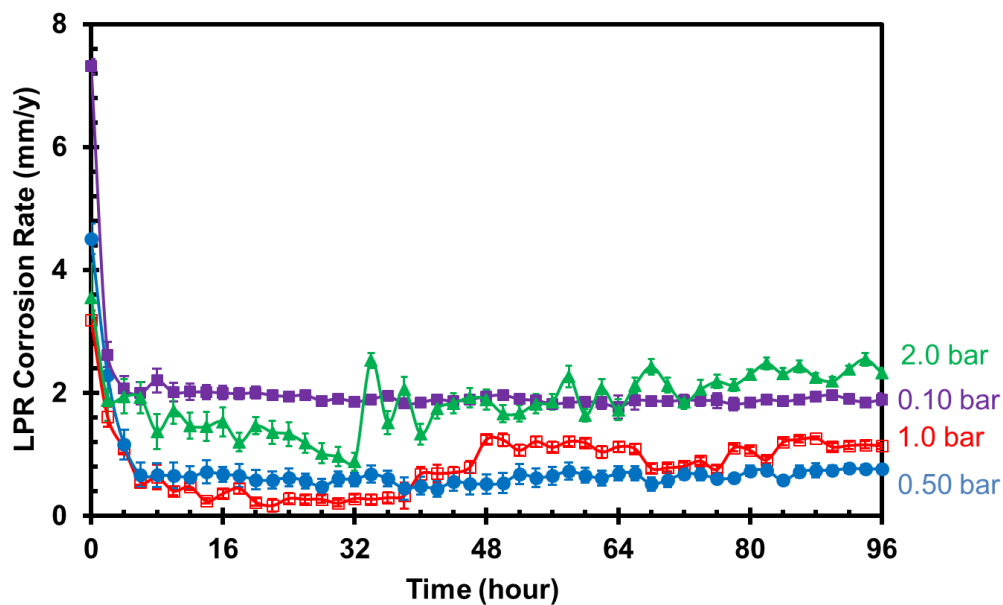


Figure 43. LPR corrosion rate at different pH<sub>2</sub>S, T=120°C, initial pH=4.0, B=23 mV/decade.

Figure 44 shows the corrosion rate measured by weight loss and compared with LPR integrated average corrosion rate. Good agreement can be observed at every studied pH<sub>2</sub>S by using a *B* value of 23 mV/decade. This demonstrates that the trend of LPR measurements is valid under these conditions. A minimum corrosion rate can be observed at 0.5 bar H<sub>2</sub>S.

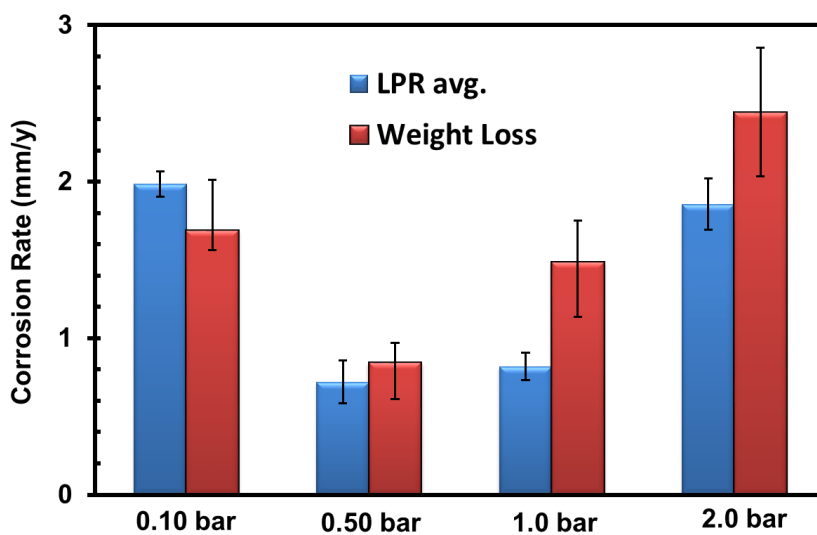


Figure 44. Comparison of corrosion rates measured by LPR average and weight loss at different pH<sub>2</sub>S, T=120°C, initial pH=4.0, 4 days.

**8.3.2 Outer iron sulfide layer.** The corrosion product layers were characterized by XRD, as shown in Figure 45. The corresponding SEM images are shown in Figure 46 and Figure 47. At 0.10 bar H<sub>2</sub>S, the main iron sulfide was identified as troilite (FeS) with a small amount of mackinawite (FeS). The elongated needle-like and flower-like troilite crystal morphologies can be seen in the SEM images. The same structure of troilite was also found in other studies [47], [48], [73]. Troilite transformed to pyrrhotite (Fe<sub>1-x</sub>S, 0 ≤ x ≤ 0.17) after increasing pH<sub>2</sub>S to 0.50 bar. SEM images show the steel surface was fully covered by a dense layer of pyrrhotite crystals with a hexagonal flake-like morphology (Figure 46(c) and (d)). When the pH<sub>2</sub>S was increased to 1.0 bar, some pyrite (FeS<sub>2</sub>) appeared in addition to the pyrrhotite. Sporadic cubic pyrite crystals can be clearly seen on the surface of the pyrrhotite. Moreover, the thickness of the pyrrhotite crystals tended to increase compared with those formed at 0.50 bar H<sub>2</sub>S. Only pure pyrite was

identified when  $\text{pH}_2\text{S}$  increased to 2.0 bar, and the specimen surface was completely covered by large cubic pyrite crystals as shown in Figure 47(c) and (d). The cubic-like morphology of pyrite is consistent with its crystal structure and the literature [74]-[76]. In conclusion, the observed sequence of iron sulfide transformation with  $\text{pH}_2\text{S}$  was troilite  $\rightarrow$  pyrrhotite  $\rightarrow$  pyrrhotite/pyrite  $\rightarrow$  pyrite, which is the same transformation order given in previous literature associated with temperature and time [77], [78]. Iron sulfide transformed to more thermodynamically stable phases with increasing  $\text{pH}_2\text{S}$ .

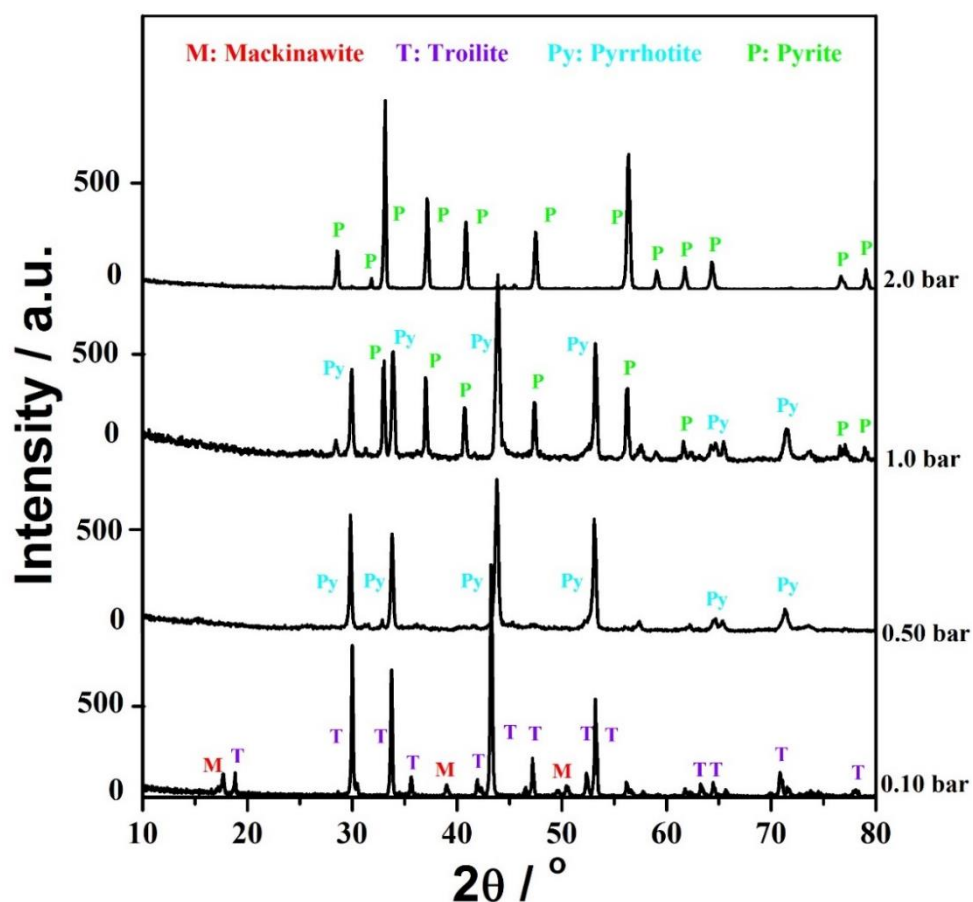


Figure 45. XRD patterns of corrosion products on the steel surface at different  $\text{pH}_2\text{S}$ ,  $T=120^\circ\text{C}$ , initial  $\text{pH}=4.0$ , 4 days.

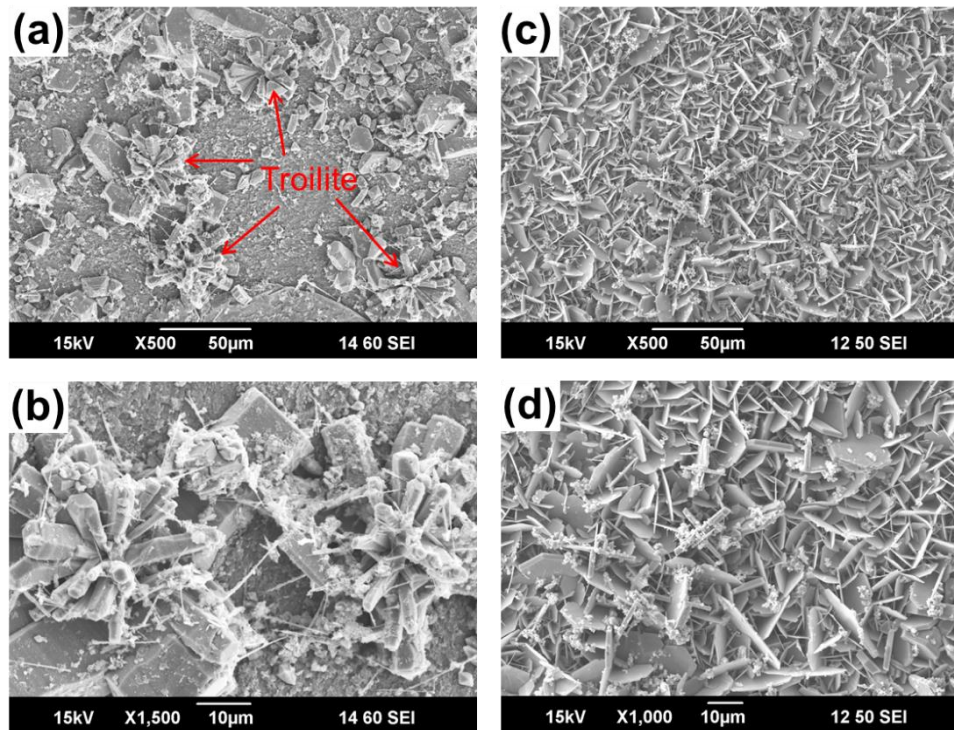


Figure 46. SEM morphologies: (a) and (b) troilite,  $\text{pH}_2\text{S}=0.10$  bar, (c) and (d) pyrrhotite,  $\text{pH}_2\text{S}=0.10$  bar,  $T=120^\circ\text{C}$ , initial  $\text{pH}=4.0$ , 4 days.

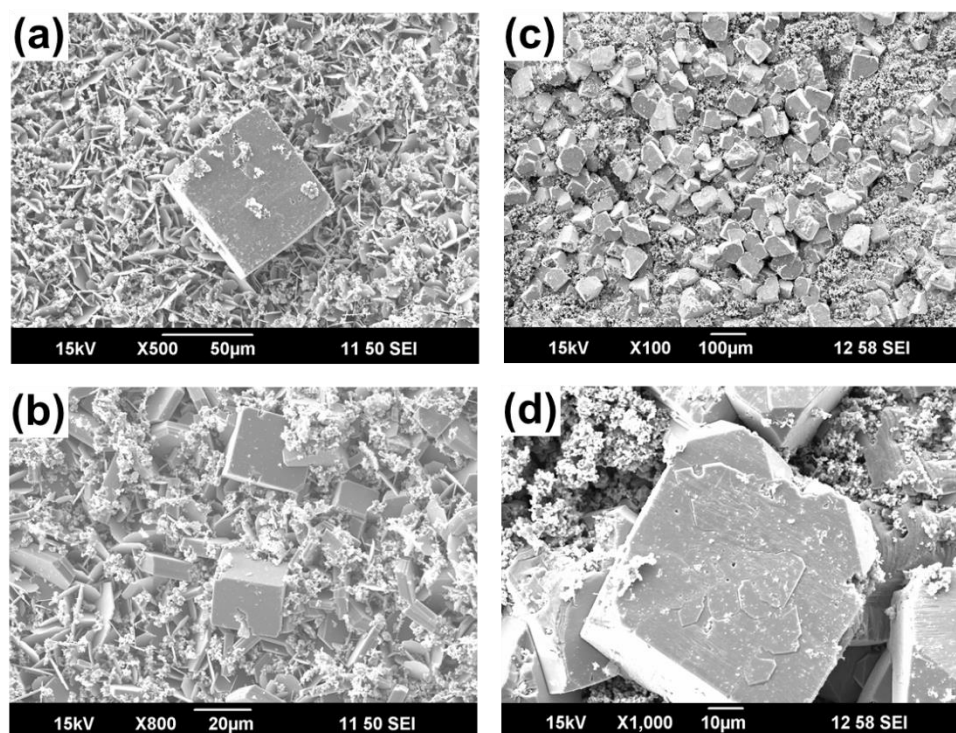


Figure 47. SEM morphologies: (a) and (b) pyrrhotite/pyrite,  $\text{pH}_2\text{S}=1.0$  bar, (c) and (d) pyrite,  $\text{pH}_2\text{S}=2.0$  bar,  $T=120^\circ\text{C}$ , initial  $\text{pH}=4.0$ , 4 days.

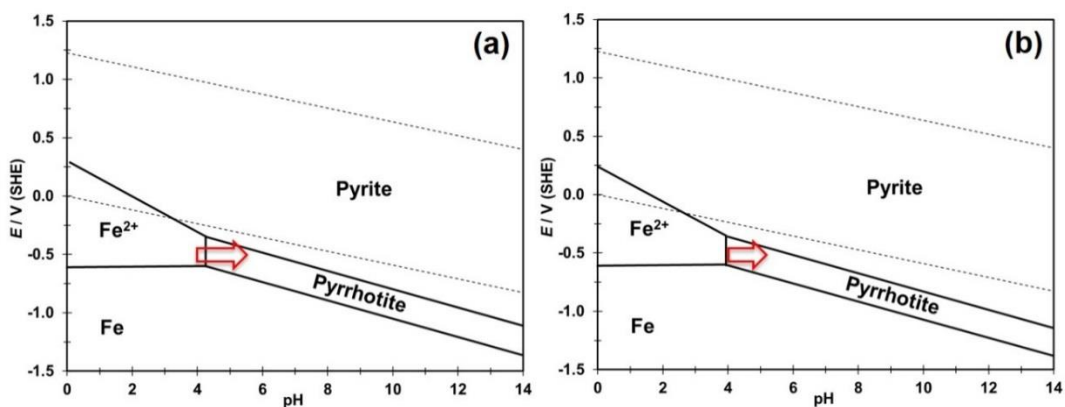
At the end of each experiment, experimental parameters were back calculated based on the method presented in Chapter 5. The calculated results are summarized in Table 12, and were used as the inputs to generate Pourbaix diagrams, as shown in Figure 48.

The vertical position of the arrow in each Pourbaix diagram represents the final experimental potential (potential range varied between  $-350$  and  $-750$  mV vs. SHE). The direction of the arrow represents the pH drift experienced during the test from initial pH 4.0 to the calculated values in Table 12. It can be seen that for all experiments the pH increased to around 5.4 during the 4-day experiments. For 0.10 and 0.50 bar  $\text{pH}_2\text{S}$ , the tip

of the arrow, which represents the final experimental conditions, is right in the stability zone of pyrrhotite. At higher  $p_{H_2S}$  (1.0 and 2.0 bar), the tip is right on the equilibrium line between pyrrhotite and pyrite, indicating the transformation between pyrrhotite and pyrite had an increased probability. The thermodynamic predictions are in good agreement with experimental results.

Table 12. Summary of the theoretical calculated final conditions at 120°C.

pH <sub>2</sub> S, bar	Final Conditions at 120°C		
	pH <sub>2</sub> S, bar	Bulk pH	Bulk Fe <sup>2+</sup> , ppm
0.10	0.11	5.5	5.8
0.50	0.47	5.3	6.2
1.0	1.02	5.4	5.9
2.0	1.98	5.3	5.7



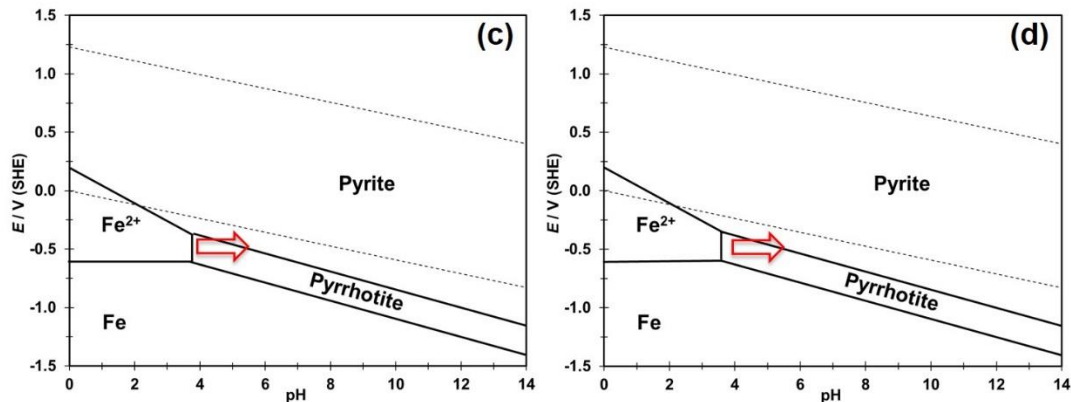


Figure 48. Pourbaix diagrams for Fe-H<sub>2</sub>S-H<sub>2</sub>O system by considering mackinawite/greigite/pyrrhotite/pyrite (a) pH<sub>2</sub>S=0.10 bar, (b) pH<sub>2</sub>S=0.50 bar, (c) pH<sub>2</sub>S=1.0 bar, (d) pH<sub>2</sub>S=2.0 bar, T=120°C, other input parameters are in Table 12.

**8.3.3 Inner Fe<sub>3</sub>O<sub>4</sub> layer.** The Fe<sub>3</sub>O<sub>4</sub> layers obtained at different pH<sub>2</sub>S values were examined via cross-section analysis. In this case, the XRD analysis could not identify the presence of Fe<sub>3</sub>O<sub>4</sub> since the outer corrosion product layer was too thick or/and compact. The colors in Figure 49 qualitatively indicate the elemental composition of each layer. Focusing on the third column in Figure 50 for the element oxygen, which indicates the location of the Fe<sub>3</sub>O<sub>4</sub> layer, the thickness of Fe<sub>3</sub>O<sub>4</sub> can be seen to decrease with increasing pH<sub>2</sub>S.

With the increase of pH<sub>2</sub>S, the thickness of Fe<sub>3</sub>O<sub>4</sub> decreased from 25 μm to 5 μm. The average thickness of the Fe<sub>3</sub>O<sub>4</sub> layer was measured and plotted in Figure 50. The results, again, demonstrate the existence of the conversion Reaction (19) from Fe<sub>3</sub>O<sub>4</sub> to iron sulfide. With more H<sub>2</sub>S present in the solution as the reactant, more Fe<sub>3</sub>O<sub>4</sub> was

converted to iron sulfide. In addition, it is important to note that  $\text{Fe}_3\text{O}_4$  did not disappear but was still present even at 2.0 bar  $\text{H}_2\text{S}$  after the 4 day test.

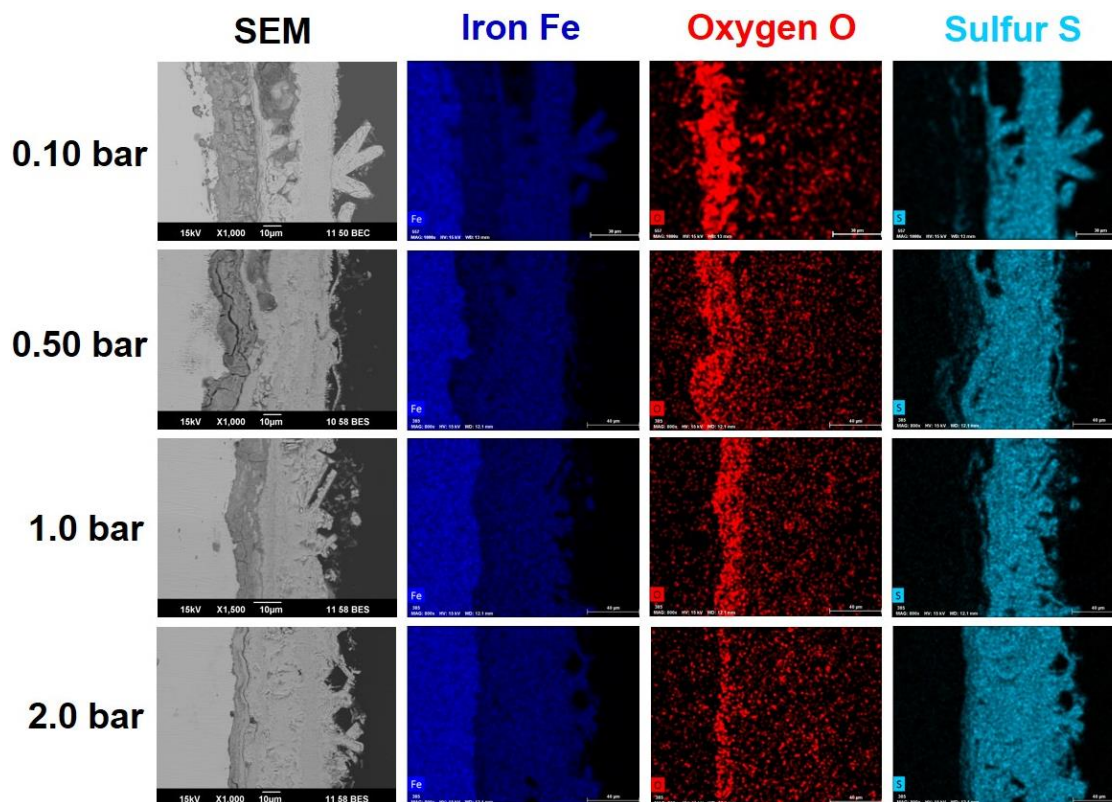


Figure 49. EDS mapping results for Fe, O and S distribution at different  $\text{pH}_2\text{S}$ ,  $T=120^\circ\text{C}$ , initial  $\text{pH}=4.0$ , 4 days.

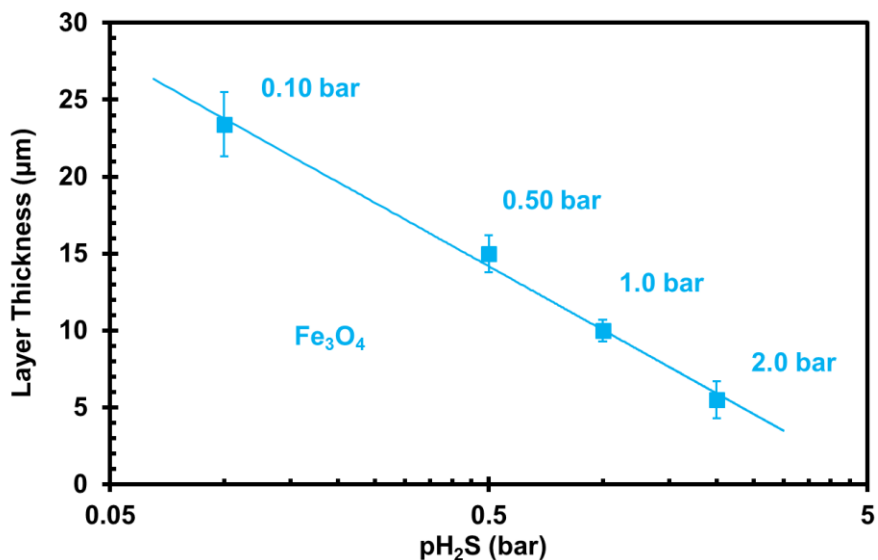


Figure 50. Layer thickness of  $\text{Fe}_3\text{O}_4$  at different  $p_{H_2S}$ ,  $T=120^\circ\text{C}$ , initial  $\text{pH}=4.0$ , 4 days.

**8.3.4 Surface profilometry.** The steel surface was examined using profilometry after removing the corrosion product layers, as shown in Figure 51. For 0.10 bar and 0.50 bar  $\text{H}_2\text{S}$ , with troilite and pyrrhotite formation, the surfaces are relatively smooth. However, at higher  $p_{H_2S}$ , severe localized corrosion occurred, coinciding with pyrite formation. From these images, the maximum calculated pit penetration rate is 6.2 mm/y and 10.1 mm/y at 1.0 bar and 2.0 bar  $p_{H_2S}$ , respectively. This observation of localized corrosion associated with pyrite formation is consistent with Ning's work [79] and previous results shown in Chapter 5 and Chapter 6.

It has been reported that any disruption leading to a discontinuity in the  $\text{FeS}$  layer could result in initiation of localized corrosion. The discontinuity or inhomogeneity in the layer can result from mechanical damage, poor adhesion to the steel surface or transformation to other sulfide phases or polymorphs. The localized corrosion then

precedes due to the galvanic effect between the underlying steel and the conductive iron sulfide layers [25]. In the current study, the disruptions were most likely caused by crystallographic dimensions changes from different iron sulfides (monoclinic for pyrrhotite to cubic for pyrite, for example, also see Figure 47) leading to differences in electrical conductivity. Moreover,  $\text{Fe}_3\text{O}_4$  has been reported to be a very good electrical conductor [9], which means the galvanic effect between the steel and iron sulfide layer was not impaired by  $\text{Fe}_3\text{O}_4$  and consequently the localized corrosion still occurs.

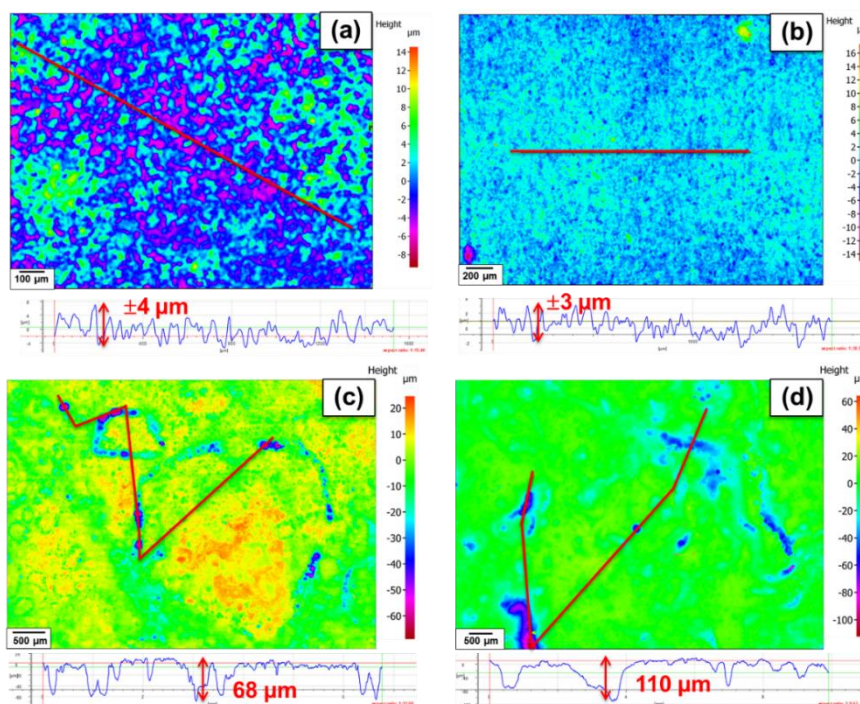


Figure 51. Surface profilometry after removing the corrosion products (a) 0.10 bar  $\text{H}_2\text{S}$ , troilite, (b) 0.50 bar  $\text{H}_2\text{S}$ , pyrrhotite, (c) 1.0 bar  $\text{H}_2\text{S}$  pyrrhotite/pyrite, (d) 2.0 bar  $\text{H}_2\text{S}$ , pyrite.  $T=120^\circ\text{C}$ , initial  $\text{pH}=4.0$ , 4 days.

## 8.4 Summary

The uniform corrosion rate tended to decrease with increasing  $p\text{H}_2\text{S}$ . Similar uniform corrosion behavior was observed in the presence of troilite and pyrrhotite. When pyrite formed, severe localized corrosion was again observed.

The observed iron sulfide formation and transformation with  $p\text{H}_2\text{S}$  at high temperature after 4 days is troilite (0.10 bar)  $\rightarrow$  pyrrhotite (0.50 bar)  $\rightarrow$  pyrrhotite/pyrite (1.0 bar)  $\rightarrow$  pyrite (2.0 bar).

The thickness of  $\text{Fe}_3\text{O}_4$  decreased with increasing  $p\text{H}_2\text{S}$ , which further infers a continuous process of  $\text{Fe}_3\text{O}_4$  formation and conversion to iron sulfide. In addition,  $\text{Fe}_3\text{O}_4$  was continuously observed in every tested condition. Efforts to model corrosion and development of corrosion product layers in high temperature  $\text{H}_2\text{S}$  environments need to take  $\text{Fe}_3\text{O}_4$  into consideration. This is presented in the next two chapters.

## Chapter 9: A Modified Thermodynamic Model for the Prediction of Mild Steel Corrosion Products at High Temperature in H<sub>2</sub>S Environments

### 9.1 Introduction

Predicting the corrosion products is of prime importance to understand the corrosion mechanisms and the protectiveness conferred by the formed layer to the steel underneath. Ning *et al.* [32] built a thermodynamic model, depicted by Pourbaix diagrams, for an Fe-H<sub>2</sub>S-H<sub>2</sub>O system and verified it up to 80°C. Actually, it has also built on literature data that should be valid up to 200°C. Comparisons have also been made with experimental results presented in Chapter 5, Chapter 6, and Chapter 8. The model predicts the most stable corrosion products based on the lowest Gibbs energy – consequently high temperatures does not constitute a limitation per-se as long as the temperature dependency of Gibbs free energy is known. However, based on the available data, Fe<sub>3</sub>O<sub>4</sub> is less stable than iron sulfide and should not show up in a Pourbaix diagram for a Fe-H<sub>2</sub>S-H<sub>2</sub>O system.

For the model to have accuracy over a wide range of conditions, it needs to have strong mechanistic foundations. For the model to have practical applications for corrosion mitigation strategies, it also needs to reflect the phenomena observed within the appropriate time scale. Since Fe<sub>3</sub>O<sub>4</sub> can greatly change the corrosion rate and it seems to be “always” present as an inner corrosion product layer according to the above results, it is necessary to have a “clue” concerning Fe<sub>3</sub>O<sub>4</sub> formation in a Pourbaix diagram at high temperature, even though the theory says it should not be present.

In this Chapter, a longer term (21 days) experiment at a higher temperature (160°C) and higher pH<sub>2</sub>S (2.0 bar) was conducted to further determine if Fe<sub>3</sub>O<sub>4</sub> is still present as a defined corrosion product layer even as exposure time is increased. These experimental conditions were all expected to favor the conversion reaction:



A new thermodynamic model (depicted in Pourbaix diagrams), slightly modified from Ning's model [32], was proposed based on this additional set of experimental data.

## 9.2 Experimental

The experimental setup, material, and procedures were the same as presented in Chapter 5. Operating parameters, such as pH and [H<sub>2</sub>S]<sub>aq</sub>, presented in the test matrix were calculated based on the water chemistry model described in Chapter 4, as summarized in Table 13.

Table 13. Experimental details for Fe<sub>3</sub>O<sub>4</sub> conversion.

Parameter	Description
System	7 L Autoclave
Electrolyte	1 wt.% NaCl
Specimen	API 5L X65
Temperature	160°C
pH <sub>2</sub> S	2.0 bar
Initial pH	4.0
Stirring speed	1000 rpm
Duration	21 days

### 9.3 Results and Discussion

**9.3.1 Does Fe<sub>3</sub>O<sub>4</sub> eventually disappear with longer exposure time?** The cross-section and EDS mapping results for the longer term (21 days) experiment at a higher temperature (160°C) and higher p<sub>H<sub>2</sub>S</sub> (2.0 bar) are shown in Figure 52. Obviously, Fe<sub>3</sub>O<sub>4</sub> was still present as an inner layer (~ 15 μm) after 21 days. This result further demonstrates that Fe<sub>3</sub>O<sub>4</sub> forms continuously at the steel surface even as a higher conversion rate was expected under these conditions (higher temperature and higher p<sub>H<sub>2</sub>S</sub>). After a steady corrosion rate was reached, the Fe<sub>3</sub>O<sub>4</sub> formation rate and conversion rate also become stable and eventually matched each other. Based on these results, it can be concluded that Fe<sub>3</sub>O<sub>4</sub> should always be present as a corrosion product layer in all the tested H<sub>2</sub>S environments at high temperatures, although it is not predicted to be as thermodynamically stable as FeS. Consequently, development of new mechanistic models for iron sulfide corrosion product layers should also consider Fe<sub>3</sub>O<sub>4</sub> since it can greatly change the corrosion rate [80].

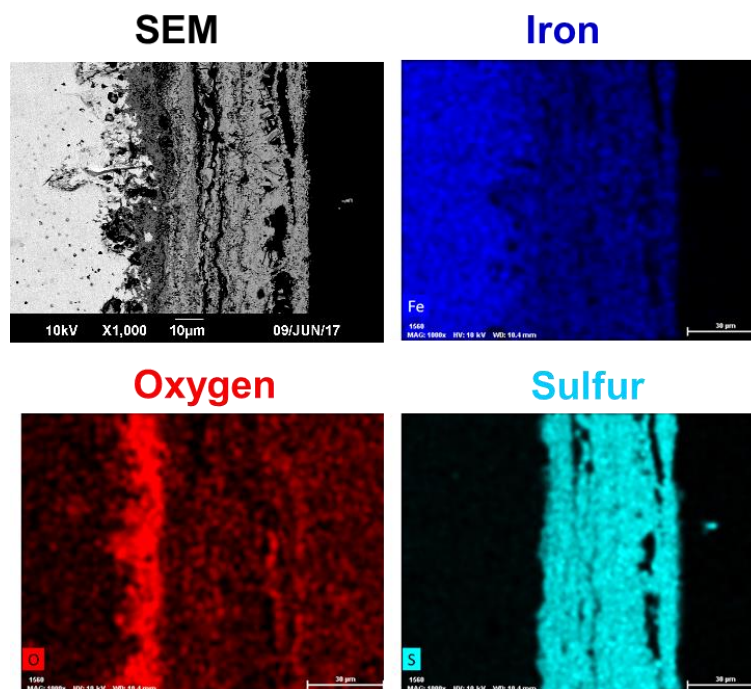


Figure 52. Cross-section and EDS mapping results for Fe, O and S distribution,  $T=160^{\circ}\text{C}$ ,  $\text{pH}_2\text{S}=2.0$  bar, initial  $\text{pH}=4.0$ , 21 days.

**9.3.2 Model modification.** A slightly modified Pourbaix diagram model, compared to the original work from Ning [32] is proposed here. For the outer iron sulfide layer, the Pourbaix diagram is kept the same as Ning reported since the thermodynamic data are valid up to  $300^{\circ}\text{C}$  [32]. Although the most thermodynamically stable forms of iron sulfide are pyrrhotite and pyrite, the user has the possibility to select any type of iron sulfides (mackinawite, troilite, pyrrhotite, and pyrite), because they are kinetically related and time-dependent. Actually, the kinetics of conversion between the different iron sulfides are not well characterized and it is not possible, at this stage, to predict which phases or polymorphs will be present depending on the exposure time and other operating variables. This is an inherent issue, which is also present in Ning's work, with trying to

predict kinetically favored phases (from experimental observations) using a Pourbaix diagram approach.

For the inner  $\text{Fe}_3\text{O}_4$  layer, the proposed modification is to keep the  $\text{Fe}_3\text{O}_4$  formation region (Figure 53(a)) in Fe- $\text{H}_2\text{O}$  system Pourbaix diagram as a dashed zone in Fe- $\text{H}_2\text{S}$ - $\text{H}_2\text{O}$  system Pourbaix diagram (Figure 53(b)). This gives an indication that  $\text{Fe}_3\text{O}_4$  is also kinetically favored at high temperatures near the metal surface, which can greatly affect the corrosion rate. Considering only mackinawite as the iron sulfide corrosion product for simplicity, both  $\text{Fe}_3\text{O}_4$  and mackinawite can form at  $120^\circ\text{C}$  under the operating conditions (represented by the red rectangle) according to Figure 53(c). Figure 53(d) shows that at low temperature,  $25^\circ\text{C}$  for example, the operating conditions are far away from the  $\text{Fe}_3\text{O}_4$  formation region, so an inner  $\text{Fe}_3\text{O}_4$  layer would not be expected.

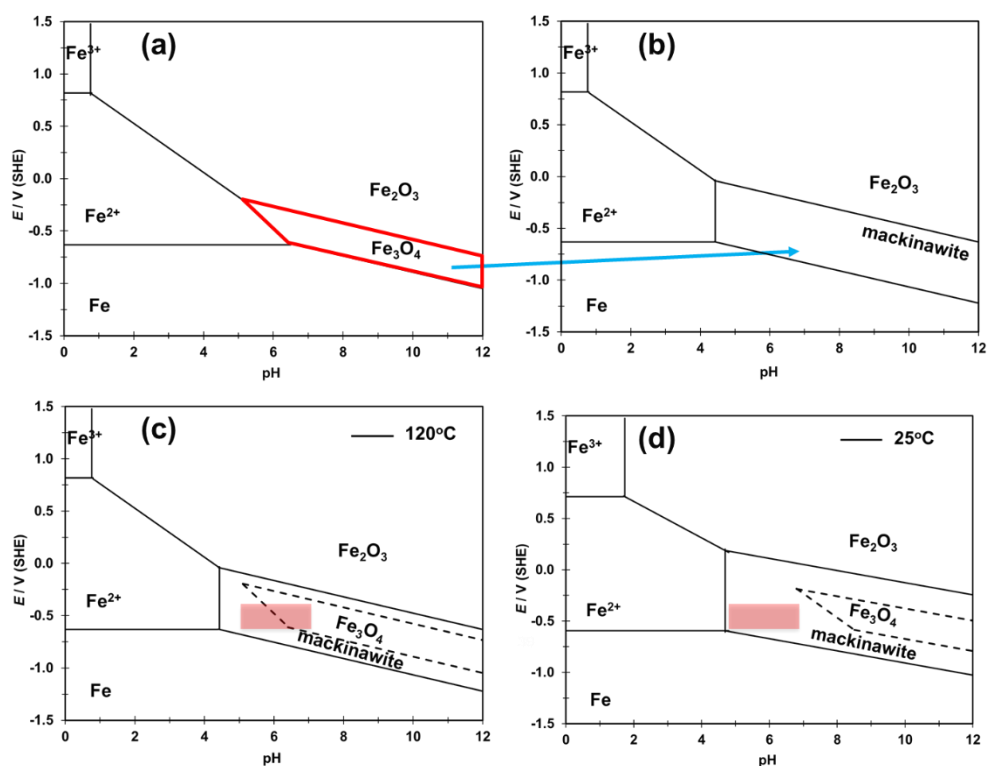


Figure 53 Pourbaix diagrams for (a) Fe-H<sub>2</sub>O system at 120°C; (b) Fe-H<sub>2</sub>S-H<sub>2</sub>O system at 120°C; modified Pourbaix diagrams for (c) Fe-H<sub>2</sub>S-H<sub>2</sub>O system at 120°C; (d) Fe-H<sub>2</sub>S-H<sub>2</sub>O system at 25°C, (b), (c), (d) consider 0.1 bar H<sub>2</sub>S, [Fe<sup>2+</sup>]=5 ppm, and mackinawite only.

Figure 54(a) shows the modified Pourbaix diagram at 120°C by considering all the possible iron sulfides (mackinawite/troilite/greigite/pyrrhotite/pyrite). It can be seen that Fe<sub>3</sub>O<sub>4</sub>, pyrrhotite, and pyrite can form under the operating conditions, which is in good agreement with the above experimental results. Again, corrosion product predictions would not need to be modified at low temperature since the operating conditions are away from the Fe<sub>3</sub>O<sub>4</sub> formation region, as shown in Figure 54(b).

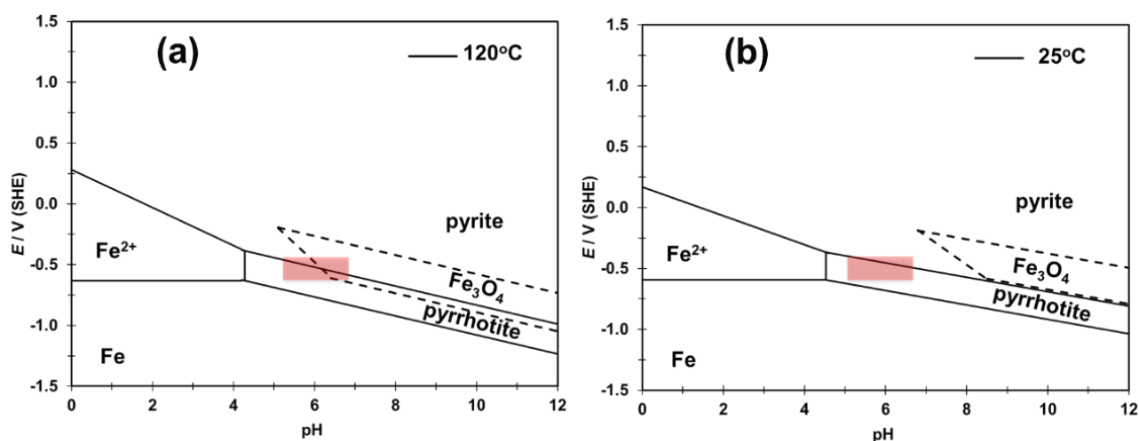


Figure 54. Modified Pourbaix diagrams for Fe-H<sub>2</sub>S-H<sub>2</sub>O system (a) 120°C; (b) 25°C, 0.1 bar H<sub>2</sub>S, [Fe<sup>2+</sup>]=5 ppm, consider mackinawite/troilite/greigite/pyrrhotite/pyrite.

**9.3.3 Model comparison.** The current modified Pourbaix diagram is also compared with two well-known software packages used in industry: Geochemist's Workbench (GWB) and OLI Corrosion Analyzer (OLI), as shown in Figure 55(a) and (b). It can be seen that GWB only predicts pyrrhotite formation and OLI only predicts FeS (unknown phase) and pyrite formation, neither of them has any sign of Fe<sub>3</sub>O<sub>4</sub> formation. Again, these two models are thermodynamically perfectly sound. However, the current modified Pourbaix diagram model would provide an indication of Fe<sub>3</sub>O<sub>4</sub> formation at higher temperatures, which is very helpful for understanding corrosion mechanisms and corrosion product prediction with an increase in temperature.

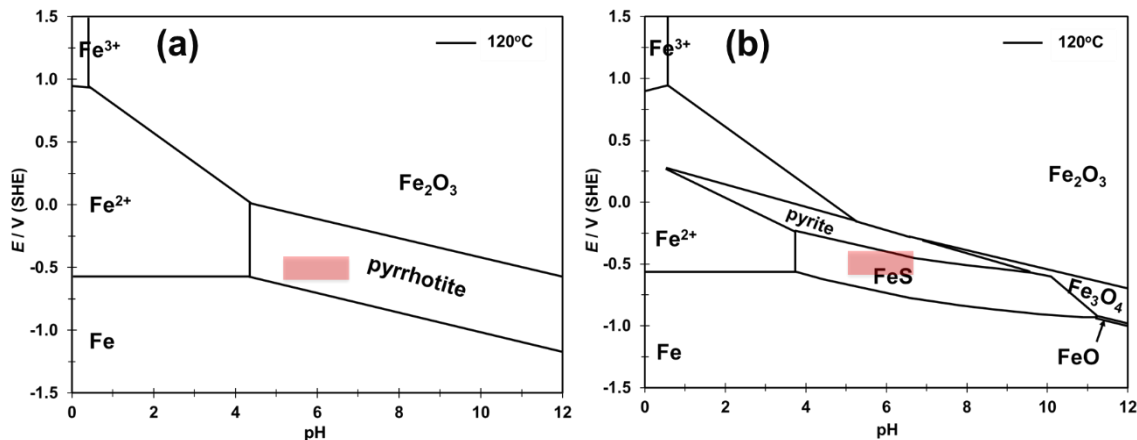


Figure 55. Pourbaix diagrams for Fe-H<sub>2</sub>S-H<sub>2</sub>O system at 120°C generated by (a) the Geochemist's Workbench (GWB) based on thermos.com.V8.R6+.dat; (b) OLI Corrosion Analyzer (OLI), 0.1 bar H<sub>2</sub>S, [Fe<sup>2+</sup>]=5 ppm, consider mackinawite/troilite/greigite/pyrrhotite/pyrite.

## 9.4 Summary

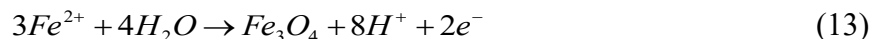
Fe<sub>3</sub>O<sub>4</sub> was always present as an inner layer (~ 15 μm) after 21 days exposure in a 2.0 bar H<sub>2</sub>S environment at 160°C. It seems that after reaching steady state, the formation rate and conversion rate of Fe<sub>3</sub>O<sub>4</sub> become equal.

A modified thermodynamic model (Pourbaix diagram) for high temperature H<sub>2</sub>S corrosion was developed by keeping the Fe<sub>3</sub>O<sub>4</sub> stability zone. It shows a better agreement with the experimental results.

## Chapter 10: A Kinetic Model for the High Temperature Corrosion of Mild Steel in Aqueous H<sub>2</sub>S Environments

### 10.1 Introduction

The current kinetic model is based on Zheng's model [9], which has been verified at low temperatures (< 80°C) and is considered the most advanced mechanistic model to date [65]. Zheng's model calculates the corrosion rate from the current densities related to the anodic and cathodic reactions (summarized in Appendix II). At high temperatures (> 80°C), two more electrochemical reactions were clearly identified in Chapter 7: Fe<sub>3</sub>O<sub>4</sub> formation (oxidation half-reaction) and Fe<sub>3</sub>O<sub>4</sub> conversion to FeS (reduction half-reaction).



In order to know the corrosion rate at high temperature, the electrochemical kinetics of Reaction (13) and (19) must be determined, which are the first two objectives in this chapter. The additional Fe<sub>3</sub>O<sub>4</sub> layer will then be incorporated into Zheng's model.

### 10.2 Electrochemical Kinetics of Fe<sub>3</sub>O<sub>4</sub> Formation

**10.2.1 Introduction.** The kinetics of Fe<sub>3</sub>O<sub>4</sub> formation at high temperature have been studied since the 1980s [81]. It is accepted that the formation of Fe<sub>3</sub>O<sub>4</sub> follows a parabolic time law [81]-[83]:

$$X^2 = K_p t \quad (28)$$

where  $X$  is  $\text{Fe}_3\text{O}_4$  thickness,  $K_p$  is the parabolic constant,  $t$  is the exposure time. Our previous results also confirmed the same phenomenon, as shown in Figure 36. The thickness of  $\text{Fe}_3\text{O}_4$  increased parabolically with time.

However, all the kinetic studies in the open literature focused on the determination of the parabolic constant  $K_p$  [82]-[85]. These results provide no assistance in determining the real-time electrochemical rate at a given  $[\text{Fe}^{2+}]$  and potential. Therefore, several experiments were conducted to determine the electrochemical kinetics of  $\text{Fe}_3\text{O}_4$  formation. The  $\text{Fe}_3\text{O}_4$  formation current can be characterized using potentiodynamic sweeps by changing the concentrations of  $[\text{Fe}^{2+}]$ . This is explained in the following section.

**10.2.2 Experimental.** The experimental details are summarized in Table 14. A 4 L stainless steel autoclave instead of the 7 L Hastelloy autoclave was used to perform the experiments since no  $\text{H}_2\text{S}$  is involved in  $\text{Fe}_3\text{O}_4$  formation Reaction (11). The electrolyte was a deaerated 1 wt% NaCl solution purged by  $\text{N}_2$  with a pH of 4.0. A cylindrical nickel electrode was employed as the working electrode instead of a carbon steel to permit better control the  $\text{Fe}^{2+}$  concentration. A commercial high temperature high pressure (HTHP) Ag/AgCl served as the reference electrode. The counter electrode was a Pt-coated Nb cylinder. A centralized impeller was used to control the flow pattern. Since it is difficult to adjust pH once the autoclave was closed and heated up to high temperature,  $\text{Fe}^{2+}$  (from  $\text{FeCl}_2 \cdot 4\text{H}_2\text{O}$ ) ions were added and pH was adjusted at  $80^\circ\text{C}$  according to the water chemistry model calculation described in Chapter 4. The pH at the experimental

temperatures (120°C and 160°C) was also directly monitored using a commercial Zr/ZrO<sub>2</sub> HTHP pH probe.

Table 14. Experimental details for the kinetics of Fe<sub>3</sub>O<sub>4</sub> formation.

Parameter	Description
System	4 L SS autoclave
Electrolyte	1 wt.% NaCl
Working electrode	Ni
Reference electrode	High temperature Ag/AgCl
Counter electrode	Nb coated with Pt
Temperature	120°C and 160°C
pH	4.0
[Fe <sup>2+</sup> ]	0~50 ppm
Stirring speed	500 rpm and 1000 rpm
Method	Potentiodynamic sweep

When performing the potentiodynamic sweeps, efforts had to be made to isolate the oxidation of Fe<sup>2+</sup> (leading to the formation of Fe<sub>3</sub>O<sub>4</sub>). Anodic polarizations lead to very noisy and unrepeatable results that were attributed to the precipitation of Fe<sub>3</sub>O<sub>4</sub> on the electrode and/or to nickel oxidation. Consequently, it was decided not to polarize anodically from the OCP to avoid these interferences. Instead, it was decided only to polarize cathodically and to evaluate the effect of Fe<sup>2+</sup> oxidation on the total current  $i_{\text{total}} = i_{\text{cathode}} - i_{\text{anode}}$  since the cathodic current, controlled by the hydrogen ion reduction, is well known; the employed methodology is explained in more detail in the following section. The potentiodynamic sweeps were consequently conducted at a scan rate of 1

mV/s, from -0.95 V to open circuit potential (OCP) vs. Ag/AgCl as Reaction (13) is an anodic electrochemical reaction. Above the OCP, Ni dissolution would become significant thus the sweeps were no longer trustworthy and thus not performed.

Before performing the high temperature experiment, the mass transfer characteristics in the 4 L autoclave were fully characterized [86], [87], as described in Appendix III.

**10.2.3 Results and discussion.** As mentioned earlier, the Fe<sub>3</sub>O<sub>4</sub> formation kinetics (through the oxidation of Fe<sup>2+</sup> ions) was not measured directly by performing anodic polarization. Instead, the rate of this reaction was derived through cathodic polarization since measured currents would include contributions from both the reduction of H<sup>+</sup> and the oxidation of Fe<sup>2+</sup> (when Fe<sup>2+</sup> ions were present in the electrolyte).

The cathodic sweeps conducted on a Ni electrode at high temperature with and without adding Fe<sup>2+</sup> are shown in Figure 56. Without Fe<sup>2+</sup>, the charge transfer current and limiting current of H<sup>+</sup> reduction can be clearly observed. The measured cathodic current was all from the H<sup>+</sup> reduction since the contributions from Ni dissolution and H<sub>2</sub>O reduction are negligible at the applied potential range (except below a potential -0.9 V vs. Ag/AgCl sat.):

$$|i_c| = |i_{H^+}| \quad (29)$$

The same cathodic polarization sweeps were performed after adding 25 ppm Fe<sup>2+</sup> and the results were compared with the data obtained without Fe<sup>2+</sup>. In the presence of 25 ppm Fe<sup>2+</sup>, two different electrochemical reactions provide contributions to the total measured cathodic current: the reduction of H<sup>+</sup> and the oxidation of Fe<sup>2+</sup> to form Fe<sub>3</sub>O<sub>4</sub>.

This is demonstrated in Figure 56, where the measured current, in the presence of 25 ppm  $\text{Fe}^{2+}$ , was lower than without  $\text{Fe}^{2+}$  over the range of potentials from -0.64 V to OCP (vs. Ag/AgCl sat.). This difference is due to the presence of an anodic current that partially compensated the total measured cathodic current:

$$|i_c| = |i_{H^+}| - |i_a| \quad (30)$$

As mentioned earlier, the only possible anodic reaction here is the  $\text{Fe}^{2+}$  oxidation associated with the  $\text{Fe}_3\text{O}_4$  formation Reaction (13). Combining Equations (29) and (30), the anodic current can be extracted, as shown in Figure 56. It is represented by the quasi-linear data plot, corresponding to the charge transfer current of Reaction (13).

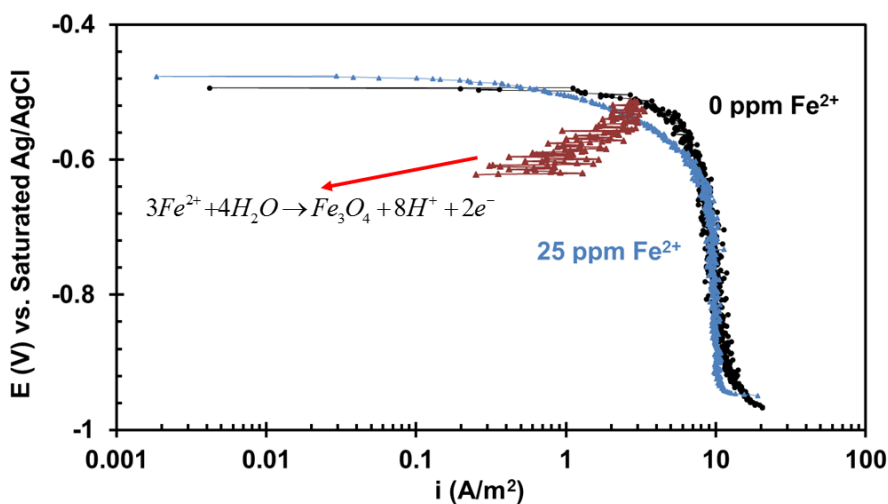


Figure 56. Potentiodynamic sweeps on Ni in 4 L autoclave with and without adding  $\text{Fe}^{2+}$ , 120°C,  $\text{N}_2$ , pH 4.0, 500 rpm.

The experiments were repeated at different rotating speeds and different concentrations of  $\text{Fe}^{2+}$  and the currents corresponding to Reaction (13) were extracted, as

shown in Figure 57. Relatively noisy data were obtained, as expected for high temperature autoclave experiments. However, the basic trends were still distinguishable.

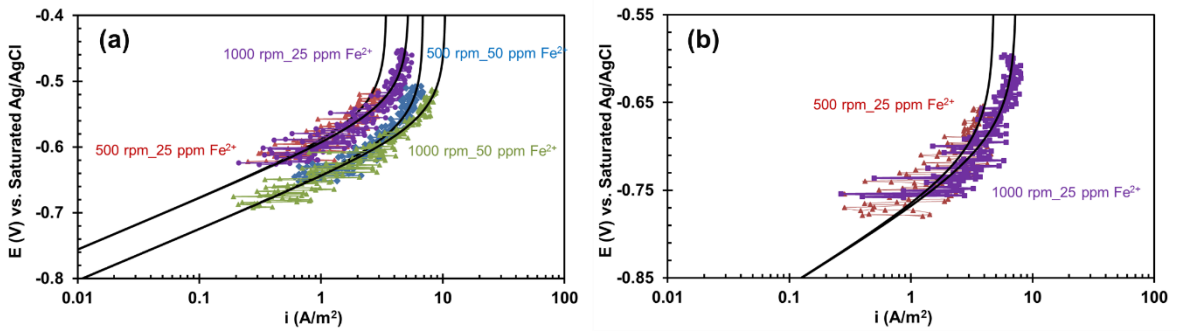


Figure 57. Potentiodynamic sweeps on Ni in 4 L autoclave with different rotating speed and different concentration of  $\text{Fe}^{2+}$ , (a) 120°C, (b) 160°C,  $\text{N}_2$ , pH 4.0, black lines: modelling data.

The current density of  $\text{Fe}_3\text{O}_4$  formation Reaction (13)  $i_{\text{Fe}_3\text{O}_4}$  can be written

following the general form of the Tafel approximation involving two components:

$$\frac{1}{i_{\text{Fe}_3\text{O}_4}} = \frac{1}{i_{\alpha, \text{Fe}_3\text{O}_4}} + \frac{1}{i_{\text{lim}, \text{Fe}^{2+}}^d} \quad (31)$$

where  $i_{\alpha, \text{Fe}_3\text{O}_4}$  is the charge transfer current density ( $\text{A}/\text{m}^2$ ),  $i_{\text{lim}, \text{Fe}^{2+}}$  ( $\text{A}/\text{m}^2$ ) is the diffusion limiting current density for  $\text{Fe}^{2+}$ . The charge transfer current can be calculated by the following equations [9], [88]:

$$i_{\alpha, \text{Fe}_3\text{O}_4} = i_{0, \text{Fe}_3\text{O}_4} \times 10^{\frac{\eta}{b_a}} \quad (32)$$

$$i_{0,Fe_3O_4} = i_0^{ref} \left( \frac{c_{Fe^{2+}}}{c_{Fe^{2+}ref}} \right)^n \times e^{-\frac{\Delta H}{R} \left( \frac{1}{T} - \frac{1}{T_{ref}} \right)} \quad (33)$$

$$b_a = \frac{2.303RT}{\alpha_c F} \quad (34)$$

$$\eta = E - E_0 \quad (35)$$

where  $i_{0,Fe_3O_4}$  (A/m<sup>2</sup>) is the exchange current density,  $\eta$  (V) is the over potential, which is equal to the difference between the applied potential and the reversible potential  $E_{rev}$ ,  $b_a$  is the anodic Tafel slope (V/decade),  $i_0^{ref}$  (A/m<sup>2</sup>) is the reference exchange current density at a reference temperature  $T_{ref}$  (K),  $c_{Fe^{2+}ref}$  (mol/L) is the reference Fe<sup>2+</sup> concentration,  $n$  is the reaction order,  $\Delta H$  (kJ/mol) is the enthalpy of activation for Reaction (13),  $E_0$  (V) is the standard potential.

The diffusion limiting current  $i_{lim,Fe^{2+}}^d$  can be calculated from Equations (36) and (79):

$$i_{lim,Fe^{2+}}^d = k_{m,Fe^{2+}} F c_{Fe^{2+}} \quad (36)$$

where  $k_{m,Fe^{2+}}$  (m/s) is the mass transfer coefficient for Fe<sup>2+</sup> (as determined in Appendix III),  $F$  is Faraday's constant,  $c_{Fe^{2+}}$  Fe<sup>2+</sup> concentration in mol/m<sup>3</sup>. The fitting parameters and modeling results are shown in Table 15 and Figure 57, respectively. Comparing the modeling results shown in the black curves, a relatively good agreement can be observed. Therefore, the electrochemical kinetics of Fe<sub>3</sub>O<sub>4</sub> formation have been determined and modeled.

Table 15. Modeling parameters for Fe<sub>3</sub>O<sub>4</sub> formation Reaction (13).

Parameter	Description
$\Delta H$ , kJ/mol	125.5 [89]
$E_0$ , V	-0.314 [90]
$i_0^{ref}$ , A/m <sup>2</sup>	0.085
$c_{Fe^{2+}ref}$ , mol/L	$1.0 \times 10^{-4}$
$T_{ref}$ , K	293.15
$n$	2
$\alpha_c$	1

### 10.3 Electrochemical Kinetics of Fe<sub>3</sub>O<sub>4</sub> Conversion

**10.3.1 Introduction.** Although the conversion Reaction (19) is mentioned in several recent papers [91]-[93], no detailed kinetic data has been proposed. Similarly, the effects of [H<sub>2</sub>S] and [H<sup>+</sup>] on the exchange current density and reversible potential of the conversion reaction are completely unknown. The following experiments constitute an attempt to determine the electrochemical kinetics of Fe<sub>3</sub>O<sub>4</sub> conversion to FeS.

**10.3.2 Experimental.** A Fe<sub>3</sub>O<sub>4</sub> electrode was acquired to perform the polarization experiments in H<sub>2</sub>S environments since the reaction of interest is the conversion of Fe<sub>3</sub>O<sub>4</sub> to FeS. However, preparing a rotating cylinder electrode (RCE) from Fe<sub>3</sub>O<sub>4</sub> holds many challenges. Alternatively, using a rotating disk electrode (RDE) instead is a lot more convenient since commercial options are available. Student grade bulk Fe<sub>3</sub>O<sub>4</sub> materials (~ 10 cm<sup>3</sup>) were purchased from Ward's Science. The material was carefully ground into a rod shape enabling a tight control over the electrode surface area (~ 0.3 cm<sup>2</sup>). Then, one side of the surface was sputter coated with Au to enhance its conductivity and connected to a wire using silver paste. Finally, the electrode was centrally embedded into a Teflon

holder and sealed with epoxy, leaving only one side exposed to the electrolyte and acting as the working disk electrode, as shown Figure 58. This preparation method was adopted from that described by Esmaeely [94].

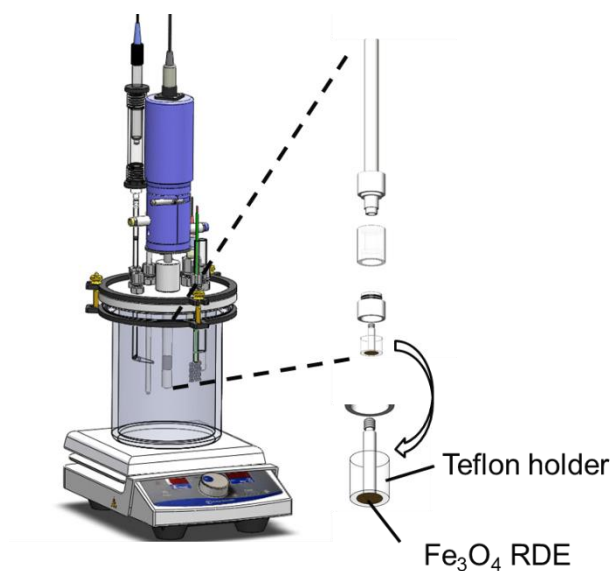


Figure 58. 2 L glass cell Fe<sub>3</sub>O<sub>4</sub> RDE setup.

Since there is no reliable reference electrode at high temperature in H<sub>2</sub>S environments and for safety and practical concerns, the experiments were carried out at low temperatures in a 2 L glass cell, as shown in Figure 58. The findings were then assumed to be valid in high temperature environments. The experimental details are summarized in Table 16. By varying H<sub>2</sub>S and H<sup>+</sup> concentrations, Fe<sub>3</sub>O<sub>4</sub> conversion current (Reaction (19)) could be characterized using potentiodynamic sweeps.



Table 16. Experimental details for Fe<sub>3</sub>O<sub>4</sub> RDE.

Parameter	Description
Electrolyte	1 wt.% NaCl
Working electrode	Fe <sub>3</sub> O <sub>4</sub> RDE
Reference electrode	Saturated Ag/AgCl
Counter electrode	Pt
Temperature	40°C, 80°C
pH	4.0, 5.0
pH <sub>2</sub> S	1%, 5%
Rotation speed	600 rpm, 1200 rpm
Method	Potentiodynamic sweep

Before each experiment, the RDE electrode was polished with 400 and 600 grit sand paper, then thoroughly rinsed with deionized water and isopropanol. The sample was then immediately assembled and put into the deaerated 1 wt.% NaCl solution (the pH and pH<sub>2</sub>S had been adjusted). Potentiodynamic sweeps were then conducted at a scan rate of 1 mV/s (different scan rates, such as 0.333 mV/s, were also tested, the results were consistent), from OCP to ~ 1.1 V vs. Sat. Ag/AgCl.

**10.3.3 Results and discussion.** The RDE glass cell system was first tested using a mild steel API 5L X65 RDE in N<sub>2</sub> purged solution with a pH of 4.0, as the related reactions on X65 are well established under this condition. These tests were performed to gain confidence in this new experimental setup and to validate the results in a well characterized environment. Figure 59 shows the cathodic sweeps on X65 RDE at a 250 and 800 rpm rotation speed. The charge transfer currents were modeled based on a RCE

model [9], while the diffusion limiting currents were calculated from the Levich equation [95]:

$$i_L = (0.620)nFAD^{2/3}\omega^{1/2}\nu^{-1/6}C \quad (37)$$

where  $i_L$  is the diffusion limiting current in  $A/m^2$ ,  $n$  is the number of electrons transferred,  $F$  is Faraday's constant ( $C/mol$ ),  $A$  the electrode area ( $cm^2$ ),  $D$  is the diffusion coefficient ( $cm^2/s$ ),  $\omega$  the angular rotation speed ( $rad/s$ ),  $\nu$  the kinematic viscosity ( $cm^2/s$ ),  $C$  is the reactant concentration ( $mol/cm^3$ ,  $H^+$  in this case).

It can be seen that the experiment results are in good agreement with the model prediction, indicating this system is behaving as expected.

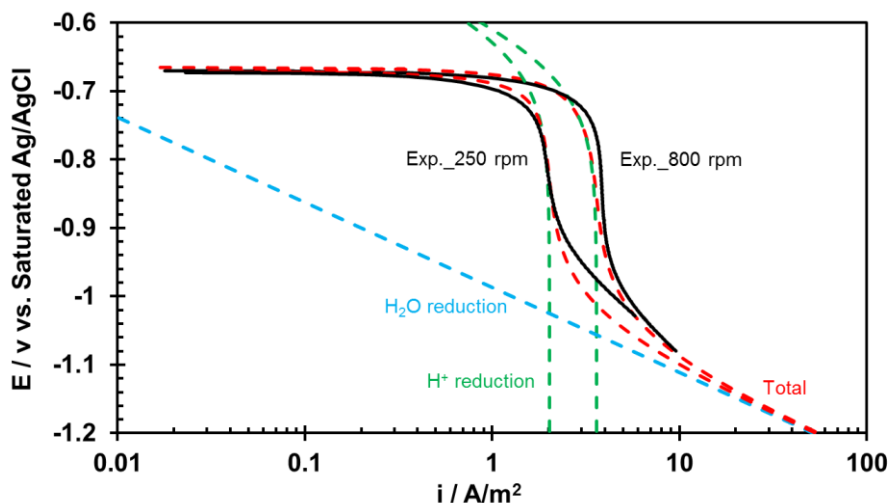


Figure 59. Potentiodynamic sweeps on X65 RDE, 40°C,  $N_2$  purged, pH 4.0, and solid black lines: experiment, dash lines: modeling data.

### Characterization of Fe<sub>3</sub>O<sub>4</sub> electrode

The API 5L X65 electrode was replaced by a Fe<sub>3</sub>O<sub>4</sub> electrode in the following experiments. Figure 60 shows the XRD pattern for the purchased Fe<sub>3</sub>O<sub>4</sub> material. Comparing with the standard data [96], the specimens did not contain any appreciable amount of impurities except at  $2\theta \approx 46^\circ$ . However, no match could be found corresponding to this peak.

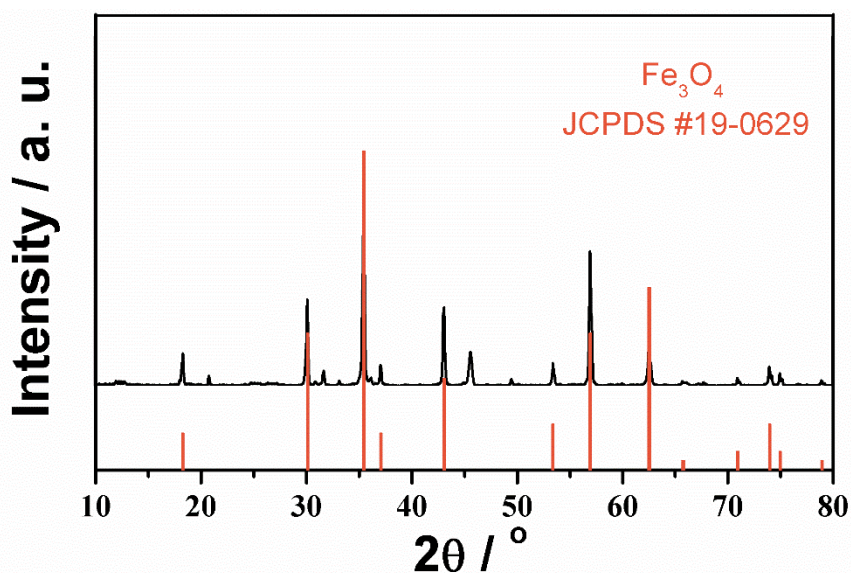
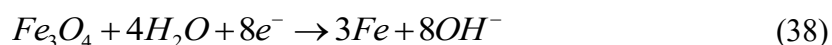


Figure 60. XRD pattern for the purchased Fe<sub>3</sub>O<sub>4</sub> material.

### Preliminary Fe<sub>3</sub>O<sub>4</sub> RDE experiments in N<sub>2</sub> environments

Additional preliminary tests were performed on the Fe<sub>3</sub>O<sub>4</sub> RDE in N<sub>2</sub> purged solution (no H<sub>2</sub>S yet) for comparison and validation purposes. The cathodic sweeps at pH 5.0, 4.0, and 3.0 are shown in Figure 61. The experimental data are somehow difficult to analyze since the nature of the reaction (single or multiple steps) is unknown. In addition,

the kinetics of  $H^+$  or  $H_2O$  reduction on a  $Fe_3O_4$  electrode are also not determined with certainty. For example, the electrochemical reaction corresponding to the linear section of the sweeps, between -0.2 and -0.6 V (vs. Ag/AgCl) is not identified. A current hump is observed between potential -0.65 ~ -0.85 V (vs. Ag/AgCl). This hump seems to respond to changes in rotation speed and pH, as the  $H^+$  reduction reaction is expected to respond. The experimental data are then compared with model predictions of  $H^+$  reduction, assuming kinetic constants valid for a steel electrode. Although the comparison should not be made directly since the electrode material are different, a potential match between the current hump and the limiting current of the  $H^+$  reduction can be inferred. However, the experiment currents are much lower than the modeling currents (established for X65). This could be due to different surface activities (i.e., exchange current density) on the different electrode materials. A similar phenomenon was reported on an iron sulfide electrode [97]. What appears to be the reduction of  $H_2O$  is more easily identified over the more negative values of applied cathodic potentials. Coming back to the linear charge transfer portion of the sweeps between -0.2 and -0.6 V (vs. Ag/AgCl), the corresponding Tafel slope is estimated as high as 1 V/decade, which means this reaction occurs at a low rate. It is hypothesized that this reaction could be linked to the reduction of  $Fe_3O_4$  [98]:



However, the investigation of this reaction is beyond the scope of this study since it is not related to  $Fe_3O_4$  conversion. In addition, the measured currents are much lower than the ones observed in  $H_2S$  environments, as is shown in the next section.

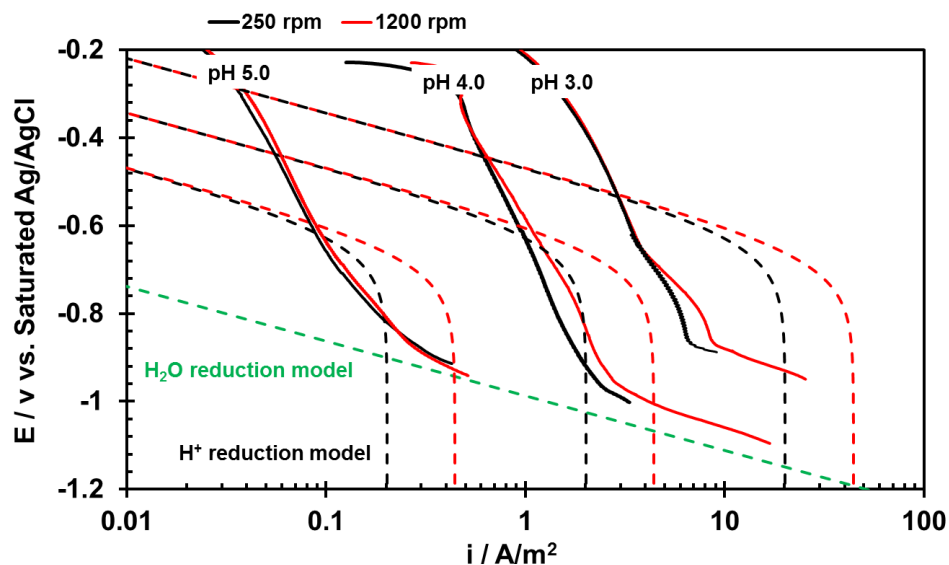


Figure 61. Potentiodynamic sweeps on  $\text{Fe}_3\text{O}_4$  RDE,  $40^\circ\text{C}$ ,  $\text{N}_2$  purged, pH 4.0, and solid lines: experiment, dash lines: modeling data (based on carbon steel electrode).

#### Investigation of the $\text{Fe}_3\text{O}_4$ conversion kinetics in $\text{H}_2\text{S}$ environments

Figure 62(a) shows the sweep after adding 1%  $\text{H}_2\text{S}$  under the same conditions (pH 4.0,  $40^\circ\text{C}$ , and 1200 rpm). The overall current increased by about a factor of five, which confirms that the above mentioned  $\text{Fe}_3\text{O}_4$  reduction current can be neglected. Five reactions can be identified from the sweep curve:

- 1) OCP to  $\sim -0.45$  V, a charge transfer current (not  $\text{Fe}_3\text{O}_4$  reduction);
- 2)  $-0.45$  to  $\sim -0.60$  V, a first diffusion limiting current, this current is dependent on pH, not dependent on  $\text{H}_2\text{S}$ , as shown in Figure 62(b);
- 3)  $-0.60$  to  $\sim -0.65$  V, a second diffusion limiting current, this current is only dependent on  $\text{H}_2\text{S}$ ;

- 4) -0.65 to  $\sim$  -0.80 V, a current hump, which is assumed to be related to the  $H^+$  reduction according to the preliminary study performed in  $N_2$  environment;
- 5) -0.80  $\sim$  -1.3 V, another charge transfer current, according to Figure 62(b), expected to overlap eventually, which should correspond to the  $H_2O$  reduction.

Therefore, it can be concluded that the first three parts of the current are related to the  $Fe_3O_4$  conversion to  $FeS$ : a charge transfer current, an  $H^+$ -dependent limiting current, and an  $H_2S$ -dependent limiting current.

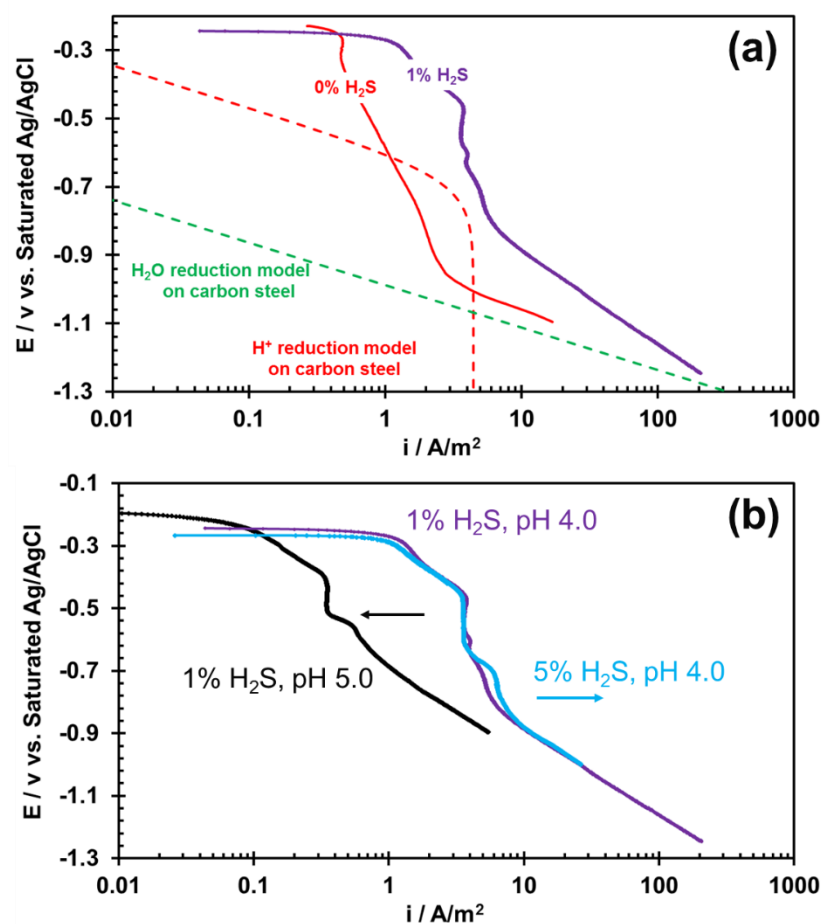


Figure 62. Potentiodynamic sweeps on  $Fe_3O_4$  RDE, 40°C, 1200 rpm, (a) pH 4.0, red: 0%  $H_2S$ , purple: 1%  $H_2S$ , (b) red: 1%  $H_2S$ , pH 4.0, blue: 5%  $H_2S$ , pH 4.0, black: 1%  $H_2S$ , pH 5.0.

After the potentialdynamic sweep, the  $Fe_3O_4$  RDE surface was examined by SEM/EDS, as shown in Figure 63. It can be seen that some tiny film-like structures have formed on the  $Fe_3O_4$  surface. The EDS result demonstrates the film is indeed iron sulfide.

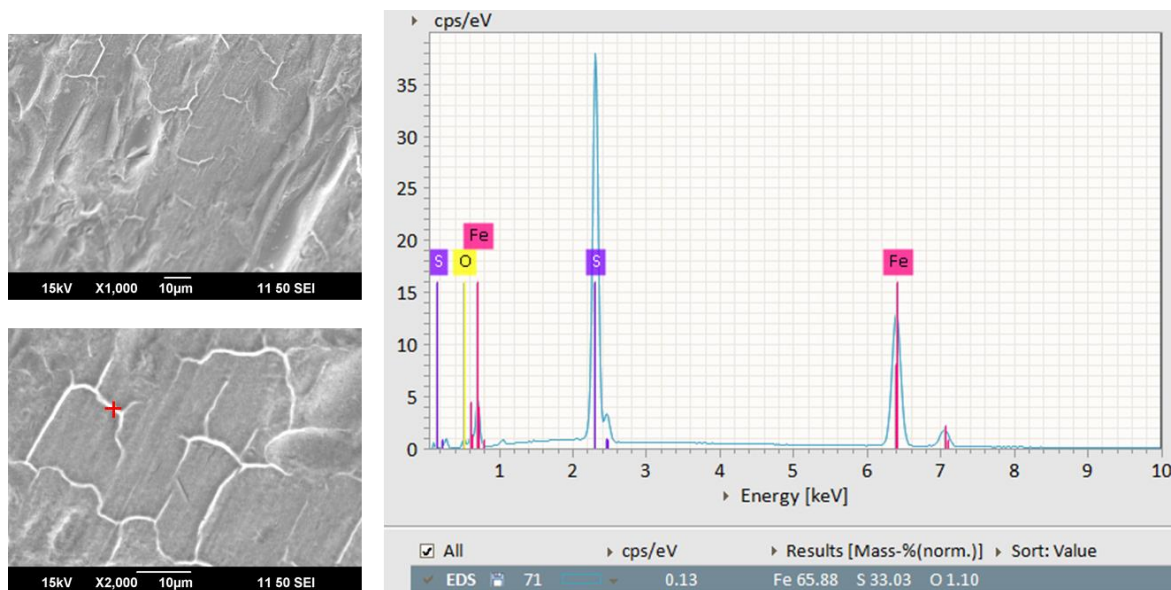


Figure 63. SEM images and EDS results for  $\text{Fe}_3\text{O}_4$  RDE after potentiodynamic sweep in 1%  $\text{H}_2\text{S}$ ,  $40^\circ\text{C}$ , pH 4.0, 1200 rpm.

Although the potentiodynamic sweeps are very useful to determine kinetics data, they can only offer limited clues for the identification of the reactions happening on the electrode surface. The  $\text{H}_2\text{O}$  and  $\text{H}^+$  reduction reactions could be identified with some level of confidence. The mechanisms involved in the  $\text{Fe}_3\text{O}_4$  conversion reaction appear a lot more complicated to determine. A clear dependence of  $\text{H}^+$  and  $\text{H}_2\text{S}$  concentrations could be identified but it is not clear if the  $\text{Fe}_3\text{O}_4$  conversion is a multi-step reaction and what is the nature of these steps. The presence of two limiting currents has traditionally been associated with two different electrochemical reactions [9]. This approach is selected in this work. However, it should be mentioned that a very different mechanism is also possible since the second limiting current could just be associated with the dissociation of  $\text{H}_2\text{S}$  [99]. By themselves, the analysis of the current results are not

sufficient to determine the mechanisms. They are, however, sufficient to develop a kinetic model by mathematically fitting experimental results and model constants. For the sake of simplicity, the presence of two independent electrochemical reactions is assumed. The modeling process is built in analogy with the  $H^+$  and  $H_2S$  reduction processes [9] and only considers the first three reactions that are related to  $Fe_3O_4$  conversion. The  $Fe_3O_4$  conversion current  $i_{FeS}$  is expressed as the sum of  $H^+$ -dependent current  $i_{H^+_d}$  and  $H_2S$ -dependent current  $i_{H_2S_d}$ :



$$i_{FeS} = i_{H^+_d} + i_{H_2S_d} \quad (39)$$

The modeling equations are summarized in Table 17.  $A_1$  and  $A_2$  are fitted correction factors depending on the surface activity of a specific electrode [97]. Other parameters have been defined in Section 10.2.3.

Table 17. Equations used for modeling  $Fe_3O_4$  conversion current.

$H^+$ -dependent current	$H_2S$ -dependent current
$\frac{1}{i_{H^+_d}} = \frac{1}{i_{\alpha,H^+_d}} + \frac{1}{i_{lim,H^+_d}^d} \quad (40)$	$\frac{1}{i_{H_2S_d}} = \frac{1}{i_{\alpha,H_2S_d}} + \frac{1}{i_{lim,H_2S_d}^d} \quad (41)$
$i_{lim,H^+_d}^d = A_1(0.620)nFAD^{\frac{2}{3}}\omega^{\frac{1}{2}}\nu^{\frac{-1}{6}}C_{H^+} \quad (42)$	$i_{lim,H_2S_d}^d = A_2(0.620)nFAD^{\frac{2}{3}}\omega^{\frac{1}{2}}\nu^{\frac{-1}{6}}C_{H_2S} \quad (43)$
$i_{\alpha,H^+_d} = i_{0,H^+_d} \times 10^{\frac{-\eta}{b_a}} \quad (44)$	$i_{\alpha,H_2S_d} = i_{0,H_2S_d} \times 10^{\frac{-\eta}{b_a}} \quad (45)$

Table 17 continued.

$i_{0,H^+_d} = i_0^{ref} \left( \frac{c_{H^+}}{c_{H^+,ref}} \right)^{n_1} \left( \frac{c_{H_2S}}{c_{H_2S,ref}} \right)^{n_2} e^{-\frac{\Delta H}{R} \left( \frac{1}{T} - \frac{1}{T_{ref}} \right)} \quad (46)$	$i_{0,H_2S_d} = i_0^{ref} \left( \frac{c_{H_2S}}{c_{H_2S,ref}} \right)^{n_1} e^{-\frac{\Delta H}{R} \left( \frac{1}{T} - \frac{1}{T_{ref}} \right)} \quad (47)$
$b_a = \frac{2.303RT}{\alpha_c F} \quad (48)$	$b_a = \frac{2.303RT}{\alpha_c F} \quad (49)$
$\eta = E - E_0 \quad (50)$	$\eta = E - E_0 \quad (51)$

Table 18. Fitting parameters for modeling Fe<sub>3</sub>O<sub>4</sub> conversion current.

H <sup>+</sup> -dependent current	H <sub>2</sub> S-dependent current
$A_1 = 0.855$	$A_2 = 0.025$
$n_1 = 1.1, n_2 = 0.7$	$n_1 = 1.5$
$c_{ref, H^+} = 1.0 \times 10^{-4}$ mol/L $c_{ref, H_2S} = 1.0 \times 10^{-4}$ mol/L	$c_{ref, H_2S} = 1.0 \times 10^{-4}$ mol/L
$\alpha_c = 0.5$	$\alpha_c = 1$
$i_0^{ref} = 0.0075$ A/m <sup>2</sup>	$i_0^{ref} = 1.0 \times 10^{-6}$ A/m <sup>2</sup>
$\Delta H = 45$ kJ/mol	$\Delta H = 60$ kJ/mol
$E_0 = -0.4$ V	$E_0 = -0.89$ V

The fitting parameters and modeling results are shown in Table 18 and Figure 64. A relatively good agreement can be observed between every experiment and model. The model covers different pH, pH<sub>2</sub>S, rotation speed, and temperature values. The electrochemical kinetics of Fe<sub>3</sub>O<sub>4</sub> conversion are consequently determined although it is acknowledged that little is known about the actual reactions occurring on the metal surface.

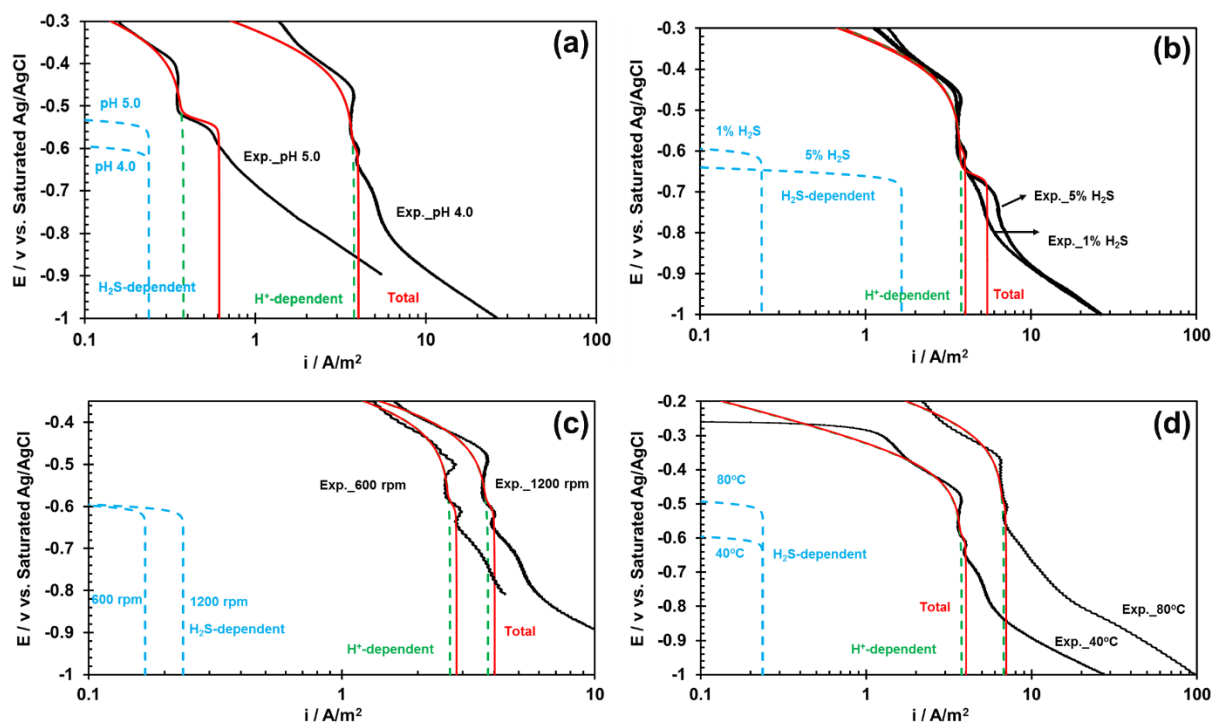


Figure 64. Modeling results for  $Fe_3O_4$  conversion, (a) different pH: pH 5.0 and 4.0, 40°C, 1%  $H_2S$ , 1200 rpm; (b) different  $H_2S$ : 1% and 5%, 40°C, pH 4.0, 1200 rpm; (c) different rotation speed: 600 and 1200 rpm, 40°C, pH 4.0, 1%  $H_2S$ ; (d) different temperature: 40°C and 80°C, pH 4.0, 1%  $H_2S$ , 1200 rpm. Black solid lines: experimental data, the rest are modeling data.

#### 10.4 Model Construction

One of the main deliverables of this study is to incorporate the effect of high temperature to the already existing  $CO_2/H_2S$  corrosion model, initially developed by Zheng [9]. This model includes all the relevant electrochemical reactions in addition to predictions of surface chemistry and formation of corrosion product layers.

**10.4.1 Review of Zheng’s model.** As mentioned earlier, the current kinetic model is based on Zheng’s model [9]. This model can predict the corrosion rates of mild steel in the presence or absence of a corrosion product layer. A brief review of this model is presented below.

Model without corrosion product

By ignoring the presence of corrosion product layers, the model can be used to predict the initial corrosion rate on a bare steel surface. The model still considers the gradient of species concentration between the bulk and the surface, as shown graphically in Figure 65. The model only considers the concentrations of species in the bulk solution  $c_{\text{bulk},j}$  and at the steel surface  $c_{\text{surface},j}$ . Consequently, it is labelled as the “2-nodes” model. The bulk concentration  $c_{\text{bulk},j}$  can be easily calculated by a water chemistry model. For the surface concentration  $c_{\text{surface},j}$ , the following mass conservation equation is used:

$$\frac{\partial c_{\text{surface},j}}{\partial t} = \frac{N_{\text{in},j} - N_{\text{out},j}}{\delta} + R_j \quad (52)$$

where  $N_{\text{in},j}$  is the mass transfer flux from bulk solution,  $N_{\text{out},j}$  is the flux of species due to electrochemical reactions at the steel surface,  $\delta$  is the thickness of the mass transfer boundary layer,  $R_j$  the production term due to homogeneous chemical reactions for species  $j$ . Once  $c_{\text{surface},j}$  is known, the corrosion rate without a corrosion product layer can be obtained using a well-established electrochemical model (summarized in Appendix II).

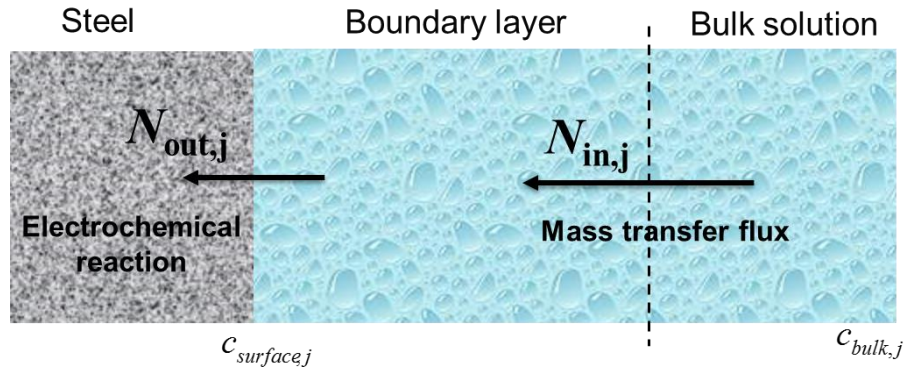


Figure 65. Zheng's model construction without a corrosion product layer.

#### Model with corrosion product

As corrosion proceeds, corrosion product layers can form on the metal surface, affecting the rate of metal dissolution. The model can predict this effect and determine the trend of corrosion rate with time as well as calculate a steady state value. To do so, an additional node is added to take into account the presence of the iron sulfide corrosion product layer, as shown in Figure 66. The calculation method for the determination of  $c_{bulk,j}$  and  $c_{scale,j}$  is still the same as without a corrosion product layer, described above. The additional concentration at the steel surface  $c_{surface,j}$  can be calculated based on a modified expression of the mass conservation equation:

$$\frac{\partial \varepsilon c_{surface,j}}{\partial t} = \frac{N_{b,j} - N_{out,j}}{\Delta x} + R_j \quad (53)$$

where  $\varepsilon$  is the porosity of the corrosion product layer,  $N_{b,j}$  is the flux of species due to mass transfer from boundary layer to the corrosion product layer,  $\Delta x$  is the thickness of the corrosion product layer,  $R_j$  the production term including homogeneous chemical

reactions for species  $j$  and the precipitation of iron sulfide layer. This model has been verified up to 80°C.

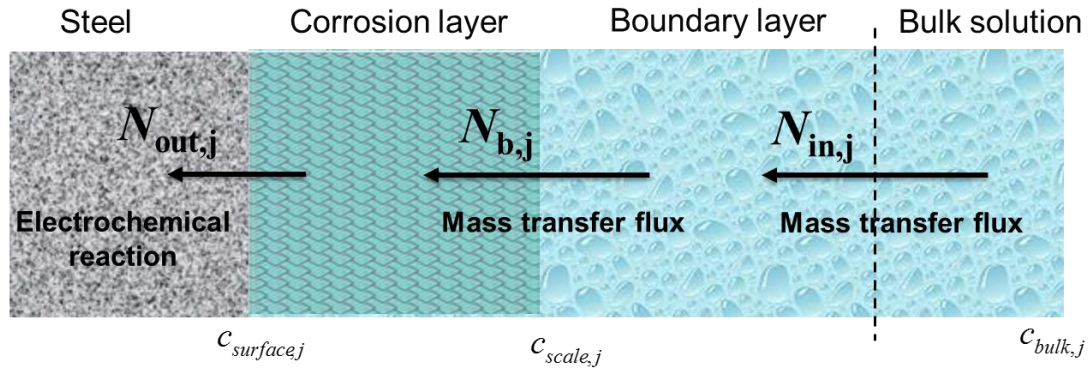


Figure 66. Zheng's model construction with a corrosion product layer.

**10.4.2 Current model construction.** Several modifications were made to Zheng's model in order to incorporate the effect of high temperature. As defined from this research, the main addition is the formation of an inner  $\text{Fe}_3\text{O}_4$  which comes into play at high temperatures ( $> 80^\circ\text{C}$ ). Therefore, one more node is included to account for the  $\text{Fe}_3\text{O}_4$  layer, as shown in Figure 67. The same method can be used as the above described "3-nodes" model to calculate  $c_{bulk,j}$ ,  $c_{scale,j}$ , and  $c_{surface,j}$ . The concentration at the steel surface  $c_{steel,j}$  can be calculated via the same mass conservation equation:

$$\frac{\partial \varepsilon' c_{surface,j}}{\partial t} = \frac{N'_{in,j} - N'_{out,j}}{\Delta x'} + R_j \quad (54)$$

where  $\varepsilon'$  is the porosity for the  $\text{Fe}_3\text{O}_4$  layer,  $N'_{in,j}$  is the mass transfer flux from the iron sulfide layer,  $N'_{out,j}$  is the flux of species due to electrochemical reactions at the steel surface,  $\Delta x'$  is the thickness of the  $\text{Fe}_3\text{O}_4$  layer.

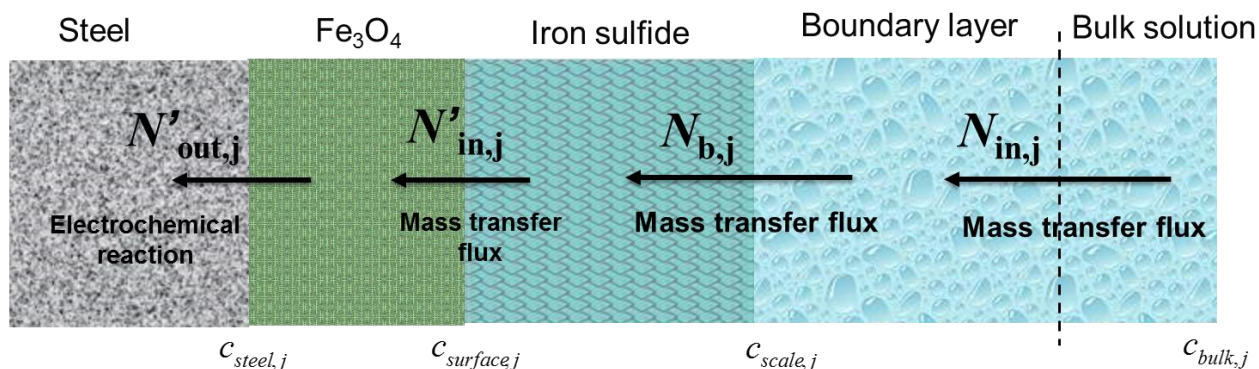


Figure 67. Current “4-nodes” model construction with two corrosion product layers.

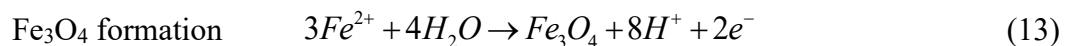
The addition of the 4<sup>th</sup> node is expected to complicate the model and calculation process to some extent. However, a few assumptions can be made for simplification purpose:

1. At the steel surface, for  $c_{steel,j}$ , only  $Fe^{2+}$ ,  $H^+$ ,  $OH^-$ ,  $Na^+$ , and  $Cl^-$  are considered.

The concentration of sulfide species [ $H_2S$ ], [ $HS^-$ ], and [ $S^{2-}$ ] are assumed to be zero since no sulfur has ever been detected in the  $Fe_3O_4$  layer through EDS analysis.

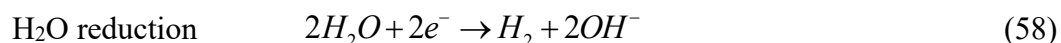
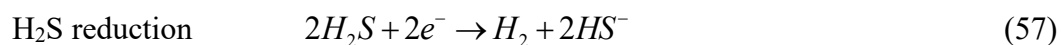
The sulfide species could have been completely consumed at the  $Fe_3O_4/FeS$  interface due to conversion Reaction (19). Therefore, the  $H_2S$  reduction reaction is assumed not to occur at this node, while the  $Fe_3O_4$  formation Reaction (13) is indeed considered.

Reactions considered at steel surface:



2. At the  $Fe_3O_4/FeS$  interface, the iron dissolution reaction does not need to be considered since iron dissolution only happens at the steel surface. However, the conversion Reaction (17) needs to be added.

Reactions considered at the  $Fe_3O_4/FeS$  interface (only (59) is not an electrochemical reaction):



The calculation parameters, such as Tafel slopes and reaction orders, for the above electrochemical reactions are summarized in Appendix II.

3. For the formation of an iron sulfide layer, only mackinawite (conversion + precipitation) is considered since the transformation kinetics among the different iron sulfides is a complex subject and are still completely unknown [100]-[102]. What is known now at high temperature is that similar uniform corrosion behavior was observed in the presence of mackinawite, troilite, and pyrrhotite, while severe localized corrosion occurred with pyrite formation according to the results presented in Chapter 5, 6, and 8.

## 10.5 Model Implementation

The mass conservation equations represented in equation (53) can be simplified following several assumptions. The derivations of these equations follow a calculation scheme initially proposed by Zheng [9]. Only the additions to Zheng's model are shown here while the original relevant equations are only briefly summarized here. A full derivation of these equations can be found in Appendix IV.

Original simplified equations at steel surface (no CO<sub>2</sub> or HAc), corresponding to the steel surface in Figure 66

(F1): H<sup>+</sup> conservation

$$0 = -(i_{H^+} + i_{H_2S} + i_{H_2O})/F + k_{m_{H^+}}(c_{H^+}_b - c_{H^+}_s) + k_{m_{H_2S}}(c_{H_2S}_b - c_{H_2S}_s) - k_{m_{S^{2-}}}(c_{S^{2-}}_b - c_{S^{2-}}_s) - k_{m_{OH^-}}(c_{OH^-}_b - c_{OH^-}_s)$$

(F2): H<sub>2</sub>O dissociation

$$c_{H^+}_s * c_{OH^-}_s \approx K_{Wa}$$

(F3): H<sub>2</sub>S conservation

$$0 = k_{m_{H_2S}}(c_{H_2S}_b - c_{H_2S}_s) + k_{m_{HS^-}}(c_{HS^-}_b - c_{HS^-}_s) + k_{m_{S^{2-}}}(c_{S^{2-}}_b - c_{S^{2-}}_s)$$

(F4): HS<sup>-</sup> equilibrium

$$c_{H^+}_s * c_{HS^-}_s = K_{hs} * c_{H_2S}_s$$

(F5): S<sup>2-</sup> equilibrium

$$c_{H^+}_s * c_{S^{2-}}_s = K_{bs} * c_{HS^-}_s$$

(F6): Fe<sup>2+</sup> conservation

$$0 = \frac{i_{Fe}}{2F} + k_{m_{Fe^{2+}}}(c_{Fe^{2+}}_b - c_{Fe^{2+}}_s)$$

where  $c_{j\_b}$  is the concentration of species  $j$  in the bulk solution,  $c_{j\_s}$  is that at the steel surface,  $k_{m\_j}$  is the total mass transfer coefficient through the boundary layer and iron sulfide layer.

New equations at  $Fe_3O_4/FeS$  interface (no Fe dissolution  $i_{Fe}$ , consider  $Fe_3O_4$  conversion  $i_{FeS}$ ), corresponding to the  $Fe_3O_4/FeS$  interface in Figure 67

(F1'):  $H^+$  conservation

$$0 = -(i_{H^+} + i_{H_2S} + i_{H_2O} + \frac{5i_{FeS}}{2})F + k_{m\_H^+}(c_{H^+\_b} - c_{H^+\_m}) + k_{m\_H_2S}(c_{H_2S\_b} - c_{H_2S\_m}) - k_{m\_S^{2-}}(c_{S^{2-}\_b} - c_{S^{2-}\_m}) - k_{m\_OH^-}(c_{OH^-\_b} - c_{OH^-\_m}) - k'_{m\_H^+}(c_{H^+\_m} - c_{H^+\_s}) + k'_{m\_OH^-}(c_{OH^-\_m} - c_{OH^-\_s})$$

(F2'):  $H_2O$  dissociation

$$c_{H^+\_m} * c_{OH^-\_m} \approx K_{Wa}$$

(F3'):  $H_2S$  conservation

$$0 = k_{m\_H_2S}(c_{H_2S\_b} - c_{H_2S\_m}) + k_{m\_HS^-}(c_{HS^-\_b} - c_{HS^-\_m}) + k_{m\_S^{2-}}(c_{S^{2-}\_b} - c_{S^{2-}\_m})$$

(F4'):  $HS^-$  equilibrium

$$c_{H^+\_m} * c_{HS^-\_m} = K_{hs} * c_{H_2S\_m}$$

(F5'):  $S^{2-}$  equilibrium

$$c_{H^+\_m} * c_{S^{2-}\_m} = K_{bs} * c_{HS^-\_m}$$

(F6'):  $Fe^{2+}$  conservation

$$0 = -k'_{m\_Fe^{2+}}(c_{Fe^{2+}\_m} - c_{Fe^{2+}\_s}) + k_{m\_Fe^{2+}}(c_{Fe^{2+}\_b} - c_{Fe^{2+}\_m})$$

Additional equations at steel surface (consider Fe dissolution  $i_{Fe}$  and  $Fe_3O_4$  formation  $i_{Fe_3O_4}$ ), corresponding to the steel surface in Figure 67

(F7'):  $H^+$  conservation

$$0 = \frac{4i_{\text{Fe}_3\text{O}_4}}{F} + k'_{m_{\text{H}^+}} (c_{\text{H}^+_s} - c_{\text{H}^+_m}) - k'_{m_{\text{OH}^-}} (c_{\text{OH}^-_s} - c_{\text{OH}^-_m})$$

(F8'): H<sub>2</sub>O dissociation

$$c_{\text{H}^+_s} * c_{\text{OH}^-_s} \approx K_{\text{Wa}}$$

(F9'): Fe<sup>2+</sup> conservation

$$0 = \frac{i_{\text{Fe}} - 3i_{\text{Fe}_3\text{O}_4}}{2F} + k'_{m_{\text{Fe}^{2+}}} (c_{\text{Fe}^{2+}_s} - c_{\text{Fe}^{2+}_m})$$

where  $c_{j\_b}$  is the concentration of species  $j$  in the bulk solution,  $c_{j\_m}$  is that at Fe<sub>3</sub>O<sub>4</sub>/FeS interface (middle layer),  $c_{j\_s}$  is that at the steel surface,  $k_{m\_j}$  is the total mass transfer coefficient through the boundary layer and iron sulfide layer,  $k'_{m\_j}$  is that through the Fe<sub>3</sub>O<sub>4</sub> layer.

There are 9 equations (F1'~F9') and 9 unknowns ( $c_{\text{Fe}^{2+}_m}$ ,  $c_{\text{H}^+_m}$ ,  $c_{\text{OH}^-_m}$ ,  $c_{\text{H}_2\text{S}_m}$ ,  $c_{\text{HS}^-_m}$ ,  $c_{\text{S}^{2-}_m}$ ,  $c_{\text{Fe}^{2+}_s}$ ,  $c_{\text{H}^+_s}$ ,  $c_{\text{OH}^-_s}$ ). The calculation process is the same as for Zheng's model [9]. First, the pH at the Fe<sub>3</sub>O<sub>4</sub>/FeS interface ( $c_{\text{H}^+_s}$ ) is guessed, then equations (F2'~F9') become linear and are solved using LU decomposition. Then, the solutions are substituted in (F1') and an iterative process, using the bisection method, is performed until (F1') is satisfied.

The precipitation rate, porosity, and mass transfer characteristics of the mackinawite layer have been addressed in the original model. The only difference is that Fe<sub>3</sub>O<sub>4</sub> conversion also contributes to mackinawite layer growth rather than solely precipitation. For the new Fe<sub>3</sub>O<sub>4</sub> layer, similar equations can be derived.

The formation rate of Fe<sub>3</sub>O<sub>4</sub> ( $R_{\text{Fe}_3\text{O}_4}$ ) in mol/m<sup>2</sup>/s can be obtained from:

$$R_{Fe_3O_4} = \frac{i_{Fe_3O_4}}{2F} \quad (60)$$

This can be converted to mm/yr by:

$$R_{Fe_3O_4} (mm / yr) = \frac{0.001 \times 365 \times 24 \times 3600 M_{Fe_3O_4} R_{Fe_3O_4}}{(1 - \varepsilon) \rho_{Fe_3O_4}} \quad (61)$$

where  $M_{Fe_3O_4}$  and  $\rho_{Fe_3O_4}$  are the molar mass (g/mol) and density (kg/m<sup>3</sup>) of Fe<sub>3</sub>O<sub>4</sub>, respectively. The porosity  $\varepsilon$  of the Fe<sub>3</sub>O<sub>4</sub> layer can be calculated from Equation (69) in successive time steps [103]:

$$\frac{\partial \varepsilon}{\partial t} = CR \frac{1 - \varepsilon}{\Delta x} - \frac{M_{Fe_3O_4} \varepsilon^2 (1 - \varepsilon)}{\rho_{Fe_3O_4} \Delta x} R_{Fe_3O_4} \quad (62)$$

where  $CR$  is the corrosion rate (mm/yr, needs to convert to m/s in calculation), 50,000 is used for  $\frac{1}{\Delta x}$  in the model [9].

The mass transfer coefficient  $k'_{m,j}$  (m<sup>2</sup>/s) through the Fe<sub>3</sub>O<sub>4</sub> layer is then calculated as:

$$k'_{m,j} = \frac{\varepsilon \tau D_j}{\Delta l} \quad (63)$$

where  $\tau$  tortuosity is the square root of porosity  $\varepsilon$  [104],  $D_j$  is the diffusion coefficient of species  $j$ ,  $\Delta l$  is the thickness increment of Fe<sub>3</sub>O<sub>4</sub> layer in time step  $\Delta t$  (s), given as:

$$\Delta l = \frac{0.001 \times R_{Fe_3O_4} (mm / yr) \times \Delta t}{365 \times 24 \times 3600} \quad (64)$$

The overall procedure to implement the model is done in successive time steps.

First, the initial corrosion rate without a corrosion product layer is calculated based on the

input water chemistry (T, pH,  $p\text{H}_2\text{S}$ , etc.). Then, the corrosion product layer growth model is invoked. The growth rate, porosity, tortuosity, thickness, mass transfer coefficient, etc., of the two layers ( $\text{Fe}_3\text{O}_4$  and mackinawite) are calculated. After that, the mass conservation equations ( $F1'$ ) ~ ( $F9'$ ) are solved. Finally, the corrosion rate for the next time step is calculated.

### 10.6 Model Verification

In this section, the corrosion rates predicted by the model are compared with the experimental results presented in Chapter 5, 6, and 8. Unfortunately, there is only limited high temperature  $\text{H}_2\text{S}$  corrosion data in the open literature that can be used for comparison. Moreover, some discrepancies between the experiment results and model predictions are fully expected. This is not surprising considering the difficulty to control and measured experimental conditions in high temperature  $\text{H}_2\text{S}$  corrosion environments.

Figure 68 shows the corrosion rates measured by LPR, predicted by the current model and Zheng's model at  $120^\circ\text{C}$  with 0.1 bar  $\text{H}_2\text{S}$ . It can be seen that the current model is more capable of predicting the fast decrease of the initial corrosion rate, while predictions from Zheng's model do not capture this trend. This is attributed to the fast formation kinetics of  $\text{Fe}_3\text{O}_4$  layer at high temperature, which is not considered in Zheng's model. The later part of the corrosion rate trend is well predicted by both models, especially the final stable value. This is also as expected because the rates of  $\text{Fe}_3\text{O}_4$  formation and conversion can be essentially equal at steady state, i.e., the effect of  $\text{Fe}_3\text{O}_4$  cancels out. In terms of uniform corrosion, it seems that the significance of  $\text{Fe}_3\text{O}_4$  layer only appears at the initial corrosion stage. Consequently, previous model predictions

(such as Zheng's model, FREECORP™, and MULTICORP™) may still apply without taking  $\text{Fe}_3\text{O}_4$  into account. However, whether this is true for  $\text{CO}_2$ -containing environments is far from being clear because the layer structure and interaction between  $\text{Fe}_3\text{O}_4$  and  $\text{FeCO}_3$  are not as well understood [27] as that in  $\text{H}_2\text{S}$  only environments investigated in this study. In addition, the occurrence of localized corrosion should be strongly dependent on the layer closer to the steel substrate – hence highlighting the importance of capturing the real corrosion mechanism.

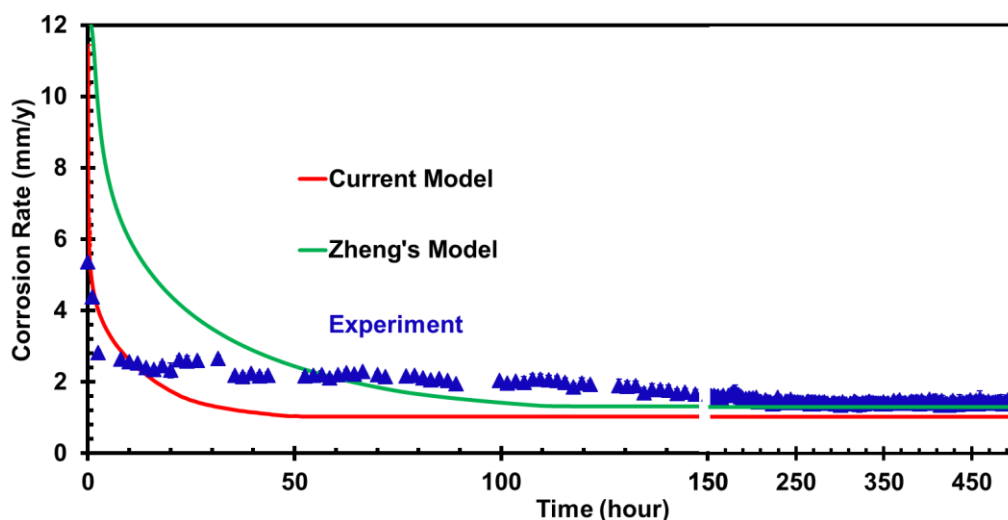


Figure 68. Current model prediction compared with experiment results and Zheng's model, 120°C, 0.1 bar  $\text{H}_2\text{S}$ , pH 4.0, 21 days.

Figure 69 shows the thickness of  $\text{Fe}_3\text{O}_4$  and iron sulfide layers predicted by the current model. Compared with the experimental results, the model also indicates that the  $\text{Fe}_3\text{O}_4$  layer quickly reaches a stable thickness ( $\sim 37 \mu\text{m}$ ). However, the model seems to slightly overpredict the experimental results ( $\sim 25 \mu\text{m}$ ). The thickness of the outer iron

sulfide layer gradually grows with increasing time which is in agreement with the experimental results. The current model only considers mackinawite as the iron sulfide layer while troilite, pyrrhotite, and pyrite were observed in the experiments. This may explain the observed discrepancies between theoretical and experimental layer thicknesses.

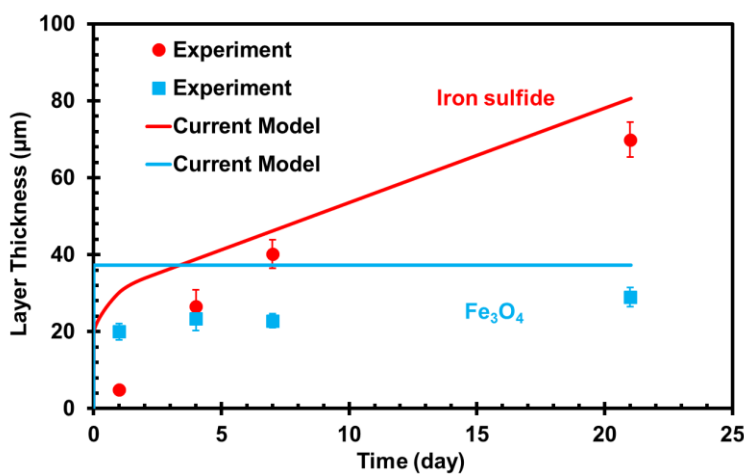


Figure 69. Layer thickness from experimental results and current model predictions, 120°C, 0.1 bar H<sub>2</sub>S, pH 4.0.

The experimental results and model predictions at different temperatures are shown in Figure 70. The model can predict the general decreasing trend of the corrosion rate at every temperature. Good agreement can be observed at 120°C and 160°C. At 80°C, the predicted stable corrosion rate (~2.5 mm/y) is lower than the experimental results (~4 mm/y). This can probably be attributed to the absence of any significant Fe<sub>3</sub>O<sub>4</sub> layer formation at that lower temperature (80°C). In this case, the original Zheng's model

would provide a better prediction. At 200°C, the experimental corrosion rates are a little bit higher than the predicted ones, most likely due to severe localized corrosion observed under this condition.

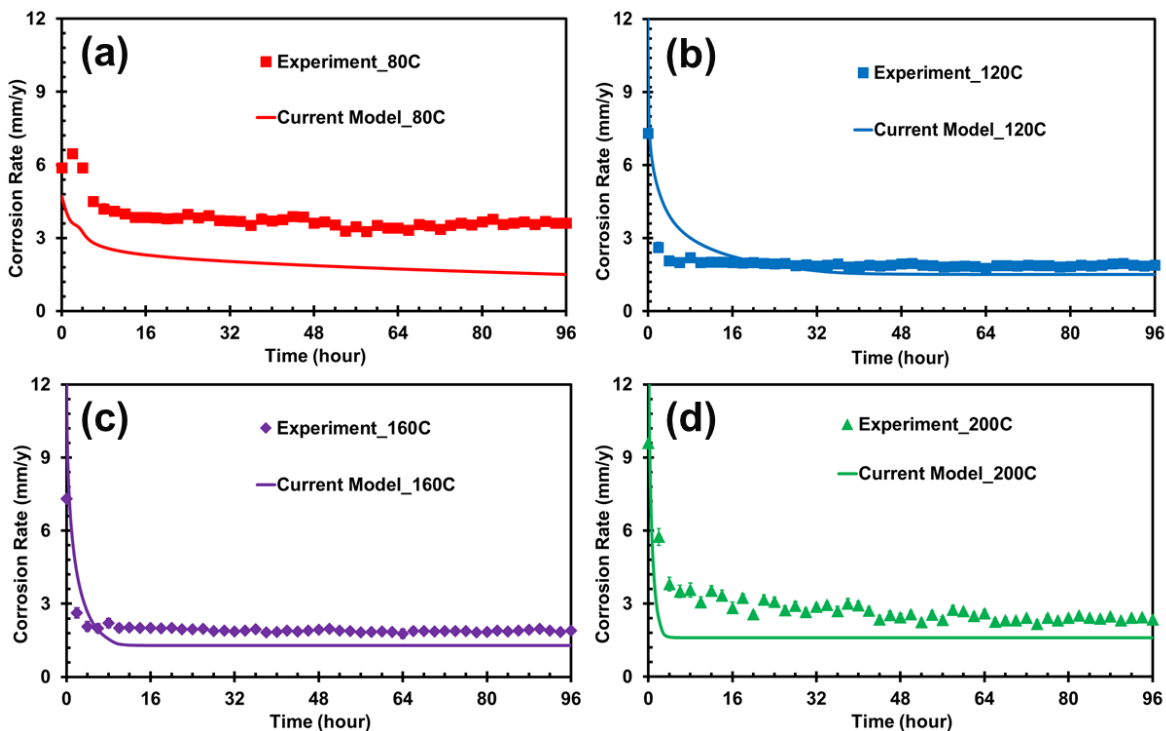


Figure 70. Experiment results (left) compared with current model predictions (right) at different temperatures, 0.1 bar H<sub>2</sub>S, pH 4.0, 4 days, (a) 80°C, (b) 120°C, (c) 160°C, (d) 200°C.

Figure 71 shows the experiment results and model predictions at different pH<sub>2</sub>S values. The general decreasing trends with increasing pH<sub>2</sub>S are also in good agreement with the experiment results except at 2.0 bar H<sub>2</sub>S with localized corrosion (and to some degree at 1.0 bar H<sub>2</sub>S after 40 h) when localized corrosion was also observed.

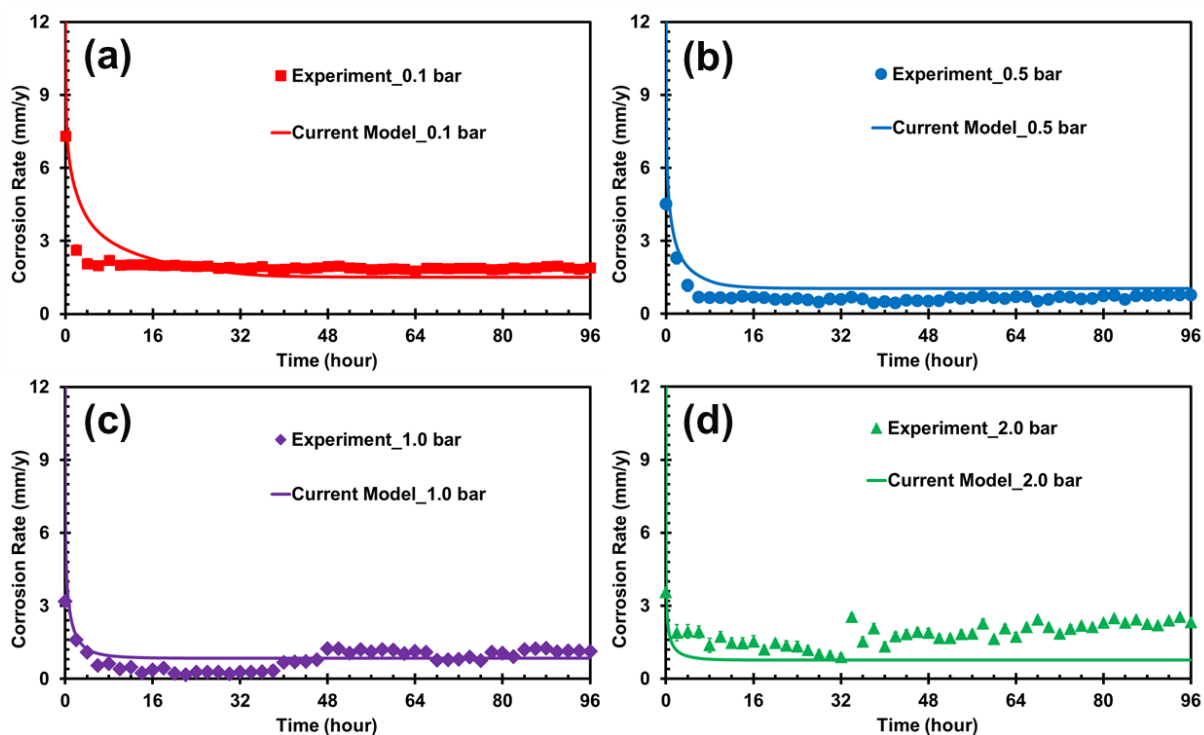


Figure 71. Experiment results compared with current model predictions with different  $p\text{H}_2\text{S}$ ,  $120^\circ\text{C}$ ,  $\text{pH } 4.0$ , 4 days, (a) 0.1 bar, (b) 0.5 bar, (c) 1.0 bar, (d) 2.0 bar.

Figure 72 shows the predicted  $\text{Fe}_3\text{O}_4$  layer thickness gradually decreases with increasing  $p\text{H}_2\text{S}$ , inferring that the rate of conversion of  $\text{Fe}_3\text{O}_4$  to  $\text{FeS}$  increases with increasing  $p\text{H}_2\text{S}$ . The decreasing trend is in good agreement with experimental results.

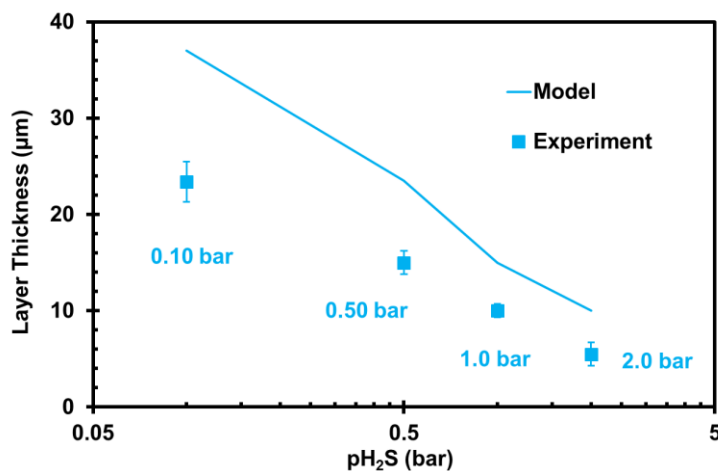


Figure 72. Layer thickness from experiment results and current model predictions at different pH<sub>2</sub>S, 120°C, pH 4.0, 4 days.

### Pros

- A unique two-layer corrosion kinetic model was successfully established and validated for high temperature H<sub>2</sub>S environments.
- The model is able to predict the corrosion rate trend at high temperature, covering the effect of temperature and pH<sub>2</sub>S.

### Cons (limitations)

Discrepancies between model predictions and experimental results can be attributed to several assumptions and model limitations:

- The kinetics of all the electrochemical reactions (except Fe<sub>3</sub>O<sub>4</sub> formation) have not been verified at high temperatures (> 80°C). Moreover, the experiments for Fe<sub>3</sub>O<sub>4</sub> formation were performed on a Ni surface rather than on a carbon steel surface. Considering that the surface activity on these different electrodes is likely

to be different, the  $\text{Fe}_3\text{O}_4$  formation reaction kinetics may require further validation.

- The bulk solution is still treated as an open system, i.e., constant pH and  $[\text{Fe}^{2+}]$ , which is not the same situation for a closed system in the autoclave. The pH and  $[\text{Fe}^{2+}]$  in the autoclave are changing during the experiment.
- The current model only considers mackinawite as the iron sulfide corrosion product layer. However, other iron sulfides such as troilite and pyrrhotite can also rapidly form at high temperature, which could influence the mass transfer and electrochemical reactions and consequently the corrosion rate.
- At higher temperature ( $200^\circ\text{C}$ ) and higher  $\text{pH}_2\text{S}$  (1.0 and 2.0 bar), pyrite can readily form which leads to localized corrosion. The current model does not predict the thickness loss due to localized corrosion.
- Iron sulfide precipitation consumes  $\text{Fe}^{2+}$  and  $\text{S}^{2-}$  ions, but the original (Zheng's) model does not include this sink term due to precipitation in the mass conservation equation. The same is true for the current model, which could affect the prediction to some extent.

### 10.7 A Parametric Study

A parametric study of this model is presented in this section to gain a better understanding of the effects of temperature,  $\text{pH}_2\text{S}$ , and pH on  $\text{H}_2\text{S}$  corrosion at high temperature.

Figure 73 illustrates the effect of high temperature on the corrosion rate predicted by the current model. It is known that temperature can accelerate both the corrosion rate

and the layer formation rate. From Figure 73, the initial corrosion rate decreases faster with increasing temperature, indicating a quicker semi-protective layer formation rate at higher temperatures. Then, the final stable corrosion rate is slightly higher at higher temperatures, implying faster corrosion kinetics at higher temperatures.

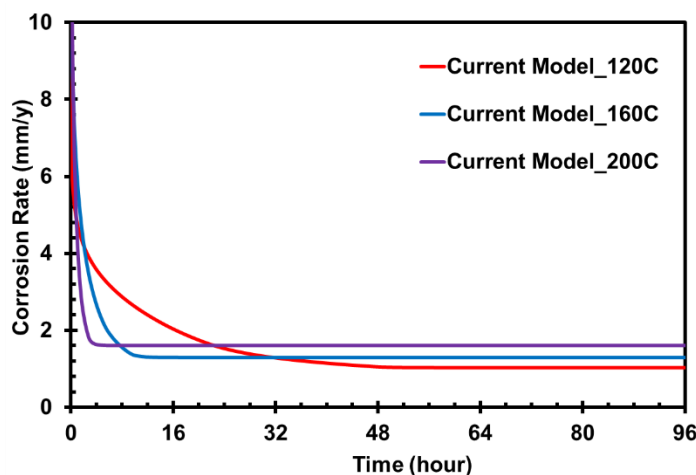


Figure 73. Effect of high temperature on the corrosion rate from current model predictions, 0.1 bar H<sub>2</sub>S, pH 4.0, 4 days.

The predicted effect of pH<sub>2</sub>S on corrosion rate is shown in Figure 74. As discussed in Section 8.1, H<sub>2</sub>S plays a dual role: it both accelerates the corrosion rate by enhancing the cathodic reaction (H<sub>2</sub>S reduction) and retards the corrosion rate due to iron sulfide layer formation. At low temperature, it was observed that the initial corrosion rate increases with increasing pH<sub>2</sub>S, while the stable corrosion rate decreases at higher pH<sub>2</sub>S because a more protective iron sulfide gradually forms [9]. However, at high temperature, it seems that the effect of layers formation (both Fe<sub>3</sub>O<sub>4</sub> and iron sulfide) takes a dominant

role almost immediately. Thus, the increase in corrosion rate due to the presence of H<sub>2</sub>S is not observed. All the corrosion rates decrease rapidly to a stable value. At higher pH<sub>2</sub>S, the initial corrosion rate decreases quicker and ends up with a lower stable corrosion rate.

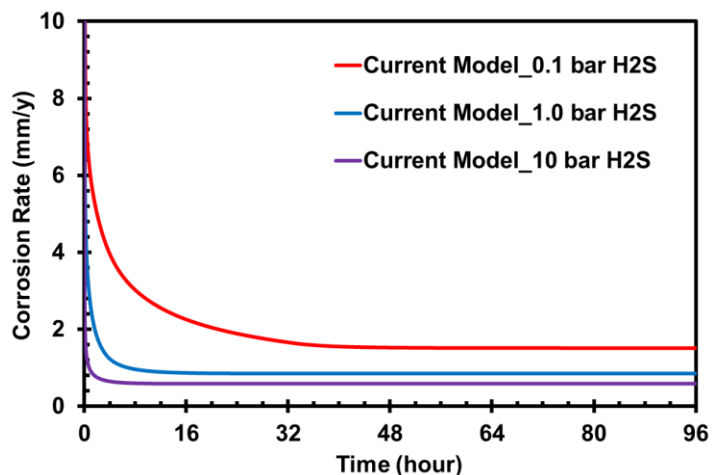


Figure 74. Effect of pH<sub>2</sub>S on the corrosion rate from current model predictions, 120°C, pH 4.0, 4 days.

Figure 75 shows the predicted corrosion rates at different pH values. As explained earlier, it is extremely difficult to control the pH at high temperature in the autoclave. H<sup>+</sup> ions can also accelerate the corrosion rate by enhancing the cathodic reaction (H<sup>+</sup> reduction). On the other hand, H<sup>+</sup> concentration can also significantly affect the saturation value of iron sulfide. Higher pH results in higher saturation value and consequently higher layer formation rate. As shown in Figure 75, with increasing pH, the corrosion rate decreases quickly and stabilizes at lower values, indicating faster iron

sulfide corrosion product layer formation at higher pH. A similar effect of pH was also observed at low temperature [9].

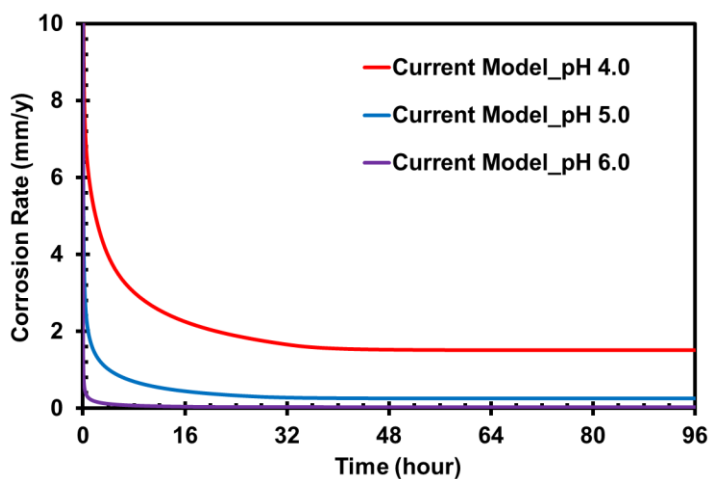


Figure 75. Effect of pH on the corrosion rate from current model predictions, 120°C, 0.1 bar H<sub>2</sub>S, 4 days.

### 10.8 Summary

The electrochemical kinetics of Fe<sub>3</sub>O<sub>4</sub> formation and conversion were determined based on experimental data. A two-layer kinetic model was successfully established based on Zheng's model. The high temperature H<sub>2</sub>S corrosion model can predict the general trend of the corrosion rate at different temperature, pH<sub>2</sub>S, and pH values.

## Chapter 11: Conclusions and Future Work

### 11.1 Conclusions

An innovative set of experiments were performed in an autoclave to investigate the mechanisms of aqueous corrosion of mild steel in H<sub>2</sub>S environments at high temperatures. The following observations could be made based on the experimental findings:

#### Corrosion product layer formation

- The observed iron sulfide formation and transformation sequence at high temperature is: mackinawite → troilite → pyrrhotite → pyrite. With the increase of temperature (80°C~200°C), time (1~21 days), and p<sub>H<sub>2</sub>S</sub> (0.10~2.0 bar), iron sulfide transformed to more thermodynamically stable phases.
- Due to its higher saturation value, thermodynamic less stable Fe<sub>3</sub>O<sub>4</sub> can also form as an inner layer in H<sub>2</sub>S environment at high temperatures (> 80°C).
- Fe<sub>3</sub>O<sub>4</sub> experiences a simultaneous and continuous process of formation at the steel/magnetite interface and conversion to mackinawite at the magnetite/mackinawite interface.

#### Corrosion rate

- Similar uniform corrosion behavior was observed in the presence of mackinawite, troilite, and pyrrhotite. Severe localized corrosion occurred with pyrite formation.
- Both the Fe<sub>3</sub>O<sub>4</sub> and mackinawite layers are responsible for the decrease of the corrosion rate in the first day, but most of the corrosion protection can be attributed to the Fe<sub>3</sub>O<sub>4</sub> layer.

The following modeling activities were completed in order to update the corrosion prediction model:

### *Modeling*

- A modified thermodynamic model (Pourbaix diagram) was developed to indicate  $\text{Fe}_3\text{O}_4$  formation.
- The electrochemical kinetics of  $\text{Fe}_3\text{O}_4$  formation and conversion were determined and modeled.
- An additional  $\text{Fe}_3\text{O}_4$  layer was successfully added into the previous mechanistic kinetic model. The model can predict the general decreasing trend of the corrosion rate at high temperature, covering different temperature,  $\text{pH}_2\text{S}$ , and pH values.

### **11.2 Future Work**

Some recommendations for future work are listed as follows:

- The effect of  $\text{CO}_2$  on  $\text{H}_2\text{S}$  corrosion at high temperature can be further investigated since oil and gas reservoirs also contain  $\text{CO}_2$ . The interaction among  $\text{Fe}_3\text{O}_4$ ,  $\text{FeS}$ , and  $\text{FeCO}_3$  is of great interest. Studies are recommended on how these corrosion products affect the corrosion rate and how they modify the kinetic model.
- The iron sulfide transformation mechanisms are still not clear. In this work, the XRD only detects a few microns of the outer most iron sulfide layer, the phase of the rest iron sulfide layer is not identified. Moreover, the conversion mechanism from  $\text{Fe}_3\text{O}_4$  to  $\text{FeS}$  is also a recommended topic for future work.

- Development of a reference electrode for high temperatures in H<sub>2</sub>S environments.

Due to the lack of a reliable reference electrode, the corrosion potential and pH were not monitored during the experiments. More information could be obtained if a reliable reference electrode is available. In addition, the validity of the electrochemical models such as Fe dissolution and H<sub>2</sub>S reduction at high temperature needs to be verified.

## References

1. G. Koch, J. Varney, N. Thompson, O. Moghissi, M. Gould, J. Payer, International Measures of Prevention, Application, and Economics of Corrosion Technologies Study, 2016.
2. M. B. Kermani, D. Harrop, The Impact of Corrosion on Oil and Gas Industry, SPE-29784-PA, 1996, 11, 186-190,
3. G. Koch, M. Brongers, N. Thompson, Y. Virmani, J. Payer, Corrosion Costs and Preventive Strategies in the United States, FWHA-RD-01-156, U.S. Department of Transportation, Federal Highway Administration, 2002.
4. L. T. Popoola, A. S. Grema, G. K. Latinwo, B. Gutti, A. S. Balogun, Corrosion problems during oil and gas production and its mitigation, International Journal of Industrial Chemistry, 2013, 4, 35.
5. B. Hou, X. Li, X. Ma, C. Du, D. Zhang, M. Zheng, W. Xu, D. Lu, F. Ma, The Cost of Corrosion in China, npj Materials Degradation 1, 2017, 4.
6. S. N. Smith, M. W. Joosten, Corrosion of Carbon Steel by H<sub>2</sub>S in CO<sub>2</sub> Containing Oilfield Environments, CORROSION 2006, paper no. 06115, Houston, TX, 2006.
7. F. Meyer, O. Riggs, R. McGlasson, J. Sudbury, Corrosion products of mild steel in hydrogen sulfide environments, Corrosion, 1958, 14(2), 109-115.
8. W. Sun, Kinetics of Iron Carbonate and Iron Sulfide Scale Formation in CO<sub>2</sub>/H<sub>2</sub>S Corrosion, Ph.D. thesis, Dept. of Chem. Eng., Ohio University, Athens, OH, 2006.
9. Y. Zheng, Electrochemical Mechanism and Model of H<sub>2</sub>S Corrosion of Carbon Steel, Ph.D. thesis, Dept. of Chem. Eng., Ohio University, Athens, OH, 2014.

10. J. Ning, The Role of Iron Sulfide Polymorphism in Localized Corrosion of Mild Steel, Ph.D. thesis, Dept. of Chem. Eng., Ohio University, Athens, OH, 2015.
11. Y. Liu, Z. Zhang, N. Bhandari, Z. Dai, F. Yan, G. Ruan, A. Y. Lu, G. Deng, F. Zhang, H. Al-Saiari, A. T. Kan, M. B. Tomson, New Approach to Study Iron Sulfide Precipitation Kinetics, Solubility, and Phase Transformation, *Industrial & Engineering Chemistry Research*, 2017, 56(31), 9016-9027.
12. X. H. Zhao, Y. Han, Z. Q. Bai, B. Wei, The Experiment Research of Corrosion Behaviour about Ni Based Alloys in Simulant Solution Containing H<sub>2</sub>S/CO<sub>2</sub>, *Electrochimica Acta*, 2011, 56, 7725-7731.
13. S. S. Prabha, Corrosion problems in petroleum industry, *European Chemical Bulletin*, 2014, 3(3), 300-307.
14. J. Sun, C. Sun, X. Lin, X. Cheng, H. Liu, Effect of chromium on corrosion behavior of P110 steels in CO<sub>2</sub>-H<sub>2</sub>S environment with high pressure and high temperature, *Materials*, 2016, 9, 200.
15. G. DeBruijn, High-pressure, High-temperature Technologies, *Oilfield Review*, 2008, 20, 46-60.
16. A. Zhong, Challenges for High-Pressure High-Temperature Applications of Rubber Materials in the Oil and Gas Industry, *Residual Stress, Thermomechanics & Infrared Imaging, Hybrid Techniques and Inverse Problems, Volume 9*, Springer, 2016.
17. W. D. Grimes, R. I. McNeil, Prediction of Hydrogen Sulfide and Carbon Dioxide in HPHT Wells, *SPE HPHT Advanced Technology Symposium*, paper no. SPE 97568, Woodlands, TX, 2005.

18. A. Shadravan, M. Amani, HPHT 101-What Petroleum Engineers and Geoscientists Should Know About High Pressure High Temperature Wells Environment, *Energy Science and Technology*, 2012, 4, 36-60.
19. S. Ramachandran, C. Menendez, V. Jovancicevic, J. Long, Film persistency of new high temperature water-based batch corrosion inhibitors for oil and gas wells, *Journal of Petroleum Exploration and Production Technology*, 2012, 2, 125-131.
20. B. Laurent, R. Harrington, B. Bennett, Development of test methods and factors for 304 evaluation of oilfield corrosion inhibitors at high temperature, *CORROSION* 2017, paper no. 9780, New Orleans, LA, 2017.
21. E. B. Backensto, R. D. Drew, C. C. Stapleford, High Temperature Hydrogen Sulfide Corrosion, *Corrosion*, 1956, 12(1), 22-32.
22. A. V. Skalunov, G. V. Sretenskaya, G. A. Tsarkov, Effect of Hydrogen Sulfide and Temperature on the Corrosion Behavior of High-alloy Metals in Precipitation Baths for Viscose Manufacture, *Fibre Chemistry*, 1987, 18(4), 321-325.
23. Y. Qi, H. Luo, S. Zheng, C. Chen, Z. Lv, M. Xiong, Effect of Temperature on the Corrosion Behavior of Carbon Steel in Hydrogen Sulphide Environments, *International Journal of Electrochemical Science*, 2014, 9, 2101-2112.
24. S. N. Esmaeely, W. Zhang, B. Brwon, M. Singer, S. Nestic, Localized corrosion of mild steel in marginally sour environments, *Corrosion*, 2017, 73(9), 1098-1106.
25. S. N. Esmaeely, G. Bota, B. Brown, S. Nestic, Influence of Pyrrhotite on the Corrosion of Mild Steel, *Corrosion*, 2017, 74(1), 37-49.

26. W. Zhang, B. Brown, D. Young, S. Netic, M. Singer, Factors Influencing Localized Corrosion of Mild Steel in Marginally Sour Environments, CORROSION 2018, paper no. 10984, Phoenix, AZ, 2018.
27. T. Tanupabrunsun, Thermodynamics and Kinetics of Carbon Dioxide Corrosion of Mild Steel at Elevated Temperatures, Ph.D. thesis, Dept. of Chem. Eng., Ohio University, Athens, OH, 2013.
28. A. Ikeda, M. Ueda, S. Mukai, CO<sub>2</sub> Corrosion Behavior and Mechanism of Carbon Steel and Alloy Steel, CORROSION 1983, paper no. 45, Anaheim, CA, 1983.
29. D. W. Shannon, Role of Chemical Components in Geothermal Brines on Corrosion, CORROSION 1978, paper no. 78057, Katy, TX, 1978.
30. G. Lin, M. Zheng, Z. Bai, X. Zhao, Effect of Temperature and Pressure on the Morphology of Carbon Dioxide Corrosion Scales, Corrosion, 2006, 62(6), 501-507.
31. Z. F. Yin, Y. R. Feng, W. Z. Zhao, Z. Q. Bai, G. F. Lin, Effect of temperature on CO<sub>2</sub> corrosion of carbon steel, Surface and Interface Analysis, 2009, 41(6), 517-523.
32. J. Ning, Y. Zheng, B. Brown, D. Young, S. Netic, A Thermodynamic Model for the Prediction of Mild Steel Corrosion Products in an Aqueous Hydrogen Sulfide Environment, Corrosion, 2015, 71(8), 945-960.
33. W. Sun, D. V. Pugh, S. N. Smith, S. Ling, J. L. Pacheco, R. J. Franco, A Parametric Study of Sour Corrosion of Carbon Steel, CORROSION 2010, paper no. 10278, San Antonio, TX, 2010.

34. Y. Zheng, J. Ning, D. Young, B. Brown, S. Netic, Mechanistic Study of the Effect of Iron Sulfide Layers on Hydrogen Sulfide Corrosion of Carbon Steel, CORROSION 2015, paper no. 5933, Dallas, TX, 2015.
35. H. Wu, L. Liu, L. Wang, Y. Liu, Influence of Chromium on Mechanical Properties and CO<sub>2</sub>/H<sub>2</sub>S Corrosion Behavior of P110 Grade Tube Steel, Journal of Iron and Steel Research, International, 2014, 21(1), 76-85.
36. X. Li, H. Hu, G. Cheng, Y. Li, W. Wu, Y. Xia, W. Wu, Numerical Predictions of Mild-Steel Corrosion in a H<sub>2</sub>S Aqueous Environment Without Protective Product Layers, Corrosion, 2017, 73(7), 786-795.
37. D. W. Shoesmith, P. Taylor, M. G. Bailey, D. G. Owen, The Formation of Ferrous Monosulfide Polymorphs During the Corrosion of Iron by Aqueous Hydrogen Sulfide at 21°C, Journal of The Electrochemical Society, 1980, 125, 1007-1015.
38. T. A. Ramanarayanan, S. N. Smith, Corrosion of Iron in Gaseous Environments and in Gas-Saturated Aqueous Environments, Corrosion, 1990, 46(1), 66-74.
39. F. Shi, L. Zhang, J. Yang, M. Lu, J. Ding, H. Li, Polymorphous FeS corrosion products of pipeline steel under highly sour conditions, Corrosion Science, 2016, 102, 103-113.
40. A. R. Lennie, D. J. Vaughan, Spectroscopic studies of iron sulfide formation and phase relations at low temperatures, Mineral Spectroscopy, 1996, 5, 117-131.
41. P. Bai, H. Zhao, S. Zheng, C. Chen, Initiation and developmental stages of steel corrosion in wet H<sub>2</sub>S environments, Corrosion Science, 2015, 93, 109-119.

42. L. Zhang, H. Li, F. Shi, J. Yang, L. Hu, M. Lu, Environmental boundary and formation mechanism of different types of H<sub>2</sub>S corrosion products on pipeline steel, *International Journal of Minerals, Metallurgy, and Materials*, 2017, 24(4), 401-409.
43. S. N. Smith, A proposed Mechanism for Corrosion in Slightly Sour Oil and Gas Production, *CORROSION* 1993, paper no. 1304, Houston, TX, 1993.
44. J. B. Sardisco, R. E. Pitts, Corrosion of Iron in an H<sub>2</sub>S-CO<sub>2</sub>-H<sub>2</sub>O System Composition and Protectiveness of the Sulfide Film as a Function of pH, *Corrosion*, 1965, 21, 350-354.
45. C. Ren, D. Liu, Z. Bai, T. Li, Corrosion behavior of oil tube steel in simulant solution with hydrogen sulfide and carbon dioxide, *Materials Chemistry and Physics*, 2005, 93(2-3), 305-309.
46. M. Liu, J. Wang, W. Ke, E. H. Han, Corrosion Behavior of X52 Anti-H<sub>2</sub>S Pipeline Steel Exposed to High H<sub>2</sub>S Concentration Solutions at 90° C, *Journal of Materials Science & Technology*, 2014, 30(5), 504-510.
47. P. Bai, S. Zheng, H. Zhao, Y. Ding, J. Wu, C. Chen, Investigations of the Diverse Corrosion Products on Steel in a Hydrogen Sulfide Environment, *Corrosion Science*, 2014, 87, 397-406.
48. P. Bai, S. Zheng, C. Chen, H. Zhao, Investigation of the Iron–sulfide Phase Transformation in Nanoscale, *Crystal Growth & Design*, 2014, 14(9), 4295-4302.
49. L. G. Benning, R. T. Wilkin, H. L. Barnes, Reaction Pathways in the Fe–S System Below 100°C, *Chemical Geology*, 2000, 167(1), 25-51.

50. S. Hunger, L. G. Benning, Greigite: a True Intermediate on the Polysulfide Pathway to Pyrite, *Geochemical Transactions*, 2007, 8(1), 1-20.
51. S. Peiffer, T. Behrends, K. Hellige, P. Larese-Casanova, M. Wan, K. Pollok, Pyrite formation and mineral transformation pathways upon sulfidation of ferric hydroxides depend on mineral type and sulfide concentration, *Chemical Geology*, 2015, 400, 44-55.
52. F. E. Jones, G. L. Harris, ITS-90 density of water formulation for volumetric standards calibration, *Journal of research of the National Institute of Standards and Technology*, 1992, 97, 335-340.
53. O. M. Suleimenov, R. E. Krupp, Solubility of hydrogen sulfide in pure water and in NaCl solutions, from 20 to 320°C and at saturation pressures, *Geochimica et Cosmochimica Acta*, 1994, 58(11), 2433-2444.
54. O. M. Suleimenov, T. M. Seward, A spectrophotometric study of hydrogen sulphide ionisation in aqueous solutions to 350°C, *Geochimica et Cosmochimica Acta*, 1997, 61(24), 5187-5198.
55. J. Ning, Y. Zheng, D. Young, B. Brown, S. Netic, Thermodynamic Study of Hydrogen Sulfide Corrosion of Mild Steel, *Corrosion*, 2014, 70(4), 375-389.
56. Y. Zheng, B. Brown, S. Netic, Electrochemical Study and Modeling of H<sub>2</sub>S Corrosion of Mild Steel, *Corrosion*, 2014, 70(4), 351-365.
57. R. Thodla, F. Gui, K. Evans, C. Joia, I. P. Baptista, Corrosion Fatigue Performance of Duplex 2507 for Riser Applications, *CORROSION 2010*, paper no. 10312, San Antonio, TX, 2010.

58. J. Ning, Y. Zheng, B. Brown, D. Young, S. Netic, Construction and Verification of Pourbaix Diagrams for Hydrogen Sulfide Corrosion of Mild Steel, CORROSION 2015, paper no. 5507, Dallas, TX, 2015.
59. D. D. N. Singh, A. Kumar, A Fresh Look at ASTM G 1-90 Solution Recommended for Cleaning of Corrosion Products Formed on Iron and Steels, Corrosion, 2003, 59(11), 1029-1036.
60. S. Netic, S. Wang, H. Fang, W. Sun, J. K. Lee, A New Updated Model of CO<sub>2</sub>/H<sub>2</sub>S Corrosion in Multiphase Flow, CORROSION 2008, paper no. 08535, New Orleans, LA, 2008.
61. J. Ning, Y. Zheng, B. Brown, D. Young, S. Netic, The Role of Iron Sulfide Polymorphism in Localized H<sub>2</sub>S Corrosion of Mild Steel, Corrosion, 2017, 73(2), 155-168.
62. T. Tanupabrungrun, B. Brown, S. Netic, Effect of pH on CO<sub>2</sub> corrosion of mild steel at elevated temperatures, CORROSION 2013, paper no. 2348, Orlando, FL, 2013.
63. M. Rohwerder, M. Stratmann, Surface modification by ordered monolayers: new ways of protecting materials against corrosion, MRS Bulletin, 1999, 24(7), 43-47.
64. S. Gao, P. Jin, B. Brown, D. Young, S. Netic, M. Singer, Corrosion behavior of mild steel in sour environments at elevated temperatures, Corrosion, 2017, 73, 915-926.
65. Y. Zheng, J. Ning, B. Brown, S. Netic, Advancement in predictive modeling of mild steel corrosion in CO<sub>2</sub>- and H<sub>2</sub>S-containing environments, Corrosion, 2016, 72, 679-691.

66. P. Sarin, V. L. Snoeyink, D. A. Lytle, W. M. Kriven, Iron corrosion scales: model for scale growth, iron release, and colored water formation, *Journal of Environmental Engineering*, 2004, 130, 364-373.
67. T. Borch, A. K. Camper, J. A. Biederman, P. W. Butterfield, R. Gerlach, J. E. Amonette, Evaluation of characterization techniques for iron pipe corrosion products and iron oxide thin films, *Journal of Environmental Engineering*, 2008, 134, 835-844.
68. W. Sun, D. V. Pugh, S. Ling, R. V. Reddy, J. L. Pacheco, R.S. Nisbet, N. M. Nor, M. S. Kersey, L. Morshidi, Understanding and Quantifying Corrosion of L80 Carbon Steel, *CORROSION* 2011, paper no. 11063, Houston TX, 2011.
69. J. S. Smith, J. D. Miller, Nature of sulfides and their corrosive effect on ferrous metals: a review, *British Corrosion Journal*, 1975, 10(3), 136-143.
70. S. N. Smith, J. L. Pacheco, Prediction of corrosion in slightly sour environments, *CORROSION* 2002, paper no. 02241, Houston, TX, 2002.
71. I. H. Omar, Y. M. Gunaltun, J. Kvalekval, A. Dugstad, H<sub>2</sub>S corrosion of carbon steel under simulated kashagan field conditions, *CORROSION* 2005, paper no. 05300, Houston, TX, 2005.
72. Z. F. Yin, W. Z. Zhao, Z. Q. Bai, Y. R. Feng, W. J. Zhou, Corrosion behavior of SM 80SS tube steel in stimulant solution containing H<sub>2</sub>S and CO<sub>2</sub>, *Electrochimica Acta*, 2008, 53(10), 3690-3700.
73. M. Singer, A. Camacho, B. Brown, S. Nesic, Sour Top-of-the-Line Corrosion in the Presence of Acetic Acid, *Corrosion*, 2011, 67, 085003-1-085003-16.

74. B. Yuan, W. Luan, S. Tu, J. Wu, One-step synthesis of pure pyrite FeS<sub>2</sub> with different morphologies in water, *New Journal of Chemistry*, 2015, 39, 3571-3577.
75. Y. Liang, P. Bai, J. Zhou, T. Wang, B. Luo, S. Zheng, An efficient precursor to synthesize various FeS<sub>2</sub> nanostructures via a simple hydrothermal synthesis method, *CrystEngComm*, 2016, 18, 6262-6271.
76. H. Xian, J. Zhu, X. Liang, H. He, Morphology controllable syntheses of micro- and nano-iron pyrite mono- and poly-crystals: a review, *RSC Advances*, 2016, 6, 31988-31999.
77. S. Gao, P. Jin, B. Brown, D. Young, S. Netic, M. Singer, Effect of High Temperature on the Aqueous H<sub>2</sub>S Corrosion of Mild Steel, *Corrosion*, 2017, 73(10), 1188-1191.
78. S. Gao, B. Brown, D. Young, S. Netic, M. Singer, Formation of Iron Oxide and Iron Sulfide at High Temperature and Their Effects on Corrosion, *Corrosion Science*, 2018, 135, 167-176.
79. J. Ning, Y. Zheng, B. Brown, D. Young, S. Netic, A Mechanistic Study of the Role of Pyrite in Localized Corrosion of Mild Steel, *CORROSION 2018*, paper no. 10905, Phoenix, AZ, 2018.
80. S. Gao, B. Brown, D. Young, S. Netic, M. Singer, Formation Mechanisms of Iron Oxide and Iron Sulfide at High Temperature in Aqueous H<sub>2</sub>S Corrosion Environment, *Journal of Electrochemical Society*, 2018, 165(3), C171-C179.
81. H. S. Gadiyar, N. S. D. Elayathu, Corrosion and Magnetite Growth on Carbon Steels in Water at 310°C – Effect of Dissolved Oxygen, pH, and EDTA Addition, *Corrosion*, 1980, 36(6), 306-312.

82. J. Robertson, the Mechanism of High Temperature Aqueous Corrosion of Steel, *Corrosion Science*, 1989, 29(11-12), 1275-1291.
83. G. Y. Lai, *High-Temperature Corrosion and Materials Applications*, ASM International, 2007.
84. G. A. Henshall, Numerical Predictions of Dry Oxidation of Iron and Low-Carbon Steel at Moderately Elevated Temperatures, 1996 Fall meeting of the Materials Research Society (MRS).
85. N. Bertrand, C. Desgranges, D. Poquillon, M. C. Lafont, D. Monceau, Iron Oxidation at Low Temperature (260-500°C) in Air and the Effect of Water Vapor, *Oxidation of Metals*, 2010, 73(1-2), 139-162.
86. J. M. Eisenberg, C. W. Tobias, C. R. Wilke, Ionic Mass Transfer and Concentration Polarization at Rotating Electrodes, *Journal of the Electrochemical Society*, 1954, 101, 306-320.
87. S. Ieamsupong, Mechanisms of Iron Carbonate Formation on Mild Steel in Controlled Water Chemistry Conditions, Ph.D. thesis, Dept. of Chem. Eng., Ohio University, Athens, OH, 2016.
88. D. Ekawati, T. Berntsen, M. Seiersten, T. Hemmingsen, Effect of Temperature, Bicarbonate, and MEG Concentrations on CO<sub>2</sub> Corrosion of Carbon Steels, *Corrosion*, 2017, 73(9), 1157-1167.
89. F. J. Shipko, D. L. Douglas, Stability of Ferrous Hydroxide Precipitates, *Journal of Physical Chemistry*, 1956, 60(11), 1519-1523.

90. K. L. Straub, M. Benz, B. Schink, Iron Metabolism in Anoxic Environments at Near Neutral pH, *FEMS Microbiology Ecology*, 2001, 34, 181-186.
91. F. T. da Silva, Hydrogen Sulphide Scavenging by Porous Magnetite, *Mineral Processing and Extractive Metallurgy*, 2005, 114, C245-C246.
92. S. S. Hla, D. J. Duffy, L. D. Morpeth, A. Cousins, D. G. Roberts, J. H. Edwards, Investigation of the Effect of H<sub>2</sub>S on the Performance of an Iron/chromium-based High-Temperature Water-gas Shift Catalyst Using Simulated Coal-derived Syngas, *Catalysis Communications*, 2009, 10, 967-970.
93. M. Robineau, A. Romaine, R. Sabot, M. Jeannin, V. Deydier, S. Necib, Ph. Refait, Galvanic Corrosion of Carbon Steel in Anoxic Conditions at 80°C Associated with a Heterogeneous Magnetite (Fe<sub>3</sub>O<sub>4</sub>)/mackinawite (FeS) layer, 2017, 255, 274-285.
94. S. N. Esmaeely, S. Nestic, Reduction Reactions on Iron Sulfides in Aqueous Acidic Solutions, *Journal of The Electrochemical Society*, 2017, 164(12), C664-C670.
95. U. A. Paulus, T. J. Schmidt, H. A. Gasteiger, R. J. Behm, Oxygen reduction on a high-surface area Pt/Vulcan carbon catalyst: a thin-film rotating ring-disk electrode study, *Journal of Electroanalytical Chemistry*, 2001, 495(2), 134-145.
96. B. Y. Yu, S. Y. Kwak, Assembly of magnetite nanocrystals into spherical mesoporous aggregates with a 3-D wormhole-like pore structure, *Journal of Materials Chemistry*, 2010, 20, 8320-8328.
97. S. N. Esmaeely, Galvanic Localized Corrosion of Mild Steel under Iron Sulfide Corrosion Product Layers, Ph.D. thesis, Dept. of Chem. Eng., Ohio University, Athens, OH, 2017.

98. Z. He, R. V. Gudavathy, J. A. Koza, J. A. Switzer, Room-temperature electrochemical reduction of epitaxial magnetite films to epitaxial iron films, *Journal of the American Chemical Society*, 2011, 133, 12358-12361.
99. A. Kahyarian, Corrosion in Weak Acid Solution, CCJIP Board Meeting, Athens OH, April 2018.
100. D. Rickard, Kinetics of pyrite formation by the H<sub>2</sub>S oxidation of iron (II) monosulfide in aqueous solutions between 25 and 125°C: The rate equation, *Geochimica et Cosmochimica*, 1997, 61(1), 115-134.
101. D. Rickard, G. W. Luther, Chemistry of Iron Sulfides, *Chemical Reviews*, 2007, 107, 514-562.
102. Z. Ma, Y. Yang, B. Brown, S. Nescic, M. Singer, Investigation of FeCO<sub>3</sub> and FeS Precipitation Kinetics by EQCM, CORROSION 2018, paper no. 11192, Phoenix, AZ, 2018.
103. S. Nescic, K. L. J. Lee, A mechanistic model for carbon dioxide corrosion of mild steel in the presence of protective iron carbonate films part 3: film growth model, *Corrosion*, 2003, 59(7), 616-628.
104. L. Pisani, Simple expression for the tortuosity of porous media, *Transport in Porous Media*, 2011, 88(2), 193-203.

### Appendix I: Thermodynamic (Pourbaix Diagrams) Calculation

This section presents a full description of the Pourbaix diagram calculations, which are based entirely on an approach initially implemented by Ning [32].

For an electrochemical reaction at equilibrium, the Gibbs energy change  $\Delta G$  (kJ/mol) is:

$$\Delta G = -zFE_{rev} \quad (65)$$

where  $z$  is the number of electrons transferred,  $F$  is Faraday's constant,  $E_{rev}$  reversible potential (V). At a given condition,  $E_{rev}$  can be calculated according to the Nernst equation:

$$E_{rev} = E_{rev}^o - \frac{RT}{zF} \sum_{i=1}^k \ln(c_i)^{n_i} \quad (66)$$

where  $c_i$  is the concentration of species  $i$ ,  $n_i$  is the corresponding stoichiometry constant of the reaction,  $E_{rev}^o$  is the standard reversible potential that can be obtained from the standard (298.15 K) Gibbs energy change  $\Delta G^o$ :

$$E_{rev}^o = -\frac{\Delta G^o}{zF} \quad (67)$$

The Gibbs energy change  $\Delta G$  can be calculated based on Gibbs energy of formation  $G_f(i)$  of the species in the reaction:

$$\Delta G = \sum_{i=1}^k n_i G_f(i) \quad (68)$$

For example, the Gibbs energy change and reversible potential of the Fe dissolution reaction (64) can be written as:



$$\Delta G = G_f(Fe) - G_f(Fe^{2+}) - 2G_f(e^{-}) \quad (69)$$

$$E_{rev(Fe^{2+}/Fe)} = E_{rev(Fe^{2+}/Fe)}^{\circ} - \frac{RT}{2F} \ln \frac{1}{[Fe^{2+}]} \quad (70)$$

$G_f(i)$  can be obtained at different temperatures from the thermodynamic data such as heat capacity  $C_p$  (J/mol/K) and standard entropy  $S_{298.15}^{\circ}$  (J/mol/K):

$$G_f(i) = \Delta G^{\circ} + \int_{298.15}^T C_p dT - T \int_{298.15}^T \frac{C_p}{T} dT - \Delta T \cdot S_{298.15}^{\circ} \quad (71)$$

All the thermodynamic data of the species considered in this study is summarized in Table 19. All the reactions considered in this study and their equilibrium potentials are summarized in Table 20.

Table 19. Thermodynamic data of species considered in current study.

Species	$\Delta G^{\circ}$ (kJ/mol)	$S_{298.15}^{\circ}$ (J/mol/K)	$C_p = a + bT + cT^{-2} + dT^2$ (J/mol/K)			
			$a$	$b \times 10^3$	$c \times 10^{-6}$	$d \times 10^6$
H <sup>+</sup> (aq)	0	0	0	0	0	0
H <sub>2</sub> S (g)	-33.329	205.757	34.911	10.686	-0.448	0
H <sub>2</sub> O (l)	-237.141	69.948	20.335	109.198	2.033	0
H <sub>2</sub> (g)	0	130.679	26.882	3.586	0.105	0
O <sub>2</sub> (g)	0	205.146	29.154	6.477	-0.184	-1.017
Fe (s)	0	27.28	28.18	-7.32	-0.29	25
Fe <sup>2+</sup> (aq)	-91.5	-105.6	-2	0	0	0
Fe <sup>3+</sup> (aq)	-17.24	-276.94	-143	0	0	0
Fe <sub>2</sub> O <sub>3</sub> (s) *	-743.523	87.4	-838.61	-2343.4	0	605.19
Fe <sub>3</sub> O <sub>4</sub> (s) **	-1017.438	146.14	2659.1	-2521.53	20.734	1368
Fe(OH) <sub>2</sub> (s)	-491.969	87.864	116.064	8.648	-2.874	0
FeS (s) mackinawite	-100.07	56.52	44.685	19.037	-0.289	0

Table 19 continued.

Species	$\Delta G^o$ (kJ/mol)	$S_{298.15}^o$ (J/mol/K)	$C_p = a + bT + cT^{-2} + dT^2$ (J/mol/K)			
			$a$	$b \times 10^3$	$c \times 10^{-6}$	$d \times 10^6$
Fe <sub>3</sub> S <sub>4</sub> (s) greigite	-311.88	182.13	143.344	76.567	0	0
FeS (s) pyrrhotite	-101.95	60.291	72.802	0	0	0
FeS <sub>2</sub> (s) pyrite	-160.06	52.928	60.952	141	-0.987	0
* $C_p(Fe_2O_3) = a + bT + cT^{-2} + dT^2 + fT^{0.5} + gT^{-1}$ , $f=86.525$ , $g=27821$						
** $C_p(Fe_3O_4) = a + bT + cT^{-2} + dT^2 + eT^{-0.5}$ , $e=-36460$						

Table 20. Equilibrium reactions considered in current study.

No.	Reaction	Equilibrium potential or pH
H	$2H^+ + 2e^- \Leftrightarrow H_2$	$E_{rev(H^+/H_2)} = E_{rev(H^+/H_2)}^o - \frac{RT}{2F} \ln \frac{pH_2}{[H^+]^2}$
O	$O_2 + 2H^+ + 4e^- \Leftrightarrow 2H_2O$	$E_{rev(O_2/H_2O)} = E_{rev(O_2/H_2O)}^o - \frac{RT}{4F} \ln \frac{1}{pO_2 \cdot [H^+]^4}$
1	$Fe^{2+} + 2e^- \Leftrightarrow Fe$	$E_{rev(Fe^{2+}/Fe)} = E_{rev(Fe^{2+}/Fe)}^o - \frac{RT}{2F} \ln \frac{1}{[Fe^{2+}]}$
2	$Fe^{3+} + e^- \Leftrightarrow Fe^{2+}$	$E_{rev(Fe^{3+}/Fe^{2+})} = E_{rev(Fe^{3+}/Fe^{2+})}^o - \frac{RT}{F} \ln \frac{[Fe^{2+}]}{[Fe^{3+}]}$
3	$Fe^{2+} + 2H_2O \Leftrightarrow Fe(OH)_2 + 2H^+$	$pH_{Fe^{2+}/Fe(OH)_2} = -0.5 \log \left( K_{(Fe^{2+}/Fe(OH)_2)} [Fe^{2+}] \right)$
4	$Fe(OH)_2 + 2H^+ + 2e^- \Leftrightarrow Fe + 2H_2O$	$E_{rev(Fe(OH)_2/Fe)} = E_{rev(Fe(OH)_2/Fe)}^o - \frac{RT}{2F} \ln \frac{1}{[H^+]^2}$
5	$Fe_3O_4 + 2H_2O + 2H^+ + 2e^- \Leftrightarrow 3Fe(OH)_2$	$E_{rev(Fe_3O_4/Fe(OH)_2)} = E_{rev(Fe_3O_4/Fe(OH)_2)}^o - \frac{RT}{2F} \ln \frac{1}{[H^+]^2}$
6	$6Fe_2O_3 + 4H^+ + 4e^- \Leftrightarrow 4Fe_3O_4 + 2H_2O$	$E_{rev(Fe_2O_3/Fe_3O_4)} = E_{rev(Fe_2O_3/Fe_3O_4)}^o - \frac{RT}{4F} \ln \frac{1}{[H^+]^4}$
7	$Fe_3O_4 + 8H^+ + 2e^- \Leftrightarrow 3Fe^{2+} + 4H_2O$	$E_{rev(Fe_3O_4/Fe^{2+})} = E_{rev(Fe_3O_4/Fe^{2+})}^o - \frac{RT}{2F} \ln \frac{[Fe^{2+}]^3}{[H^+]^8}$
8	$2Fe_2O_3 + 12H^+ + 4e^- \Leftrightarrow 4Fe^{2+} + 6H_2O$	$E_{rev(Fe_2O_3/Fe^{2+})} = E_{rev(Fe_2O_3/Fe^{2+})}^o - \frac{RT}{4F} \ln \frac{[Fe^{2+}]^4}{[H^+]^{12}}$

Table 20 continued.

No.	Reaction	Equilibrium potential or pH
9	$2Fe^{3+} + 3H_2O \Leftrightarrow Fe_2O_3 + 6H^+$	$pH_{(Fe^{3+}/Fe_2O_3)} = -\frac{1}{6} \log(K_{(Fe^{3+}/Fe_2O_3)} [Fe^{3+}]^2)$
10	$FeS_m + 2H^+ + 2e^- \Leftrightarrow Fe + H_2S(g)$	$E_{rev(FeS_m/Fe)} = E_{rev(FeS_m/Fe)}^o - \frac{RT}{2F} \ln \frac{pH_2S}{[H^+]^2}$
11	$FeS_m + 2H^+ \Leftrightarrow Fe^{2+} + H_2S(g)$	$pH_{(FeS_m/Fe^{2+})} = -0.5 \log \left( \frac{[Fe^{2+}] pH_2S}{K_{(FeS_m/Fe^{2+})}} \right)$
12	$Fe_2O_3 + 2H_2S(g) + 2H^+ + 2e^- \Leftrightarrow 2FeS_m + 3H_2O$	$E_{rev(Fe_2O_3/FeS_m)} = E_{rev(Fe_2O_3/FeS_m)}^o - \frac{RT}{2F} \ln \frac{1}{pH_2S^2 [H^+]^2}$
13	$Fe_3O_4 + 3H_2S(g) + 2H^+ + 2e^- \Leftrightarrow 3FeS_m + 4H_2O$	$E_{rev(Fe_3O_4/FeS_m)} = E_{rev(Fe_3O_4/FeS_m)}^o - \frac{RT}{2F} \ln \frac{1}{pH_2S^3 [H^+]^2}$
14	$Fe(OH)_2 + H_2S(g) \Leftrightarrow FeS_m + 2H_2O$	$K_{(Fe(OH)_2/FeS_m)} = \frac{1}{pH_2S}$
15	$Fe_3S_4 + 8H^+ + 8e^- \Leftrightarrow 3Fe + 4H_2S(g)$	$E_{rev(Fe_3S_4/Fe)} = E_{rev(Fe_3S_4/Fe)}^o - \frac{RT}{8F} \ln \frac{pH_2S^4}{[H^+]^8}$
16	$Fe_3S_4 + 8H^+ + 2e^- \Leftrightarrow 3Fe^{2+} + 4H_2S(g)$	$E_{rev(Fe_3S_4/Fe^{2+})} = E_{rev(Fe_3S_4/Fe^{2+})}^o - \frac{RT}{2F} \ln \frac{[Fe^{2+}]^3 pH_2S^4}{[H^+]^8}$
17	$3Fe^{3+} + 4H_2S(g) + e^- \Leftrightarrow Fe_3S_4 + 8H^+$	$E_{rev(Fe^{3+}/Fe_3S_4)} = E_{rev(Fe^{3+}/Fe_3S_4)}^o - \frac{RT}{F} \ln \frac{[H^+]^8}{[Fe^{3+}]^3 pH_2S^4}$
18	$3Fe_2O_3 + 8H_2S(g) + 2H^+ + 2e^- \Leftrightarrow 2Fe_3S_4 + 9H_2O$	$E_{rev(Fe_2O_3/Fe_3S_4)} = E_{rev(Fe_2O_3/Fe_3S_4)}^o - \frac{RT}{2F} \ln \frac{1}{[H^+]^2 pH_2S^8}$
19	$Fe_3S_4 + 2H^+ + 2e^- \Leftrightarrow 3FeS_m + H_2S(g)$	$E_{rev(Fe_3S_4/FeS_m)} = E_{rev(Fe_3S_4/FeS_m)}^o - \frac{RT}{2F} \ln \frac{pH_2S}{[H^+]^2}$
20	$FeS_p + 2H^+ + 2e^- \Leftrightarrow Fe + H_2S(g)$	$E_{rev(FeS_{pyrrhotite}/Fe)} = E_{rev(FeS_{pyrrhotite}/Fe)}^o - \frac{RT}{2F} \ln \frac{pH_2S}{[H^+]^2}$
21	$FeS_p + 2H^+ \Leftrightarrow Fe^{2+} + H_2S(g)$	$pH_{(FeS_{pyrrhotite}/Fe^{2+})} = -0.5 \log \left( \frac{pH_2S [Fe^{2+}]}{K_{(FeS_{pyrrhotite}/Fe^{2+})}} \right)$
22	$Fe_2O_3 + 2H_2S(g) + 2H^+ + 2e^- \Leftrightarrow 2FeS_p + 3H_2O$	$E_{rev(Fe_2O_3/FeS_{pyrrhotite})} = E_{rev(Fe_2O_3/FeS_{pyrrhotite})}^o - \frac{RT}{2F} \ln \frac{1}{pH_2S^2 [H^+]^2}$
23	$Fe_3S_4 + 2H^+ + 2e^- \Leftrightarrow 3FeS_p + H_2S(g)$	$E_{rev(Fe_3S_4/FeS_{pyrrhotite})} = E_{rev(Fe_3S_4/FeS_{pyrrhotite})}^o - \frac{RT}{2F} \ln \frac{pH_2S}{[H^+]^2}$
24	$FeS_{Pyrrhotite} \Leftrightarrow FeS_{Machinawite}$	$K_{(FeS_p/FeS_m)} = 1$

Table 20 continued.

No.	Reaction	Equilibrium potential or pH
25	$FeS_2 + 4H^+ + 2e^- \Leftrightarrow Fe^{2+} + 2H_2S(g)$	$E_{rev(FeS_2/Fe^{2+})} = E_{rev(FeS_2/Fe^{2+})}^o - \frac{RT}{2F} \ln \frac{[Fe^{2+}]pH_2S^2}{[H^+]^4}$
26	$FeS_2 + 4H^+ + 4e^- \Leftrightarrow Fe + 2H_2S(g)$	$E_{rev(FeS_2/Fe)} = E_{rev(FeS_2/Fe)}^o - \frac{RT}{4F} \ln \frac{pH_2S^2}{[H^+]^4}$
27	$2FeS_2 + 3H_2O + 2H^+ + 2e^- \Leftrightarrow Fe_2O_3 + 4H_2S(g)$	$E_{rev(Fe_2O_3/FeS_2)} = E_{rev(Fe_2O_3/FeS_2)}^o - \frac{RT}{2F} \ln \frac{pH_2S^4}{[H^+]^2}$
28	$FeS_2 + 2H^+ + 2e^- \Leftrightarrow FeS_{Machinawite} + H_2S(g)$	$E_{rev(FeS_m/FeS_2)} = E_{rev(FeS_m/FeS_2)}^o - \frac{RT}{2F} \ln \frac{pH_2S}{[H^+]^2}$
29	$FeS_2 + 2H^+ + 2e^- \Leftrightarrow FeS_{Pyrrhotite} + H_2S(g)$	$E_{rev(FeS_{pyrrhotite}/FeS_2)} = E_{rev(FeS_{pyrrhotite}/FeS_2)}^o - \frac{RT}{2F} \ln \frac{pH_2S}{[H^+]^2}$
30	$FeS_2 + 4H^+ + e^- \Leftrightarrow Fe^{3+} + 2H_2S(g)$	$E_{rev(Fe^{3+}/FeS_2)} = E_{rev(Fe^{3+}/FeS_2)}^o - \frac{RT}{F} \ln \frac{[Fe^{3+}]pH_2S^2}{[H^+]^4}$
31	$3FeS_2 + 4H^+ + 4e^- \Leftrightarrow Fe_3S_4 + 2H_2S(g)$	$E_{rev(Fe_3S_4/FeS_2)} = E_{rev(Fe_3S_4/FeS_2)}^o - \frac{RT}{4F} \ln \frac{pH_2S^2}{[H^+]^4}$

## Appendix II: Calculation Parameters for the Electrochemical Reactions

Table 21 summarizes the calculation parameters for all the electrochemical reactions used in the current kinetic model [9].

Table 21. Calculation parameters for the electrochemical reactions

Fe dissolution: $Fe \rightarrow Fe^{2+} + 2e^-$
$i_{Fe} = i_{0,Fe} \times 10^{\frac{\eta}{b_a}}$ $i_{0,Fe} = i_{0,Fe}^{ref} \times \theta_{HS^-} \times e^{-\frac{\Delta H}{T}(\frac{1}{T} - \frac{1}{T_{ref}})}$ $i_{0,Fe}^{ref} = 0.33 A / m^2, \Delta H = 37.5 kJ / mol, T_{ref} = 293.15 K$ $\theta_{HS^-} = \frac{K_2 c_{HS^-}}{1 + K_2 c_{HS^-}}, K_2 = 3.5 \times 10^6$ $\eta = E - E_{rev}, E_{rev} = -0.488 V$ $b_a = \frac{2.303 RT}{\alpha F}, \alpha = 1.5$
H <sup>+</sup> reduction: $2H^+ + 2e^- \rightarrow H_2$

Table 20 continued.

$i_{H^+} = i_{0,H^+} \times 10^{\frac{\eta}{b_c}}$ $i_{0,H^+} = i_{0,H^+}^{ref} \times \left( \frac{c_{H^+}^2}{c_{H^+,ref}^2} \right)^{0.5} \times e^{\frac{\Delta H}{T} \left( \frac{1}{T} - \frac{1}{T_{ref}} \right)}$ $i_{0,H^+}^{ref} = 0.03 A / m^2, c_{H^+,ref} = 1 \times 10^{-4} mol / L, \Delta H = 30 kJ / mol, T_{ref} = 293.15 K$ $\eta = E - E_{rev}, E_{rev} = 0 V$ $b_c = \frac{2.303 RT}{\alpha F}, \alpha = 0.5$
H <sub>2</sub> S reduction: $2H_2S + 2e^- \rightarrow H_2 + 2HS^-$
$i_{H_2S} = i_{0,H_2S} \times 10^{\frac{\eta}{b_c}}$ $i_{0,H_2S} = i_{0,H_2S}^{ref} \times c_{H_2S}^{0.2} \times c_{H_2S,ref}^{0.3} \times e^{\frac{\Delta H}{T} \left( \frac{1}{T} - \frac{1}{T_{ref}} \right)}$ $i_{0,H_2S}^{ref} = 1.5 \times 10^{-4} A / m^2, c_{H_2S,ref} = 1 \times 10^{-4} mol / L, \Delta H = 60 kJ / mol, T_{ref} = 293.15 K$ $\eta = E - E_{rev}, E_{rev} = 0 V$ $b_c = \frac{2.303 RT}{\alpha F}, \alpha = 0.5$
H <sub>2</sub> O reduction: $2H_2O + 2e^- \rightarrow H_2 + 2OH^-$

Table 20 continued.

$$i_{H_2O} = i_{0,H_2O} \times 10^{-\frac{\eta}{b_c}}$$

$$i_{0,H_2O} = i_{0,H_2O}^{ref} \times c_{H_2S,ref}^{0.1} \times c_{H^+,ref}^{0.5} \times e^{-\frac{\Delta H}{T} \left( \frac{1}{T} - \frac{1}{T_{ref}} \right)}$$

$$i_{0,H_2O}^{ref} = 1 \times 10^{-6} \text{ A / m}^2, c_{H_2S,ref} = 1 \times 10^{-4} \text{ mol / L}, c_{H^+,ref} = 1 \times 10^{-4} \text{ mol / L}$$

$$\Delta H = 90 \text{ kJ / mol}, T_{ref} = 293.15 \text{ K}$$

$$\eta = E - E_{rev}, E_{rev} = 0 \text{ V}$$

$$b_c = \frac{2.303RT}{\alpha F}, \alpha = 0.5$$

### Appendix III: Mass Transfer Characterization in the Autoclave

#### Experimental

Before performing the high temperature experiment, the mass transfer characteristics in the 4 L autoclave were defined in deaerated equimolar aqueous solution of 0.01 M  $K_3Fe(CN)_6$  + 0.01 M  $K_4Fe(CN)_6 \cdot 3H_2O$  + 0.5 M KOH. The ferri-ferrocyanide redox reaction is given in Reaction (27):



The purpose of these experiments was to determine the mass transfer coefficient necessary to calculate the limiting current associated with the electrochemical reactions. This set of coupled electrochemical reactions is typically used to study mass transfer for various types of flow geometries and hydrodynamics [86], [87]. This series of potentiodynamic sweeps were also conducted on nickel electrode at 40°C and 80°C. The same setup and procedures were applied as in Section 10.2.2. otherwise stated.

#### Mass transfer correlation

The potentiodynamic sweeps performed on Ni electrode in 0.5 M KOH + 0.01 M  $K_3Fe(CN)_6$  + 0.01 M  $K_4Fe(CN)_6 \cdot 3H_2O$  solution are shown in Figure 76. The limiting current in the cathodic part was then recorded and used to calculate the mass transfer coefficient  $k_m$  (m/s) and consequently Sherwood, Reynolds, and Schmidt numbers [86]:

$$k_m = \frac{i_{lim}}{nFC_b} \quad (73)$$

$$Sh = \frac{k_m d}{D} \quad (74)$$

$$Re = \frac{d^2 N}{\nu} \quad (75)$$

$$Sc = \frac{\nu}{D} \quad (76)$$

where  $D$  diffusion coefficient ( $\text{m}^2/\text{s}$ )

$d$  diameter of impeller (m)

$\nu$  kinematic viscosity ( $\text{m}^2/\text{s}$ )

$N$  revolutions per second (r/s)

$i_{\text{lim}}$  limiting current density ( $\text{A}/\text{m}^2$ )

$n$  number of electrons transferred

$F$  Faraday's constant ( $\text{A}\cdot\text{s}/\text{mol}$ )

$C_b$  concentration of active species ( $\text{mol}/\text{m}^3$ )

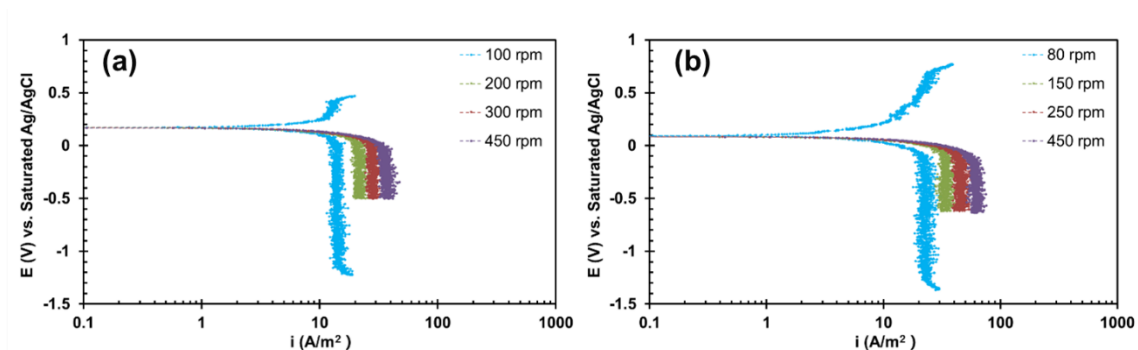


Figure 76. Potentiodynamic sweeps on Ni electrode in 0.5 M KOH + 0.01 M  $\text{K}_3\text{Fe}(\text{CN})_6$  + 0.01 M  $\text{K}_4\text{Fe}(\text{CN})_6 \cdot 3\text{H}_2\text{O}$  solution, (a) 40°C, (b) 80°C, 4 L SS autoclave.

The data was then used to fit the following correlation equation:

$$Sh = a Re^b Sc^c \quad (77)$$

Taking the logarithm gives

$$Sh = \ln a + b \ln Re + c \ln Sc \quad (78)$$

Parameters  $a$ ,  $b$ , and  $c$  can be easily fitted by performing a linear regression, the determined mass transport correlation is:

$$Sh = 0.313 Re^{0.608} Sc^{0.371} \quad (79)$$

The fitted results are shown in Figure 77; a good agreement can be observed.

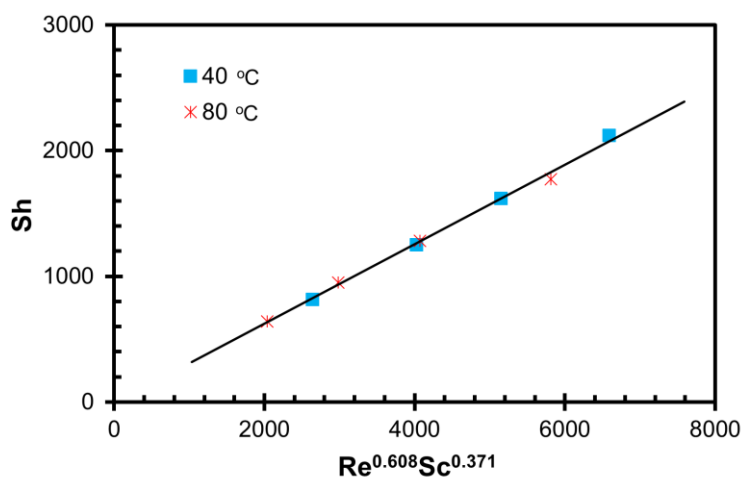


Figure 77. Experimental Sherwood, Reynolds, and Schmidt numbers (points), and Equation (79) fitting (black line), 4 L SS autoclave.

For the high temperature experiments with  $H_2S$ , the 7 L Hastelloy autoclave was used rather than the 4 L SS autoclave. The same mass transfer correlation procedure was repeated. The results are shown in Figure 78, Figure 79, and Equation (35).

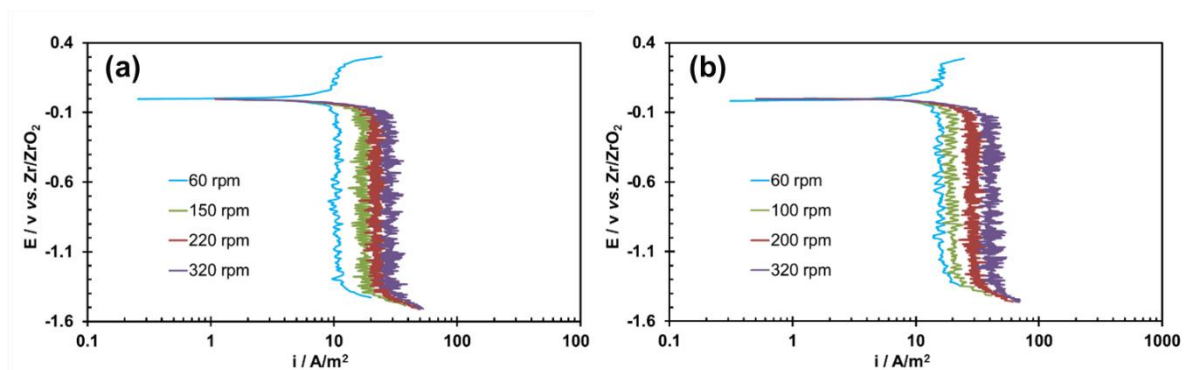


Figure 78. Potentiodynamic sweeps on Ni electrode in 0.5 M KOH + 0.01 M  $\text{K}_3\text{Fe}(\text{CN})_6$  + 0.01 M  $\text{K}_4\text{Fe}(\text{CN})_6 \cdot 3\text{H}_2\text{O}$  solution, (a) 40°C, (b) 60°C, 7 L Hastelloy autoclave.

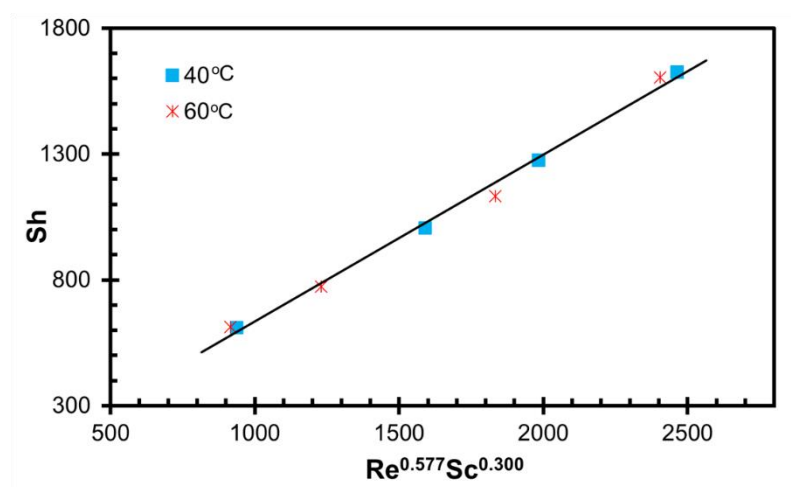


Figure 79. Experimental Sherwood, Reynolds, and Schmidt numbers (points), and equation (80) fitting (black line), 7 L Hastelloy autoclave.

$$Sh = 0.647 Re^{0.577} Sc^{0.300} \quad (80)$$

A low temperature (40°C) experiment was carried out to test the validity of the mass transfer correlation in the 4 L SS autoclave. The polarization curve for X65 steel is shown in Figure 80, by using the mass transfer correlation determined in Equation (34)

and the modeling procedure described in [9], the experimental results are in good agreement with the modeling data. Therefore, the validity of Equation (34) is verified and can be applied in mass transfer correlation.

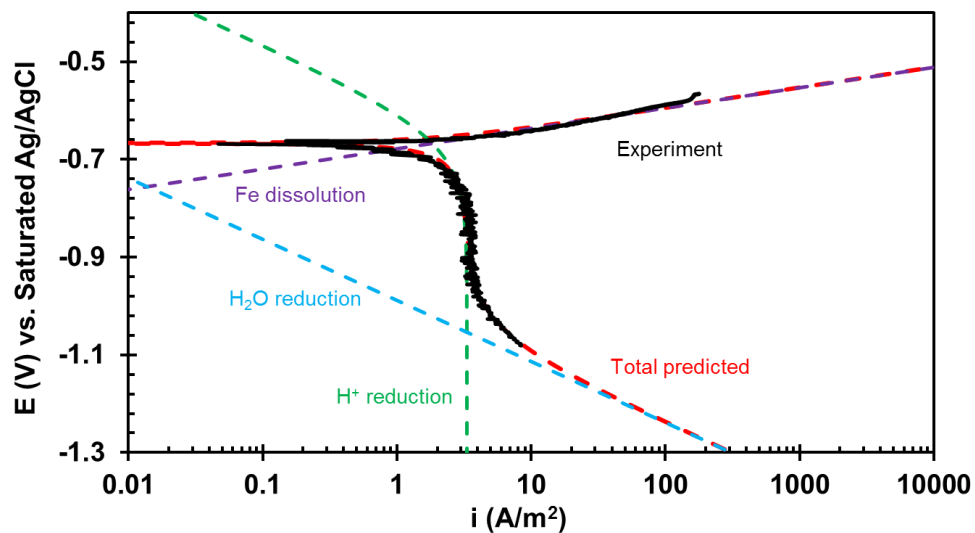


Figure 80. Potentiodynamic sweeps on X65 in 4 L Autoclave, 40°C,  $N_2$ , pH 4.0, 1000 rpm, black line: experiment data, dash lines: modeling data.

## Appendix IV: The Mathematical Derivations for the Mass Conservation Equations

The mass conservation equations presented in Section 10.5 are derived from the original equations [9]. The derivations and assumptions are described below.

### Original equations in Zheng's Model (including CO<sub>2</sub> and HAC, Figure 66)

(F1): H<sup>+</sup> conservation

$$\frac{\partial c_{H^+}_s}{\partial t} = 0 = -\frac{i_{H^+}}{F} + k_{m_{H^+}}(c_{H^+}_b - c_{H^+}_s) + \Delta X \bullet (k_{f_{H_2S}}c_{H_2S}_s - k_{b_{H_2S}}c_{H^+}_s c_{HS^-}_s + k_{f_{HS}}c_{HS}_s - k_{b_{HS}}c_{H^+}_s c_{S^{2-}}_s + k_{f_{wa}} - k_{b_{wa}}c_{H^+}_s c_{OH^-}_s + k_{f_{ca}}c_{H_2CO_3}_s - k_{b_{ca}}c_{HCO_3^-}_s c_{H^+}_s + k_{f_{bi}}c_{HCO_3^-}_s - k_{b_{bi}}c_{CO_3^{2-}}_s c_{H^+}_s + k_{f_{HAC}}c_{HAC}_s - k_{b_{HAC}}c_{H^+}_s c_{Ac^-}_s)$$

(F2): OH<sup>-</sup> conservation

$$\frac{\partial c_{OH^-}_s}{\partial t} = 0 = \frac{i_{H_2O}}{2F} + k_{m_{OH^-}}(c_{OH^-}_b - c_{OH^-}_s) + \Delta X \bullet (k_{f_{wa}} - k_{b_{wa}}c_{H^+}_s c_{OH^-}_s)$$

(F3): H<sub>2</sub>S conservation

$$\frac{\partial c_{H_2S}_s}{\partial t} = 0 = -\frac{i_{H_2S}}{F} + k_{m_{H_2S}}(c_{H_2S}_b - c_{H_2S}_s) + \Delta X \bullet (-k_{f_{H_2S}}c_{H_2S}_s + k_{b_{H_2S}}c_{H^+}_s c_{HS^-}_s)$$

(F4): HS<sup>-</sup> conservation

$$\frac{\partial c_{HS^-}_s}{\partial t} = 0 = \frac{i_{H_2S}}{F} + k_{m_{HS^-}}(c_{HS^-}_b - c_{HS^-}_s) + \Delta X \bullet (k_{f_{H_2S}}c_{H_2S}_s - k_{b_{H_2S}}c_{H^+}_s c_{HS^-}_s - k_{f_{HS}}c_{HS}_s + k_{b_{HS}}c_{H^+}_s c_{S^{2-}}_s)$$

(F5): S<sup>2-</sup> conservation

$$\frac{\partial c_{S^{2-}}_s}{\partial t} = 0 = k_{m_{S^{2-}}}(c_{S^{2-}}_b - c_{S^{2-}}_s) + \Delta X \bullet (k_{f_{HS}}c_{HS}_s - k_{b_{HS}}c_{H^+}_s c_{S^{2-}}_s)$$

(F6): CO<sub>2</sub> conservation

$$\frac{\partial c_{CO_2}_s}{\partial t} = 0 = k_{m_{CO_2}}(c_{CO_2}_b - c_{CO_2}_s) + \Delta X \bullet (-k_{f_{hy}}c_{CO_2}_s + k_{b_{hy}}c_{H_2CO_3}_s)$$

(F7): H<sub>2</sub>CO<sub>3</sub> conservation

$$\frac{\partial c_{H_2CO_3}_s}{\partial t} = 0 = -\frac{i_{H_2CO_3}}{F} + k_{m_{H_2CO_3}}(c_{H_2CO_3}_b - c_{H_2CO_3}_s) + \Delta X \bullet (k_{f_{hy}}c_{CO_2}_s - k_{b_{hy}}c_{H_2CO_3}_s - k_{f_{ca}}c_{H_2CO_3}_s + k_{b_{ca}}c_{HCO_3^-}_s c_{H^+}_s)$$

(F8): HCO<sub>3</sub><sup>-</sup> conservation

$$\frac{\partial c_{HCO_3^-}_s}{\partial t} = 0 = \frac{i_{H_2CO_3}}{F} + k_{m_{HCO_3^-}} (c_{HCO_3^-}_b - c_{HCO_3^-}_s) + \Delta x \bullet (k_{f_{ca}} c_{H_2CO_3_s} - k_{b_{ca}} c_{HCO_3^-}_s c_{H^+}_s - k_{f_{bi}} c_{HCO_3^-}_s + k_{b_{bi}} c_{CO_3^{2-}}_s c_{H^+}_s)$$

(F9):  $CO_3^{2-}$  conservation

$$\frac{\partial c_{CO_3^{2-}}_s}{\partial t} = 0 = k_{m_{CO_3^{2-}}} (c_{CO_3^{2-}}_b - c_{CO_3^{2-}}_s) + \Delta x \bullet (k_{f_{bi}} c_{HCO_3^-}_s - k_{b_{bi}} c_{CO_3^{2-}}_s c_{H^+}_s)$$

(F10):  $Fe^{2+}$  conservation

$$\frac{\partial c_{Fe^{2+}}_s}{\partial t} = 0 = \frac{i_{Fe}}{2F} + k_{m_{Fe^{2+}}} (c_{Fe^{2+}}_b - c_{Fe^{2+}}_s)$$

where  $c_{j_s}$  represents the concentration of species  $j$  at the steel surface,  $c_{j_b}$  means that in the bulk solution.  $k_{m_j}$  is the total mass transfer coefficient of species  $j$ ,  $i_j$  is the current of electrochemical reaction  $j$ ,  $\Delta x$  the thickness of mass transfer layer [9].

The current model does not consider  $CO_2$  or  $HAc$ , thus all the terms related to  $CO_2$  and  $HAc$  in (F1) ~ (F10) are eliminated. The concentration  $c_{j_s}$  at the steel surface will become  $c_{j_m}$  at the  $Fe_3O_4/FeS$  interface (middle layer);  $c_{j_s}$  still represents the concentration at the steel surface (steel/ $Fe_3O_4$  interface). In addition, at the  $Fe_3O_4/FeS$  interface,  $Fe_3O_4$  conversion reaction current  $i_{FeS}$  also consumes  $H^+$  and  $H_2S$  (Reaction (19)), which should be added into  $H^+$  and  $H_2S$  conservation equations. At the steel surface (steel/ $Fe_3O_4$  interface), the  $Fe_3O_4$  formation reaction current  $i_{Fe_3O_4}$  generates  $H^+$  and consumes  $Fe^{2+}$  (Reaction (13)), which should be added into the  $H^+$  and  $Fe^{2+}$  conservation equations. Therefore, the above mass conservation become:

Modified equations at the  $Fe_3O_4/FeS$  interface (no  $CO_2$  or  $HAc$ , Figure 67)

(F1):  $H^+$  conservation

$$\frac{\partial c_{H^+}_m}{\partial t} = 0 = -\frac{i_{H^+} + i_{FeS}}{F} + k_{m_{H^+}} (c_{H^+}_b - c_{H^+}_m) - k'_{m_{H^+}} (c_{H^+}_m - c_{H^+}_s) + \Delta x \bullet (k_{f_{H_2S}} c_{H_2S}_m - k_{b_{H_2S}} c_{H^+}_m c_{HS^-}_m + k_{f_{HS}} c_{HS}_s - k_{b_{HS}} c_{H^+}_m c_{S^{2-}}_m + k_{f_{wa}} - k_{b_{wa}} c_{H^+}_m c_{OH^-}_m)$$

(F2): OH<sup>-</sup> conservation

$$\frac{\partial c_{OH^-_m}}{\partial t} = 0 = \frac{i_{H_2O}}{2F} + k_{m_{OH^-}}(c_{OH^-_b} - c_{OH^-_m}) - k'_{m_{OH^-}}(c_{OH^-_m} - c_{OH^-_s}) + \Delta x \bullet (k_{f_{wa}} - k_{b_{wa}} c_{H^+}_m c_{OH^-_m})$$

(F3): H<sub>2</sub>S conservation

$$\frac{\partial c_{H_2S_m}}{\partial t} = 0 = -\frac{2i_{H_2S} + 3i_{FeS}}{2F} + k_{m_{H_2S}}(c_{H_2S_b} - c_{H_2S_m}) + \Delta x \bullet (-k_{f_{H_2S}} c_{H_2S_m} + k_{b_{H_2S}} c_{H^+}_m c_{HS^-_m})$$

(F4): HS<sup>-</sup> conservation

$$\frac{\partial c_{HS^-_m}}{\partial t} = 0 = \frac{i_{H_2S}}{F} + k_{m_{HS^-}}(c_{HS^-_b} - c_{HS^-_m}) + \Delta x \bullet (k_{f_{H_2S}} c_{H_2S_s} - k_{b_{H_2S}} c_{H^+}_m c_{HS^-_m} - k_{f_{HS}} c_{HS^-_m} + k_{b_{HS}} c_{H^+}_m c_{S^{2-}_m})$$

(F5): S<sup>2-</sup> conservation

$$\frac{\partial c_{S^{2-}_m}}{\partial t} = 0 = k_{m_{S^{2-}}}(c_{S^{2-}_b} - c_{S^{2-}_m}) + \Delta x \bullet (k_{f_{HS}} c_{HS^-_m} - k_{b_{HS}} c_{H^+}_m c_{S^{2-}_m})$$

(F6): Fe<sup>2+</sup> conservation

$$\frac{\partial c_{Fe^{2+}_m}}{\partial t} = 0 = k_{m_{Fe^{2+}}}(c_{Fe^{2+}_b} - c_{Fe^{2+}_m}) - k'_{m_{Fe^{2+}}}(c_{Fe^{2+}_m} - c_{Fe^{2+}_s})$$

Additional equations at steel surface (Figure 67)

(F7): H<sup>+</sup> conservation

$$\frac{\partial c_{H^+_s}}{\partial t} = 0 = \frac{4i_{Fe_3O_4}}{F} + k'_{m_{H^+}}(c_{H^+_s} - c_{H^+_m}) + \Delta x \bullet (k_{f_{wa}} - k_{b_{wa}} c_{H^+_s} c_{OH^-_s})$$

(F8): OH<sup>-</sup> conservation

$$\frac{\partial c_{OH^-_s}}{\partial t} = 0 = k'_{m_{OH^-}}(c_{OH^-_m} - c_{OH^-_s}) + \Delta x \bullet (k_{f_{wa}} - k_{b_{wa}} c_{H^+_s} c_{OH^-_s})$$

(F9): Fe<sup>2+</sup> conservation

$$0 = \frac{i_{Fe} - 3i_{Fe_3O_4}}{2F} + k'_{m_{Fe^{2+}}}(c_{Fe^{2+}_s} - c_{Fe^{2+}_m})$$

where  $k'_{m_j}$  is the mass transfer coefficient through Fe<sub>3</sub>O<sub>4</sub> layer.

As it is assumed that the chemical reaction rates for the first and second dissociation of  $H_2S$  are fast [9], (F3) ~ (F5) will become one mass conservation equation for the total sulfide species and two more chemical equilibria equations, (F3') ~ (F5'). The same is true for  $H_2O$  dissociation, i. e.,  $H_2O$  dissociation is also at equilibrium, this gives (F2') and (F8'). Combining (F1) ~ (F5) gives (F1'): (F1') = (F1) – (F2) + (F3) – (F5). Combining (F7) and (F8) gives (F7'): (F7') = (F7) – (F8). (F6) and (F9) are kept as the same. The final equations are summarized below.

At  $Fe_3O_4/FeS$  interface

(F1'):  $H^+$  conservation

$$0 = -(i_{H^+} + i_{H_2S} + i_{H_2O} + \frac{5i_{FeS}}{2})/F + k_{m_{H^+}}(c_{H^+_{-b}} - c_{H^+_{-m}}) + k_{m_{H_2S}}(c_{H_2S_{-b}} - c_{H_2S_{-m}}) - k_{m_{S^{2-}}}(c_{S^{2-}_{-b}} - c_{S^{2-}_{-m}}) - k_{m_{OH^-}}(c_{OH^-_{-b}} - c_{OH^-_{-m}}) - k'_{m_{H^+}}(c_{H^+_{-m}} - c_{H^+_{-s}}) + k'_{m_{OH^-}}(c_{OH^-_{-m}} - c_{OH^-_{-s}})$$

(F2'):  $H_2O$  dissociation

$$c_{H^+_{-m}} * c_{OH^-_{-m}} \approx K_{Wa}$$

(F3'):  $H_2S$  conservation

$$0 = k_{m_{H_2S}}(c_{H_2S_{-b}} - c_{H_2S_{-m}}) + k_{m_{HS^-}}(c_{HS^-_{-b}} - c_{HS^-_{-m}}) + k_{m_{S^{2-}}}(c_{S^{2-}_{-b}} - c_{S^{2-}_{-m}})$$

(F4'):  $HS^-$  equilibrium

$$c_{H^+_{-m}} * c_{HS^-_{-m}} = K_{hs} * c_{H_2S_{-m}}$$

(F5'):  $S^{2-}$  equilibrium

$$c_{H^+_{-m}} * c_{S^{2-}_{-m}} = K_{bs} * c_{HS^-_{-m}}$$

(F6'):  $Fe^{2+}$  conservation

$$0 = -k'_{m_{Fe^{2+}}}(c_{Fe^{2+}_{-m}} - c_{Fe^{2+}_{-s}}) + k_{m_{Fe^{2+}}}(c_{Fe^{2+}_{-b}} - c_{Fe^{2+}_{-m}})$$

At steel surface (steel/Fe<sub>3</sub>O<sub>4</sub> interface)

(F7'): H<sup>+</sup> conservation

$$0 = \frac{4i_{\text{Fe}_3\text{O}_4}}{F} + k'_{m_{\text{H}^+}} (c_{\text{H}^+_{\text{s}}} - c_{\text{H}^+_{\text{m}}}) - k'_{m_{\text{OH}^-}} (c_{\text{OH}^-_{\text{s}}} - c_{\text{OH}^-_{\text{m}}})$$

(F8'): H<sub>2</sub>O dissociation

$$c_{\text{H}^+_{\text{s}}} * c_{\text{OH}^-_{\text{s}}} \approx K_{\text{Wa}}$$

(F9'): Fe<sup>2+</sup> conservation

$$0 = \frac{i_{\text{Fe}} - 3i_{\text{Fe}_3\text{O}_4}}{2F} + k'_{m_{\text{Fe}^{2+}}} (c_{\text{Fe}^{2+}_{\text{s}}} - c_{\text{Fe}^{2+}_{\text{m}}})$$



**OHIO**  
UNIVERSITY

Thesis and Dissertation Services